

INSTITUTE OF PHYSICS PAS

DOCTORAL THESIS

---

# Practical Spin-Squeezing with Ultra-Cold Atoms in Optical Lattices

---

*Author:*

M.Sc. Tanausú Hernández Yanes

*Supervisor:*

Dr. Hab. Emilia Witkowska

September 11, 2024





---

## Abstract

Developing quantum technologies aim to employ quantum phenomena in practical implementations. For instance, more robust quantum cryptography and information tasks, such as self-testing, randomness amplification and expansion, quantum key distribution, and quantum sensing and metrology. Spin squeezed states are such quantum states particularly useful for sensing. They provide improved phase sensitivity over the classical shot-noise limit  $\Delta\phi \propto 1/\sqrt{N}$ . Their quantum fluctuations for the collective spin operator are reduced in one direction at the expense of the fluctuations in the orthogonal direction. This allows for improvement of the phase sensitivity of the state along the reduced fluctuations direction. Spin squeezed states are advantageous over other highly entangled states for metrological applications because they have a sufficiently large mean spin value and are resilient to different types of decoherence processes. While spin squeezed states have been proposed theoretically and even realized experimentally, states entangled close to the theoretical bound  $\Delta\phi \propto 1/N$  are still out of reach. In this thesis we present different setups of ultra-cold atoms in the optical lattice, designed as potentially simple experimental implementations, for dynamical spin squeezing generation from classical coherent states. We propose different additional terms over the bare two-component Fermi- and Bose-Hubbard models like long-range dipolar interactions, spin-orbit coupling, contact interactions anisotropy or inhomogeneous magnetic fields to generate effective models capable of generating maximally squeezed spin-1/2 states. We also analyze how imperfections in the different models affect entanglement generation through parameter detuning, perturbative regimes, or particle losses at the preparation stage.

---

## Abstract (Polish)

Rozwój technologii kwantowych ma na celu wykorzystanie zjawisk kwantowych w praktycznych implementacjach, przykładowo w kryptografii kwantowej i informacji (samotestowanie, wzmocnienie i ekspansja losowości, dystrybucja klucza kwantowego) lub metrologii kwantowej. Stany ściśnięte spinowo to stany kwantowe, które są szczególnie przydatne do niezwykle precyzyjnej metrologii. Zapewniają one czułość fazową lepszą w porównaniu z klasyczną granicą szumu śrutowego  $\Delta\phi \propto 1/\sqrt{N}$ . Ich fluktuacje kwantowe dla kolektywnego operatora spinowego są redukowane w jednym kierunku kosztem fluktuacji w kierunku ortogonalnym. Pozwala to na poprawę czułości fazowej stanu wzdłuż kierunku zmniejszonych fluktuacji. Stany ściśnięte spinowo są korzystniejsze od innych silnie splątanych stanów w zastosowaniach metrologicznych ponieważ mają wystarczająco dużą średnią wartość spinu i są bardziej odporne na różne typy procesów dekoherencji. Podczas gdy stany ze ściśniętym spinem zostały zaproponowane teoretycznie, a nawet zrealizowane w układach ulata-zimnych atomów, to ich praktyczne zastosowanie, w szczególności blisko teoretycznej granicy  $\Delta\phi \propto 1/N$ , jest nadal poza zasięgiem obecnych eksperymentów. W niniejszej rozprawie rozważamy układy ultra-zimnych atomów umieszczonych w periodycznej sieci optycznej, zaprojektowane jako potencjalnie proste implementacje eksperymentalne do dynamicznej generacji stanów ściśniętych spinowo. Rozważając dwuskładnikowe modele Bose– i Fermi–Hubbarda, proponujemy nowe mechanizmy w celu wygenerowania efektywnych modeli zdolnych do generowania maksymalnie ściśniętych stanów. Te mechanizmy są wytwarzane przez fizyczne procesy, t.j. długozasięgowe oddziaływania dipolowe, sprzężenie spin-orbita, anizotropia oddziaływań kontaktowych lub niejednorodne pola magnetyczne. Analizujemy również, w jaki sposób niedoskonałości w przygotowaniu stanów początkowych lub parametrów modelu wpływają na możliwość wytworzenia stanów ściśniętych spinowo oraz ich użyteczność do praktycznych zastosowań.

---

## Authorship attribution statement

This thesis contains nine body chapters and includes a series of published articles that all fit into a cohesive scheme in the context of spin squeezing generation in the optical lattice. These chapters are self-contained and begin with a short motivation, constructing a natural progression with respect to the central topic of the thesis. Chapters may also include results and conclusions made entirely by me which were unpublished because of length or time constraints. These extensions are too short to justify a separate publication on their own, but I expect them to be useful and informative to the reader. Each chapter ends with the compilation of corresponding publications in their original published format. This statement declares my authorship contribution to each chapter of this thesis and acknowledges any editorial help I received and, where appropriate, attributes the co-authors.

All numerical calculations in the following chapters, as well as most calculations in the included published articles, were performed based on exact diagonalization methods using code developed by me. The core library I built and some example scripts can be found in:

<https://gitlab.com/tanahy/1d-hubbard-model>.

I gave detailed explanations on how to implement such calculations from scratch in the course *Lectures on Computational Physics of Cold Atoms*, imparted by Maciej Kruk and I under the supervision of Emilia Witkowska. The course took place in the winter semester of the 2022-2023 academic year at the Institute of Physics of the Polish Academy of Sciences. The course materials can be found in:

<https://gitlab.com/tanahy/cophyca>.

## Chapters 1 to 4 and 9

The contents in Chapter 1 provides an introduction and motivation to the research topic of spin squeezing in the optical lattice. The contents in Chapter 2 introduce the research topic with a historical background on the core concepts and key findings of the phenomena under study, spin squeezing. The contents in Chapter 3 put the focus on the system of interest we use to produce spin squeezed states, ultra-cold atoms in the optical lattice. The contents in Chapter 4 present the necessary background to employ a precise perturbation theory method on many body systems, the Schieffer-Wolff transformation. The contents in Chapter 9 are a brief summary and outlook of the thesis. These chapters were researched and written by me.

## Chapter 5

The research article included in Chapter 5 has been published as:

---

M. Dziurawiec, T. Hernández Yanes, M. Płodzień, M. Gajda, M. Lewenstein, and E. Witkowska, “Accelerating Many-Body Entanglement Generation by Dipolar Interactions in the Bose-Hubbard Model”, *Physical Review A* **107**, 013311 (2023)

*Contribution:* I independently reproduced all the analytical and numerical results. At the time, Marlena Dziurawiec was a Master student doing an internship in our group and we maintained weekly discussions about the project under the supervision and direction of Emilia Witkowska. I supervised Marlena Dziurawiec to help her write her own programs for simulations using exact diagonalization. Once the project advanced, we also started to receive the input of Marcin Płodzień and Mariusz Gajda during our weekly meetings. Marlena Dziurawiec and I prepared the first draft of the publication. We received editorial contributions from the other authors for the final version of the manuscript for publication.

## Chapter 6

The research articles included in Chapter 6 have been published as:

T. Hernández Yanes, M. Płodzień, M. Mackoitis Sinkevičienė, G. Žlabys, G. Juzeliūnas, and E. Witkowska, “One- and Two-Axis Squeezing via Laser Coupling in an Atomic Fermi-Hubbard Model”, *Physical Review Letters* **129**, 090403 (2022)

T. Hernández Yanes, G. Žlabys, M. Płodzień, D. Burba, M. M. Sinkevičienė, E. Witkowska, and G. Juzeliūnas, “Spin Squeezing in Open Heisenberg Spin Chains”, *Physical Review B* **108**, 104301 (2023)

*Contribution:* I am the first author of both publications and was responsible for the numerical simulations. I also contributed to the analytical calculations, in particular to the derivation of the effective models using the Schieffer-Wolff transformation. I produced all the figures, except for Fig. 1 of the second publication. Emilia Witkowska and I wrote the first drafts of the publications. This work was the result of a close collaboration between the two theory groups led by Emilia Witkowska and Gediminas Juzeliūnas, respectively. Emilia Witkowska made the initial proposal of the project, which organically evolved through the collaboration thanks to the collective efforts of the members involved. The analytical framework was developed during our regular meetings with propositions and cross-checking among Emilia Witkowska, Gediminas Juzeliūnas, Giedrius Žlabys and me. Marcin Płodzień provided DMRG calculations for results with large number of particles for the first publication. Domantas Burba contributed in the appendix E in the second publication. All of the authors made editorial contributions for the final versions of the publications.

---

## Chapter 7

The research article included in Chapter 7 has been published as:

T. Hernández Yanes, A. Niezgoda, and E. Witkowska, “Exploring spin squeezing in the Mott insulating regime: Role of anisotropy, inhomogeneity, and hole doping”, *Physical Review B* **109**, 214310 (2024)

*Contribution:* I am the first author of this publication and performed all numerical simulations, except for calculations regarding temperature effects; which were done by Artur Niezgoda. Emilia Witkowska led the research direction and defined the structure of the publication. Emilia Witkowska and I wrote the text of the publication, with minor editorial contributions from Artur Niezgoda. I produced all the figures of the publication.

## Chapter 8

The contents in Chapter 8 are yet to be published, but are the result of a collaboration with the group led by Alice Sinatra. We expect to publish our results in a scientific article soon. The pre-print of the research article can be found as:

T. H. Yanes, Y. Bamaara, A. Sinatra, and E. Witkowska, *Bounds on detection of Bell correlations with entangled ultra-cold atoms in optical lattices under occupation defects*, (Sept. 4, 2024) <http://arxiv.org/abs/2409.02873> (visited on 09/08/2024), pre-published

*Contribution:* I performed all numerical and analytical calculations presented in section V of the attached manuscript. The research direction was the result of a collaboration between Youcef Baamara, Alice Sinatra, Emilia Witkowska and I. The main theoretical model, which we refer to as toy model, was developed through discussions involving all the previously mentioned authors.

In addition to the statements above, in cases where I am not the corresponding author of a published item, permission to include the published material has been granted by the corresponding author.

Tanausú Hernández Yanes, September 11, 2024

As supervisor for the candidature upon which this thesis is based, I can confirm that the authorship attribution statements above are correct.

Emilia Witkowska, September 11, 2024



---

## Acknowledgements

I deeply thank my supervisor Dr. Hab. Emilia Witkowska for giving me the opportunity to work together over these four years in a healthy and highly-driven environment. While the path was never straight, she always managed to guide me in positive and productive directions. Thanks to her guidance I have learned how to be organized, effective, and confident in a research environment in general and in the field of ultra-cold atoms in particular.

I learned a lot from the expertise and astonishing intuition of Prof. Dr. Hab. Gediminas Juzeliūnas. My experience with him, Dr. Giedrius Žlabys, and Dr. Mažena Mackoit Sinkevičienė was invaluable and I remember fondly my short stays in Vilnius. Collaborating with Dr. Youcef Baamara and Prof. Alice Sinatra was a pleasure and our discussions were always eye-opening to me. I also thank M.Sc. Marlena Dziurawiec, Dr. Marcin Płodzień, Dr. Artur Niezgoda, Prof. Dr. Hab. Mariusz Gajda, and Prof. Dr. Maciej Lewenstein. Working with them was an enriching experience and I also owe them the success of our joint research.

I thank Univ. Prof. Dr. Francesca Ferlaino and Dr. Manfred Mark for giving me the opportunity to join their experimental group in Innsbruck and learn more about ultra-cold atoms and dipolar interactions. I particularly thank Dr. Luca Barbiero and my colleagues at the theory sub-group Dr. Thomas Bland, Dr. Pramodh Senarath Yapa, M.Sc. Leonardo Bellinato Giacomelli, and M.Sc. Elena Poli for the scientific discussions, their support, and their warmth.

Prof. Jan Mostowski allowed me to inhabit his office for a good while and gave me nuggets of wisdom which I treasure. For all the coffee breaks, chats and support through my stay at the Institute of Physics, I must thank my colleagues Mgr. Soheil Arbabi, Mgr. Luís Carnevale da Cunha, Mgr. Pamela Smardz, Mgr. Hubert Dunikowski, Dr. King Lun Ng, Dr. Quyen V. Vu, Dr. Paolo Comaron, and Dr. Hab. Piotr Deuar.

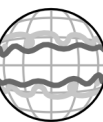
On a more personal note, the support of my family and friends, even from afar, immensely helped me push through the doctorate. The visits of my mother Carmen Rosa, my sister Atasara, my brother-in-law David, my nephew Quebehi, and my friends Alejandro, Jennifer and Itahisa always gave me energy and confidence. But the person I owe the most in this regard is my partner Águeda for her love, care, and unlimited amounts of healthy food for the curious mind. Thank you.

This work was supported by the Polish National Science Center DEC-2019/35/O/ST2/01873. I acknowledge support from the Polish National Agency for Academic Exchange through the Foreign Doctoral Internship Grant NAWA Preludium BIS 1 No. PPN/STA/2021/1/00080. A part of the computations included in this thesis was done at the Centre of Informatics Tricity Academic Supercomputer & Network.



# Contents

<b>Contents</b>	<b>vii</b>
<b>List of Figures</b>	<b>ix</b>
<b>1 Introduction</b>	<b>1</b>
<b>2 Spin Squeezing</b>	<b>5</b>
2.1 Bosonic coherent states . . . . .	5
2.2 Squeezed coherent states . . . . .	6
2.3 Pseudo-spin and collective operators . . . . .	7
2.4 Spin coherent states . . . . .	9
2.5 Spin-squeezing parameter . . . . .	11
2.6 Paradigmatic models . . . . .	18
<b>3 Ultra-cold Atoms in the Optical Lattice</b>	<b>25</b>
3.1 Hubbard model . . . . .	25
3.2 Two-mode model . . . . .	28
3.3 Heisenberg model . . . . .	29
<b>4 Perturbation Theory</b>	<b>39</b>
4.1 Schieffer–Wolff Transformation . . . . .	39
<b>5 Spin Squeezing through Dipolar Interactions in the Superfluid Phase</b>	<b>43</b>
5.1 Dipolar interactions for arbitrary geometry in second quantisation form . . . . .	44
5.2 Effective model under Periodic and Open Boundary Conditions	47
5.3 Limitations of the model . . . . .	50
<b>6 Spin Squeezing through Spin Orbit Coupling in the Mott Insulating Phase</b>	<b>61</b>
6.1 Perturbation theory for the Mott Insulating Phase . . . . .	61
6.2 Squeezing via Spin Orbit Coupling in the Mott Insulating Phase	64
<b>7 Spin Squeezing under Imperfections and Holes</b>	<b>89</b>



---

7.1	Squeezing via Contact Interactions in the Mott Insulating Phase	89
7.2	Squeezing via Inhomogeneous Magnetic Field in the Mott Insulating Phase . . . . .	91
7.3	Effect of hole doping . . . . .	92
7.4	Movement of holes . . . . .	93
<b>8</b>	<b>Entanglement of squeezed states under occupation defects</b>	<b>113</b>
8.1	Two-body Bell Correlator . . . . .	114
8.2	Occupation defects and toy model . . . . .	116
8.3	Realistic implementations . . . . .	117
<b>9</b>	<b>Conclusions</b>	<b>133</b>
	<b>Bibliography</b>	<b>135</b>

# List of Figures

2.1	Bloch sphere representation of the spin directions of interest for a given squeezed state. . . . .	13
2.2	Evolution of the one-axis twisting model (2.55) with $N = 100$ particles for an arbitrary $\chi$ . . . . .	21
2.3	Evolution of the twist and turn model (2.64) with $N = 100$ particles and $\Omega = N\chi/2$ for an arbitrary $\chi$ . . . . .	22
2.4	Evolution of the two-axis counter twisting model (2.68) with $N = 100$ particles for an arbitrary $\chi$ . . . . .	24
5.1	Comparison of the spin-squeezing parameter $\xi^2$ and condensate fraction $f_c$ dynamics between periodic and open boundary conditions for the Hubbard model with dipolar interactions in the Superfluid regime. . . . .	51
6.1	Sketch of energy manifolds and couplings among a selected number of possible states in the Fermi–Hubbard Hamiltonian for a lattice of three sites and two particles of opposite spin. . . . .	62
6.2	Similar sketch as in fig. 6.1, but including the spin-orbit coupling term for a two-site lattice at half-filling. . . . .	64
6.3	Illustrative example of transition from TACT dynamics to OAT dynamics through a linear term. . . . .	67
7.1	Spin squeezing dynamics induced by anisotropy of the contact interactions in the presence of a hole in the system. . . . .	94
7.2	Spin squeezing dynamics induced by an inhomogeneous magnetic field in the presence of a hole in the system. . . . .	95
7.3	Evolution of spin squeezing parameter induced by anisotropy and inhomogeneous magnetic field for different values of the tunnelling rate and filling factor. . . . .	97





# Chapter 1

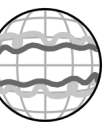
## Introduction

We define the state of a quantum system by a combination of configurations in a given Hilbert space, which yields a certain probability distribution. Such space of configurations can be probed using certain observables that can be measured. For instance a wave-packet of light moving across space can be characterized by the observables  $\hat{x}, \hat{p}$ . These observables are conjugate if their commutator  $[\hat{x}, \hat{p}] \equiv \hat{x}\hat{p} - \hat{p}\hat{x} \neq 0$ . Their uncertainties obey the inequality  $\Delta\hat{x}\Delta\hat{p} \geq \hbar/2$ . We certify a minimal variance state when the inequality saturates to an equality, as no quantum state can violate this restriction. Moreover, we can find states where the variance of one observable is reduced with respect to the corresponding conjugate, while saturating the previous inequality. These kind of states yield a sub-binomial distribution, which is tighter in a given direction than a binomial distribution. These states are usually referred to as *squeezed* states, as a reference to the deformation of the probability distribution with respect to the state where the variance is isotropic in the phase space of interest.

In this work, we refer to spin as the quantum number associated with the intrinsic angular momentum of an atom. While this has implications on the statistics of the atoms, as bosons are characterised by integer valued spin and fermions are characterised by half-integer valued spin, we will take the approach of isolating a number of internal energy levels of the atoms to construct a pseudo-spin manifold. This allows us to, for instance, describe spin-1/2 dynamics while using two-level bosons.

The change in statistics allows us to construct different dynamics that are advantageous for squeezing the probability distributions of a state in the pseudo-spin phase space. We refer to this concept as spin squeezing. As we explain later on, defining spin squeezing can be challenging due to the inherent symmetries of the spin phase space. We can nevertheless find satisfactory and compact definitions for metrological purposes [6–8].

Spin squeezed states offer improved sensitivity on spectroscopic measurements in contrast with other classes of highly entangled states [9]. In fact,



spin squeezing itself can be used as a relevant entanglement witness in many scenarios, as it only requires collective measurements and is quite robust to different decoherence channels [10–12]. Because of its collective measurement nature, spin squeezing is also useful in the study of quantum phase transitions [13, 14] and quantum chaos [15, 16]. It is no surprise that spin squeezing is regarded as one of the main quantum resources to probe fundamental physics questions like the electric dipole moment or dark matter [17].

Squeezing generation has been proposed through various methods like feedback loops in quantum non-demolition measurements [18–20] or tweezer arrays [21], quantum state transfer from light to atoms [22, 23], cavity feedback [24], or interactions in magnetic microchip traps (atom chips) for neutral atoms [25]. However, we will focus on dynamical generation of spin squeezing from an uncorrelated state as proposed in the pioneering work of Kitawaga and Ueda in 1993 [6].

To certify spin squeezing, we must first find an adequate definition of it. While bosonic squeezing is well constrained to a given complex plane in which squeezing is easy to represent and derive, spin squeezing happens in the phase space corresponding to the  $SU(2)$  symmetry of the spin components. This requires more careful analysis and generalization to arbitrary spin lengths becomes non-trivial [26]. We will review some of the main definitions of spin squeezing, but we will focus on the well-known definition focused on spectroscopic phase sensitivity for spin-1/2 atoms [7]. This definition is very compact and makes intuitive sense of the main features of spin squeezing, while also having a well defined lower bound to compare our results with [27].

We pay special attention to ultra-cold atoms in the optical lattice as our implementation platform of reference, since it provides high tunability and control while allowing the inclusion of many modifications that make it an ideal quantum simulator for other platforms [28, 29]. In fact, spin squeezing in the optical lattice has received special attention in recent years for its direct application to quantum clocks and quantum sensors [30–32]. Moreover, this platform offers enticing spatial resolution and constrains at the single particle level. Such advantages allow us to study fundamental aspects of correlations under short and long range interactions in ranges of parameters inaccessible to other setups [32, 33]. The optical lattice is also attractive as a platform in which to certify correlations by local measurements. These are not included in the typical definitions of spin squeezing, but can help in probing entanglement more exhaustively.

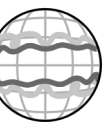
While some of the results derived in this work are applicable to higher dimensional systems, we mainly concern ourselves with one-dimensional systems. Low dimensional systems are simpler to describe, analyse and engineer. They also have an advantage in constraining the degrees of freedom such that we may find different behaviour with respect to higher dimensional systems.

States composed of particles with spin  $j > 1/2$  are also subject to spin squeezing [34, 35] and are experimentally relevant [36]. In fact, spin squeezing

definitions have been generalised to large spin in the past and are the main subject of current works [26, 37, 38]. Nevertheless, we limit our analysis to spin-1/2 particles to obtain a solid understanding of the phenomena and serve as a stepping stone for richer studies in higher spin manifolds in the future.

We employ different kinds of external fields and couplings among atoms in the optical lattice to generate the required correlations during dynamics and obtain highly squeezed states. In the first chapters of this work we introduce the main concepts and tools to perform the required approximations and obtain effective models which describe squeezing dynamics in the rest of the work. In the following chapters we explore long-range dipolar interactions in the superfluid phase of the Bose–Hubbard model, spin-orbit coupling in the Mott-insulating phase of the Fermi–Hubbard model, and anisotropic contact interactions as well as inhomogeneous magnetic fields in the Mott-insulating phase of the Bose–Hubbard model in search of these effective models.

Throughout this work, we set  $\hbar = 1$  to ease the notation and define  $M$  as the system size,  $N$  as the number of particles and  $S$  as the spin quantum number.







## Chapter 2

# Spin Squeezing

### 2.1 Bosonic coherent states

The origin of spin squeezing can be traced back all the way to the conception of coherent states by Glauber in 1963 [39]. Coherent states were developed to study the correlation properties of the electromagnetic field [40, 41], but they rapidly became powerful tools to tackle other problems after being constructed for arbitrary Lie groups [42, 43]. Over the years, coherent states found applications in calculations involving path integrals [44], thermodynamics [45], decoherence [46, 47], the quantum-classical correspondence problem [48, 49], and many more areas [50, 51]. A fantastic overview of coherent states and their applications can be found in [52].

The inception of coherent states spur from the insight that part of the electromagnetic field operator can be decomposed in the eigenstates of the bosonic (since we are talking about light) annihilation operator. We may think this was a simple assumption, but at the time it was very innovative since the scientific community was focused on Hermitian operators, as they are experimentally observable.

We have defined the coherent states  $|\alpha\rangle$  as eigenstates of the bosonic annihilation operator  $\hat{a}$  such that

$$\hat{a} |\alpha\rangle = \alpha |\alpha\rangle . \quad (2.1)$$

We can also define them as the displaced form of the ground state

$$|\alpha\rangle = \hat{D}(\alpha) |0\rangle , \quad (2.2)$$

where  $\hat{D}(\alpha)$  is a unitary operator acting on the annihilation operator  $\hat{a}$ , such that

$$\hat{D}^{-1}(\alpha) \hat{a} \hat{D}(\alpha) = \hat{a} + \alpha . \quad (2.3)$$

By wisely applying  $\hat{D}^{-1}(\alpha)$  in eq. (2.3) and eq. (2.2) we can recover the definition in eq. (2.1). Continuing with the derivation, we choose a global



phase for the coherent states by setting  $\hat{D}(0) = 1$ . By expanding eq. (2.3) with an infinitesimal displacement  $d\alpha$  we get

$$\hat{D}(d\alpha) = 1 + \hat{a}^\dagger d\alpha - \hat{a} d\alpha^*. \quad (2.4)$$

We can then calculate the finite displacement as

$$\hat{D}(\alpha) = e^{\alpha \hat{a}^\dagger - \alpha^* \hat{a}} = e^{-\frac{1}{2}|\alpha|^2} e^{\alpha \hat{a}^\dagger} e^{-\alpha^* \hat{a}}. \quad (2.5)$$

With this result and using the definition of the  $n$ -th excited state  $|n\rangle = (\hat{a}^\dagger)^n |0\rangle / \sqrt{n!}$ , we can derive [52]

$$|\alpha\rangle = e^{-\frac{1}{2}|\alpha|^2} \sum_n \frac{(\alpha)^n}{\sqrt{n!}} |n\rangle. \quad (2.6)$$

Bosonic coherent states construct an over-complete basis, meaning they are not guaranteed to be orthogonal but describe the full Hilbert space of the system [53]. Moreover, they are all minimum uncertainty states which satisfy the uncertainty relation  $\Delta x \Delta p = \hbar/2$ . This last property is useful for metrological applications, as they provide the highest accuracy for which  $\Delta x = \Delta p$ . Nevertheless, we can obtain states of increased metrological advantage by deforming the quadrature in phase space of a coherent state. As we described before, the resulted states are *squeezed*.

## 2.2 Squeezed coherent states

Bosonic coherent states show minimal uncertainty, but they have in principle equal quantum fluctuations for two conjugate variables like position and momentum. While already useful, we can still increase the precision of a measurement by reducing the quantum fluctuations or variance of one variable by sacrificing the other. This idea of reducing the quantum fluctuations to provide an enhancement in precision is traditionally referred to as *squeezing*, since we squeeze the probability distribution in the direction of interest in phase space.

These states of light have received much attention with their key role in the detection of gravitational waves by the LIGO [54] and Virgo interferometers [55], as sub-atomic size measurements are needed to detect such phenomena [56].

To squeeze the coherent states, we define the squeeze operator as

$$\hat{S}(\xi) = \exp\left\{\frac{1}{2} \left( \xi^* \hat{a}^2 - \xi \hat{a}^{\dagger 2} \right)\right\}, \quad (2.7)$$

where  $\xi = r e^{i\theta}$  is an arbitrary complex number. Notice a certain resemblance with the displacement operator in eq. (2.5), but we create or annihilate two bosons. In fact, the squeeze operator was first conceived for the radiation states of idealised two-photon lasers [57].

We then define a squeezed coherent states as the application of the squeeze operator on a bosonic coherent state  $|\alpha\rangle$

$$|\alpha, \xi\rangle = \hat{S}(\xi) |\alpha\rangle = \hat{S}(\xi) \hat{D}(\alpha) |0\rangle. \quad (2.8)$$

It is convenient to obtain an operator for which these are eigenstates, much like coherent states are eigenstates of the annihilation operator. Since we are also working with the coherent states, a transformation of the annihilation operator using the squeeze operator becomes ideal, since  $\hat{S}(\xi) \hat{a} \hat{S}^\dagger(\xi) |\alpha, \xi\rangle = \hat{S}(\xi) \hat{a} |\alpha\rangle = \alpha |\alpha, \xi\rangle$ . Thus, by expansion of the exponential operator  $\hat{S}(\xi)$  we obtain the canonical transformation

$$\hat{A} = \hat{S}(\xi) \hat{a} \hat{S}^\dagger(\xi) = \mu \hat{a} + \nu \hat{a}^\dagger, \quad (2.9)$$

where  $\mu = \cosh r$  and  $\nu = \sinh r e^{i\theta}$ .

From the creation and annihilation operators we can recover the position and momentum operators as  $\hat{q} = (\hat{a} + \hat{a}^\dagger)/\sqrt{2}$  and  $\hat{p} = (\hat{a} - \hat{a}^\dagger)/(\sqrt{2}i)$ . Then, we can calculate the variances of this operators using eq. (2.9) to obtain

$$(\Delta \hat{q})_{\alpha, \xi}^2 (\Delta \hat{p})_{\alpha, \xi}^2 = \frac{1}{4} (1 + \sinh^2 2r \sin^2 \theta)^2 \geq \frac{1}{4}. \quad (2.10)$$

The squeezed coherent states will show minimum uncertainty when  $r = 0$  or  $\theta = 0$  or  $\pi$ . The case  $r = 0$  is trivial, as we simply recover the coherent states. On the former case, we either obtain

$$\Delta \hat{q} = \frac{e^{-r}}{\sqrt{2}}, \quad \Delta \hat{p} = \frac{e^r}{\sqrt{2}}, \quad (2.11)$$

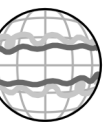
for  $\xi = r e^{i0} = r$ , or

$$\Delta \hat{q} = \frac{e^r}{\sqrt{2}}, \quad \Delta \hat{p} = \frac{e^{-r}}{\sqrt{2}}, \quad (2.12)$$

for  $\xi = r e^{i\pi} = -r$ . For the results  $\xi = \pm r$ , we obtain the desired squeezing of the probability distribution, as the quantum fluctuations in one variable are reduced with  $e^{-r}$  at the expense of the increase in the conjugate variable. In the context of bosonic coherent states,  $r$  is naturally referred to as the *squeeze parameter*.

## 2.3 Pseudo-spin and collective operators

It becomes natural to wonder if coherent and squeezed states can be found in other Lie algebras. This is indeed the case, and we will now explore the scenario of the spin 1/2, which can be mapped from a two-level atom. Moving forward we will use atoms as our particles of interest in the rest of this work, so we will refer to them as such. But first, we must define the operators defining such an algebra to describe said states in the spin phase space.



We define the pseudo-spin of our atoms from a well defined subspace coming from the internal degrees of freedom of the atoms. Throughout this work, we will only consider atoms with two isolated internal states labelled as  $|\uparrow\rangle, |\downarrow\rangle$ . Any superposition of such states belongs to the  $SU(2)$  Lie group, so we can describe their generator operators using the Pauli matrices  $\sigma_\alpha, \alpha \in x, y, z$ . The Pauli matrices obey the commutation relations  $[\sigma_\alpha, \sigma_\beta] = 2i\varepsilon_{\alpha\beta\gamma}\sigma_\gamma$ , where  $\varepsilon_{\alpha\beta\gamma}$  is the Levi-Civita symbol. This is because the single-atom operator must obey the usual angular momentum commutation relations, respecting the  $SU(2)$  algebra. We then define the spin-1/2 operators as

$$\hat{S}_j^\alpha = \frac{1}{2}\sigma_j^\alpha, \quad (2.13)$$

where  $\alpha$  indicates one of the three generators of the algebra  $\{x, y, z\}$  and  $j$  is the label for an atom. This still holds when multiple atoms occupy the same position and internal state, as the corresponding Hilbert space is a direct sum for individual atoms.

It is practical to represent the spin operators in terms of the creation and annihilation operators

$$\hat{S}_j^x = \frac{1}{2}(\hat{S}_j^+ + \hat{S}_j^-), \quad (2.14)$$

$$\hat{S}_j^y = \frac{1}{2i}(\hat{S}_j^+ - \hat{S}_j^-), \quad (2.15)$$

$$\hat{S}_j^z = \frac{1}{2}(\hat{u}_j^\dagger \hat{u}_j - \hat{d}_j^\dagger \hat{d}_j), \quad (2.16)$$

where  $\hat{u}_j$  ( $\hat{d}_j$ ) corresponds to the atom annihilation operator of state  $|\uparrow\rangle$  ( $|\downarrow\rangle$ ) at site  $j$  and  $\hat{S}_j^+ = \hat{u}_j^\dagger \hat{d}_j$ ,  $\hat{S}_j^- = \hat{d}_j^\dagger \hat{u}_j$ . Since these operators are constructed by a pair of creation-annihilation operators, they not only conserve atom number but parity. Thus, there is no need to distinguish between fermionic or bosonic systems at this stage.

It follows that the collective spin of the system can be equally described as a direct sum of the Hilbert space of a collection of spins, obtaining

$$\hat{S}_\alpha = \sum_{j=1}^N \hat{S}_j^\alpha. \quad (2.17)$$

The collective spin operator thus describes the spin quantum number of maximal value  $S = N/2$ , where  $N$  is the number of spins in the system. The collective state can be easily visualised if we assume the state is separable, but it becomes harder to picture when quantum correlations appear. In such case, we can rely on a quasi-probability distribution like the Husimi function  $Q(\theta, \phi)$  to portray the correlations of the system over the Bloch Sphere with radius equal to the expectation value of the mean spin direction operator.

## 2.4 Spin coherent states

We have defined the bosonic coherent states as a result of the diagonalization of the boson annihilation operator. Naturally, we may ask ourselves if we can define similar coherent states for atomic particles defined by their spin [58, 59]. The initial construction of the spin coherent states in quantum optics relied on the application of a classical electromagnetic field onto the spin particles of interest. The goal here was to see if we could retrieve the coherent states by identical principles of their bosonic counterpart, since the electromagnetic field could be the indirect generator of such states.

We can express the Hamiltonian of an assembly of  $N$  two-level atoms interacting with a classical electromagnetic field using the collective operators as

$$\hat{H} = \Omega \hat{S}_z + \lambda(t) \hat{S}_+ + \lambda^*(t) \hat{S}_-. \quad (2.18)$$

When the driving field  $\lambda(t)$  is turned off, the Hamiltonian reduces to

$$\hat{H}_0 = \Omega \hat{S}_z, \quad (2.19)$$

which is, by construction, diagonal with respect to the angular momentum eigenstates  $|S, m\rangle$  where  $m \in [-S, S]$ , such that  $\hat{H}_0 |S, m\rangle = m\Omega |S, m\rangle$ . We also refer to these eigenstates as Dicke states.

We can then express the original Hamiltonian in the interaction picture as

$$\hat{H}_I = e^{i\hat{H}_0 t} \left( \lambda(t) \hat{S}_+ + \lambda^*(t) \hat{S}_- \right) e^{-i\hat{H}_0 t}, \quad (2.20)$$

$$= i \left( \zeta(t) \hat{S}_+ - \zeta^*(t) \hat{S}_- \right), \quad (2.21)$$

with  $i\zeta(t) = \lambda(t)e^{i\Omega t}$ . If we then initialise the evolution of the system with the natural choice of the lowest energy state  $|S, -S\rangle$ , we obtain

$$|\Psi_I(t)\rangle = e^{\zeta(t)\hat{S}_+ - \zeta^*(t)\hat{S}_-} |S, -S\rangle, \quad (2.22)$$

up to a given phase factor.

If we compare this result with the displacement operator in eq. (2.5) which generates the bosonic coherent states, we can see a clear path to compute the spin coherent states. The first step is to identify  $\zeta(t) \rightarrow \zeta$  as our parameter to generate the coherent states and split the unitary operator  $e^{\zeta\hat{S}_+ - \zeta^*\hat{S}_-}$  using the Baker–Campbell–Hausdorff formula to obtain

$$e^{\zeta\hat{S}_+ - \zeta^*\hat{S}_-} = e^{\tau\hat{S}_+} e^{\ln(1+|\tau|^2)\hat{S}_z} e^{-\tau^*\hat{S}_-}. \quad (2.23)$$

with  $\tau = \tan|\zeta|e^{i\arg\zeta}$ . The action of the lowering operator  $\hat{S}_-$  on the state  $|S, -S\rangle$  vanishes, so the computation reduces to expanding the spin coherent



state in terms of the angular momentum eigenstates  $|S, m\rangle$  using the ladder operator such that

$$|S, m\rangle = \sqrt{\frac{(S-m)!}{(2S)!(S+m)!}} \left(\hat{S}_+\right)^{S+m} |S, -S\rangle. \quad (2.24)$$

Then, we obtain

$$\begin{aligned} |S, -S\rangle_\zeta &= e^{\zeta \hat{S}_+ - \zeta^* \hat{S}_-} |S, -S\rangle, \\ &= e^{\tau \hat{S}_+} e^{\ln(1+|\tau|^2) \hat{S}_z} e^{-\tau^* \hat{S}_-} |S, -S\rangle, \\ &= (1 + |\tau|^2)^{-S} e^{\tau \hat{S}_+} |S, -S\rangle, \\ &= (1 + |\tau|^2)^{-S} \sum_{m=-S}^S \frac{(\tau \hat{S}_+)^{S+m}}{(S+m)!} |S, -S\rangle, \\ &= (1 + |\tau|^2)^{-S} \sum_{m=-S}^S \sqrt{\binom{2S}{S+m}} \tau^{S+m} |S, m\rangle. \end{aligned} \quad (2.25)$$

If we inspect the unitary operator again, we can see it as a rotation around a given axis in the  $x - y$  plane since  $\hat{S}_\pm = \hat{S}_x \pm i\hat{S}_y$ . We can parameterise the operator as

$$\hat{R}(\theta, \phi) = e^{-i\theta(\sin \phi \hat{S}_x - \cos \phi \hat{S}_y)}, \quad (2.26)$$

for  $\zeta = 1/2\theta e^{-i\phi}$ . This means spin coherent states are but rotations of the angular momentum state  $|S, -S\rangle$ , so they will be eigenstates of the corresponding rotated  $\hat{S}_z$  operator. We can illustrate more clearly the angles of rotation by performing this rotation on the quantisation axis such that

$$\begin{aligned} \hat{R}(\theta, \phi) \hat{S}_z |S, -S\rangle &= -S |S, -S\rangle_\zeta, \\ &= \hat{R}(\theta, \phi) \hat{S}_z \hat{R}^{-1}(\theta, \phi) \hat{R}(\theta, \phi) |S, -S\rangle, \\ &= \left( -\sin \theta \left( \cos \phi \hat{S}_x - \sin \phi \hat{S}_y \right) + \cos \theta \hat{S}_z \right) |S, -S\rangle_\zeta, \end{aligned} \quad (2.27)$$

which illustrates that the spin coherent state  $|S, -S\rangle_\zeta$  is an eigenstate of the spin operator  $\hat{R}(\theta, \phi) \hat{S}_z \hat{R}^{-1}(\theta, \phi)$  along the direction of the vector  $(S, \theta + \pi, \phi)$  in spherical coordinates. Notice that here we have shown that the spin coherent state is an eigenstate of the rotated quantisation axis  $z$ , not of the ladder operator  $\hat{S}_-$ , as we could in principle expect from the derivation of the bosonic coherent states. In any case, we will find more convenient and intuitive to express the spin coherent states with these angles, so we can rewrite eq. (2.25) with  $\tau = \tan(\theta/2) e^{-i\phi}$  to obtain

$$\begin{aligned}
|\theta, \phi\rangle &\equiv |S, -S\rangle \zeta, \\
&= \sum_{m=-S}^S \sqrt{\binom{2S}{S+m}} \left(\cos \frac{\theta}{2}\right)^{S-m} \left(\sin \frac{\theta}{2} e^{-i\phi}\right)^{S+m} |S, m\rangle. \quad (2.28)
\end{aligned}$$

We can further decompose the coherent states to picture them more easily as a product state of individual spins polarised in the same direction. To do so, we can use two key ingredients: First, the lowest angular momentum state of an ensemble of  $N$  spins is uniquely defined as  $|S = N/2, -S\rangle = \otimes_j^N |\downarrow_j\rangle$ . Second, collective rotations act identically on the subspace of each spin. Thus, the spin coherent states can also be written as

$$|\theta, \phi\rangle = \hat{R}(\theta, \phi) \bigotimes_j^N |\downarrow_j\rangle = \bigotimes_j^N \left( \cos \frac{\theta}{2} |\downarrow_j\rangle + e^{i\phi} \sin \frac{\theta}{2} |\uparrow_j\rangle \right). \quad (2.29)$$

Since the spin coherent states are constructed in a very similar fashion to the bosonic coherent states, we may expect similar properties like the formation of a complete basis or the fulfilment of minimum variance in Heisenberg's uncertainty. While it can be shown that the former is true, the later is more subtle since the quadrature changes from a complex plane to an spherical surface. The uncertainty relation in spin space may be written as  $(\Delta \hat{S}_x)^2 (\Delta \hat{S}_y)^2 \geq |\langle \hat{S}_z \rangle|^2 / 4$ . From the previous definitions of the coherent states as rotations we can find that, for a spin coherent state  $|\theta, \phi\rangle$ ,

$$\left(\Delta \hat{S}_x\right)^2 \left(\Delta \hat{S}_y\right)^2 - \frac{1}{4} \left|\langle \hat{S}_z \rangle\right|^2 = \frac{1}{4} S^2 \sin^4 \theta \cos^2 \phi \sin^2 \phi. \quad (2.30)$$

This result only vanishes when  $\theta = 0, \pi$  or  $\phi = n\pi/2; \forall n \in \mathbb{Z}$ . Thus, the uncertainty in the quadrature  $x - y$  is minimised only when the state is polarised along  $z$  or projects onto the  $x$  or  $y$  directions. In contrast with the bosonic coherent states, we do not minimise the uncertainty in all directions, but must choose wisely to take advantage of a particular coherent state. This issue is immediately solved when we remember that the spin coherent states are a result of the rotation of the state polarised along  $\hat{S}_z$  for the spherical coordinates  $(\theta, \phi)$ . Thus, for each coherent state, we find minimum product uncertainty in the plane perpendicular to it's polarisation direction, given by said angles.

## 2.5 Spin-squeezing parameter

Squeezed states are, broadly speaking, those which reduce the measurement uncertainty of the observable of interest due to entanglement with respect to an uncorrelated state, up to the limit set by Heisenberg's uncertainty principle. In



the case of the bosonic coherent states, the squeeze operator in eq. (2.7) acting on a coherent state generates an arbitrarily squeezed state when  $\xi = \pm r$ ;  $r \in \mathbb{R}$ , where  $r$  is the bosonic squeezing parameter. The bosonic squeezed state is then obtained as in eq. (2.8). This, however, is not so trivially found on spin systems, as the quadrature depends on the polarisation direction of a given state and other relevant variables like the spin length may vary during the squeezing process.

There are different definitions of spin-squeezing depending on their utility and we will give a brief overview of some of them.

We mainly aim to use spin squeezed states to improve measurement precision brought by this reduction in uncertainty. Thus, spin squeezing has immediate applications in Ramsey spectroscopy [9], gravitational-wave interferometry [55] or atomic clocks [60].

However, we will also acknowledge definitions focused on detection of quantum entanglement in the form of Bell violations, as spin squeezed states are more resilient to different decoherence channels than highly entangled states like the GHZ state [10, 61].

To simplify notation, we refer to the mean spin direction, which can be calculated from three orthogonal directions, as  $n$ ; as it is normal to the plane of interest. We refer to the direction of minimal variance orthogonal to  $n$  as  $\min$ . Finally, we refer to the orthogonal direction to these previous two as  $\perp$ . In the next subsections we will write the set of three orthogonal spin operators in this frame of reference as  $\hat{S}_n, \hat{S}_{\min}, \hat{S}_{\perp}$ . We illustrate this coordinate system in fig. 2.1.

### Minimal Variance of Spin

The minimal variance is the main value to measure squeezing and obtain a metrological advantage. However, depending on the evolution of the system, the direction in which this variance is found can change in time. While it is possible to find the direction of minimal variance of the spin components numerically, this task can be tackled analytically by finding the minimal eigenvalue of the corresponding covariance matrix [62]. Moreover, with this direction we can obtain theoretical results of the squeezing parameter for models where the expectation values are known. While this calculation can become a bit tedious [62, 63], we will simplify it by working on a rotated reference frame to reduce the optimisation problem to a single variable.

For convenience, let us rotate our reference frame such that the z-direction coincides with the mean spin direction  $n$ ,

$$\hat{S}_{x'} = \cos \theta (\cos \phi \hat{S}_x + \sin \phi \hat{S}_y) - \sin \theta \hat{S}_z, \quad (2.31)$$

$$\hat{S}_{y'} = -\sin \phi \hat{S}_x + \cos \phi \hat{S}_y, \quad (2.32)$$

$$\hat{S}_{z'} = \hat{S}_n = \sin \theta (\cos \phi \hat{S}_x + \sin \phi \hat{S}_y) + \cos \theta \hat{S}_z, \quad (2.33)$$



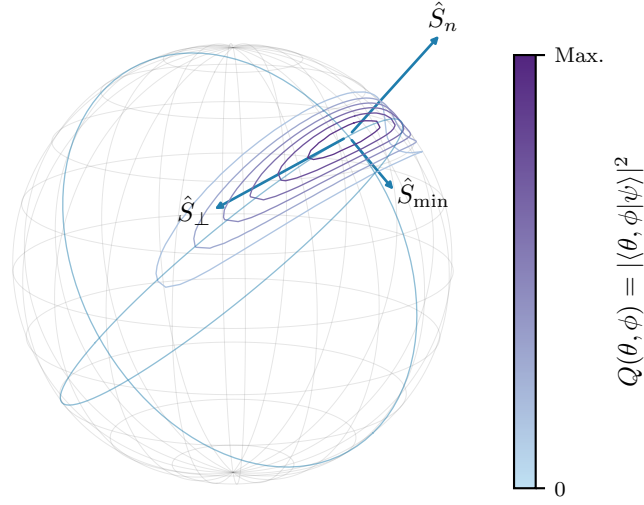


Figure 2.1: Bloch sphere representation of the spin directions of interest for a given squeezed state.

where

$$\theta = \arccos \frac{\langle \hat{S}_z \rangle}{\sqrt{\langle \hat{S}_x \rangle^2 + \langle \hat{S}_y \rangle^2 + \langle \hat{S}_z \rangle^2}},$$

$$\phi = \text{sgn} \langle \hat{S}_y \rangle \arccos \frac{\langle \hat{S}_x \rangle}{\sqrt{\langle \hat{S}_x \rangle^2 + \langle \hat{S}_y \rangle^2}}.$$

The variance of interest is then calculated in the  $(\hat{S}_{x'}, \hat{S}_{y'})$  plane, so we can define the minimal variance direction as a vector characterised by the angle  $\alpha$ . The spin operator along the minimal variance direction is then

$$\hat{S}_{\min} = \vec{n}_{\min} \cdot (\hat{S}_{x'}, \hat{S}_{y'}, \hat{S}_{z'}) = \cos \alpha \hat{S}_{x'} + \sin \alpha \hat{S}_{y'}. \quad (2.34)$$

with corresponding variance

$$\begin{aligned} (\Delta \hat{S}_{\min})^2 &= \langle \hat{S}_{\min}^2 \rangle - \langle \hat{S}_{\min} \rangle^2, \\ &= \frac{1 + \cos 2\alpha}{2} (\Delta \hat{S}_{x'})^2 + \frac{1 - \cos 2\alpha}{2} (\Delta \hat{S}_{y'})^2 + \frac{\sin 2\alpha}{2} (\Delta \hat{S}_{x'} \hat{S}_{y'}), \end{aligned}$$

where the variance along the direction  $\vec{n}$  is  $(\Delta \hat{S}_{\vec{n}})^2 = \langle \hat{S}_{\vec{n}}^2 \rangle - \langle \hat{S}_{\vec{n}} \rangle^2$  and  $(\Delta \hat{S}_{\vec{n}} \hat{S}_{\vec{m}}) = \langle \hat{S}_{\vec{n}} \hat{S}_{\vec{m}} + \hat{S}_{\vec{m}} \hat{S}_{\vec{n}} \rangle - 2 \langle \hat{S}_{\vec{n}} \rangle \langle \hat{S}_{\vec{m}} \rangle$ .



By minimising  $(\Delta\hat{S}_{\min})^2$  with respect to  $\alpha$  we obtain

$$2(\Delta\hat{S}_{\min})^2 = (\Delta\hat{S}_{x'})^2 + (\Delta\hat{S}_{y'})^2 + \sqrt{\left((\Delta\hat{S}_{x'})^2 - (\Delta\hat{S}_{y'})^2\right)^2 + (\Delta\hat{S}_{x'}\hat{S}_{y'})^2}, \quad (2.35)$$

for

$$\cos 2\alpha = -\frac{(\Delta\hat{S}_{x'})^2 - (\Delta\hat{S}_{y'})^2}{\sqrt{\left((\Delta\hat{S}_{x'})^2 - (\Delta\hat{S}_{y'})^2\right)^2 + (\Delta\hat{S}_{x'}\hat{S}_{y'})^2}}. \quad (2.36)$$

In eq. (2.36)  $\alpha$  is undefined with a phase  $n\pi; \forall n \in \mathbb{Z}$ . This is irrelevant, as the variance only depends on the direction of the resulting vector, which is identical in all cases. While this result is expressed in the rotated frame, it is simple to write in the original frame by expanding the variances and co-variances using eqs. (2.31) and (2.32).

The result implies that as long as we have the expectation values of the first and second moments of the collective spin in three arbitrary orthogonal directions, we can find the minimal variance and its direction immediately at each instance in time. On the other hand, it allows us to predict the minimal variance direction and require fewer measurements in an experiment. This minimal variance can be used to calculate the spin squeezing parameter definitions given in the following subsections.

### Definition by Kitagawa and Ueda

The first definition of spin squeezing was given by Kitagawa and Ueda in 1993 with their seminal work "Squeezed spin states" [6]. Borrowing the results of bosonic squeezed states, they adapted the concept for two-level atoms instead of photons. With the spin coherent states being well understood and defined [58, 59], the next step was to define under which conditions squeezing can happen. Due to the SU(2) algebra, the quadrature of the spin components to minimise the variance product is not uniquely defined. As we have seen in section 2.4, we can pick the plane perpendicular to the initial coherent state to guarantee the Heisenberg's uncertainty is minimal. Without loss of generality, we can assume the mean spin direction is preserved and we only need to pay attention to the initially defined quadrature. In the original paper [6], the authors only looked at the changes in the variances by means of different unitary transformations that we will see in detail in section 2.6. Still, we can extract a normalised spin-squeezing parameter from their results by normalising the minimal variance perpendicular to the mean spin  $((\Delta\hat{S}_{\min})^2)$  as

$$\xi_S^2 = \frac{(\Delta\hat{S}_{\min})^2}{S/2} = \frac{4(\Delta\hat{S}_{\min})^2}{N}, \quad (2.37)$$

since the spin length for a spin coherent state is given by  $S = N/2$ , where  $N$  is the number of spins in the system. It is easy to see that  $\xi_S^2 = 1$  for a spin coherent state, as in such case  $(\Delta\hat{S}_{\min})^2 = (\Delta\hat{S}_{\perp})^2 = N/4$ . As the coherent states lack quantum correlations, we may expect certain correlated states to yield  $\xi_S^2 < 1$ . In fact, it has been shown that  $\xi_S^2$  is related to negative correlations [9] and concurrence [64].

### Definition by Wineland et al.

Around the same time, Wineland et al. constructed a squeezing parameter to measure accuracy enhancement in Ramsey spectroscopy [7, 8]. In this framework the spin coherent states act as a noise reference. This parameter is derived through the definition of phase sensitivity, rather than the quadrature approach of bosonic squeezing that  $\xi_S^2$  relies on.

Let us suppose we want to measure a phase  $\phi$  which characterises a rotation of a given state on a perpendicular axis. Without loss of generality, we assume the state is originally located along the  $z$  direction ( $\langle\hat{S}_x\rangle = \langle\hat{S}_y\rangle = 0$ ) and we rotate it by phase  $\phi$  around the  $x$  direction such that

$$\hat{S}_{y'} = \hat{R}_x(\phi)\hat{S}_y\hat{R}_x^{-1}(\phi) = \cos\phi\hat{S}_y - \sin\phi\hat{S}_z, \quad (2.38)$$

is the new axis  $y$  in the rotated frame. It follows that

$$\begin{aligned} \langle\hat{S}_{y'}\rangle &= \cos\phi\langle\hat{S}_y\rangle - \sin\phi\langle\hat{S}_z\rangle = -\sin\phi\langle\hat{S}_z\rangle, \\ (\Delta\hat{S}_{y'})^2 &= \cos^2\phi(\Delta\hat{S}_y)^2 + \sin^2\phi(\Delta\hat{S}_z)^2 - \frac{1}{2}\sin 2\phi\langle\hat{S}_y\hat{S}_z + \hat{S}_z\hat{S}_y\rangle. \end{aligned}$$

Then, phase sensitivity can be accounted for through error propagation as

$$\Delta\phi = \frac{\Delta\hat{S}_{y'}}{\left|\partial\langle\hat{S}_{y'}\rangle/\partial\phi\right|} = \frac{\Delta\hat{S}_{y'}}{\left|\cos\phi\langle\hat{S}_z\rangle\right|}. \quad (2.39)$$

If  $\phi$  is sufficiently small, we can approximate  $\cos\phi \sim 1$  and  $(\Delta\hat{S}_{y'})^2 \sim (\Delta\hat{S}_y)^2$ . Then

$$\Delta\phi = \frac{\Delta\hat{S}_y}{\left|\langle\hat{S}_z\rangle\right|}. \quad (2.40)$$

We can write this result for the phase sensitivity achievable along the direction of minimal variance as

$$\Delta\phi = \frac{\Delta\hat{S}_{\min}}{\langle\hat{S}_n\rangle}, \quad (2.41)$$

where  $\langle\hat{S}_n\rangle = \sqrt{\langle\hat{S}_x\rangle^2 + \langle\hat{S}_y\rangle^2 + \langle\hat{S}_z\rangle^2}$ .



For instance, for a spin coherent state we obtain

$$(\Delta\phi)_{\text{SCS}} = \frac{1}{\sqrt{N}}. \quad (2.42)$$

which is generally referred to as the shot-noise limit or standard quantum limit.

The spin squeezing parameter proposed by Wineland et al. is constructed as

$$\xi_R^2 = \frac{(\Delta\phi)^2}{(\Delta\phi)_{\text{SCS}}^2} = \frac{N \left( \Delta \hat{S}_{\min} \right)^2}{\langle \hat{S}_n \rangle^2}. \quad (2.43)$$

In this framework the spin squeezing parameter is established as a sensitivity ratio between an arbitrary state and the spin coherent states. If the state is highly correlated, the sensitivity increases and  $\xi_R^2 < 1$ . In such case, the state provides a phase sensitivity advantage over the shot-noise limit.

Moreover, we can compare it with the previously defined spin squeezing parameter  $\xi_S^2$

$$\frac{\xi_R^2}{\xi_S^2} = \left( \frac{N/2}{\langle \hat{S}_n \rangle} \right)^2 \geq 1, \quad (2.44)$$

since  $N/2 = S \geq \langle \hat{S}_n \rangle$ , to deduce the spin squeezing parameter proposed by Wineland et al. is strictly more restrictive.

Lastly,  $\xi_R^2$  has a lower bound due to the uncertainty relation

$$\left( \Delta \hat{S}_{\min} \right)^2 \left( \Delta \hat{S}_{\perp} \right)^2 \geq \frac{1}{4} |\langle \hat{S}_n \rangle|^2, \quad (2.45)$$

which can be written as

$$\xi_R^2 \geq \frac{N}{4 \left( \Delta \hat{S}_{\perp} \right)^2}. \quad (2.46)$$

We can show the eigenstates with the largest eigenvalue of  $(\Delta \hat{S}_{\perp})^2$  are of the form [8]

$$|\psi_{\perp}\rangle = \frac{1}{\sqrt{2}} \left( |S, S\rangle_{\perp} + e^{i\phi} |S, -S\rangle_{\perp} \right), \quad (2.47)$$

and yield  $(\Delta \hat{S}_{\perp})^2 = S^2$ . So in general,  $(\Delta \hat{S}_{\perp})^2 \leq S^2 = (N/2)^2$  and we obtain

$$\xi_R^2 \geq \frac{1}{N}. \quad (2.48)$$

If we saturate this inequality, we have reached the so-called Heisenberg limit [27], which is the ideal scenario where the state is maximally squeezed.

Through the rest of this work, we refer to  $\xi_R^2$  as simply the spin squeezing parameter  $\xi^2$ .

### Spin squeezing as an entanglement witness

Spin squeezing is attractive to detect entanglement, as it constitutes an experimentally more accessible quantity than other observables like concurrence of entanglement entropy. In some systems the individual spins are, in fact, not accessible. This makes spin squeezing a relevant quantity, which also has the advantage of requiring few measurements.

However, particular definitions of spin squeezing might be able to show different kinds of entanglement. In other words, spin squeezing definitions can construct different entanglement criteria. For instance, it has been shown that  $\xi_S^2 < 1$  implies negative pairwise correlations [9]. This is clear to picture if we recall that, to generate spin squeezing, we require quantum correlations to surpass the shot-noise limit offered by the spin coherent states.

As the state becomes more non-separable in this scheme, entanglement is built up [65], which can be shown by introducing a Lagrange multiplier in results for  $\xi_R^2$ . This can also be represented in the following spin squeezing criteria [66]

$$\frac{(\Delta \hat{S}_{\min})^2}{\langle \hat{S}_n \rangle^2 + \langle \hat{S}_\perp \rangle^2} \geq \frac{1}{N}, \quad (2.49)$$

which certifies many-body entanglement as the state becomes non-separable. It can be found that symmetric states that violate eq. (2.49) are two-qubit entangled [64], which is not the case in general [67].

This pattern of spin squeezing criteria tailored towards a specific type of entanglement, but fails to detect entanglement in general, is repeated for criteria for many-body singlet states [68, 69], entangled Dicke states [69] and three-qubit entanglement [70, 71].

An alternative path to singular criteria that can only separate certain entangled states from others is to accumulate a number of inequalities such that their combined results give us more information about entanglement of spin squeezed states [70, 71]. Thus, it is possible to combine several generalised spin squeezing inequalities for different criteria to determine if a given arbitrary spin squeezed state of spin-1/2 is entangled [67, 72]:

$$\langle \hat{S}_x^2 \rangle + \langle \hat{S}_y^2 \rangle + \langle \hat{S}_z^2 \rangle \leq \frac{N(N+2)}{4}, \quad (2.50)$$

$$(\Delta \hat{S}_x)^2 + (\Delta \hat{S}_y)^2 + (\Delta \hat{S}_z)^2 \geq \frac{N}{2}, \quad (2.51)$$

$$\langle \hat{S}_\alpha^2 \rangle + \langle \hat{S}_\beta^2 \rangle - \frac{N}{2} \leq (N-1)(\Delta \hat{S}_\gamma)^2, \quad (2.52)$$

$$(N-1) \left[ (\Delta \hat{S}_\alpha)^2 + (\Delta \hat{S}_\beta)^2 \right] \geq \langle \hat{S}_\gamma^2 \rangle + \frac{N(N-2)}{4}, \quad (2.53)$$

where  $\alpha, \beta, \gamma$  take all the possible permutations of  $x, y, z$ . While not as compact as the spin squeezing parameters, this set of simple inequalities is complete in the sense of unequivocally detecting entanglement when information about



the state is limited to the first and second moments of the collective spin components. No other inequality based on these observables will be able to detect more entangled states. Interestingly, this set of criteria can also detect separable two-body entanglement despite not including correlations among multiple parties.

It is possible to map this set of criteria to the case of particles with spin  $j > 1/2$  [26] through the use of modified second moments of spin components. These criteria can be recovered from a generalized entanglement witness for local observables when the local spin components are chosen as the observables of interest [38]. This witness is constructed on the violation of separability in a data-driven approach, it provides a more compact, while less explicit, criteria to study entanglement detection.

It is also possible to use this data-driven perspective to construct Bell inequalities that detect separability which depend only on first and second collective moments [37]. They can be adapted to spin squeezed states to detect entanglement in a wider variety of scenarios, since they can include any number of outcomes and settings in the measurements. We will explore these advantages in Chapter 8 to detect entanglement for spin-1/2 systems in the presence of occupancy defects.

## 2.6 Paradigmatic models

Kitawaga and Ueda [6] took the idea of dynamical generation of squeezed light and applied it to a system of atoms with total spin  $S$ . While they admit squeezing generation can happen with higher order terms, they defined the simplest non-linear Hamiltonians which could generate squeezing in a spin system, One-Axis Twisting (OAT) and Two-Axis Counter Twisting (TACT). These models are clearly based on the Kerr medium dynamics [73] and squeeze operator (2.7), found in quantum optics. The success of these models rely on the conservation of total spin, while forcing the probability distribution to change non-linearly over the surface of the Bloch sphere. Any linear term would introduce a rotation of the state, without incurring in deformations of the probability distribution by itself. Thus, the simplest form of non-linearity we can introduce are second moment operators. These models allow us to breach the standard quantum limit, obtaining much higher correlations than an ensemble of  $N$  uncorrelated measurements.

### One-Axis Twisting

To obtain the desired squeezing of the probability distribution, we may look for a unitary transformation over the coherent state that changes relative phases of the state components but not its mean direction. That way, the centre of the distribution stays in the same place but correlations can build up entanglement, and thus squeezing. Since spin coherent states can be expanded in angular

momentum states, we might look for a unitary operator  $\hat{U}(t) = e^{i\hat{H}t} = e^{itF(\hat{S}_z)}$ , as they are eigenstates of  $\hat{S}_z$ . If we work in the Heisenberg picture to see the evolution of the ladder operators, we obtain

$$\hat{S}_+(t) = \left(\hat{S}_-(t)\right)^\dagger = \hat{U}(t)\hat{S}_+(0)\hat{U}^\dagger(t) = \hat{S}_+(0)e^{itf(\hat{S}_z)}, \quad (2.54)$$

where  $f(\hat{S}_z) = F(\hat{S}_z + 1) - F(\hat{S}_z)$ . If we plug  $F(\hat{S}_z) = \chi\hat{S}_z$ , the phase shift is global and no correlations can build up over time. If instead we pick  $F(\hat{S}_z) = \chi\hat{S}_z^2$ ,  $f(\hat{S}_z) = 2\chi(\hat{S}_z + 1/2)$  so we can obtain phase correlations among the total angular momentum components of the state.

Thus, we define the one-axis twisting model as

$$\hat{H}_{\text{OAT}} = \chi\hat{S}_z^2. \quad (2.55)$$

This model is in fact analogous to the dynamics found for coherent light in an optical Kerr non-linear medium, which is characterised by [73].

$$\hat{H} = \kappa(\hat{a}^\dagger\hat{a})^2, \quad (2.56)$$

where  $\hat{a}$  is the photon annihilation operator.

In order to maximise the correlations, we want our initial spin coherent state to be perpendicular to the twisted axis [6], for instance along the  $x$  direction.

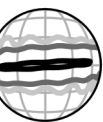
Equation (2.55) is a convenient Hamiltonian, as expectation values can be calculated analytically, so the minimum variance (2.35) is well defined in this case. We can approximate the minimal value of the squeezing parameter (2.43) generated by eq. (2.55) for  $N \gg 1, |2\chi t| \ll 1$  as [74]

$$\xi_{\text{best,OAT}}^2 \simeq \frac{3^{2/3}}{2} \frac{1}{N^{2/3}}. \quad (2.57)$$

It is relevant to point out the direction of minimal variance changes over time and at the optimal time it goes like  $\alpha \sim \arctan(N^{-1/3})/2$  [6]. The corresponding best squeezing time is found to be [74]

$$\chi t_{\text{best,OAT}} \simeq 3^{1/6} \frac{1}{N^{2/3}}. \quad (2.58)$$

A semi-classical approach might help us understand the dynamics of the one-axis twisting Hamiltonian. One precise method could be the mapping of operators in Hilbert space to differential operators on the classical phase space. This representation is widely successful and relies on the over-completeness of the coherent states as a basis [50, 75]. In our particular case we can rely on a simpler mean-field approximation, since we want a quick description of the coherent states trajectories for a given energy functional [76]. This approximation assumes the coherent state is not distorted during evolution, but should be



sufficient to understand the dynamics of the probability distribution at short times. For this mean-field approximation, we replace the creation-annihilation operators by complex numbers such that

$$S_x \rightarrow S \sin \theta \cos \phi, \quad (2.59)$$

$$S_y \rightarrow S \sin \theta \sin \phi, \quad (2.60)$$

$$S_z \rightarrow S \cos \theta, \quad (2.61)$$

represent the mean-field spin operators parameterised for conjugate variables  $\theta, \phi$ .

The mean-field Hamiltonian for  $\hat{H} = \chi \hat{S}_z^2$  would be  $H = \chi S^2 \cos^2 \theta$ , so the corresponding equations of motion are

$$\frac{d\phi}{dt} = \frac{1}{S} \frac{\partial H}{\partial \theta} = -\chi S \sin 2\theta, \quad (2.62)$$

$$\frac{d\theta}{dt} = -\frac{1}{S} \frac{\partial H}{\partial \phi} = 0. \quad (2.63)$$

With  $\theta \in (0, \pi]$ , the energy fluctuations change sign at  $\theta = \pi/2$ , so upper hemisphere coherent states move in one direction while lower half ones move in the opposite direction. Not only that, but the magnitude of this displacement varies with the latitude. We can expect the probability distribution to nearly follow these rules too in a fashion similar to a shear force applied to the initially coherent state.

This thesis in printed form allows the reader to see an animation of the one-axis twisting model dynamics by flipping the right corners of the document pages from end to beginning. The Husimi distribution corresponding to the best squeezing time from eq. (2.58) is drawn in a different color to easily identify the time at which spin squeezing is optimized. While later distributions might look more squeezed, the mean spin length is reduced in time and at some point the Gaussian character of the state is also lost. However, cat states or a revival of the initial coherent state can be obtained at later times [77]. The animation is computed for  $N = 100$  particles and  $t \leq 4t_{\text{best, OAT}}$ .

The one-axis twisting model has been widely studied due to its simplicity and ubiquity in many systems and scenarios. In fact, its application has been proposed in many platforms like Bose-Einstein condensates [66, 78], optical cavities [79], lattice clocks [80, 81], or bulk molecular gases [32, 82].

### Twist And Turn

Interestingly, it has been found that the addition of a linear term orthogonal to the twisting axis in eq. (2.55), aptly named as the twist and turn (TAT) Hamiltonian

$$\hat{H}_{\text{TAT}} = \chi \hat{S}_z^2 + \Omega \hat{S}_x, \quad (2.64)$$



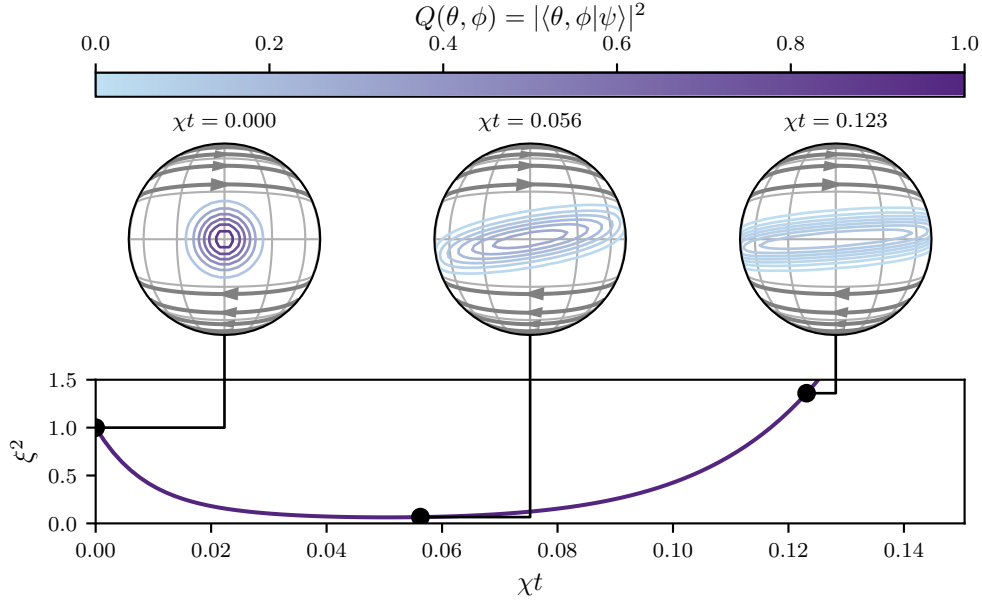


Figure 2.2: Evolution of the one-axis twisting model (2.55) with  $N = 100$  particles for an arbitrary  $\chi$ . Bloch spheres in Hammer projection show the quasi-probability Husimi distribution  $Q(\theta, \phi) = |\langle \theta, \phi | \psi(t) \rangle|^2$ , for certain points in time. Grey quiver lines in the Bloch spheres portray the mean-field results from eqs. (2.62) and (2.63). The lower panel shows the evolution of the squeezing parameter  $\xi^2$ .

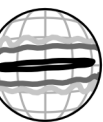
can provide squeezing acceleration over eq. (2.55) [83, 84]. While the twisting provides a shear on the probability distribution, the linear term allows a faster spread of the distribution as it realigns the already squeezed distribution with the twisting axis. We can again obtain an understanding of the dynamics under this model at short times through a semi-classical picture.

$$\frac{d\phi}{dt} = -\chi S \sin 2\theta + \Omega \cos \theta \cos \phi, \quad (2.65)$$

$$\frac{d\theta}{dt} = \Omega \sin \theta \sin \phi. \quad (2.66)$$

While with one-axis twisting we find instability along the equator, the solutions on this case gives us an unstable fixed point along the axis of rotation  $\hat{S}_x$ . We can see an example of these dynamics in fig. 2.3.

States that maximise Ramsey spectroscopy sensitivity are eigenstates of eq. (2.64) [85]. Moreover, control over the linear term can lead to longer coherence times of the squeezed states with the simple implementation of an external field [86]. The twist and turn Hamiltonian can generate more entanglement than eq. (2.55) [84], but its detection requires high-order non-linear



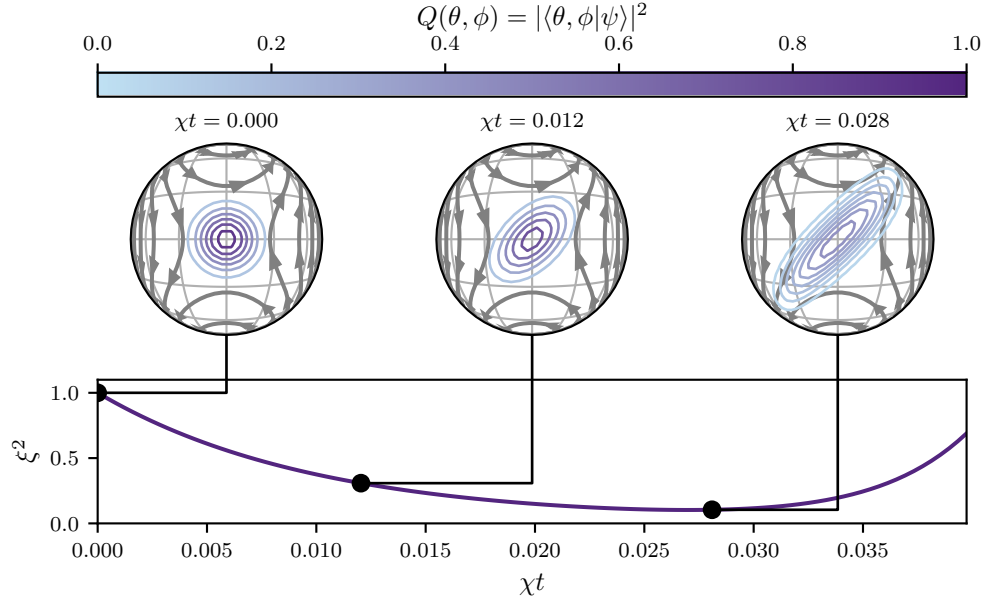


Figure 2.3: Evolution of the twist and turn model (2.64) with  $N = 100$  particles and  $\Omega = N\chi/2$  for an arbitrary  $\chi$ . Bloch spheres in Hammer projection show the quasi-probability Husimi distribution  $Q(\theta, \phi) = |\langle \theta, \phi | \psi(t) \rangle|^2$ , for certain points in time. Grey quiver lines in the Bloch spheres portray the mean-field results from eqs. (2.65) and (2.66). The lower panel shows the evolution of the squeezing parameter  $\xi^2$ .

definitions of the squeezing parameter or measuring quantum Fisher information [87].

### Two-Axis Counter Twisting (TACT)

While the one-axis twisting model appears in many contexts naturally, it is unable to reach the lower bound of the spin squeezing parameter  $\xi_R^2 \sim N^{-2/3} > N^{-1}$ . There are, potentially, better options to generate squeezing and reach the Heisenberg limit, rivalling the entanglement of the GHZ states [88]. Moreover, the optimal squeezing angle changes with time and number of particles, which can be problematic for direct experimental measurements. We may imagine that if we compensate the *twisting* of the probability distribution with an action at an orthogonal direction, we might find not only a fixed squeezing angle but even more squeezing.

Similarly to the one-axis twisting model, we can take inspiration from another result of quantum optics like the squeeze operator (2.7) to obtain the Hamiltonian

$$\hat{H}_{\text{TACT}} = \chi \left( \hat{S}_z^2 - \hat{S}_y^2 \right). \quad (2.67)$$

This is the two-axis counter twisting model (TACT), also simply known as the two-axis twisting model (TAT). Notice this last naming convention can be confusing when taking into account the twist and turn model (TAT). The negative sign in eq. (2.68) is important, as

$$\hat{S}^2 = \hat{S}_x^2 + \hat{S}_y^2 + \hat{S}_z^2. \quad (2.68)$$

is conserved unless our Hamiltonian breaks the  $SU(2)$  symmetry. Such scenario is explicitly detrimental for eq. (2.43), as it would inevitably reduce the spin length  $\langle \hat{S}_n \rangle$ . Otherwise,  $\hat{S}_z^2 + \hat{S}_y^2 = \hat{S}^2 - \hat{S}_x^2$  simply recovers the one-axis twisting result with a global phase factor.

As with the one-axis twisting model, the choice of twisting axes is arbitrary as long as they are orthogonal to each other, so it might be more natural to define it as

$$\hat{H}_{\text{TACT}} = \chi \left( \hat{S}_+^2 - \hat{S}_-^2 \right), \quad (2.69)$$

since the evolution of a spin coherent state expanded in the angular momentum basis  $|S, m\rangle$  is more explicit in this form and directly mimics eq. (2.7).

The model can be solved analytically on short times and  $N \gg 1$ , showing its maximally squeezed state can almost reach the Heisenberg limit sensitivity [76] as

$$\xi_{\text{best, TACT}}^2 = \frac{e}{2} \frac{1}{N}, \quad (2.70)$$

at time

$$\chi t_{\text{best, TACT}} = \frac{\ln 2N}{2N}. \quad (2.71)$$

To optimise squeezing, the initial spin coherent state has to be orthogonal to the twisting axes. We can get an intuition about this fact by employing the mean-field approximation [76] on eq. (2.69). In this case  $H = -2i\chi \sin^2 \theta \sin 2\phi$  and the equations of motion are

$$\frac{d\phi}{dt} = -2iS\chi \sin 2\theta \sin 2\phi, \quad (2.72)$$

$$\frac{d\theta}{dt} = 4iS\chi \sin^2 \theta \cos 2\phi. \quad (2.73)$$

These derivatives represent a velocity field in the phase space, which we can use to calculate unstable fixed points where the mean spin will not drift but will have competing pulls to generate squeezing. The stability of the fixed points  $\frac{d\phi}{dt} = \frac{d\theta}{dt} = 0$  can be extracted from the stability matrix [1]. In this case, we obtain that the unstable fixed points are located at  $\theta = 0, \pi, \forall \phi$ . Our optimal initial coherent states should be located at the poles of the Bloch sphere.

The energy fluctuations also show us how the squeezing evolves approximately in fig. 2.4, and numerical simulations show the dynamics are faster than for one-axis twisting.



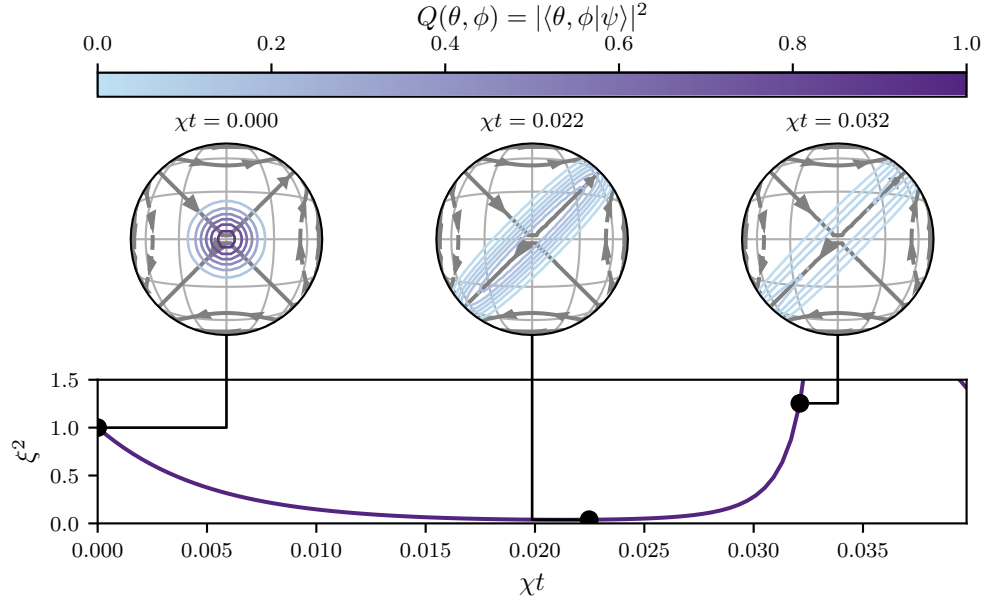


Figure 2.4: Evolution of the two-axis counter twisting model (2.68) with  $N = 100$  particles for an arbitrary  $\chi$ . Bloch spheres in Hammer projection show the quasi-probability Husimi distribution  $Q(\theta, \phi) = |\langle \theta, \phi | \psi(t) \rangle|^2$  for certain points in time. Grey quiver lines in the Bloch spheres portray the mean-field results from eqs. (2.72) and (2.73). The line width is fixed in this case to better visualize the direction of the energy fluctuations. The lower panel shows the evolution of the squeezing parameter  $\xi^2$ .

Heisenberg limited squeezing is still difficult to reach with two-axis counter twisting models, due to different decoherence channels in experimental setups [89]. But it is predicted to generate highly entangled states much more resilient to decoherence than other proposals if implemented, for instance, using interactions mediated by photon exchange [90]. Very recently, some experiments claimed to have observed the two-axis counter twisting model through polar molecules and Floquet engineering [91], and optical cavities [92].

## Chapter 3

# Ultra-cold Atoms in the Optical Lattice

In the past, many experimental platforms have been explored to realise spin squeezing, as seen in Chapter 1. We choose ultra-cold atoms in the optical lattice since its a novel platform which describes theoretical models found in statistical and condensed matter physics [28], with a remarkable level of control and tunability. In fact, optical lattices are seen as very flexible and currently one of the best platforms for quantum simulations [29]. This is not only because of the degree of control and reliability they posses, but for the sheer variety of models that can be achieved, even at the level of the Hubbard model [93, 94].

While the wide range of reproducible models can be overwhelming, we focus on the simplest implementations of the Hubbard model for two component systems where slight modifications may give rise to effective models that induce spin squeezing. We hope the exploration contained in this work can serve as a stepping stone to predict spin squeezing phenomena in more complex models. In this chapter, we sketch the derivation of our main models of interest in the optical lattice, the two-component Hubbard model and the Heisenberg model.

### 3.1 Hubbard model

We may describe the Hamiltonian of a periodic atomic system in second quantisation form as

$$\begin{aligned}\hat{H} = & \int d\mathbf{r} \Psi^\dagger(\mathbf{r}) H(\mathbf{r}) \Psi(\mathbf{r}) \\ & + \frac{1}{2} \int d\mathbf{r} \int d\mathbf{r}' \Psi^\dagger(\mathbf{r}) \Psi^\dagger(\mathbf{r}') V(\mathbf{r}, \mathbf{r}') \Psi(\mathbf{r}) \Psi(\mathbf{r}'),\end{aligned}\tag{3.1}$$



where  $H(\mathbf{r}) = \frac{\hbar^2 \nabla^2}{2m} + V_{\text{lattice}}(\mathbf{r})$  is the single particle Hamiltonian and  $\Psi(\mathbf{r}) = \sum_i \phi_i(\mathbf{r}) \hat{c}_i$  is the field operator written as a sum over the complete set of single particle quantum numbers with  $\hat{c}_i$  being the annihilation operator and  $\phi_i(\mathbf{r})$  the spatial component of the wave-function of quantum numbers determined by  $i$ . Depending on the particle statistics being a bosonic or fermionic, the operator shall respect commutation or anti-commutation relations, respectively. Notice the second term in 3.1 accounts for two-body interactions through the potential  $V(\mathbf{r}, \mathbf{r}')$ .

For now, let us focus on the first part of the right-hand side of eq. (3.1). The single particle Hamiltonian  $H(\mathbf{r})$  describes the movement of a particle in a periodic potential  $V_{\text{lattice}}(\mathbf{r}) = V_{\text{lattice}}(\mathbf{r} + \mathbf{R}_i)$ , where the vector  $\mathbf{R}_i$  characterizes its periodicity. The solutions of the corresponding Schrodinger equation along  $\mathbf{R}_i$  are the so-called Bloch functions [95]

$$\Phi_{\mathbf{q},\sigma}^{(n)}(\mathbf{r}) = e^{i\mathbf{q}\cdot\mathbf{r}} u_{\mathbf{q},\sigma}^{(n)}(\mathbf{r}), \quad (3.2)$$

for a periodic function

$$u_{\mathbf{q},\sigma}^{(n)}(\mathbf{r} + \mathbf{R}_i) = u_{\mathbf{q},\sigma}^{(n)}(\mathbf{r}), \quad (3.3)$$

where  $\mathbf{q}$  is the quasi-momentum which comes from the translational symmetry of the potential,  $\sigma$  is a given internal state of the particle and  $n$  enumerates the possible solutions for a given  $\mathbf{q}$ . These solutions are usually referred to as bands, since they form a band structure in the first Brillouin zone. Throughout the text we will refer to the internal states  $\sigma$  as *spin components*, as we can reconstruct the SU(2) algebra required for the spin from a superposition of such internal states. This does not necessarily mean these internal states are actual spin degrees of freedom, as they can be treated as a pseudo-spin without any loss of generality in our current framework.

We can apply a discrete Fourier transformation to the Bloch functions to obtain the Wannier functions

$$w_{\sigma,n}(\mathbf{r} - \mathbf{R}_i) = w_{i,\sigma,n}(\mathbf{r}) = \frac{1}{\sqrt{M}} \sum_{\mathbf{q}} e^{-i\mathbf{q}\cdot\mathbf{R}_i} \Phi_{\mathbf{q},\sigma}^{(n)}(\mathbf{r}). \quad (3.4)$$

As they are a linear combination of the Bloch functions, they are solutions to the single particle Hamiltonian  $H(\mathbf{r})$ .

If the depth of the periodic potential is large enough, the lowest band,  $n = 0$ , is well separated from the higher energy bands. In such case, we can expect the particles to not leave the lowest band at sufficiently low temperatures. It is then safe to expand the field operator in the Wannier function basis for  $n = 0$ , such that

$$\Psi(\mathbf{r}) = \sum_{i,\sigma} w_i(\mathbf{r}) \hat{c}_{i,\sigma}, \quad (3.5)$$

where we have assumed  $w_i(\mathbf{r}) = w_{i,\sigma}(\mathbf{r})$ ;  $\forall \sigma$  and omitted the band structure index  $n$ . This assumption about the isolation of the lowest Bloch band is called

the *tight-binding* approximation. The Hamiltonian can then be expressed as

$$\begin{aligned}\hat{H} = & \sum_{i,j} \sum_{\sigma_i, \sigma_j} \hat{c}_{i, \sigma_i}^\dagger (H_{ij}) \hat{c}_{j, \sigma_j} \\ & + \frac{1}{2} \sum_{i,j,k,l} \sum_{\sigma_i, \sigma_j, \sigma_k, \sigma_l} \hat{c}_{i, \sigma_i}^\dagger \hat{c}_{j, \sigma_j}^\dagger (V_{ijkl}) \hat{c}_{k, \sigma_k} \hat{c}_{l, \sigma_l},\end{aligned}\quad (3.6)$$

where

$$H_{ij} = \int d\mathbf{r} w_i^*(\mathbf{r}) H(\mathbf{r}) w_j(\mathbf{r}), \quad (3.7)$$

$$V_{ijkl} = \int d\mathbf{r} \int d\mathbf{r}' w_i^*(\mathbf{r}) w_j^*(\mathbf{r}') V(\mathbf{r}, \mathbf{r}') w_k(\mathbf{r}) w_l(\mathbf{r}'), \quad (3.8)$$

are the matrix (tensor) elements that can construct associated operators based on the values of the integrals.

Wannier functions are highly localized around  $\mathbf{r} - \mathbf{R}_i$ , which allows us to perform certain approximations. For instance, we may only consider tunnelling of the particles among nearest-neighbour sites of the lattice. This is not the case when the periodic potential is very shallow, as the tight-binding approximation stops being valid. On the other hand, if two-body interactions are well described by a contact potential  $V(\mathbf{r}, \mathbf{r}') = g\delta(\mathbf{r} - \mathbf{r}')$ , the dominating contribution will be on-site.

If our system is composed of spin-1/2 fermions, the previous approximations yield the Fermi–Hubbard model

$$\hat{H}_{\text{FH}} = -J \sum_{\sigma=\uparrow, \downarrow} \sum_{\langle i, j \rangle} \left( \hat{c}_{i, \sigma}^\dagger \hat{c}_{j, \sigma} + \text{h.c.} \right) + U \sum_i \hat{n}_{i, \uparrow} \hat{n}_{i, \downarrow}, \quad (3.9)$$

where  $\langle i, j \rangle$  indicates nearest neighbours,  $\left\{ \hat{c}_{i, \sigma}^\dagger, \hat{c}_{j, \sigma'} \right\} = \delta_{i, j} \delta_{\sigma, \sigma'}$ ,  $\hat{n}_{i, \sigma} = \hat{c}_{i, \sigma}^\dagger \hat{c}_{i, \sigma}$  and

$$J = - \int d\mathbf{r} w_i^*(\mathbf{r}) H(\mathbf{r}) w_j(\mathbf{r}) \Big|_{\langle i, j \rangle}, \quad (3.10)$$

$$U = g \int d\mathbf{r} |w_i(\mathbf{r})|^4, \quad (3.11)$$

for arbitrary  $i, j$  if the lattice potential is isotropic. We may also find the tunnelling coefficient  $J$  marked as  $t$  in the literature.

Similarly, if our system is composed of bosons with two internal states, we obtain the two-component Bose–Hubbard model

$$\begin{aligned}\hat{H}_{\text{BH}} = & -J \sum_{\sigma=\uparrow, \downarrow} \sum_{\langle i, j \rangle} \left( \hat{b}_{i, \sigma}^\dagger \hat{b}_{j, \sigma} + \text{h.c.} \right) + U_{\uparrow\downarrow} \sum_i \hat{n}_{i, \uparrow} \hat{n}_{i, \downarrow} \\ & + \frac{U_{\uparrow\uparrow}}{2} \sum_i \hat{n}_{i, \uparrow} (\hat{n}_{i, \uparrow} - 1) + \frac{U_{\downarrow\downarrow}}{2} \sum_i \hat{n}_{i, \downarrow} (\hat{n}_{i, \downarrow} - 1),\end{aligned}\quad (3.12)$$



where  $[\hat{b}_{i,\sigma}^\dagger, \hat{b}_{j,\sigma'}] = \delta_{i,j} \delta_{\sigma,\sigma'}, \hat{n}_{i,\sigma} = \hat{b}_{i,\sigma}^\dagger \hat{b}_{i,\sigma}$  and

$$U_{\sigma,\sigma'} = g_{\sigma,\sigma'} \int d\mathbf{r} |w_i(\mathbf{r})|^4. \quad (3.13)$$

While sophisticated methods to calculate this coefficients exists [96], approximating the Wannier functions yields reasonable results on certain lattice depths. Let us assume the periodic potential of the lattice is sufficiently deep. The three-dimensional lattice potential obtained from counter-propagating light beams can be expressed as

$$V_{\text{lattice}}(\mathbf{r}) = \sum_{l=x,y,z} V_{0,l} \sin^2(\mathbf{k}_l \cdot \mathbf{r}), \quad (3.14)$$

where  $V_{0,l}$  is the potential depth and  $\mathbf{k}_l = 2\pi/\lambda_l$  with  $\lambda_l$  the potential wavelength along a given direction. If the potential depth is sufficiently large, each potential minima can be replaced by a harmonic well. In turn, this allows to approximate the Wannier functions as Gaussian's, such that

$$w_i(\mathbf{r}) \approx \prod_{l=x,y,z} \phi_l(\mathbf{r} - \mathbf{R}_i), \quad (3.15)$$

where

$$\phi_l(\mathbf{r} - \mathbf{R}_i) = \frac{e^{-((\mathbf{r}-\mathbf{R}_i)\cdot\hat{l})^2/2\sigma_l^2}}{\pi^{1/4}\sqrt{\sigma_l}}, \quad (3.16)$$

with  $\sigma_l$  being the harmonic oscillator length along unitary direction  $\hat{l}$ .

As the Hubbard models contain only particle creation-annihilation terms and are particle number conserving, it is natural to describe them in an occupation basis, also referred to as Fock states. This basis makes computations intuitive, as it simplifies the picture of the system to particles allocated to different lattice sites. The construction of the Fock basis depends on the particle statistics, as the order in which the creation-annihilation operators act on a given Fock state is relevant for the sign of the resulting state in the case of fermions [97].

While we can obtain a rich phase diagram for both two-component Hubbard models [98, 99], we focus our attention on the two regimes found for their single-component counterparts, the superfluid regime ( $J \gg U$ ) and the Mott insulating regime ( $U \gg J$ ). We will find relevant models for these two scenarios in the next sections.

## 3.2 Two-mode model

If the tunnelling parameter  $J$  is much larger than the contact interactions  $U_{\sigma,\sigma'}$ , the particles delocalize over the whole lattice such that the occupation per site



flattens and the system behaves as a condensate. We can assume this is the case if the condensate fraction  $f_c = \sum_{i,j} \sum_{\sigma} \langle \hat{c}_{i,\sigma}^\dagger \hat{c}_{j,\sigma} \rangle / (NM)$  approximately equals one at unit-filling ( $M = N$ ). Under this scenario we can severely reduce our Hilbert space if we go to quasi-momentum representation of the operators via a discrete Fourier transform. That is,

$$\hat{c}_{j,\sigma} = \frac{1}{\sqrt{M}} \sum_q e^{i2\pi jq/M} \tilde{c}_{q,\sigma}, \quad (3.17)$$

where  $q \in [0, M-1]$  and  $\tilde{c}_{q,\sigma}^\dagger |n_{q,\sigma}\rangle = \sqrt{n_{q,\sigma}+1} |n_{q,\sigma}+1\rangle$ . As the particles move without friction over the lattice, we may only occupy the states of different spin with  $q = 0$ . The states in the  $q = 0$  manifold can be expressed as

$$|n, N-n\rangle = \frac{(\tilde{c}_{q=0,\uparrow}^\dagger)^n (\tilde{c}_{q=0,\downarrow}^\dagger)^{N-n}}{\sqrt{n!} \sqrt{(N-n)!}} |0, 0\rangle, \quad (3.18)$$

for  $n \in [0, N]$ .

This approximation fails in the case of fermions due to the Pauli exclusion principle, forcing higher momentum states to be populated. However, for bosons we do not have this limitation. By introducing eq. (3.17) in eq. (3.12) and then setting  $q = 0$  [100], we obtain the following two-mode model

$$\hat{H}_{\text{TMM}} = -2J\tilde{N} + \omega\tilde{N}^2 + \phi\tilde{S}_z\tilde{N} + \chi\tilde{S}_z^2, \quad (3.19)$$

where

$$\omega = \frac{U_{\uparrow\uparrow} + U_{\downarrow\downarrow} + 4U_{\uparrow\downarrow}}{8M}, \quad (3.20)$$

$$\phi = \frac{U_{\uparrow\uparrow} - U_{\downarrow\downarrow}}{2M}, \quad (3.21)$$

$$\chi = \frac{U_{\uparrow\uparrow} + U_{\downarrow\downarrow} - 2U_{\uparrow\downarrow}}{2M}, \quad (3.22)$$

and  $\tilde{N} = \tilde{n}_{q=0,\uparrow} + \tilde{n}_{q=0,\downarrow}$  with  $\tilde{n}_{q,\sigma} = \tilde{b}_{q,\sigma}^\dagger \tilde{b}_{q,\sigma}$ , and  $\tilde{S}_z = \hat{S}_z / \sqrt{M} = \sum_j (\hat{b}_{j,\uparrow}^\dagger \hat{b}_{j,\uparrow} - \hat{b}_{j,\downarrow}^\dagger \hat{b}_{j,\downarrow}) / (2\sqrt{M})$ . As we expect the state to stay in the  $q = 0$  manifold, we may assume  $\tilde{N} \approx N$ . The term  $\phi\tilde{S}_z\tilde{N}$  constitutes a rotation of the state in the Bloch sphere around the  $z$  direction. The last term on the right side of eq. (3.19) matches the one-axis twisting model from Section 2.6 and is able to generate spin squeezing by itself.

### 3.3 Heisenberg model

If we go to the opposite regime where  $U_{\sigma,\sigma'} \gg J$ , the energy spectrum shows a separation between the single-occupied states and states with multiple occupied sites. This happens because the kinetic energy contribution is not sufficient to compensate for the large on-site contact interactions.



To derive an effective model under these circumstances at unit-filling ( $N = M$ ), we may employ second order perturbation theory. To do so we have to separate the spectrum according to a perturbation term threshold. In this case, the spectrum is given by the contact interactions, which are naturally diagonalized by the Fock occupation basis. The tunnelling term acts naturally as the perturbation in this regime and allows to couple, at least, single occupied states with double occupied states. Details on how to perform this calculation can be found in Chapters 4 and 6. After appropriate derivation, we obtain the so called XXZ Heisenberg model

$$\hat{H}_{\text{XXZ}} = -J_{\perp} \sum_{i=1}^M \left( \hat{S}_i^x \hat{S}_{i+1}^x + \hat{S}_i^y \hat{S}_{i+1}^y + \Delta \hat{S}_i^z \hat{S}_{i+1}^z \right). \quad (3.23)$$

If  $\Delta = 1$ , we go from the XXZ to the XXX model, also known as spin exchange model. In our case, we find that for fermions  $J_{\perp} = 4J^2/U$ ,  $\Delta = 1$ ; so we obtain the XXX model. However, we find that for bosons  $J_{\perp} = 4J^2/U_{\uparrow\downarrow}$ ,  $\Delta = U_{\uparrow\downarrow}/U_{\downarrow\downarrow} + U_{\uparrow\downarrow}/U_{\uparrow\uparrow} - 1$ ; which allows us to obtain the XXZ model.

If the system is not at unit-filling, tunnelling may happen between single occupied states directly. This yields the so-called  $t$ - $J$  model, which is exactly like the Heisenberg model with the additional tunnelling term projected onto the single occupied states only.

The Heisenberg model was first postulated by Werner Heisenberg and Paul Dirac at the dawn of quantum mechanics, as a way to solve the long standing problem of ferromagnetism [101, 102]. Some time after this proposal, Hans Bethe obtained the eigenstates of the model under periodic boundary conditions through a well chosen *ansatz* [103, 104]. These type of solutions are now referred to as the coordinate Bethe ansatz [105], a tool that exceeded its initial conception as an ad-hoc solution and is employed in some way or another to obtain the eigenenergies of different Hamiltonians like the Lieb-Lininger model [106]. The solutions are usually presented as quasi-particles, called magnons or spin waves depending on the sub-field, that travel through the spin chain and may interact with each other. We are interested in the eigenenergies and eigenstates of the Heisenberg model in order to perform perturbation theory appropriately. In the following subsection, we describe the spin wave solutions and their derivation in more unusual settings like open boundary conditions.

### Magnons in the isotropic Heisenberg model

The reason the Bethe ansatz works in the first place, is because the model is integrable due to the symmetries it has. For instance, we can see it commutes with the operator  $\hat{S}_z$ , but it also commutes with  $\hat{S}^2$ . Thus, Dicke states are well defined eigenstates of the model.

The ansatz solutions are usually introduced following the argument that we can define a vacuum state as  $|0\rangle = \otimes_j |\downarrow_j\rangle$ . This state will be an eigenstate

with the lowest eigenvalue possible, and the ansatz uses it as a reference to construct the excited eigenstates. The excited eigenstates are then constructed from local excitations, such that each sector is diagonalised to obtain the full spectrum.

Let us solve the one and two magnon excitations, so that we can generalise to any number of them. We may refer to the local excited states from the vacuum state as

$$|l\rangle = \hat{S}_l^+ |0\rangle = \hat{S}_l^+ \bigotimes_{j=1}^M |\downarrow_j\rangle. \quad (3.24)$$

To solve the single excitation sector, we can rely on the translational symmetry of the system, such that we can define a translator operator  $U |l\rangle = |l+1\rangle$ . The eigenstates of this operator are characterised by the eigenvalues  $e^{-i2\pi q/M}$ , where  $q \in (0, M-1]$  is the quasi-momenta of the solution. We can solve the eigenvalue problem by writing the eigenstates as a superposition of the locally excited states  $|l\rangle$

$$|q\rangle = \sum_l^M a(l) |l\rangle, \quad (3.25)$$

and apply the translator operator to find the recursion relation  $\langle l+1|q\rangle = e^{i2\pi q/M} a(l)$  to obtain

$$|q\rangle = \frac{1}{\sqrt{M}} \sum_l^M e^{i2\pi ql/M} |l\rangle. \quad (3.26)$$

Unsurprisingly, this is equivalent to a discrete Fourier transform of the locally excited states. These states are also eigenstates of the Heisenberg Hamiltonian, with eigenvalues

$$E_q - E_0 = J(1 - \cos(2\pi q/N)). \quad (3.27)$$

Notice that when  $q = 0$ , the energy is the same as the vacuum state  $|0\rangle$ , but the state is a trivial superposition of states with a single spin flipped. It is, in fact, the Dicke state  $|S, -(S+1)\rangle$ . In any case, we refer to the solution (3.26) as a single magnon excitation, where the magnon is a collective spin excitation of quasi-momenta  $q$ .

While this sector is trivially solved, the sector with two spin flips is more complicated, as scattering processes among spin excitations have to be taken into account. For this reason, let us repeat this calculation with the Bethe ansatz. We want to solve the eigenvalue problem with the state in eq. (3.25), so we assume this is the case and solve  $\hat{H} |q\rangle = E_q |q\rangle$  as a system of equations of the form

$$2(E_q - E_0)a(l) = J(2a(l) - a(l-1) - a(l+1)), \quad (3.28)$$



$\forall j \in [1, M]$  with  $a(l + M) = a(l)$ . The Bethe ansatz here is the plane wave solution  $a(l) = e^{i2\pi q/M}$ ,  $\forall q \in (0, M - 1]$ , such that we recover eq. (3.26) after renormalisation.

The relevance of the ansatz appears when we want to solve the two excitations sector. In such case, the solution will still be a superposition of states with two spin flipped  $|l_1, l_2\rangle$  as

$$|q_1, q_2\rangle = \sum_{l_1 < l_2} a(l_1, l_2) |l_1, l_2\rangle. \quad (3.29)$$

The insight of Bethe was that we can see the coefficients as a sum of two plane wave solutions, one accounts for two magnons travelling freely, and the other is the scattering process between them.

$$a(l_1, l_2) = A(q_1, q_2) e^{i2\pi(q_1 l_1 + q_2 l_2)/M} + A'(q_1, q_2) e^{i2\pi(q_1 l_2 + q_2 l_1)/M}. \quad (3.30)$$

The ansatz solves the system of equations for the eigenvalue problem obtained from eq. (3.29) when  $|l_1 - l_2| > 1$  and the corresponding eigenvalue is

$$E_{q_1, q_2} - E_0 = J \sum_{n=1}^2 (1 - \cos(2\pi q_n/M)). \quad (3.31)$$

This makes sense, as it is equivalent to two freely moving magnons. However, there is a set of  $M$  equations corresponding to the scenario  $|l_1 - l_2| = 1$  which are unfulfilled unless

$$\frac{A}{A'} \equiv e^{i\theta} = - \frac{e^{i2\pi(q_1+q_2)/M} + 1 - 2e^{i2\pi q_1/M}}{e^{i2\pi(q_1+q_2)/M} + 1 - 2e^{i2\pi q_2/M}}. \quad (3.32)$$

Thus, we can rewrite the ansatz as

$$a(l_1, l_2) = e^{i2\pi(q_1 l_1 + q_2 l_2)/M + \theta/2} + e^{i2\pi(q_1 l_2 + q_2 l_1)/M - \theta/2}. \quad (3.33)$$

Applying periodic boundary conditions and translation invariance, we obtain

$$Mq_1 = \lambda_1 + \frac{\theta}{2\pi}, \quad (3.34)$$

$$Mq_2 = \lambda_2 - \frac{\theta}{2\pi}, \quad (3.35)$$

where  $\lambda_1, \lambda_2 \in [0, M - 1]$  are the so-called Bethe quantum numbers. An analysis on the eigenvalue solutions gives relevant physical interpretation to the wave-function and the resulting eigenvalues. However, we continue our discussion with the generalisation to any number of magnon excitations, as we are only interested in the form of the solution.

We can again postulate that an eigenstate of the Hamiltonian can have the form

$$|\{q_n\}\rangle = \sum_{l_1 < \dots < l_n} a(l_1, \dots, l_n) |l_1, \dots, l_n\rangle. \quad (3.36)$$

The solution for this case can be found from the two magnon scattering as

$$a(l_1, \dots, l_n) = \sum_{\mathcal{P} \in S_n} \exp \left( i \frac{2\pi}{M} \sum_{j=1}^n q_{\mathcal{P}_j} l_j + \frac{i}{2} \sum_{k < j} \theta_{\mathcal{P}_k \mathcal{P}_j} \right), \quad (3.37)$$

where  $\mathcal{P}$  indicates all possible permutations of the  $n$  magnons. This solution yields the energy value

$$E_{\{q_n\}} - E_0 = J \sum_{j=1}^n (1 - \cos(2\pi q_j/M)). \quad (3.38)$$

Again, explicit solutions can be found, some analytically but most of them numerically. We are, however, only interested in the integrable aspect of this analysis, as well as the possibility to decompose the sectors into different subspaces.

For our purposes of separating the states into subspaces of different energy, we must collect all of these states and reformulate the different excited states sectors using operators with quasi-momenta different than zero in all cases. We accommodate the states generated with one magnon of quasi-momenta  $q = 0$  as a member of the lower subspace. For example, if we have two-magnon states  $|q_1, q_2\rangle$  where  $q_1 = 0$ , this is equivalent to a single magnon excitation and we relegate this state to the single magnon manifold. If in this same example,  $q_1 = q_2 = 0$ , then there are effectively no magnons, even if the magnetisation changes by two, and the state is relegated to the lowest energy manifold.

Notice that the states defined for different magnetisation with all magnons  $\{q_n\} = 0$  are equivalent to the action of a collective ladder operator  $n$  times (with the corresponding normalisation factor) on the vacuum state  $|0\rangle = \otimes_j |\downarrow_j\rangle = |S, -S\rangle$ . Thus, we find that the lowest energy manifold is composed of the states  $|S, m\rangle; \forall m \in [-S, S]$ . We also refer to these states as Dicke states [107]. We can argue the Dicke states are eigenstates of the Heisenberg model without the Bethe ansatz, because of the  $SU(2)$  symmetry of the model. Since  $[\hat{H}_{\text{XXX}}, \hat{S}_{\pm}] = 0$ , coherent states are also eigenstates of the isotropic Heisenberg model.

We can follow this logic to properly collect all the states of similar nature, independently of their magnetisation, in the different subspaces by constructing them using generators based on  $n$  number of magnons of  $q_j \neq 0 \forall j \in [1, n]$ .

In this framework, we can generate these magnon states  $|m + n, \{q_n\}\rangle$  from an arbitrary Dicke state  $|S, m\rangle$ , as long as the required symmetry conditions are fulfilled. To check this, we define the generator operator

$$\tilde{S}_{\{q_n\}}^+ |S, m\rangle = |m + n, \{q_n\}\rangle, \quad (3.39)$$

which acts on an arbitrary Dicke state and returns an state excited with a set of  $n$  magnons from the Bethe ansatz in eq. (3.37). We can check that there



is a limit in the magnetisation where flipping more spins can only lead to the state vanishing. Naturally, the hermitian operator  $\tilde{S}_{\{q_n\}}^- = (\tilde{S}_{\{q_n\}}^+)^{\dagger}$  will also be a generator of this subspace, which allow us to see the size of the generated subspace is restricted in magnetisation by the number of spins flipped. It can be shown these are eigenstates of  $\hat{S}^2, \hat{S}_z$  with eigenvalues

$$\hat{S}^2 |m + n, \{q_n\}\rangle = (S - n)(S - n + 1) |m + n, \{q_n\}\rangle, \quad (3.40)$$

$$\hat{S}_z |m + n, \{q_n\}\rangle = (m + n) |m + n, \{q_n\}\rangle, \quad (3.41)$$

$$\forall - (S - n) < m < S - n.$$

We have not only separated the subspaces properly by number of non-zero magnons present, but we can see these magnon states have restrictions both in total spin and corresponding magnetisation. This insight is key in the search of metrologically useful states, as lowering the total spin of the state is directly detrimental to the measurement precision, since is analogous with the reduction of spin length or number of particles.

Another important realisation is that these subspaces of different number of magnons can have similar energies for at least part of their spectrum. For example, it is clear that for  $E_{q_1=M-1} = J(1 - \cos(2\pi(M-1)/M)) \sim 2J$  and  $E_{q_1=1, q_2=1} = 2J(1 - \cos(2\pi/M)) \sim 4J/M$ , we have  $E_{q_1=M-1} > E_{q_1=1, q_2=1}$  if  $M > 2$ . Since the energy increases with  $q_n$ , the energy of the two-magnon states will catch up and surpass the energy of the given single magnon state.

While this degeneracy may seem problematic since we wanted to separate the different subspaces, states of different number of magnons are orthogonal to each other and they form isolated orthonormal basis. This follows from the fact that they are eigenstates of  $\hat{S}^2$  and  $\hat{S}_z$  with different quantum numbers, and such states must be orthogonal. If our system does not have a term that couples states of different number of magnons, we can safely ignore this issue for the application of perturbation theory.

### Single magnon solutions under open boundary conditions

In the case of open boundary conditions, the plane wave ansatz is incorrect, as the translation symmetry is broken at the boundaries. However, the solution is simple to obtain and can be instructive for similar problems.

We propose the eigenstates for single magnon excitations under open boundary conditions to be

$$|q\rangle = \sum_{l=1}^M a(l) |l\rangle, \quad (3.42)$$

in the same manner as with periodic boundary conditions. However, we do not solve the eigenvalue problem through a trial solution in a recurrence relation.

The eigenvalue problem can then be written as

$$\begin{cases} 2(E - E_0)a(1) = J[a(2) - a(1)], \\ 2(E - E_0)a(l) = J[a(l-1) - a(l)] + (a(l+1) - a(l)), \quad \forall 1 < l < M, \\ 2(E - E_0)a(M) = J[a(M-1) - a(M)], \end{cases} \quad (3.43)$$

Special equations for the boundary terms can be annoying to work with, so we can employ the fact that the coefficients outside the system are undefined [108]. In other words,  $a(0), a(M+1)$  are free parameters that we can use to redefine the equations at the boundaries and recover the same equation for all sites.

Thus, we can have

$$2(E - E_0)a(l) = J[(a(l-1) - a(l)) + (a(l+1) - a(l))]; \quad (3.44)$$

$\forall l$  if  $a(0) \equiv a(1)$  and  $a(M+1) \equiv a(M)$ .

We can solve this equation by writing it as a recurrence relation

$$a(l-1) - 2ca(l) + a(l+1) = 0, \quad (3.45)$$

where  $c = 1 + (E - E_0)/J$ .

The natural trial solution is  $a(l) = r^l$ , so we shift indexes by one and obtain

$$a(l) - 2ca(l+1) + a(l+2) = r^l(r^2 - 2cr + 1) = 0. \quad (3.46)$$

This equation has  $l$  trivial solutions and  $r_{\pm} = c \pm \sqrt{c^2 - 1}$ . As we have two characteristic roots, the solution is a linear combination of both, yielding

$$a(l) = Ar_+^l + A'r_-^l. \quad (3.47)$$

We can further simplify the solution by noticing that  $r_+r_- = 1$ , so that  $r_-^l = r_+^{-l}$ . Let us relabel  $r \equiv r_+$ , for simplicity. Coefficients  $A, A'$  can be found by applying the boundary constraints and the normalisation condition. From the boundary constraints we find

$$r^{2(M+1)} = 1, \quad (3.48)$$

and we get

$$a(l) = Ar^{M-1/2} \left( r^{l-(M-1/2)} + r^{-(l-(M-1/2))} \right). \quad (3.49)$$

From eq. (3.48), it's clear the solution can be a complex number such that  $|r| = 1$ , so solving the equation with  $r = e^{i\theta}$  yields

$$r = e^{i\pi q/M}; \quad \forall q \in [0, M-1], \quad (3.50)$$

with eigenvectors after normalisation

$$|q\rangle = \sqrt{\frac{2}{M}} \sum_{l=1}^M \cos \left[ \frac{\pi}{M} q \left( l - \frac{1}{2} \right) \right], \quad (3.51)$$

and eigenvalues

$$E_q - E_0 = J(1 - \cos(\pi q/M)). \quad (3.52)$$



### Single magnon solutions for spin chains with vacancies

This possible scenario is analogous to open boundary conditions, as introducing a single vacancy in a ring is the same as creating open boundary conditions, since our Hamiltonian only acts on nearest neighbours. Thus, vacancies in between partial chains of spins will yield a system of independent magnons among partial chains.

While the final result is already quite clear, we will proceed to develop a properly derived solution from the ground up as an exercise for more complicated systems where longer range spin interactions are present.

We will refer to the set of locations of vacancies or holes for a given moment in time, or realisation if they are fixed in place, as  $\{h\}$ .

We propose the eigenstates for single magnon excitations to be defined as

$$|\psi\rangle = \sum_{l \notin \{h\}} a(l) |l\rangle, \quad (3.53)$$

where  $|l\rangle$  is defined with respect of a given vacuum state with vacancies on sites  $\{h\}$ .

The eigenvalue problem can then be written as

$$2(E - E_0)a(l) = J [\delta_{l+1 \notin \{h\}}(a(l-1) - a(l)) + \delta_{l-1 \notin \{h\}}(a(l+1) - a(l))], \quad (3.54)$$

for the  $N$  equations where  $l \notin \{h\}$ . To get rid of the Kronecker deltas, the trick is identical to the one employed with open boundaries: use vacancy coefficients as free parameters. We can rewrite the set of equations as

$$2(E - E_0)a(l) = J [(a(l-1) - a(l)) + (a(l+1) - a(l))], \quad (3.55)$$

if and only if

$$\begin{cases} a(l-1) = a(l), & \text{if } l-1 \in \{h\}, \\ a(l+1) = a(l), & \text{if } l+1 \in \{h\}, \end{cases} \quad (3.56)$$

for  $l \notin \{h\}$ . We may be wary of the scenario where only one vacancy appears between occupied sites, creating the constraint  $a(l) = a(l+1) = a(l+2)$  where the vacancy is located at site  $l+1$ . This constraint is artificial, since we argued that empty sites act as free parameters for the solution, so we can write in that particular scenario that  $a(l+1) = a(l) + a(l+2)$ , without any loss of generality.

This equation yields the same recurrence relation as per the open boundaries case, so the solution for a partial chain of occupied sites from site  $l_k$  to  $l_k + L_k - 1$  is

$$a_k(l) = \begin{cases} \sqrt{\frac{2}{L_k}} \cos \left[ \frac{\pi}{L_k} q_k \left( l - \left( l_k - \frac{1}{2} \right) \right) \right]; & \forall l \in [l_k, l_k + L_k - 1], \\ 0; & \text{otherwise,} \end{cases} \quad (3.57)$$

with  $q_k \in (0, L_k - 1]$ . Each solution  $a_k(l)$  is independent, so we have  $L_k$  solutions for each partial chain  $k$ . In other words, each partial chain is independent



and the quasi-momenta of the single magnon solution on each one depends on its length.





## Chapter 4

# Perturbation Theory

The typical textbook introduction to perturbation theory frames it as a tool to implement corrections of increasing precision to the calculation of a given eigenenergy of the system of interest [109]. However, perturbation theory also allow us to reconstruct a complete effective Hamiltonian, including all matrix elements up to a given order.

Perturbation theory relies on the assumption that we can decompose the system Hamiltonian  $\hat{H}$  into a dominating part which can be diagonalised in a given basis and treat the rest as a small off-diagonal contribution,  $\hat{H} = \hat{H}_0 + \hat{V}$ . If the perturbation is sufficiently small with respect to some energy scale, we can compute an effective Hamiltonian based on sensible approximations and project onto a given energy manifold. The resulting effective Hamiltonian will have the advantage of a reduced Hilbert space and thus simplify the analysis of the dynamics. In most cases, this effective Hamiltonian will be only an approximation of the original, but it will portray its main features.

While other methods allow us to obtain an effective Hamiltonian  $\hat{H}_{\text{eff}}$  for many-body systems, like the Feynman-Dyson diagram technique or the self-energy formalism [110], we will focus on the Schieffer–Wolff transformation as our tool of trade. Other perturbative expansions might not be as reliable in their approximations, to the point of even yielding non-Hermitian Hamiltonians as an output [111]. It is important to remark that the effective Hamiltonian is only defined up to a unitary rotation of the projected energy manifold. This means different methods produce different Taylor series of  $\hat{H}_{\text{eff}}$ , so the cutoff greatly affects the similarity between applications of perturbation theory. A detailed comparison with alternative perturbative methods can be found in [112].

### 4.1 Schieffer–Wolff Transformation

This particular application of perturbation theory relies on the use of a unitary transformation on the exact Hamiltonian to decouple energetically separated



state manifolds. The core idea is simple: given a large energy gap  $\Delta E$  between the low and high energy manifolds given by  $\hat{H}_0$ , if the perturbation  $\epsilon\hat{V}$  couples them but is small enough when compared with  $\Delta E$ , we can obtain an effective Hamiltonian by projecting onto the target energy manifold appropriately. We define it as

$$\hat{H}_{\text{eff}} = \hat{P}_0 \hat{U} \left( \hat{H}_0 + \epsilon\hat{V} \right) \hat{U}^\dagger \hat{P}_0, \quad (4.1)$$

where  $\hat{P}_0$  is the projector operator to the target energy manifold or subspace  $\mathcal{P}_0$  and  $\hat{U}$  is a unitary transformation that preserves  $\mathcal{P}_0$ . By definition,  $\mathcal{P}_0$  is invariant under  $\hat{H}_0$ , but not under  $\hat{V}$ . Notice we are free to choose which energy manifold we project to, as the procedure only relies on the energy gap between manifolds.

The unitary transformation  $\hat{U}$  is in fact the Schieffer–Wolff transformation. We can see  $\hat{U}$  as a direct rotation between subspaces, which can be written as  $\hat{U} = \exp(\hat{W})$  where  $\hat{W}$  is an anti-hermitian operator that acts off-diagonally between subspaces. This operator is uniquely defined and has the following properties:

1.  $\exp(\hat{W}) \hat{P}_\perp \exp(-\hat{W}) = \hat{P}_0$ ,
2.  $\hat{P}_0 \hat{W} \hat{P}_0 = \hat{P}_\perp \hat{W} \hat{P}_\perp = 0$ ,
3.  $\|\hat{W}\| < \pi/2$ ,

as long as  $\|\hat{P}_\perp - \hat{P}_0\| < 1$ . In other words, we can represent the operator  $\hat{W}$  as

$$\hat{W} = \begin{pmatrix} 0 & \hat{W}_{0,\perp} \\ -\hat{W}_{0,\perp}^\dagger & 0 \end{pmatrix}, \quad (4.2)$$

where the sub-indices in the matrix blocks correspond to the subspaces  $\mathcal{P}_0, \mathcal{P}_\perp$ . This decomposition makes clear the block-off-diagonal shape of  $\hat{W}$  and will be relevant when we try to derive a practical form of the transformation. Likewise, we can decompose the perturbation in two contributions: a block-diagonal part  $\hat{V}_d$  and a block-off-diagonal part  $\hat{V}_{od}$  such that

$$\hat{V} = \hat{V}_d + \hat{V}_{od}. \quad (4.3)$$

We have defined the functional form of the operators concerning the transformation. Now, we perform an expansion of 4.1 through the Baker-Campbell-Haussdorf formula [113] to obtain

$$\hat{H}_{\text{eff}} = \hat{P}_0 \left( \hat{H}_0 + \epsilon\hat{V} + [\hat{W}, \hat{H}_0] + [\hat{W}, \epsilon\hat{V}] + \frac{1}{2} [\hat{W}, [\hat{W}, \hat{H}_0]] + \mathcal{O}(\hat{V}^3) \right) \hat{P}_0 \quad (4.4)$$

We can make the effective Hamiltonian block-diagonal to first order if we choose

$$[\hat{H}_0, \hat{W}] = \epsilon \hat{V}. \quad (4.5)$$

Since  $\hat{W}$  is block-off-diagonal, it conveniently implies  $[\hat{W}, \hat{V}] = [\hat{W}, \hat{V}_{\text{od}}]$ . On the other hand, 4.5 becomes ill-defined if  $\hat{V}_{\text{d}} \neq 0$ . To fix this, we must extract the block-diagonal contribution so that

$$[\hat{H}_0, \hat{W}] = \epsilon \hat{V}_{\text{od}}. \quad (4.6)$$

Then

$$\hat{H}_{\text{eff}} = \hat{P}_0 \left( \hat{H}_0 + \epsilon \hat{V}_{\text{d}} + \frac{1}{2} [\hat{W}, \epsilon \hat{V}_{\text{od}}] + \mathcal{O}(\hat{V}^3) \right) \hat{P}_0. \quad (4.7)$$

We represent 4.6 in the eigenbasis of  $\hat{H}_0$  to define  $\hat{W}$ . Let  $\{|n\rangle\}$  be an orthonormal eigenbasis such that  $\hat{H}_0 |n\rangle = E_n |n\rangle$ ,  $\forall n$ . Since  $\hat{W}, \hat{V}_{\text{od}}$  are block-off-diagonal, we can only solve 4.6 for two eigenvectors of different subspaces, such that  $|n\rangle \in \mathcal{P}_i, |m\rangle \in \mathcal{P}_j$  but  $\mathcal{P}_i \not\subset \mathcal{P}_j$ . In such case,

$$E_n W_{nm} - W_{nm} E_m = \epsilon V_{nm}^{\text{od}}, \quad (4.8)$$

where  $n, m$  correspond to eigenvectors of different subspaces, which guarantees  $E_n \neq E_m$ . We can finally define the matrix elements of the generator  $\hat{W}$  as

$$W_{nm} = \begin{cases} \frac{\epsilon V_{nm}^{\text{od}}}{E_n - E_m}, & \text{iif } |n\rangle \in \mathcal{P}_i, |m\rangle \in \mathcal{P}_j, \mathcal{P}_i \not\subset \mathcal{P}_j, \\ 0, & \text{else.} \end{cases} \quad (4.9)$$

The previous expansion of the unitary transformation is then justified if the generator is infinitesimal, implying  $|\Delta E| \gg |\epsilon \hat{V}_{\text{od}}|$ . The upper bound of this constrain can be defined with high accuracy [112], but this loose condition is sufficient for our purposes.

After projecting on the subspace of interest, we obtain

$$\hat{H}_{nm}^{\text{eff}} = E_{nm} \delta_{nm} + \epsilon \hat{V}_{nm}^{\text{d}} + \frac{\epsilon^2}{2} \sum_l \left( \frac{V_{nl}^{\text{od}} V_{lm}^{\text{od}}}{E_n - E_l} + \frac{V_{nl}^{\text{od}} V_{lm}^{\text{od}}}{E_m - E_l} \right) + \mathcal{O}(\hat{V}^3), \quad (4.10)$$

where  $|n\rangle, |m\rangle \in \mathcal{P}_0, |l\rangle \in \mathcal{P}_{\perp}$ . It is important to remember that this projection is also applied to the eigenbasis, meaning we constrain the Hilbert space to  $\mathcal{P}_0$ .

While we have derived the Schieffer–Wolff transformation up to second-order contributions, the transformation can be extended to infinite terms. The price for such increase in accuracy is the use of a formalism that relies on super-operators and recursive relations [112]. Said formalism has the advantage of



skipping the full spectral decomposition of  $\hat{H}_0$ . This will be unnecessary for us since our goal is to define quadratic Hamiltonians; higher order terms might only increase the complexity of our results unnecessarily.

## Chapter 5

# Spin Squeezing through Dipolar Interactions in the Superfluid Phase

Until now, we had overview on the phenomena of spin squeezing, ultra-cold atoms in the optical lattice as our physical platform of interest and perturbation theory as a tool to derive effective models. From this chapter until the end of this work, we introduce brand new results from our research about the topic of spin squeezing. In this chapter, we present a proposal for its implementation with ultra-cold atoms in the lattice using dipole interactions; published as:

M. Dziurawiec, T. Hernández Yanes, M. Płodzień, M. Gajda, M. Lewenstein, and E. Witkowska, “Accelerating Many-Body Entanglement Generation by Dipolar Interactions in the Bose-Hubbard Model”, *Physical Review A* **107**, 013311 (2023).

A first good guess in our quest to obtain experimentally feasible spin squeezed states through dynamical protocols could be to look for systems that explicitly resemble the characteristics of the OAT and TACT models. In them we can see how the unitary evolution operator  $\hat{U}(t) = e^{-i\hat{H}t}$  generates all-to-all correlations by virtue of the second moments of the collective spin operators. It is then reasonable to suspect long-range interactions might play a similar role in the generation of entanglement, as they create pairwise correlations among all particles in the system.

For instance, the dipolar interaction can be a good candidate for the required correlation generation. Dipolar interaction decays with a power law  $\propto r^{-3}$  where  $r$  is the distance between them. Even so, such interactions might add up in time to generate highly entangled states. In fact, lattice models using dipolar interactions with spin dynamics as the only degree of freedom can show spin squeezing [60, 114].

Nevertheless, the self-imposed constraints of dimensionality and derivation from the Hubbard model brought us to a different hypothesis: dipolar interac-



tions might add up to all-to-all correlations if particles travel without friction across the lattice. Under this assumption we derived the dipolar interactions for two-component bosons in second quantization form and studied the effective model in the superfluid phase of the Bose Hubbard Model ( $J \gg U$ ).

Calculation of the dipolar interactions in the lattice is difficult to perform precisely, as in this case second quantisation formalism yields a complicated integral. But if we assume that Wannier functions heavily localise the integrand, we can take the rest as constant and integration becomes trivial. This naive approximation was already shown in [28] for the single component Bose Hubbard model, but we extended it to the case of two-components with polarisation direction of the dipoles along the quantisation axis of the spins in the lattice.

In the superfluid phase, when the condensate fraction is close to unity, the dynamics are dominated by the operators of quasi-momenta  $q = 0$  in the Fourier representation. This allows us to represent the effective model as a two-mode system, since only the  $q = 0$  momenta will be occupied.

If we write the model in this fashion and skip the constant terms, we arrive at

$$\hat{H}_{\text{eff}} = \chi \left( \tilde{S}_z^2 - \eta \tilde{S}_x^2 \right), \quad (5.1)$$

where the tilde stands for the  $q = 0$  component of a given operator discrete Fourier transform,  $\chi = (U_{\uparrow\uparrow} + U_{\downarrow\downarrow} - 2U_{\uparrow\downarrow})/2M$ , and  $\eta \approx 3\gamma^2\zeta(3)/\chi$ . The first term in the effective model comes purely from the Bose–Hubbard model, as described in Section 3.2, while the second term comes from the dipolar interactions. As we will see,  $\eta$  weakly depends on the boundary conditions of the system, but it will converge when  $M \rightarrow \infty$ .

This means we have two main tunable parameters, the anisotropy in the two-component contact interactions ( $U_{\uparrow\uparrow} + U_{\downarrow\downarrow} \neq 2U_{\uparrow\downarrow}$ ) and the dipolar interactions. We can use these not only to generate optimal squeezing but also to study the continuous transition between the OAT and TACT models.

Remarkably, we have found that anisotropic TACT ( $0 < \eta < 1$ ) yields identical scaling of the spin-squeezing parameter to pure TACT ( $\eta = 1$ ) unless  $\eta \ll 1$  by orders of magnitude, where we recover the OAT model. The only discrepancy is a slight time re-scaling of the squeezing process.

To understand these results, it is important to explain with some detail the calculations we performed to arrive at them.

## 5.1 Dipolar interactions for arbitrary geometry in second quantisation form

In this section, we derive the dipolar interactions in second quantisation form to express said interactions at the same level as the Hubbard model, derived in section 3.1. We follow similar approximations to [93, 115], but extend the



results to two-component bosons and the spin operator. To fully understand the derivation, it is helpful to describe the dipole moment in second quantisation form as well, since its construction as a form factor provides direct insight in how to express it in terms of spin operators. We adopt the notation of chapter 3 to express this formalism. For instance, we define  $\hat{c}_{i,\sigma_i}$  as the annihilation operator associated with the Wannier function  $w_i(\mathbf{r})$  under the tight-binding approximation in the optical lattice. We also adopt the tensor notation for the two-body interactions introduced in eqs. (3.6) and (3.8).

### Definition of dipole moment in second quantisation form

For pedagogical reasons, let us imagine the magnetic dipole moment is part of the single particle Hamiltonian such that  $H_d(\mathbf{r}) = f(\mathbf{r})\mu^\alpha(\mathbf{r})$ , with  $\alpha$  being a given projection direction in coordinate space. Once this concept is established for a single particle properly, we will study the dipolar interaction.

We can express the magnetic dipole moment as proportional to the spin length on a given projection as

$$\mu^\alpha(\mathbf{r}) = -\gamma \langle \hat{S}^\alpha(\mathbf{r}) \rangle. \quad (5.2)$$

As we are working in the lattice, we can define the state measuring eq. (5.2) as a combination of all Wannier functions in the system. It becomes useful to express eq. (5.2) in terms of the matrix elements among the Wannier functions. We can define the spin operators which describe the interaction of two Wannier functions  $w_i^*(\mathbf{r}), w_k(\mathbf{r})$  as

$$\hat{S}_{ik}^x = \frac{1}{2} \left( \hat{S}_{ik}^+ + \hat{S}_{ik}^- \right), \quad (5.3)$$

$$\hat{S}_{ik}^y = \frac{1}{2i} \left( \hat{S}_{ik}^+ - \hat{S}_{ik}^- \right), \quad (5.4)$$

$$\hat{S}_{ik}^z = \frac{1}{2} \left( \hat{c}_{i,\uparrow}^\dagger \hat{c}_{k,\uparrow} + \hat{c}_{i,\downarrow}^\dagger \hat{c}_{k,\downarrow} \right), \quad (5.5)$$

where  $\hat{S}_{ik}^+ = \hat{c}_{i,\uparrow}^\dagger \hat{c}_{k,\downarrow}$ ,  $\hat{S}_{ik}^- = \hat{c}_{i,\downarrow}^\dagger \hat{c}_{k,\uparrow}$ . In general, we would not require such a definition of the spin operators in light of the high localisation of the Wannier functions in the lattice. But since we have separated the spatial wave-function from the corresponding operator, we must continue the analysis before integration with this concept in mind. In practice, one may see this kind of term as a scattering at the spin level.

It follows that the dipole moment projection acts as a tensor that reconstructs the corresponding spin operator when summed over with all the pairs of creation-annihilation operators required. In other words,

$$\sum_{\sigma_i, \sigma_j} \hat{c}_{i,\sigma_i}^\dagger \mu^\alpha(\mathbf{r}) \hat{c}_{j,\sigma_j} = -\gamma \hat{S}_{ij}^\alpha. \quad (5.6)$$



If we apply this concept to the calculation of the single particle Hamiltonian given by  $H_d(\mathbf{r})$  we obtain

$$\hat{H}_d = -\gamma \sum_{i,j} f_{ij} \hat{S}_{ij}^\alpha, \quad (5.7)$$

where  $f_{ij} = \int d\mathbf{r} \omega_i^*(\mathbf{r}) f(\mathbf{r}) \omega_j(\mathbf{r})$ . For instance, if  $f(\mathbf{r}) = 1$ , the orthogonality of the Wannier functions trivially yields the result  $\hat{H}_d = -\gamma \sum_i \hat{S}_i^\alpha = -\gamma \hat{S}^\alpha$  with  $\hat{S}_i^\alpha = \hat{S}_{ii}^\alpha$  being the on-site spin operator of spatial projection  $\alpha$  and  $\hat{S}^\alpha$  the corresponding collective spin operator.

### Dipolar interactions in second quantisation form

If we express the dipole moment as a vector of orthogonal projections  $\boldsymbol{\mu}(\mathbf{r}) = (\mu^x(\mathbf{r}), \mu^y(\mathbf{r}), \mu^z(\mathbf{r}))$ , we can express the interaction between two dipoles as

$$V_{dd}(\mathbf{r}, \mathbf{r}') = \gamma^2 \frac{\boldsymbol{\mu}(\mathbf{r}) \cdot \boldsymbol{\mu}(\mathbf{r}')}{|\mathbf{r} - \mathbf{r}'|^3} - 3\gamma^2 \frac{\boldsymbol{\mu}(\mathbf{r}) \cdot (\mathbf{r} - \mathbf{r}') \boldsymbol{\mu}(\mathbf{r}') \cdot (\mathbf{r} - \mathbf{r}')}{|\mathbf{r} - \mathbf{r}'|^5}. \quad (5.8)$$

In view of the derivation for a single dipole, we must take into account the spin degrees of freedom to calculate the dipolar interactions. If we include the corresponding creation-annihilation operators and sum over the spin degrees of freedom we get

$$\hat{V}_{dd}(\mathbf{r}, \mathbf{r}') = \sum_{\sigma_i, \sigma_j, \sigma_k, \sigma_l} \hat{c}_{i, \sigma_i}^\dagger \hat{c}_{j, \sigma_j}^\dagger V_{dd}(\mathbf{r}, \mathbf{r}') \hat{c}_{k, \sigma_k} \hat{c}_{l, \sigma_l} \quad (5.9)$$

$$= \gamma^2 \frac{\mathbf{S}_{ik} \cdot \mathbf{S}_{jl}}{|\mathbf{r} - \mathbf{r}'|^3} - 3\gamma^2 \frac{\mathbf{S}_{ik} \cdot (\mathbf{r} - \mathbf{r}') \mathbf{S}_{jl} \cdot (\mathbf{r} - \mathbf{r}')}{|\mathbf{r} - \mathbf{r}'|^5} \quad (5.10)$$

where  $\mathbf{S}_{ik} = (\hat{S}_{ik}^x, \hat{S}_{ik}^y, \hat{S}_{ik}^z)$  is a vector of orthogonal projections.

At this point is relevant to separate the integral calculation in two cases, when the dipoles are in the same lattice site ( $|\mathbf{r} - \mathbf{r}'| < d$ ) and when not ( $|\mathbf{r} - \mathbf{r}'| \gtrsim d$ ). In the former case the influence of the lattice is the same for both dipoles and calculations are to be done in momentum space. The result is simply a contribution to the contact interaction terms [28]. In the latter case the depth of the lattice potential strongly localises the dipoles and certain approximations can be taken. The Wannier functions are very well localised around the lattice sites and make other arguments in the integral almost constant. Then, we can assume the Wannier functions act as a delta function for other arguments in the integral so that

$$\begin{aligned}
 \hat{V}_{\text{dd},ijkl}\Big|_{i \neq j} &= \int d\mathbf{r} \int d\mathbf{r}' w_i^*(\mathbf{r}) w_j^*(\mathbf{r}') \left[ \hat{V}_{\text{dd}}(\mathbf{r}, \mathbf{r}') \right]_{|\mathbf{r}-\mathbf{r}'| \geq d} w_k(\mathbf{r}) w_l(\mathbf{r}') \\
 &\approx \hat{V}_{\text{dd}}(\mathbf{R}_i, \mathbf{R}_j) \int d\mathbf{r} w_i^*(\mathbf{r}) w_k(\mathbf{r}) \int d\mathbf{r}' w_j^*(\mathbf{r}') w_l(\mathbf{r}') \\
 &\approx \hat{V}_{\text{dd}}(\mathbf{R}_i, \mathbf{R}_j) \delta(\mathbf{R}_i - \mathbf{R}_k) \delta(\mathbf{R}_j - \mathbf{R}_l).
 \end{aligned}$$

We now have all the ingredient to obtain the dipolar interactions in second quantization form in accordance with eq. (3.6). If we change labels and express the vector  $\mathbf{R}_j - \mathbf{R}_k$  in spherical coordinates  $|\mathbf{R}_j - \mathbf{R}_k|, \theta_{jk}, \phi_{jk}$  we obtain

$$\begin{aligned}
 \hat{V}_{\text{dd}} &= \frac{1}{2} \sum_{i,j,k,l} \hat{V}_{\text{dd},ijkl}\Big|_{i \neq j} \\
 &= \frac{1}{2} \sum_{j,k \neq j} \frac{\gamma^2}{|\mathbf{R}_j - \mathbf{R}_k|^3} \left( (1 - 3 \cos^2 \theta_{jk}) \hat{S}_j^z \hat{S}_k^z \right. \\
 &\quad - \frac{1 - 3 \cos^2 \theta_{jk}}{4} (\hat{S}_j^+ \hat{S}_k^- + \hat{S}_j^- \hat{S}_k^+) \\
 &\quad - \frac{3 \sin 2\theta_{jk} e^{-i\phi_{jk}}}{4} (\hat{S}_j^+ \hat{S}_k^z + \hat{S}_j^z \hat{S}_k^+) \\
 &\quad - \frac{3 \sin 2\theta_{jk} e^{i\phi_{jk}}}{4} (\hat{S}_j^- \hat{S}_k^z + \hat{S}_j^z \hat{S}_k^-) \\
 &\quad \left. - \frac{3}{4} \sin^2 \theta_{jk} (e^{-i2\phi_{jk}} \hat{S}_j^+ \hat{S}_k^+ + e^{i2\phi_{jk}} \hat{S}_j^- \hat{S}_k^-) \right), \tag{5.11}
 \end{aligned}$$

where  $\hat{S}_j^\pm = \hat{S}_j^x \pm i\hat{S}_j^y$ .

For simplicity we will focus on particles in a line, where  $\theta_{jk} = \frac{\pi}{2} \forall j, k$ ;  $\phi_{jk} = 0 \forall k > j$ ;  $\phi_{jk} = \pi \forall k < j$  and  $|\mathbf{R}_j - \mathbf{R}_k| = d|j - k|$  so that

$$\hat{V}_{\text{dd}} = \frac{1}{2} \sum_{j,k \neq j} \frac{\gamma^2}{d^3 |j - k|^3} \left( \hat{S}_j^z \hat{S}_k^z - 2\hat{S}_j^x \hat{S}_k^x + \hat{S}_j^y \hat{S}_k^y \right). \tag{5.12}$$

For simplicity we either assume  $d$  is absorbed into  $\gamma$  or  $d = 1$ .

## 5.2 Effective model under Periodic and Open Boundary Conditions

### Periodic Boundary Conditions

To assume periodic boundary conditions means that, if we sit in a particular lattice site  $j$ , we interact with the  $k$  site in the same manner as with sites  $k \pm M$ ; where  $M$  is the periodicity of the lattice. The difference between these



cases is that one of them will be spatially closer than the others to site  $j$  and since the dipolar interaction inversely depends on the cube of the distance  $d = |j - k| \geq 1$ , we only consider the contribution from the closest site of the three. Such minimal distance can be expressed as

$$d_{\min}(j, k) = \min(|j - (k - M)|, |j - k|, |j - (k + M)|).$$

It can be found that

$$d_{\min}(j, k) = \begin{cases} |j - k|; & |j - k| \leq \lfloor \frac{M}{2} \rfloor, \\ M - |j - k|; & |j - k| > \lfloor \frac{M}{2} \rfloor. \end{cases} \quad (5.13)$$

Then the dipolar interactions under periodic boundary conditions will look like

$$\hat{V}_{\text{dd}} = \frac{1}{2} \sum_j^M \sum_{k \neq j}^M \frac{\gamma^2}{d_{\min}^3(j, k)} \left( \hat{S}_j^z \hat{S}_k^z - 2\hat{S}_j^x \hat{S}_k^x + \hat{S}_j^y \hat{S}_k^y \right), \quad (5.14)$$

If we go to the momentum representation with the transformation

$$\tilde{S}_q^\alpha = \frac{1}{\sqrt{M}} \sum_j e^{i2\pi qj/M} \hat{S}_j^\alpha, \quad (5.15)$$

and assume that we are in the superfluid phase ( $J \gg U$ ), we can consider the system to be at  $q = 0$  only. From eq. (5.15) we have  $\hat{S}_\alpha = \sqrt{M} \tilde{S}_\alpha \equiv \sqrt{M} \tilde{S}_{q=0}^\alpha$ . The  $q = 0$  approximation implies  $\hat{S}_j^\alpha = \tilde{S}_\alpha / \sqrt{M}; \forall j \in [1, M]$ , which simplifies calculations as now the dipolar interactions look like

$$\hat{V}_{\text{dd}} = \frac{\gamma^2}{2M} \left( \sum_{j, k \neq j}^{M, M} \frac{1}{d_{\min}^3(j, k)} \right) \left( \tilde{S}^2 - 3\tilde{S}_x^2 \right), \quad (5.16)$$

where  $\tilde{S}^2 = \tilde{S}_x^2 + \tilde{S}_y^2 + \tilde{S}_z^2$ , allowing us to focus on the calculation of the sum. This can be expressed in terms of the collective operators in coordinate space as

$$\hat{V}_{\text{dd}} = \frac{\gamma^2}{2M^2} \left( \sum_{j, k \neq j}^{M, M} \frac{1}{d_{\min}^3(j, k)} \right) \left( \hat{S}^2 - 3\hat{S}_x^2 \right). \quad (5.17)$$

However, we will maintain the two-mode notation  $\tilde{S}_\alpha$ , as is more explicit for the superfluid regime and the two-mode model is numerically more advantageous than its coordinate space counterpart. We can proceed with a change of variable  $d = j - k$  to rewrite this sum.

$$\sum_{j, k \neq j}^{M, M} \frac{1}{d_{\min}^3(j, k)} = \sum_j^M \sum_{\substack{d=j-1 \\ d \neq 0}}^{j-M} \frac{1}{\min(|d|, M - |d|)^3} \quad (5.18)$$

After a change of variables  $d = j - k$  and making use of 5.13, we obtain

$$\sum_{j,k \neq j}^{M,M} \frac{1}{d_{\min}^3(j,k)} = 2M \sum_{d=1}^{\lfloor \frac{M}{2} \rfloor} \frac{1}{d^3} - 2 \left( \left\lfloor \frac{M}{2} \right\rfloor + 1 - \left\lceil \frac{M}{2} \right\rceil \right) \frac{1}{\lfloor \frac{M}{2} \rfloor^2}. \quad (5.19)$$

If  $M$  is odd ( $\lceil \frac{M}{2} \rceil = \lfloor \frac{M}{2} \rfloor + 1$ ) the last term vanishes, but if  $M$  is even ( $\lceil \frac{M}{2} \rceil = \lfloor \frac{M}{2} \rfloor = \frac{M}{2}$ ) the last term survives. However, it's still half the last term of the sum so we can safely ignore this discrepancy between even and odd cases.

The result is a very fast converging sum which at the large  $M$  limit recovers the Riemann zeta function evaluated at  $s = 3$ , also called Apéry's constant,  $\zeta(3) = \sum_{n=1}^{\infty} \frac{1}{n^3}$ .

With this result, we finally obtain

$$\hat{V}_{\text{dd}} \simeq \gamma^2 \zeta(3) (\tilde{S}^2 - 3\tilde{S}_x^2). \quad (5.20)$$

In the periodic boundary conditions case,  $\eta = 3\gamma^2 \zeta(3)/\chi$ .

The final effective Hamiltonian, ignoring constant terms is

$$\hat{H}_{\text{eff}}^{(\text{PBC})} = \chi (\tilde{S}_z^2 - \eta \tilde{S}_x^2), \quad (5.21)$$

### Open boundary conditions

The effective model under open boundary conditions looks exactly like eq. (5.21). However, the Hamiltonian written in momentum representation in the superfluid phase will be incorrect if we repeat the previous zero momentum approximation, since boundary conditions matter. However, numerical evidence shows we can still apply said approximation if we re-normalize with respect to the condensate fraction, as contributions from  $q \neq 0$  terms seem to be negligible. This is possible because the condensate fraction in the open boundary conditions case, while non-unitary, remains largely constant. Then,

$$\hat{S}_j^\alpha \approx \frac{1}{f_c \sqrt{M}} \tilde{S}_\alpha, \quad (5.22)$$

which can also be expressed as

$$\tilde{S}_\alpha \approx \frac{f_c}{\sqrt{M}} \hat{S}_\alpha. \quad (5.23)$$

With this correction in mind, we obtain

$$\hat{V}_{\text{dd}} \simeq \frac{\gamma^2}{2M f_c^2} \left( \sum_{j,k \neq j}^{M,M} \frac{1}{|j-k|^3} \right) (\tilde{S}^2 - 3\tilde{S}_x^2). \quad (5.24)$$



We can solve the double sum factor in the same manner as the previous case of periodic boundary conditions, obtaining

$$\sum_{j,k \neq j}^{M,M} \frac{1}{|j-k|^3} = 2M \sum_{d=1}^{M-1} \frac{1}{d^3} - 2 \sum_{d=1}^{M-1} \frac{1}{d^2}. \quad (5.25)$$

Both sums in the right hand side converge to the Riemann zeta function at different values of  $s$ . The final result can then be approximated to

$$\hat{V}_{\text{dd}} \simeq \frac{\gamma^2}{f_c^2} \left( \zeta(3) - \frac{\zeta(2)}{M} \right) \left( \tilde{S}^2 - 3\tilde{S}_x^2 \right). \quad (5.26)$$

In the open boundary conditions case, if we take  $1/f_c^2$  as a prefactor, we obtain  $\eta = 3\gamma^2(\zeta(3) - \zeta(2)/M)/\chi$ . In the limit  $M \rightarrow \infty$ , the result converges to that of the periodic boundary conditions case since  $\zeta(2)$  is a constant.

As such, the effective Hamiltonian becomes

$$\hat{H}_{\text{eff}}^{(\text{OBC})} = \frac{\chi}{f_c^2} \left( \tilde{S}_z^2 - \eta \tilde{S}_x^2 \right). \quad (5.27)$$

We compare the obtained effective models with exact numerical calculations of the extended Bose–Hubbard model including the dipolar interactions of eq. (5.12) in fig. 5.1. The condensate fraction remains mostly constant throughout the dynamics, which allows us to apply the zero-momentum approximation safely. This approximation works well even under open boundary conditions if the re-normalization over  $f_c$  is applied. Without the re-normalization, the effective model would show a slower squeezing process than the periodic boundary conditions counterpart since  $\eta^{(\text{OBC})} < \eta^{(\text{PBC})}$ , which is not the case.

### 5.3 Limitations of the model

Nevertheless, this setup has a number of issues. For instance, we assume the the geometry of the system under periodic boundary conditions is a line, not a ring. The ring geometry is feasible, but it would complicate the calculation of the dipolar interactions contribution to the effective model. The interaction can be forced to act as if in a line by applying a strong confinement trap, but this may affect the experimental feasibility. Moreover, the dipolar interactions we calculated require a strong localization approximation and might yield different results under careful scrutiny. In a realistic setting, particles experience some friction when tunnelling in the superfluid phase and we might see single, double or even triple particle losses due to collisions. This is detrimental for squeezing [63].

These disadvantages motivates us to find scalable spin squeezing in other experimentally feasible settings. For instance in the Mott insulating phase, where particle losses due to collisions are far less likely. The cost for such

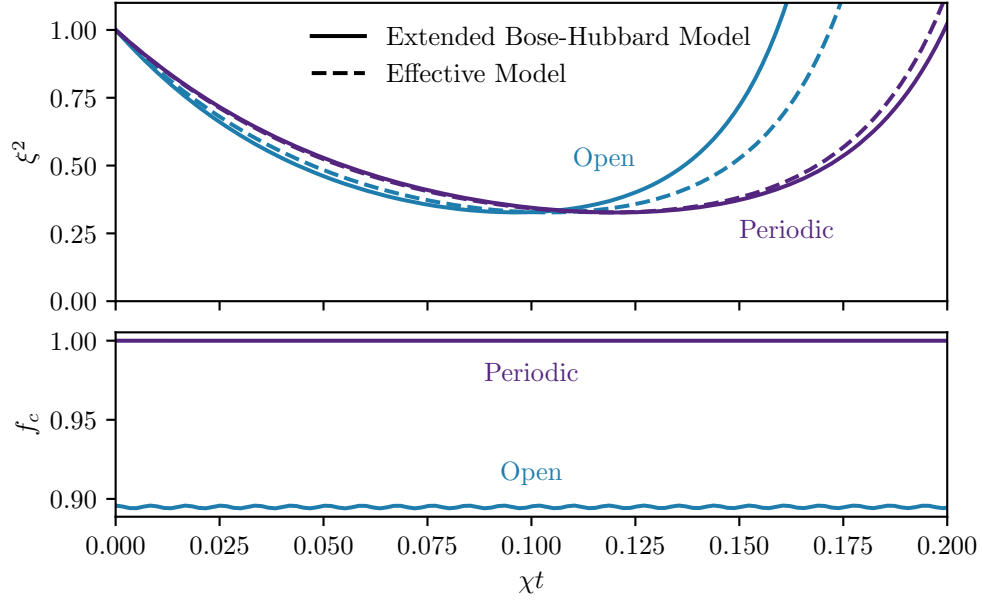







Figure 5.1: Comparison of the spin-squeezing parameter  $\xi^2$  (left) and condensate fraction  $f_c$  (right) dynamics between periodic and open boundary conditions for the Hubbard model with dipolar interactions in the Superfluid regime.  $M = N = 8, J = 100E_{\text{recoil}}, U = (1, 1, 0.05) E_{\text{recoil}}, \gamma = 5.13E_{\text{recoil}}$ . Thus,  $\chi = 0.16E_{\text{recoil}}$  and  $\eta^{(\text{PBC})} = 1, \eta^{(\text{OBC})} = 0.83$ .

schemes is that the recovery of OAT and TACT models require more sophisticated techniques due to the absence of the zero-momentum approximation.



# Accelerating many-body entanglement generation by dipolar interactions in the Bose-Hubbard model

Marlena Dziurawiec <sup>1</sup>, Tanausú Hernández Yanes <sup>1</sup>, Marcin Płodzień <sup>2</sup>, Mariusz Gajda <sup>1</sup>,  
Maciej Lewenstein <sup>2,3</sup> and Emilia Witkowska<sup>1</sup>

<sup>1</sup>*Institute of Physics Polish Academy of Sciences, Aleja Lotników 32/46, 02-668 Warszawa, Poland*

<sup>2</sup>*Institut de Ciències Fotoniques, The Barcelona Institute of Science and Technology, 08860 Castelldefels, Barcelona, Spain*

<sup>3</sup>*Institución Catalana de Investigación y Estudios Avanzados, Pg. Lluís Companys 23, 08010 Barcelona, Spain*



(Received 19 September 2022; accepted 28 November 2022; published 24 January 2023)

The spin-squeezing protocols allow the dynamical generation of massively correlated quantum many-body states, which can be utilized in entanglement-enhanced metrology and technologies. We study a quantum simulator generating twisting dynamics realized in a two-component Bose-Hubbard model with dipolar interactions. We show that the interplay of contact and long-range dipolar interactions between atoms in the superfluid phase activates the anisotropic two-axis countertwisting mechanism, accelerating the spin-squeezing dynamics and allowing the Heisenberg-limited accuracy in spectroscopic measurements.

DOI: [10.1103/PhysRevA.107.013311](https://doi.org/10.1103/PhysRevA.107.013311)

## I. INTRODUCTION

The second quantum revolution's main objective lies in multipartite entangled states: their production, storage, certification, and application. Such states, i.e., many-body entangled and many-body Bell correlated states, are essential resources for quantum-based technologies and quantum-enhancement metrology [1–6]. As such, a general protocol allowing the controlled generation of such states is an extensive research direction in modern quantum science. Spin squeezing represents such a protocol paving the way for high-precision measurements, allowing overcoming the shot-noise limit [7,8], generating many-body entangled [9–13], and many-body Bell correlated states [14–20]. The spin squeezing applies to a system of  $N$  quantum particles in two internal states corresponding to a spin-1/2 degree of freedom and further described by the collective spin of the quantum number  $S = N/2$ . The uncertainty of spectroscopic measurements is  $\xi/\sqrt{N}$ , where

$$\xi^2 = \frac{N\Delta^2\hat{S}_{\perp\min}}{\langle S \rangle^2}, \quad (1)$$

is the spin-squeezing parameter and  $\Delta^2\hat{S}_{\perp\min}$  is the minimal variance in the plane perpendicular to the total spin vector. The spin squeezing is a witness of entanglement depth, i.e., the quantum state is not  $k$  producible when  $\xi < 1/k$  [21–24].

The paradigmatic theoretical models realizing spin squeezing through unitary evolution are given by the so-called one-axis twisting (OAT), and two-axis countertwisting (TACT) Hamiltonians [7]. The OAT Hamiltonian has the form of the nonlinear operator, often cast as

$$\hat{H}_{\text{OAT}} = \hbar\chi\hat{S}_z^2, \quad (2)$$

where  $z$  is the twisting axis and  $\chi^{-1}$  is the timescale on which spin-squeezing parameter has the lowest value  $\xi_{\text{best}}^2$ .

The lowest value of the squeezing parameter scales with particle numbers and for OAT it is  $\xi_{\text{best}} \propto N^{-1/3}$  at  $\chi t_{\text{best}} \simeq N^{-2/3}$  [7]. The TACT Hamiltonian reads

$$\hat{H}_{\text{TACT}} = \hbar\chi(\hat{S}_z^2 - \hat{S}_x^2), \quad (3)$$

where the clockwise and counterclockwise twisting take places around two orthogonal axes  $z$  and  $x$ . The advantage of the TACT is that it gives the Heisenberg limited level of the best squeezing, namely,  $\xi_{\text{best}} \propto N^{-1/2}$ . In addition, the timescale of the best squeezing is accelerated with respect to OAT and it is given by  $\chi t_{\text{best}} \sim N^{-1}\ln(2N)$  [25].

Realizing the quantum simulators of OAT or TACT dynamics is essential for quantum enhancement metrology. Ultracold atoms form a perfect platform for quantum simulators mimicking such twisting dynamics. OAT has been realized with Bose-Einstein condensates utilizing atom-atom collisions [21,26–30] and atom-light interactions [31,32]. Other research directions are ultracold platforms simulating the Hubbard and Heisenberg models, which generate twisting dynamics. In the case of bosons, twisting dynamics is induced by atom-atom collisions [33–36], while for spinful fermions a synthetic spin-orbit coupling is necessary [34,36–40]. Finally, twisting dynamics can be activated with long-range interacting bosons, which provides a platform for spin-squeezing simulators by casting the original Hamiltonian onto the long-range interacting spin chain [41–47].

In this work, we propose a quantum simulator for the TACT model realized in a one-dimensional two-component Bose-Hubbard model in the superfluid phase, considering both contact and dipolar interactions. With the help of full many-body dynamics and an effective two-mode model (TMM) description, we show that the realized squeezing dynamics capture properties of the anisotropic TACT model where the clockwise and counterclockwise twisting take place with different rates. Next, we show that scaling with the system size



of the best squeezing parameter and best squeezing time is equivalent to the scaling obtained for the TACT model. Our results show the significant acceleration of the spin-squeezing dynamics by dipolar interactions, which is an essential effect from the experimental point of view

The paper is organized as follows. In Sec. II we introduce the considered model. Starting with a general many-body description of the system we provide an effective two-mode model accounting for both contact and long-range dipolar interactions. Next, in Sec. III, we perform an analysis of the mean-field phase space of the anisotropic TACT model. In Sec. IV, with the help of the Bogoliubov-Born-Green-Kirkwood-Yvon (BBGKY) hierarchy of equations [48,49], we analyze the scaling of the best squeezing and the best squeezing time with the system size. We describe a proposition of an experimental realization of our model in Appendix A and we conclude in Sec. V.

## II. EXACT AND EFFECTIVE MODELS

We consider  $N$  bosonic atoms in the two internal states  $|\uparrow\rangle, |\downarrow\rangle$  which corresponds to the ensemble of  $N$  spin-1/2 particles (qubits). The atoms are described by the following Hamiltonian:

$$\hat{H} = \hat{H}_0 + \hat{H}_d, \quad (4)$$

$$\hat{H}_0 = \int d^3\mathbf{r} \hat{\Psi}^\dagger(\mathbf{r}) \left( -\frac{\hbar^2 \nabla^2}{2m} + V_{\text{latt}} \right) \hat{\Psi}(\mathbf{r}), \quad (5)$$

$$\hat{H}_d = \int d^3\mathbf{r}_1 \int d^3\mathbf{r}_2 \hat{\Psi}^\dagger(\mathbf{r}_1) \hat{\Psi}^\dagger(\mathbf{r}_2) V_{12} \hat{\Psi}(\mathbf{r}_2) \hat{\Psi}(\mathbf{r}_1), \quad (6)$$

where the vector of the bosonic field operators is  $\hat{\Psi}^T(\mathbf{r}) = [\hat{\Psi}_\uparrow(\mathbf{r}), \hat{\Psi}_\downarrow(\mathbf{r})]$  with  $\hat{\Psi}_\sigma(\mathbf{r})$  describing an atom at the position  $\mathbf{r}$  in the state  $\sigma = \uparrow, \downarrow$ . The interaction potential  $V_{12}$  is a sum of two terms,  $V_{12} = V_c + V_d$ , the short-range contact interaction

$$V_c = \frac{4\pi\hbar^2 a_s}{m} \delta(\mathbf{r}_1 - \mathbf{r}_2), \quad (7)$$

where  $m$  is the atomic mass and  $a_s$  is the  $s$ -wave scattering length. The long-range dipolar interaction

$$V_d = \frac{\mu_0}{4\pi} \left( \frac{\boldsymbol{\mu}_1 \boldsymbol{\mu}_2}{|\mathbf{r}_1 - \mathbf{r}_2|^3} - \frac{3[\boldsymbol{\mu}_1(\mathbf{r}_1 - \mathbf{r}_2)][\boldsymbol{\mu}_2(\mathbf{r}_1 - \mathbf{r}_2)]}{|\mathbf{r}_1 - \mathbf{r}_2|^5} \right), \quad (8)$$

where  $\mu_0$  is the magnetic constant and  $\boldsymbol{\mu}_{1,2}$  is the dipole moment associated with the spin operators  $\boldsymbol{\mu}_{1,2} = -\gamma\hbar\mathbf{s}_{1,2}$ , where  $\mathbf{s} = \frac{1}{2}(\sigma_x, \sigma_y, \sigma_z)$ ,  $\gamma = g\mu_B/\hbar$  is the gyromagnetic ratio,  $g$  is the  $g$  factor, and  $\mu_B$  is the Bohr magneton.

The atoms are loaded into a three-dimensional optical lattice, which is assumed to have strong transverse confinement while tunneling is allowed in one dimension only. Effectively, the optical lattice potential leads to  $V_{\text{latt}} = V_0 \sin^2 kx$ , where  $k = 2\pi/\lambda_{\text{latt}}d$  is a wave vector associated with the lattice wavelength  $\lambda_{\text{latt}} = 2d$ , where  $d$  is a lattice constant. We consider the unit filling, so the number of lattice sites  $M$  equals the total number of atoms  $N$  ( $M = N$ ), and periodic boundary conditions. We assume the atoms occupy the lowest Bloch band. In the tight-binding approximation, the field operator is conveniently expanded in the basis of the Wannier functions, and the Hamiltonian of the system (4) reduces to the

two-component Bose-Hubbard model (BHM) extended by the dipolar term, namely,

$$\hat{H} = \hat{H}_{\text{BH}} + \hat{H}_d \equiv \hat{H}_{\text{dBH}}. \quad (9)$$

The two-component Bose-Hubbard Hamiltonian  $\hat{H}_{\text{BH}}$  reads

$$\begin{aligned} \hat{H}_{\text{BH}} = & -J \sum_{\sigma=\uparrow,\downarrow} \sum_j (\hat{a}_{\sigma,j}^\dagger \hat{a}_{\sigma,j+1} + \hat{a}_{\sigma,j}^\dagger \hat{a}_{\sigma,j-1}) + \sum_j \\ & \times \left( \frac{U_{\uparrow\uparrow}}{2} \hat{n}_{j\uparrow}(\hat{n}_{j\uparrow}-1) + \frac{U_{\downarrow\downarrow}}{2} \hat{n}_{j\downarrow}(\hat{n}_{j\downarrow}-1) + U_{\uparrow\downarrow} \hat{n}_{j\uparrow} \hat{n}_{j\downarrow} \right), \end{aligned} \quad (10)$$

where  $\hat{a}_{\sigma,j}$  and  $\hat{n}_{\sigma,j}$  are the on-site annihilation and number operators of atoms in the state  $|\sigma\rangle$  at the site  $j$ . The hopping amplitude  $J$ , set as the energy unit, does not depend on the spin state  $\sigma$ , while the interaction coefficients  $U_{\sigma\sigma'}$  contain the contributions of both the on-site contact and the on-site dipolar interaction [50]. The dipolar interaction term  $\hat{H}_d$  reads

$$\hat{H}_d = \sum_{j,k \neq j} W_{jk} (\hat{S}_{z,j} \hat{S}_{z,k} - 2\hat{S}_{x,j} \hat{S}_{x,k} + \hat{S}_{y,j} \hat{S}_{y,k}), \quad (11)$$

where  $W_{jk} = W_0/|j-k|^3$ ,  $W_0 = \gamma^2 \hbar^2 \mu_0 / 4\pi d^3$  is a dipole-dipole coupling constant. The on-site spin operators are  $\hat{S}_j^+ = \hat{a}_{\uparrow,j}^\dagger \hat{a}_{\downarrow,j}$ ,  $\hat{S}_j^- = \hat{a}_{\downarrow,j}^\dagger \hat{a}_{\uparrow,j}$ ,  $\hat{S}_j^\pm = \hat{S}_{x,j} \pm i\hat{S}_{y,j}$ , and  $\hat{S}_{z,j} = (\hat{n}_{j\uparrow} - \hat{n}_{j\downarrow})/2$ , while the collective spin operators read  $\hat{S}_x = \frac{1}{2} \sum_j \hat{S}_{x,j}$ ,  $\hat{S}_y = \frac{1}{2i} \sum_j \hat{S}_{y,j}$ , and  $\hat{S}_z = \frac{1}{2} \sum_j \hat{S}_{z,j}$ . The range of the dipole potential extends over several lattice sites under typical experimental conditions. Therefore, it is approximately constant on scales comparable to the spatial localization of Wannier functions. Under this condition, the dipolar part of the Hamiltonian can be simplified in the form (11), see Appendix B for a derivation.

We consider the dynamical generation of spin-squeezed states from an initial spin coherent state when the system is in the superfluid phase  $U_{\sigma\sigma} \ll J$  and contact interactions compete with the long-range one. This regime corresponds to the situation when the wave functions of atoms are delocalized over the entire lattice and the condensate fraction  $f_c \equiv \frac{1}{N^2} \sum_{i,j} \sum_{\sigma=\uparrow,\downarrow} \langle \hat{a}_{\sigma,i}^\dagger \hat{a}_{\sigma,j} \rangle$  approximately equals 1. The implementation of the Hamiltonian  $\hat{H}$  under these conditions by using chromium-52 atoms is discussed in Appendix A for parameters as in the recent experiment [51].

The two-component Bose-Hubbard model can simulate the OAT dynamics via contact interactions among bosons in the superfluid phase [35]. Here we show that the system can simulate the anisotropic TACT dynamics when dipolar interactions between the bosonic atoms are taken into account. To understand why the twisting mechanism is simulated by the system Hamiltonian (9) we perform the following analysis. First, we consider  $\hat{H}_{\text{dBH}}$  in the quasimomentum representation by using the Fourier transforms  $\hat{a}_{\sigma,j} = \frac{1}{\sqrt{N}} \sum_n e^{i\frac{2\pi}{N}jn} \hat{a}_{\sigma,q_n}$ , which leads to the following transformation for spin operators:  $\hat{S}_{\sigma,j} = \frac{1}{\sqrt{N}} \sum_n e^{i\frac{2\pi}{N}jn} \hat{S}_{\sigma,q_n}$ , where the quasimomentum reads  $q_n = \frac{2\pi}{N}n$  for  $n = 0, 1, 2, \dots, N-1$  [52]. Next, by keeping the zero-momentum mode  $q_n = 0$  contributions only, one can show that  $\hat{H}_{\text{dBH}}$  reduces to the effective model that is a sum of



two terms

$$\hat{H}_{d\text{BH},q_n=0} = \hat{H}_{\text{BH},q_n=0} + \hat{H}_{d,q_n=0}. \quad (12)$$

The first term,  $\hat{H}_{\text{BH},q_n=0}$ , comes from the zero quasimomentum mode of the Bose-Hubbard Hamiltonian

$$\begin{aligned} \hat{H}_{\text{BH},q_n=0} = & -2J\hat{N}_{q_n=0} + \Omega_{NN}\hat{N}_{q_n=0}^2 \\ & + \Omega_{SN}\hat{S}_{z,q_n=0}\hat{N}_{q_n=0} + \Omega_{SS}\hat{S}_{z,q_n=0}^2, \end{aligned} \quad (13)$$

where

$$\Omega_{NN} = \frac{U_{\uparrow\uparrow} + U_{\downarrow\downarrow} + 4U_{\uparrow\downarrow}}{8N}, \quad (14)$$

$$\Omega_{SN} = \frac{U_{\uparrow\uparrow} - U_{\downarrow\downarrow}}{2N}, \quad (15)$$

$$\Omega_{SS} = \frac{U_{\uparrow\uparrow} + U_{\downarrow\downarrow} - 2U_{\uparrow\downarrow}}{2N}, \quad (16)$$

and realizes OAT dynamics [35]. The second term,  $\hat{H}_{d,q_n=0}$ , consists of the zero-momentum component of the dipolar interactions

$$\hat{H}_{d,q_n=0} = 2h_{[N/2]}^{(3)} \frac{W_0}{N} (\hat{S}_{q_n=0}^2 - 3\hat{S}_{x,q_n=0}^2), \quad (17)$$

with  $h_{[N/2]}^{(3)} = \sum_{l=1}^{[N/2]} 1/l^3 \approx 1.2$  for  $N > 5$  and  $\hat{S}_q^2 = \hat{S}_{x,q}^2 + \hat{S}_{y,q}^2 + \hat{S}_{z,q}^2$ , see Appendix B for details. Finally, by collecting the particular terms in (12) we obtain

$$\hat{H}_{d\text{BH},q_n=0} = \frac{U - U_{\uparrow\downarrow}}{N} \hat{S}_{z,q_n=0}^2 - 6h_{[N/2]}^{(3)} \frac{W_0}{N} \hat{S}_{x,q_n=0}^2, \quad (18)$$

where we neglect the constant energy terms assuming  $\hat{N}_{q_n=0} = N$  and  $U_{\uparrow\uparrow} = U_{\downarrow\downarrow} = U$ . Note here that the zero quasimomentum component of the spin operators corresponds to the collective spin operators in the position representation, namely,  $\hat{S}_{\beta,q_n=0} = \frac{1}{\sqrt{N}} \sum_j \hat{S}_{\beta,j}$  with  $\beta = x, y, z$ . As such, we will refer to  $\hat{S}_{\beta,q_n=0}$  as the operators  $\hat{S}_\beta$ . Taking this into account, we identify the effective two-mode model (TMM)

$$\hat{H}_{\text{TMM}} = \hbar\chi(\hat{S}_z^2 - \eta\hat{S}_x^2), \quad (19)$$

which is the anisotropic TACT with

$$\hbar\chi = \frac{U - U_{\uparrow\downarrow}}{N}, \quad (20)$$

$$\hbar\chi\eta = 6h_{[N/2]}^{(3)} \frac{W_0}{N}, \quad (21)$$

where  $\eta \approx 7.2W_0/(U - U_{\uparrow\downarrow})$  is the anisotropy parameter and  $\chi$  sets the energy scale. Note here that  $\chi$  sets the timescale, which is independent of the tunneling rate  $J$ . In the two limiting cases  $\eta = 0$  and  $\eta = 1$  the effective model (19) reduces to the OAT and TACT models, respectively.

In Fig. 1(a) we show the spin-squeezing parameter (1) obtained from the exact many-body numerical simulation of the system dynamics under the dipolar Bose-Hubbard Hamiltonian (9) and the effective two-mode model (19), see Appendix D for more details concerning numerical simulations. For the chosen set of parameters, the condensate fraction is approximately 1,  $f_c \approx 1$ , at the timescale corresponding to the best squeezing, which justifies our two-mode

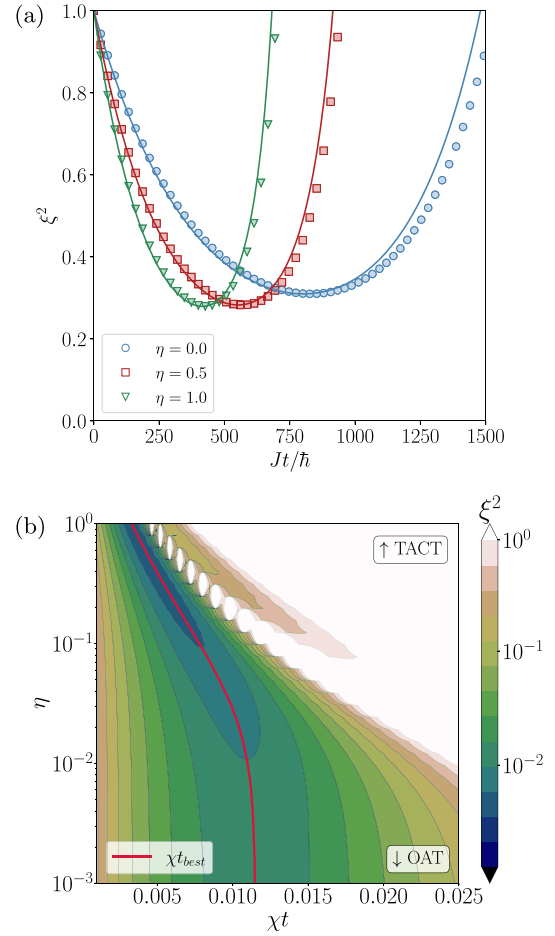


FIG. 1. (a) Time evolution of the spin-squeezing parameter  $\xi^2$  defined in (1) for different values of anisotropy parameter  $\eta = \{0.0, 0.5, 1.0\}$  (lines from right to left). The two limiting cases, i.e.,  $\eta = 0$  and  $\eta = 1$  correspond to OAT and TACT dynamics, respectively. Points correspond to the results from the exact many-body numerical simulation of  $\hat{H}_{\text{dBH}}$  given by (9), while solid lines to the numerical results from the effective two-mode model (19) when  $N = M = 10$ ,  $U/J = 0.01$  and  $U_{\uparrow\downarrow}/J = 0.95U/J$ . (b) Color-encoded values of the spin-squeezing parameter  $\xi^2$  versus  $\chi t$  and  $\eta$  obtained from the numerical simulations of the two-mode model (19) for  $N = 10^3$  atoms. The solid red line indicates the best squeezing time.

approximation. In the case of the chromium atoms considered in Appendix A, the best squeezing time  $Jt_{\text{best}}/\hbar \approx 500$  corresponds to  $t_{\text{best}} \approx 35\text{ms}$  when  $V_0 = 3E_R$ , where  $E_R$  is the recoil energy. The overall agreement between the two models can be noticed. The acceleration of the squeezing dynamics is visible by increasing the value of the anisotropy parameter. In Fig. 1(b) we present a variation of the spin-squeezing parameter  $\xi^2$  in time and the anisotropy parameter  $\eta$  from the two-mode model (19) for  $N = 10^3$ . We can observe the two limiting cases corresponding to OAT and TACT dynamics for  $\eta = 0$  and  $\eta = 1$ , respectively. We observe a smooth transition between OAT and TACT dynamics in the intermediate region.

In the next section, we provide an intuitive explanation for the OAT-TACT crossover with the help of phase portrait analysis of the two-mode model (19). In Sec. IV we derive

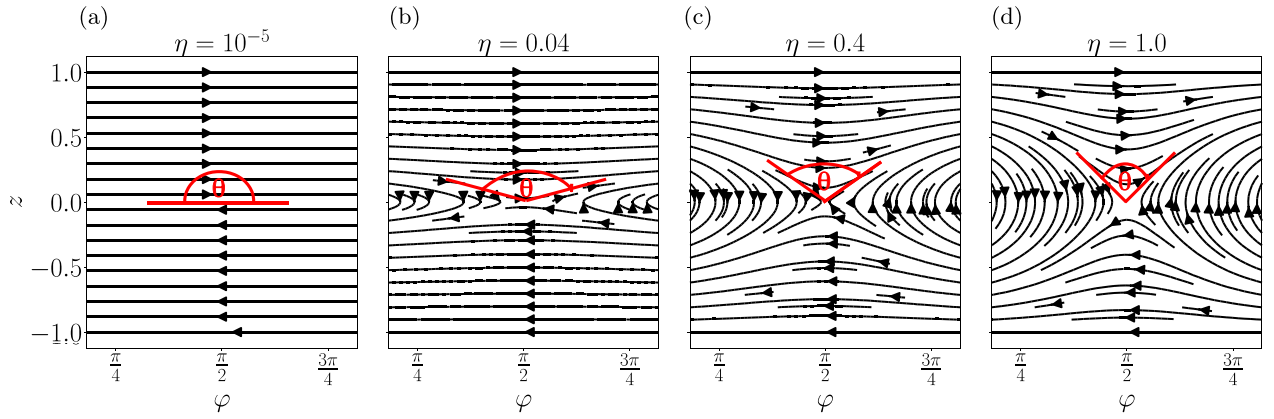


FIG. 2. Mean-field phase portraits  $\epsilon(\phi, z)$  indicating geometrical representations of trajectories and directions of evolution for the effective two-mode model (19) for the anisotropy parameter  $\eta = \{10^{-5}, 0.04, 0.4, 1.0\}$  (from left to right). Arrows show the direction set by the vector  $\vec{n} = (\dot{\phi}, \dot{z})$ . The angles  $\theta$  between ingoing and outgoing flow along constant energy lines around the unstable fixed point are marked by red (see main text). The corresponding values of angles  $\theta$  are approximately  $\pi, 0.87\pi, 0.64\pi, 0.5\pi$  (from left to right). The left-most panel  $\eta \approx 0$  corresponds to OAT, where the distribution of a state localized around  $z = 0$  is stretched during the evolution. While increasing  $\eta$  (consecutive panels) we show how the trajectories around  $z = 0$  change to form the saddle point resulting in stretching of the initial distribution located nearby the saddle in two different directions with relative angle  $\theta$ , realizing TACT at  $\theta = \pi/2$  when  $\eta = 1.0$ .

the scaling of the best squeezing and the best squeezing time with  $N$  showing the acceleration of squeezing dynamics by the dipolar interactions.

### III. MEAN-FIELD PHASE PORTRAITS

The activation of the TACT dynamics by dipolar interactions can be intuitively explained by analyzing the structure of the mean-field phase space of the two-mode model (19). It is a good navigator for the dynamical spin squeezing [25] as the eigenstates of the quantum Hamiltonian localize on classical phase-space energy contours [53] and quantum evolution distinguishes between stable and unstable classical fixed points [54].

The analysis of the mean-field phase space is performed by replacing the annihilation and creation operators by complex numbers [55],  $\hat{a}_\uparrow \rightarrow \sqrt{N\rho_\uparrow}e^{i\phi_\uparrow}$ ,  $\hat{a}_\downarrow \rightarrow \sqrt{N\rho_\downarrow}e^{i\phi_\downarrow}$ . This allows to introduce the new canonical variables  $z = \rho_\uparrow - \rho_\downarrow$  and  $\phi = \phi_\uparrow - \phi_\downarrow$  and transforms the spin operators to  $\hat{S}_x \rightarrow N\frac{\sqrt{1-z^2}}{2}\cos\phi$ ,  $\hat{S}_y \rightarrow N\frac{\sqrt{1-z^2}}{2}\sin\phi$ ,  $\hat{S}_z \rightarrow \frac{N}{2}z$ . The Hamiltonian (19) takes the form of the energy functional  $\epsilon(\phi, z)$ :

$$\epsilon(\phi, z) = \frac{N}{4}z^2 - \frac{\eta N}{4}(1 - z^2)\cos^2\phi. \quad (22)$$

Equations of motions for the canonical position  $\phi$  and the conjugate momentum  $z$  are set by the Hamilton equations

$$\begin{aligned} \dot{\phi} &= \frac{\partial\epsilon(\phi, z)}{\partial z} = \frac{N}{2}z + \frac{\eta N}{2}z\cos^2\phi, \\ \dot{z} &= -\frac{\partial\epsilon(\phi, z)}{\partial\phi} = -\frac{\eta N}{2}(1 - z^2)\cos\phi\sin\phi. \end{aligned} \quad (23)$$

In the following, we will analyze the topology of phase portraits, which are a geometrical representation of the trajectories of a dynamical system in the phase space. In our case, the trajectories are tangent to the velocity field  $(\dot{\phi}, \dot{z})$ . The phase portrait consists of fixed points or closed orbits corresponding to a steady state and satisfies  $(\dot{\phi}, \dot{z}) = (0, 0)$ . Spin

squeezing takes place in the vicinity of unstable fixed points. We are interested in the fixed point located at  $z = 0$  and  $\phi = \frac{\pi}{2}$  according to the location of our initial spin coherent state. The classification of fixed points can be found by analysis of the eigenproblem of the stability matrix  $\mathcal{M}$ , which in our case is

$$\mathcal{M} = \begin{bmatrix} \frac{\partial^2\epsilon}{\partial z\partial\phi} & \frac{\partial^2\epsilon}{\partial z^2} \\ -\frac{\partial^2\epsilon}{\partial^2\phi} & -\frac{\partial^2\epsilon}{\partial z\partial\phi} \end{bmatrix} = \frac{N}{2} \begin{bmatrix} 0 & 1 \\ \eta & 0 \end{bmatrix}. \quad (24)$$

When  $\eta \neq 0$ , the matrix  $\mathcal{M}$  has two nondegenerate real eigenvalues of the opposite sign  $(\lambda_1, \lambda_2) = \frac{1}{2}\sqrt{\eta}N(-1, 1)$  and two real eigenvectors

$$v_1 = \begin{bmatrix} -\frac{1}{\sqrt{\eta}} \\ 1 \end{bmatrix}, \quad v_2 = \begin{bmatrix} \frac{1}{\sqrt{\eta}} \\ 1 \end{bmatrix}. \quad (25)$$

The scalar product of the two eigenvectors  $\{v_1, v_2\}$  defines the angle  $\theta$  between ingoing and outgoing trajectories crossing at the center of the unstable saddle fixed points

$$\theta = \arccos \frac{\langle v_1 | v_2 \rangle}{|v_1||v_2|}. \quad (26)$$

In Fig. 2 we show examples of the mean-field phase portraits, i.e., the constant energy lines for  $\eta = \{10^{-5}, 0.04, 0.4, 1\}$ . The arrows indicate the direction of the evolution and visualize the dynamics in the vicinity of the fixed point. For  $\eta \approx 0$  the angle between ingoing and outgoing trajectories is  $\theta \approx \pi$  and corresponds to the pure OAT dynamics with a nonisolated unstable fixed point. For  $\eta > 0$  the nature of the fixed point changes to the unstable saddle fixed point, see Figs. 2(b) to 2(d), which in the limiting case  $\eta = 1$  corresponds to the TACT dynamics, Fig. 2(d). Note the angle  $\theta$  is approximately  $\pi/2$  when the value of the anisotropy parameter  $\eta$  is 1. The change in the nature of the unstable fixed point is responsible for the change in the scaling properties of the best squeezing.



#### IV. SCALING WITH THE SYSTEM SIZE

In this section, we study the scaling of the best squeezing for the anisotropic TACT model (19). We apply the Gaussian approach within the BBGKY hierarchy [48,49], which was used in [25] to explain the scaling for the TACT model. Here, we generalize the theory taking into account the values of parameter  $\eta$  different than one.

We start with equations of motion for expectation values of spin operators  $\langle \hat{S}_j \rangle$ , which involve terms that depend on the first-order moments  $\langle \hat{S}_j \rangle$  and second-order moments  $\langle \hat{S}_i \hat{S}_j \rangle$ . Subsequently, the time evolution of the second-order moments depend on themselves and on third-order moments, and so on. It leads to the BBGKY hierarchy of equations of motion for expectation values of operator products. The hierarchy is then truncated by keeping the first- and the second-order moments

$$\langle \hat{S}_i \hat{S}_j \hat{S}_k \rangle \simeq \langle \hat{S}_i \hat{S}_j \rangle \langle \hat{S}_k \rangle + \langle \hat{S}_j \hat{S}_k \rangle \langle \hat{S}_i \rangle + \langle \hat{S}_j \hat{S}_i \rangle \langle \hat{S}_k \rangle - \langle \hat{S}_i \rangle \langle \hat{S}_j \rangle \langle \hat{S}_k \rangle. \quad (27)$$

To perform the scaling analysis, we first introduce a small parameter  $\epsilon = 1/N$  and transform the spin components into  $\hat{J}_j = \sqrt{\epsilon} \hat{S}_j$  which obey cyclic commutation relations  $[\hat{J}_x, \hat{J}_y] = i\sqrt{\epsilon} \hat{J}_z$ . The Hamiltonian (19) then reads  $\hat{H} = \frac{\hbar\chi}{\epsilon} (\hat{J}_z^2 - \eta \hat{J}_x^2)$ . Equations of motion for expectation values of the spin operators  $\langle \hat{J}_j \rangle \equiv h_j$ , second-order moments  $\langle \hat{J}_i \hat{J}_j \rangle \equiv \Delta_{ij}$ , and  $\langle \hat{J}_j^2 \rangle - \langle \hat{J}_j \rangle^2 \equiv \delta_j$  read

$$\dot{h}_y = 2(1 + \eta)\Delta_{xz}, \quad (28)$$

$$\dot{\Delta}_{xz} = -2(\delta_z + \eta\delta_x)h_y, \quad (29)$$

$$\dot{\delta}_z = -4\eta\Delta_{xz}h_y, \quad (30)$$

$$\dot{\delta}_x = -4\Delta_{xz}h_y, \quad (31)$$

where time is measured in the dimensionless unit  $\tau = \chi t / \sqrt{\epsilon}$ . The initial coherent state at the unstable saddle fixed point  $|\Psi(0)\rangle = |\theta = \pi/2, \varphi = \pi/2\rangle$  gives the following initial conditions:  $h_y(0) = (2\sqrt{\epsilon})^{-1}$ ,  $\delta_z(0) = \delta_x(0) = 1/4$ , and  $\Delta_{xz}(0) = 0$ . To find the approximate solution we introduce the two quadratures  $X = \delta_z + \sqrt{\eta}\Delta_{xz}$  and  $Y = \delta_z - \sqrt{\eta}\Delta_{xz}$  obeying the dynamical equations  $\dot{X} = -4\sqrt{\eta}Xh_y$  and  $\dot{Y} = -4\sqrt{\eta}Yh_y$ , which have the following solutions:

$$X(t) = X(0)e^{-4\sqrt{\eta}f(\tau)}, \quad (32)$$

$$Y(t) = Y(0)e^{4\sqrt{\eta}f(\tau)}, \quad (33)$$

where  $f(\tau) = \int_0^\tau h_y(\tau')d\tau'$  for  $\eta \neq 0$ . This gives

$$\delta_z(\tau) = \delta_z(0) \cosh[4\sqrt{\eta}f(\tau)], \quad (34)$$

$$\Delta_{xz}(\tau) = -\frac{\delta_z(0)}{\sqrt{\eta}} \sinh[4\sqrt{\eta}f(\tau)], \quad (35)$$

$$h_y(\tau) - h_y(0) = -\frac{\delta_z(0)}{\sqrt{\eta}} \int_0^\tau \sinh[4\sqrt{\eta}f(\tau')]d\tau'. \quad (36)$$

In principle, the solution for  $h_y$  can be found in a self-consistent way, here, however, we approximate it by taking the

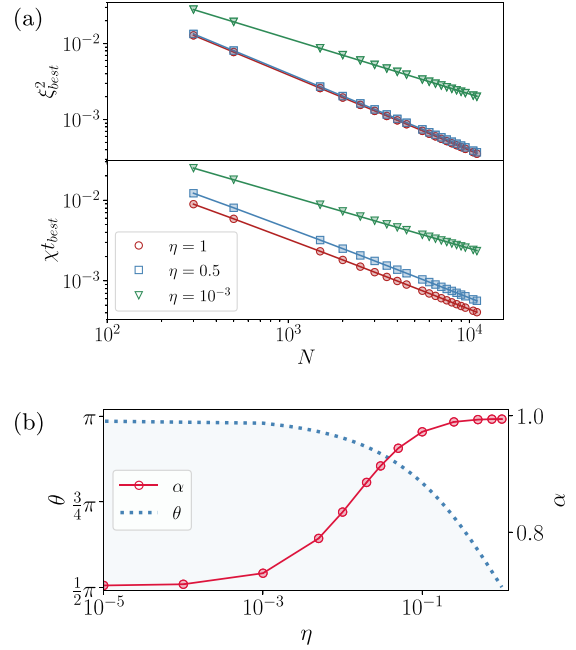


FIG. 3. (a) Examples of the scaling of the best squeezing  $\xi_{\text{best}}^2$  and the best squeezing time  $\chi t_{\text{best}}$  with the number of atoms  $N$  for various values of the parameter of anisotropy  $\eta = \{1, 0.5, 10^{-3}\}$ . (b) Scaling exponents  $\alpha$  obtained by fitting the function  $\propto N^{-\alpha}$  to the best squeezing  $\xi_{\text{best}}^2$  is shown by the red points (red solid line is added to guide the eye). The angle  $\theta$  between the ingoing and outgoing mean-field trajectories (see main text) is shown by the dashed blue line.

first iteration, namely,  $f(\tau) \simeq f(0) + f'(0)\tau$ , which results in

$$h_y(\tau) = \frac{1}{2\sqrt{\epsilon}} \left\{ 1 + \frac{(1+\eta)\epsilon}{2\eta} [1 - \cosh(2\tau\sqrt{\eta/\epsilon})] \right\}. \quad (37)$$

Next, one evaluates the evolution of (34) and (35) by taking (37) in  $f(\tau)$ . Finally, noting that the spin-squeezing parameter (1) is determined by the quadrature  $X(t)$ , namely,  $\xi^2 \approx X(t)$  when approximating  $\langle S \rangle \approx h_y(0)/\sqrt{\epsilon}$ , we obtain the scaling of the best squeezing and the best squeezing time with  $N$  by keeping the leading-order terms in  $\epsilon$ , which results in

$$\xi_{\text{best}}^2 \sim 1/N, \quad \chi t_{\text{best}} \sim \frac{\ln(\eta N)}{\sqrt{\eta} N}, \quad (38)$$

when  $\eta$  is of the order of one. We compared the above analytical predictions with the numerically solved set of differential equations (28) to (31) and confirmed the scaling (38) when  $\eta \in (0.3, 1)$ .

The quantitative illustration of the above results can be provided by analyzing the scaling of the best squeezing with  $N$  obtained from the numerical time evolution of the TMM Hamiltonian (19). Figure 3(a) presents the best squeezing  $\xi_{\text{best}}^2$  and the best squeezing time  $\chi t_{\text{best}}$  as a function of particle number  $N$ . Power-law behavior can be noticed for various  $\eta$ . Therefore, for each value of the anisotropy parameter  $\eta$  we extracted the scaling exponent  $\alpha$  by fitting  $\xi_{\text{best}}^2 \sim N^{-\alpha}$ . Figure 3(b) shows the change of the fitted exponent  $\alpha$  as the function of anisotropy parameter  $\eta$  and is compared to the variation of the angle  $\theta$ . A characteristic feature is a change



in the value of  $\alpha$  when  $\eta \in (10^{-3}, 10^{-1})$ . In the same range  $\theta$  diminishes from  $\pi$  to approximately  $\pi/2$ . We conclude the variation of  $\alpha$  is driven by the change in the structure of the unstable fixed point. It is worth mentioning here that  $\alpha \approx 1$  when  $\eta \approx 1$ . Our results show that the Heisenberg limited level of squeezing is possible in the proposed realization of the anisotropic TACT model.

## V. CONCLUSION

In this work, we show how the OAT mechanism, generating many-body entanglement, can be accelerated by the long-range interactions via activation of the anisotropic TACT mechanisms. We explain the activation of the TACT mechanism during competition of contact and dipolar interactions between bosons in a superfluid phase. We propose the experimentally feasible quantum simulator for the anisotropic TACT dynamics based on dipolar two-component Bose-Hubbard in a one-dimensional optical lattice. With the help of the scaling analysis, we show that it is possible to obtain a Heisenberg-limited level of squeezing for a weak anisotropy. The anisotropic TACT model accelerates the spin-squeezing dynamics compared to OAT with the improvement of the level of squeezing. Our protocol allows for fast generation of many-body entangled states with entanglement depth larger than in a standard OAT scenario.

Our work provides an essential step toward generating many-body-entangled states during the two-axis counter-twisting protocol in state-of-the-art experimental setups, paving the way for obtaining the Heisenberg limit of spectroscopic measurements in ultracold atoms systems.

## ACKNOWLEDGMENTS

We gratefully acknowledge discussions with B. B. Laburthe-Tolra. This work was supported by the Polish National Science Centre Projects No. DEC-2019/35/O/ST2/01873 (T.H.Y.), No. DEC-2020/38/L/ST2/00375 (M.D.), and Grant No. 2019/32/Z/ST2/00016 through the project MAQS under QuantERA, which received funding from the European Union's Horizon 2020 research and innovation program under Grant No. 731473 (E.W. and M.G.). M.P. acknowledges the support of the Polish National Agency for Academic Exchange, the Bekker Program No. PPN/BEK/2020/1/00317. ICFO group acknowledges support from: ERC AdG NOQIA; Ministerio de Ciencia y Innovation Agencia Estatal de Investigaciones (PGC2018-097027-B-I00/10.13039/501100011033, CEX2019-000910-S/10.13039/501100011033, Plan National FIDEUA PID2019-106901GB-I00, FPI, QUANTERA MAQS PCI2019-111828-2, QUANTERA DYNAMITE PCI2022-132919, Proyectos de I+D+I "Retos Colaboración" QUSPIN RTC2019-007196-7); European Union NextGenerationEU (PRTR); Fundació Cellex; Fundació Mir-Puig; Generalitat de Catalunya (European Social Fund FEDER and CERCA program (AGAUR Grant No. 2017 SGR 134, QuantumCAT U16-011424, cofunded by ERDF Operational Program of Catalonia 2014-2020); Barcelona Supercomputing Center MareNostrum (FI-2022-1-0042); EU Horizon 2020 FET-OPEN OPTologic (Grant No

899794); National Science Centre, Poland (Symfonia Grant No. 2016/20/W/ST4/00314); European Union's Horizon 2020 research and innovation program under the Marie-Sklodowska-Curie Grants No 101029393 (STREDCH) and No 847648 ("La Caixa" Junior Leaders fellowships ID100010434: LCF/BQ/PI19/11690013, LCF/BQ/PI20/11760031, LCF/BQ/PR20/11770012, LCF/BQ/PR21/11840013). Part of the computations were carried out at the Centre of Informatics Tricity Academic Supercomputer & Network.

## APPENDIX A: IMPLEMENTATION OF THE METHOD

To estimate the characteristic energy and timescales we assume the tunneling is possible only along the  $x$  direction while transversely the atoms are in a localized wave function that is approximated by a Gaussian with a characteristic length  $L_{\perp}$ . In the absence of the lattice, the system is homogeneous, the atoms being confined in a flat-bottom potential. In the range of parameters  $V_0/E_R > 1$ , the Wannier functions can be approximated by Gaussian functions whose width is set by the frequency associated to each lattice site minimum [56]. Therefore,  $w(x) \approx (\frac{k^2}{\pi})^{1/4} (\frac{V_0}{E_R})^{1/8} e^{-\sqrt{V_0/E_R} k^2 x^2/2}$ . Here,  $k = 2\pi/\lambda_{\text{latt}}$  and further  $d = \lambda_{\text{latt}}/2$ . This is a fairly good approximation to obtain the interaction coefficient

$$\frac{U_{\sigma\sigma'}}{E_R} \approx \sqrt{\frac{32}{\pi}} \frac{a_{\sigma\sigma'} d}{L_{\perp}^2} \left(\frac{V_0}{E_R}\right)^{1/4}. \quad (\text{A1})$$

The tunneling rate is then well approximated by [57], yielding

$$\frac{J}{E_R} \approx \frac{4}{\sqrt{\pi}} \left(\frac{V_0}{E_R}\right)^{3/4} e^{-2\sqrt{\frac{V_0}{E_R}}}, \quad (\text{A2})$$

see also [35] for more details. The above two approximated formulas give access to the estimation of the corresponding energy scales.

In the observed dynamics generated by the nonisotropic TACT the considered atoms must be magnetic to have a large dipole moment resulting in the value of  $\eta$  of the order of one, for example, chromium atoms [51] or the lanthanides Er and Dy [58]. The high degree of tunability of interatomic interactions opened the path to a study of magnetic dipolar effects and their role in Hubbard dynamics. These magnetic atoms usually have spin larger than  $1/2$ . Therefore, methods for the restriction of the dynamics to two Zeeman states, as, e.g., in [59], are necessary. To be concrete, let us consider magnetic chromium atoms  $^{52}\text{Cr}$  as in the recent experiment [51]. The atoms are loaded into an optical lattice generated by laser light of the wavelength  $\lambda_{\text{latt}} = 532$  nm. The corresponding recoil energy is then  $E_R/\hbar = 2\pi \times 13.5$  kHz. The external magnetic field aligned along  $z$  axis and the corresponding Zeeman shift split the magnetic components. Initially, the atoms are prepared in a superposition of  $m_s = -3$  and  $m_s = -2$  Zeeman states. The later term corresponds to the  $\downarrow$  and  $\uparrow$  states, respectively. The magnetic field can be used to bring these two states on-resonance and separate them from the others. Therefore, the short-range contact interactions of atoms is only within  $S = 6$  and  $S = 4$  channels characterized by the two scattering lengths  $a_6 = 103a_B$  and  $a_4 = 64a_B$  [51,60], respectively, where  $a_B$  is the Bohr radius.



To have strong tunneling  $J$  with respect to the interaction strength  $U_{\sigma\sigma'}$ , we can tune either the scattering length  $a_{\sigma\sigma'}$  using Feshbach resonances [61], properly set the characteristic transverse length  $L_{\perp}$ , or adapt both of them. According to (A1) and (A2), the corresponding relation for  $J > U$  gives us  $L_{\perp}^2/(a_{\uparrow\uparrow}d) > e^{2\sqrt{V_0/E_R}}\sqrt{2E_R/V_0}$  [62]. The tunneling estimated by (A2) is  $J/\hbar = 2\pi \times 2.17\text{kHz}$  when  $V_0 = 3E_R$ .

The characteristic dipole-dipole energy for chromium atoms is  $W_0/\hbar = \gamma^2\hbar^2\mu_0/4\pi d^3 \approx 2\pi \times 2.8\text{Hz}$ , or equivalently,  $W_0/J \approx 10^{-3}$  for  $V_0/E_R \approx 3$ . Therefore, to have  $\eta \approx 1$  the relation between interaction coefficients should be  $(U - U_{\uparrow\downarrow})/J \approx 7.2 \times 10^{-3}$ . Tuning of the scattering lengths  $a_{\sigma\sigma'}$  or the system geometry via  $L_{\perp}$  would be necessary to meet this condition. We stress that assumption  $U_{\uparrow\uparrow} = U_{\downarrow\downarrow}$  in (18) was made to make the term proportional to  $\hat{S}_{z,q_n=0}$  equal to zero in (13). The assumption does not need to be fully fulfilled to achieve the same level of squeezing and time as long as  $\Omega_{SS} \gg \Omega_{SN}$ , regardless of the specific values of  $U_{\sigma\sigma'}$ .

A properly chosen external magnetic field is needed to provide a sufficiently large Zeeman splitting preventing any spin dynamics, both due to spin-changing collisions triggered by contact and dipole-dipole interaction. As such, the effective spin-1/2 model assumed here is a valid approximation. In the absence of spin-changing collisions as well as demagnetization, the coherence time can be of the order of seconds [63]. The anisotropy parameter  $\eta$  can be tuned by changing  $U_{\sigma\sigma'}$  via optical Feshbach resonances [64] to obtain the value of  $\eta$  close to 1. Standard Feshbach tuning of a scattering length by utilizing a magnetic field might also be used, provided that the resonant value of the magnetic field is large enough to ensure sufficiently large Zeeman splitting, as discussed above.

Finally, to measure the spin-squeezing parameter  $\xi^2$ , the two-body correlators of the collective spin operators are needed. Such measurements were recently successfully demonstrated in experiments [63].

## APPENDIX B: DIPOLAR INTERACTION

To obtain the lattice version of dipolar interaction we start with the Hamiltonians (6) and (8)

$$\begin{aligned} \hat{H}_d = & \int d^3\mathbf{r}_1 \int d^3\mathbf{r}_2 \frac{\gamma^2\mu_0\hbar^2}{4\pi|\mathbf{r}_1 - \mathbf{r}_2|^3} \\ & \times \left\{ (1 - 3\cos^2\theta_{12}) \left( \hat{J}_1^z \hat{J}_2^z - \frac{\hat{J}_1^+ \hat{J}_2^- + \hat{J}_1^- \hat{J}_2^+}{4} \right) \right. \\ & - \frac{3}{4} \sin^2\theta_{12} (e^{2i\phi_{12}} \hat{J}_1^- \hat{J}_2^- + \text{H.c.}) \\ & \left. - \frac{3}{4} \sin 2\theta_{12} [e^{i\phi_{12}} (\hat{J}_1^z \hat{J}_2^- + \hat{J}_1^- \hat{J}_2^z) + \text{H.c.}] \right\}, \quad (\text{B1}) \end{aligned}$$

with  $\mathbf{r}_1 \neq \mathbf{r}_2$ , and where  $\hat{J}_1^+ = \hat{\Psi}_{\uparrow}^{\dagger}(\mathbf{r}_1)\hat{\Psi}_{\downarrow}(\mathbf{r}_1)$ ,  $\hat{J}_1^- = \hat{\Psi}_{\downarrow}^{\dagger}(\mathbf{r}_1)\hat{\Psi}_{\uparrow}(\mathbf{r}_1)$ ,  $\hat{J}_1^z = [\hat{\Psi}_{\uparrow}^{\dagger}(\mathbf{r}_1)\hat{\Psi}_{\uparrow}(\mathbf{r}_1) - \hat{\Psi}_{\downarrow}^{\dagger}(\mathbf{r}_1)\hat{\Psi}_{\downarrow}(\mathbf{r}_1)]/2$ , and similarly at  $\mathbf{r}_2$ . The two angles  $\phi, \theta$  parametrize the normal vector along the  $\mathbf{r}_1 - \mathbf{r}_2$  direction, namely,  $\vec{n}_{12} = \frac{\mathbf{r}_1 - \mathbf{r}_2}{|\mathbf{r}_1 - \mathbf{r}_2|} = (\cos\phi_{12}\sin\theta_{12}, \sin\phi_{12}\sin\theta_{12}, \cos\theta_{12})$ .

We assume the system is loaded into the one-dimensional optical lattice potential, while remaining in its ground state in transverse directions. We assume also the atomic gas is

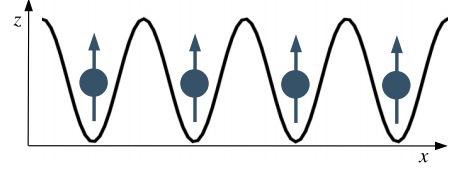


FIG. 4. Schematic of the geometry of the system: gray arrows indicate an initial configuration of the elementary dipoles and the green curve of the optical lattice potential.

polarized initially along the  $z$  axis and the polarization axis sets the quantization axis, as illustrated in Fig. 4. Therefore, we consider the following form of the field operator:

$$\hat{\Psi}_{\uparrow}(\mathbf{r}) = \hat{\Phi}_{\uparrow}(x)\phi(y)\phi(z), \quad (\text{B2})$$

and we expand  $\hat{\Phi}_{\uparrow}(x)$  in the basis of Wannier functions  $w(x - x_j)$  localized around lattice sites, where  $x_j$  denotes the position of the  $j$ th site in the lowest-energy band

$$\hat{\Phi}_{\uparrow}(x) = \sum_j \hat{a}_{\uparrow,j} w(x - x_j), \quad (\text{B3})$$

where  $\hat{a}_{j,\uparrow}$  annihilates an atom in the single-particle Wannier state  $w(x - x_j)$  of the lowest-energy band localized on the  $j$ th site, in the internal state  $\uparrow$ . In (B2) we assume  $\phi(y)$  and  $\phi(z)$  are the ground-state wave functions of the system in the  $y$  and  $z$  directions. The same applies to the  $\downarrow$  operator.

The geometry of the system we chose determines the normal vector  $\vec{n} = (1, 0, 0)$  and sets the value of  $\theta_{12} = \pi/2$  and  $\phi_{12} = 0$ . Taking this into account, in the tight-binding limit the dipolar Hamiltonian reduces to (11) due to the normalization of the wave functions.

It is worth commenting here about the importance of the geometry chosen. There is a symmetry between the  $x$  and  $y$  axes, i.e., if the lattice was along the  $y$  axis, the resulting Hamiltonian (11) would have the factor of  $-2$  in the front of the  $\hat{S}_j^y \hat{S}_k^y$  term. On the other hand, if the lattice was along the  $z$  axis, the factor  $-2$  would appear in the front of  $\hat{S}_j^z \hat{S}_k^z$ . This has an important consequence in the resulting effective model (19), which would be the OAT one.

## APPENDIX C: DIPOLAR INTERACTIONS AND TWO-MODE MODEL

The approximation leading to the two-mode model relies on the macroscopic occupation of the zero quasimomentum mode. It is controlled by the condensate fraction. Here we show how the dipolar part of the two-mode effective model can be derived from (11). To be more specific, we consider (11) in the Fourier space

$$\begin{aligned} \hat{H}_d = & \frac{1}{N} \sum_{q_1, q_2} \sum_{j, k \neq j} W_{jk} (\hat{S}_{z, q_1} \hat{S}_{z, q_2} - 2\hat{S}_{x, q_1} \hat{S}_{x, q_2} \\ & + \hat{S}_{y, q_1} \hat{S}_{y, q_2}) e^{i2\pi(q_1 j + q_2 k)/N}, \quad (\text{C1}) \end{aligned}$$

which, by keeping the parts for  $q_1 = q_2 = 0$ , reads

$$\hat{H}_{d, q_n=0} = \frac{1}{N} \sum_{j, k \neq j} W_{jk} (\hat{S}_{z, q_n=0}^2 - 2\hat{S}_{x, q_n=0}^2 + \hat{S}_{y, q_n=0}^2). \quad (\text{C2})$$

Finally, as the total spin is conserved we can always use  $\hat{S}_{z,q_n=0}^2 + \hat{S}_{y,q_n=0}^2 = \hat{S}_{q_n=0}^2 - \hat{S}_{x,q_n=0}^2$ , which leads to

$$\hat{H}_{d,q_n=0} = \frac{1}{N} \sum_{j,k \neq j} W_{jk} (\hat{S}_{q_n=0}^2 - 3\hat{S}_{x,q_n=0}^2). \quad (C3)$$

To obtain the equation of the form (17) we set  $\sum_{j,k \neq j} W_{jk} = 2h_{[N/2]}^{(3)} W_0$ , where  $h_{[N/2]}^{(3)} = \sum_{l=1}^{[N/2]} 1/l^3$ .

#### APPENDIX D: NUMERICAL EVALUATION OF SPIN SQUEEZING PARAMETER

##### 1. Dipolar Bose-Hubbard model

We performed the full many-body numerical simulations of  $\hat{H}_{dBH} = \hat{H}_{BH} + \hat{H}_d$  with (10) and (11). To this end, we constructed the Fock states basis, as described in [35]. We implemented numerically the matrix representation of the Hamiltonian  $\hat{H}_{dBH}$ , and the initial spin coherent state is

$$|\Psi(0)\rangle = |\theta, \psi\rangle = e^{-i\hat{S}_z\psi} e^{-i\hat{S}_y\theta} |\Psi_a\rangle, \quad (D1)$$

where  $|\Psi_a\rangle$  is the system's ground state when all atoms are in the  $|\uparrow\rangle$  state. The system evolves according to the unitary operator, namely,

$$|\Psi(t)\rangle = e^{-i\hat{H}_{dBH}t/\hbar} |\Psi(0)\rangle, \quad (D2)$$

and the spin-squeezing parameter (1) is calculated.

##### 2. Two-mode model

To find the scaling exponents, we perform numerical time evolution of the TMM. We express Hamiltonian (19) in the Fock-state basis consisting of the vectors of the form  $|n, N-n\rangle$ , where  $N$  is the total number of atoms,  $n$  is the number of the particles in the  $|\uparrow\rangle$  state, and  $N-n$  is the number of the particles in the  $|\downarrow\rangle$  state.

Our initial state is the spin-coherent state, which we obtain as a double rotation of the state  $|N, 0\rangle$  according to

$$|\Psi(0)\rangle = |\theta, \psi\rangle = e^{-i\hat{S}_z\psi} e^{-i\hat{S}_y\theta} |N, 0\rangle. \quad (D3)$$

Next, we apply the unitary evolution

$$|\Psi(t)\rangle = e^{-i\hat{H}_{TMM}t/\hbar} |\Psi(0)\rangle, \quad (D4)$$

we calculate the spin squeezing parameter (1) and find its first minimum  $\xi_{\text{best}}^2$ , as well as the time at which it occurs  $\chi t_{\text{best}}$ .

- 
- [1] A. Acín, I. Bloch, H. Buhrman, T. Calarco, C. Eichler, J. Eisert, D. Esteve, N. Gisin, S. J. Glaser, F. Jelezko, S. Kuhr, M. Lewenstein, M. F. Riedel, P. O. Schmidt, R. Thew, A. Wallraff, I. Walmsley, and F. K. Wilhelm, *New J. Phys.* **20**, 080201 (2018).
  - [2] J. Eisert, D. Hangleiter, N. Walk, I. Roth, D. Markham, R. Parekh, U. Chabaud, and E. Kashefi, *Nat. Rev. Phys.* **2**, 382 (2020).
  - [3] A. Kinos, D. Hunger, R. Kolesov, K. Mølmer, H. de Riedmatten, P. Goldner, A. Tallaie, L. Morvan, P. Berger, S. Welinski, K. Karrai, L. Rippe, S. Kröll, and A. Walther, *arXiv:2103.15743*.
  - [4] A. Laucht, F. Hohls, N. Ubbelohde, M. F. Gonzalez-Zalba, D. J. Reilly, S. Stobbe, T. Schröder, P. Scarlino, J. V. Koski, A. Dzurak, C.-H. Yang, J. Yoneda, F. Kuemmeth, H. Bluhm, J. Pla, C. Hill, J. Salfi, A. Oiwa, J. T. Muhonen, E. Verhagen, M. D. LaHaye, H. H. Kim, A. W. Tsen, D. Culcer, A. Geresdi, J. A. Mol, V. Mohan, P. K. Jain, and J. Baugh, *Nanotechnology* **32**, 162003 (2021).
  - [5] C. Becher, W. Gao, S. Kar, C. Marciniak, T. Monz, J. G. Bartholomew, P. Goldner, H. Loh, E. Marcellina, K. E. J. Goh, T. S. Koh, B. Weber, Z. Mu, J.-Y. Tsai, Q. Yan, S. Gyger, S. Steinhauer, and V. Zwiller, *arXiv:2202.07309*.
  - [6] J. Fraxanet, T. Salamon, and M. Lewenstein, *arXiv:2204.08905*.
  - [7] M. Kitagawa and M. Ueda, *Phys. Rev. A* **47**, 5138 (1993).
  - [8] D. J. Wineland, J. J. Bollinger, W. M. Itano, and D. J. Heinzen, *Phys. Rev. A* **50**, 67 (1994).
  - [9] M. Fadel, T. Zibold, B. Décamps, and P. Treutlein, *Science* **360**, 409 (2018).
  - [10] A. Evrard, V. Makhalov, T. Chalopin, L. A. Sidorenkov, J. Dalibard, R. Lopes, and S. Nascimbene, *Phys. Rev. Lett.* **122**, 173601 (2019).
  - [11] O. Hosten, N. J. Engelsen, R. Krishnakumar, and M. A. Kasevich, *Nature (London)* **529**, 505 (2016).
  - [12] E. Pedrozo-Peñafiel, S. Colombo, C. Shu, A. F. Adiyatullin, Z. Li, E. Mendez, B. Braverman, A. Kawasaki, D. Akamatsu, Y. Xiao *et al.*, *Nature (London)* **588**, 414 (2020).
  - [13] H. Bao, J. Duan, S. Jin, X. Lu, P. Li, W. Qu, M. Wang, I. Novikova, E. E. Mikhailov, K.-F. Zhao, K. Mølmer, H. Shen, and Y. Xiao, *Nature (London)* **581**, 159 (2020).
  - [14] J. Tura, R. Augusiak, A. B. Sainz, T. Vértesi, M. Lewenstein, and A. Acín, *Science* **344**, 1256 (2014).
  - [15] R. Schmied, J.-D. Bancal, B. Allard, M. Fadel, V. Scarani, P. Treutlein, and N. Sangouard, *Science* **352**, 441 (2016).
  - [16] A. Aloy, J. Tura, F. Baccari, A. Acín, M. Lewenstein, and R. Augusiak, *Phys. Rev. Lett.* **123**, 100507 (2019).
  - [17] F. Baccari, J. Tura, M. Fadel, A. Aloy, J.-D. Bancal, N. Sangouard, M. Lewenstein, A. Acín, and R. Augusiak, *Phys. Rev. A* **100**, 022121 (2019).
  - [18] J. Tura, A. Aloy, F. Baccari, A. Acín, M. Lewenstein, and R. Augusiak, *Phys. Rev. A* **100**, 032307 (2019).
  - [19] G. Müller-Rigat, A. Aloy, M. Lewenstein, and I. Frérot, *PRX Quantum* **2**, 030329 (2021).
  - [20] M. Płodzień, M. Lewenstein, E. Witkowska, and J. Chwedeńczuk, *Phys. Rev. Lett.* **129**, 250402 (2022).
  - [21] A. Sørensen, L.-M. Duan, J. I. Cirac, and P. Zoller, *Nature (London)* **409**, 63 (2001).
  - [22] L. Pezzé and A. Smerzi, *Phys. Rev. Lett.* **102**, 100401 (2009).
  - [23] P. Hyllus, W. Laskowski, R. Krischek, C. Schwemmer, W. Wieczorek, H. Weinfurter, L. Pezzé, and A. Smerzi, *Phys. Rev. A* **85**, 022321 (2012).
  - [24] G. Tóth, *Phys. Rev. A* **85**, 022322 (2012).
  - [25] D. Kajtoch and E. Witkowska, *Phys. Rev. A* **92**, 013623 (2015).



- [26] A. Sørensen and K. Mølmer, *Phys. Rev. Lett.* **83**, 2274 (1999).
- [27] M. F. Riedel, P. Böhi, Y. Li, T. W. Hänsch, A. Sinatra, and P. Treutlein, *Nature (London)* **464**, 1170 (2010).
- [28] C. Gross, T. Zibold, E. Nicklas, J. Estève, and M. K. Oberthaler, *Nature (London)* **464**, 1165 (2010).
- [29] C. D. Hamley, C. S. Gerving, T. M. Hoang, E. M. Bookjans, and M. S. Chapman, *Nat. Phys.* **8**, 305 (2012).
- [30] A. Qu, B. Evrard, J. Dalibard, and F. Gerbier, *Phys. Rev. Lett.* **125**, 033401 (2020).
- [31] I. D. Leroux, M. H. Schleier-Smith, and V. Vuletić, *Phys. Rev. Lett.* **104**, 073602 (2010).
- [32] K. Maussang, G. E. Marti, T. Schneider, P. Treutlein, Y. Li, A. Sinatra, R. Long, J. Estève, and J. Reichel, *Phys. Rev. Lett.* **105**, 080403 (2010).
- [33] D. Kajtoch, E. Witkowska, and A. Sinatra, *Europhys. Lett.* **123**, 20012 (2018).
- [34] P. He, M. A. Perlin, S. R. Muleady, R. J. Lewis-Swan, R. B. Hutson, J. Ye, and A. M. Rey, *Phys. Rev. Res.* **1**, 033075 (2019).
- [35] M. Płodzień, M. Kościelski, E. Witkowska, and A. Sinatra, *Phys. Rev. A* **102**, 013328 (2020).
- [36] M. Mamaev, I. Kimchi, R. M. Nandkishore, and A. M. Rey, *Phys. Rev. Res.* **3**, 013178 (2021).
- [37] M. L. Wall, A. P. Koller, S. Li, X. Zhang, N. R. Cooper, J. Ye, and A. M. Rey, *Phys. Rev. Lett.* **116**, 035301 (2016).
- [38] S. Kolkowitz, S. L. Bromley, T. Bothwell, M. L. Wall, G. E. Marti, A. P. Koller, X. Zhang, A. M. Rey, and J. Ye, *Nature (London)* **542**, 66 (2017).
- [39] S. L. Bromley, S. Kolkowitz, T. Bothwell, D. Kedar, A. Safavi-Naini, M. L. Wall, C. Salomon, A. M. Rey, and J. Ye, *Nat. Phys.* **14**, 399 (2018).
- [40] T. Hernández Yanes, M. Płodzień, M. Mackoitis Sinkevičienė, G. Žlabys, G. Juzeliūnas, and E. Witkowska, *Phys. Rev. Lett.* **129**, 090403 (2022).
- [41] O. Civitarese, M. Reboiro, L. Rebon, and D. Tielas, *Phys. Lett. A* **374**, 424 (2010).
- [42] M. A. Perlin, C. Qu, and A. M. Rey, *Phys. Rev. Lett.* **125**, 223401 (2020).
- [43] T. Bilitewski, L. De Marco, J.-R. Li, K. Matsuda, W. G. Tobias, G. Valtolina, J. Ye, and A. M. Rey, *Phys. Rev. Lett.* **126**, 113401 (2021).
- [44] T. Roscilde, F. Mezzacapo, and T. Comparin, *Phys. Rev. A* **104**, L040601 (2021).
- [45] H. Wu, X.-Y. Lin, Z.-X. Ding, S.-B. Zheng, I. Lesanovsky, and W. Li, *Sci. China Phys. Mech. Astron.* **65**, 280311 (2022).
- [46] T. Comparin, F. Mezzacapo, and T. Roscilde, *Phys. Rev. Lett.* **129**, 150503 (2022).
- [47] T. Comparin, F. Mezzacapo, and T. Roscilde, *Phys. Rev. A* **105**, 022625 (2022).
- [48] J. R. Anglin and A. Vardi, *Phys. Rev. A* **64**, 013605 (2001).
- [49] A. André and M. D. Lukin, *Phys. Rev. A* **65**, 053819 (2002).
- [50] O. Dutta, M. Gajda, P. Hauke, M. Lewenstein, D.-S. Lühmann, B. A. Malomed, T. Sowiński, and J. Zakrzewski, *Rep. Prog. Phys.* **78**, 066001 (2015).
- [51] B. Pasquiou, G. Bismut, Q. Beaufils, A. Crubellier, E. Maréchal, P. Pedri, L. Vernac, O. Gorceix, and B. Laburthe-Tolra, *Phys. Rev. A* **81**, 042716 (2010).
- [52] M. Gaudin, *The Bethe Wavefunction* (Cambridge University Press, Berlin, 2014).
- [53] F. Trimborn, D. Witthaut, and H. J. Korsch, *Phys. Rev. A* **79**, 013608 (2009).
- [54] V. S. Shchesnovich and V. V. Konotop, *Phys. Rev. A* **77**, 013614 (2008).
- [55] A. Smerzi, S. Fantoni, S. Giovanazzi, and S. R. Shenoy, *Phys. Rev. Lett.* **79**, 4950 (1997).
- [56] I. Bloch, J. Dalibard, and W. Zwerger, *Rev. Mod. Phys.* **80**, 885 (2008).
- [57] W. Zwerger, *J. Opt. B: Quantum Semiclassical Opt.* **5**, S9 (2003).
- [58] M. A. Norcia and F. Ferlino, *Nat. Phys.* **17**, 1349 (2021).
- [59] S. Baier, D. Petter, J. H. Becher, A. Patscheider, G. Natale, L. Chomaz, M. J. Mark, and F. Ferlino, *Phys. Rev. Lett.* **121**, 093602 (2018).
- [60] J. Pietraszewicz, T. Sowiński, M. Brewczyk, M. Lewenstein, and M. Gajda, *Phys. Rev. A* **88**, 013608 (2013).
- [61] C. Chin, R. Grimm, P. Julienne, and E. Tiesinga, *Rev. Mod. Phys.* **82**, 1225 (2010).
- [62] However, we would like to stress here that the validity condition of our method is set by the condensate fraction close to 1 rather, than solely the ratio  $J/U$ .
- [63] Y. A. Alaoui, B. Zhu, S. R. Muleady, W. Dubosclard, T. Roscilde, A. M. Rey, B. Laburthe-Tolra, and L. Vernac, *Phys. Rev. Lett.* **129**, 023401 (2022).
- [64] K. M. Jones, E. Tiesinga, P. D. Lett, and P. S. Julienne, *Rev. Mod. Phys.* **78**, 483 (2006).



## Chapter 6

# Spin Squeezing through Spin Orbit Coupling in the Mott Insulating Phase

In the previous chapter we proposed a setup in the superfluid regime that achieves a continuous transition between OAT and TACT, in principle reaching the Heisenberg limit. However, this proposal has several experimental difficulties like particle losses due to collisions and changes in the dipole interactions due to more realistic geometries of the lattice. In this chapter we propose to work in the Mott insulating regime to tackle these issues. To generate squeezing, we rely on second-order perturbation theory and build an optimal perturbation through the so-called spin-orbit coupling term. Finally, we find interesting differences between working under periodic and open boundary conditions, even yielding non-vanishing discrepancies when  $M \rightarrow \infty$ .

The results shown in this chapter are the result of our own research and have been published as:

T. Hernández Yanes, M. Płodzień, M. Mackoīt Sinkevičienė, G. Žlabys, G. Juzeliūnas, and E. Witkowska, “One- and Two-Axis Squeezing via Laser Coupling in an Atomic Fermi-Hubbard Model”, *Physical Review Letters* **129**, 090403 (2022),

T. Hernández Yanes, G. Žlabys, M. Płodzień, D. Burba, M. M. Sinkevičienė, E. Witkowska, and G. Juzeliūnas, “Spin Squeezing in Open Heisenberg Spin Chains”, *Physical Review B* **108**, 104301 (2023).

### 6.1 Perturbation theory for the Mott Insulating Phase

One way to minimise particle losses is to reduce the number of collisions possible in the system. Fermions are a natural choice for this because of the



exclusion principle, which allows to have up to two particles of different spin per site. This automatically reduces the collisions with respect to bosons.

Another strategy to reduce collisions is to work in a phase of matter where they are highly unlikely. In contrast with the superfluid phase, the Mott insulating phase ( $J \ll U$ ) keeps the system into the single occupied states manifold. Even if our initial state had double occupied sites in it, particle losses due to collisions will be more favourable due to the strong contact interactions and we will eventually reach a state of single occupied sites. Alternatively, quantum distillation [116] allow us to retrieve a state of single occupied sites and discard the double occupied sites as they move to the boundaries of the system.

As described in section 3.3, in the Mott insulating phase particles can still tunnel freely if holes are present, obtaining the so-called  $t$ - $J$  model [117]. But if the system is at half-filling ( $M = N$ ) the lattice is fully occupied and tunnelling processes are effectively suppressed.

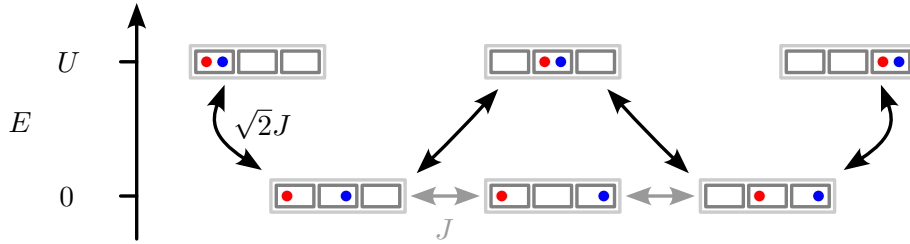


Figure 6.1: Sketch of energy manifolds and couplings among a selected number of possible states in the Fermi-Hubbard Hamiltonian for a lattice of three sites and two particles of opposite spin ( $M = 3, N_{\uparrow} = 1, N_{\downarrow} = 1$ ). Lattice sites are represented by rectangles while particles are represented with circles of different colour for the spin. Couplings are given by  $\langle \psi_i | \hat{H}_{\text{tun}} | \psi_j \rangle$  while energies are calculated with  $\langle \hat{H}_{\text{int}} \rangle$ . Couplings of magnitude  $\sqrt{2}J, J$  are represented with black and grey arrows, respectively. If  $\Delta E = U \gg \sqrt{2}J$ , we may apply perturbation theory to obtain an effective Hamiltonian from second-order processes.

In such case, the Fermi-Hubbard model (introduced in section 3.1, eq. (3.9)) becomes Ising-like, which is usually referred to as a Heisenberg model [101]. In the case of the Fermi-Hubbard model, the result reduces directly to the Heisenberg XXX model, also known as the Spin Exchange Hamiltonian

$$\hat{H}_{\text{SE}} = J_{\text{SE}} \sum_j \left( \hat{S}_j^x \hat{S}_{j+1}^x + \hat{S}_j^y \hat{S}_{j+1}^y + \hat{S}_j^z \hat{S}_{j+1}^z - \frac{1}{4} \right), \quad (6.1)$$

where  $J_{\text{SE}} = 4J^2/U$ .

While these constraints are beneficial to avoid particle losses by collisions, generating quadratic Hamiltonians under these conditions is more involved than in the superfluid regime.

One way to find them is to use the exact same tool which allows us to map to the XXX model, the Schrieffer-Wolff transformation introduced in chapter 4. If a given state belongs to a certain energy manifold given by the partial Hamiltonian  $\hat{H}_0$ , but another part of the full Hamiltonian  $\hat{V}$  couples said state to a different manifold, we can use perturbation theory to treat this coupling as a virtual transition. If the energy gap is sufficiently large, the transition will be fast enough so that the result is an effective transition between states of the initial manifold. If such a process is second-order only, it produces an effective coupling which is quadratic, or at the very least a product of two terms that correspond to the coupling term  $\hat{V}$ . For more details, see section 4.1.

With this in mind, we can start thinking on the required constraints so that spin squeezing is optimal, like the energy manifold we want to isolate the excited states manifold we want to use for the required virtual processes.

By inspection of the spin squeezing parameter (2.43), it becomes clear we want a state that maximises  $\langle \hat{S}_n \rangle$ , so we want our initial state to have the maximal total spin possible. Naturally, we can pick a spin coherent state as our initial state so satisfy this condition. These states are also eigenstates of  $\hat{H}_{\text{SE}}$ , since they conserve the SU(2) symmetry.

We must now look for the high energy manifold we plan to use as a stepping stone for our quadratic Hamiltonian. Since we want our perturbation to be proportional to the spin operators to obtain the result we desire, a natural proposition is to construct an eigenstate from local spin excitations. If we solve the eigenvalue problem in such a way for PBC, we will find the so called spin wave states, also known as magnons in the literature [105], which can also be obtained through the Bethe ansatz [104], as explained in section 3.3.

$$|S = N/2 - 1, m, q\rangle = \sum_j e^{2\pi qj/M} \hat{S}_j^\pm |S = N/2, m \mp 1\rangle, \quad (6.2)$$

where  $q \in [1, M - 1]$ .

These states belong to a lower total spin manifold and are eigenstates of  $\hat{H}_{\text{SE}}$  with eigenvalue  $E_q = J_{\text{SE}}(1 - \cos 2\pi q/M)$ .

With all other pieces in place, the only elements missing are the perturbation that matches the coupling between energy manifolds and to make the magnitude of this perturbation sufficiently small with respect to the energy gap.



## 6.2 Squeezing via Spin Orbit Coupling in the Mott Insulating Phase

We found the historically called spin orbit coupling (SOC), more aptly referred to as atom light coupling in this context, matches the generator of the spin waves states with the form

$$\hat{H}_{\text{SOC}} = \Omega \sum_j \left( e^{i\phi j} \hat{S}_j^+ + e^{-i\phi j} \hat{S}_j^- \right). \quad (6.3)$$

This term can be derived from the interaction of a classical light field with the particles in the lattice when the angle of incidence and wavelength of said light source doesn't match those of the lattice potential.

We analytically found the SOC term survives and mostly doesn't affect the Mott insulating phase mapping if  $J \ll U, \Omega \ll U$ . If applied as is, this term will generate on-site spin flips which will complicate the perturbation theory analysis. However, if we apply a unitary transformation so this term is diagonal, we will see virtual processes involving tunnelling and spin flipping at the same time. After application of perturbation theory, we go back to the lab frame by applying again the unitary transformation to obtain the first effective Hamiltonian. While some corrections appear like the Dzyaloshinskii–Moriya interaction, they are highly suppressed if these conditions are fulfilled.

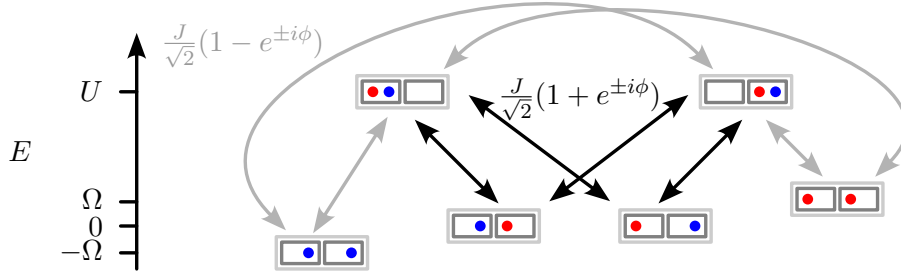


Figure 6.2: Similar sketch as in fig. 6.1, but including the spin-orbit coupling term for a two-site lattice at half-filling ( $M = N = 2$ ). The Hamiltonian has also been transformed to diagonalise the spin-orbit coupling term. Black and grey arrows correspond to coupling strengths  $\frac{J}{\sqrt{2}}(1 + e^{\pm i\phi})$ ,  $\frac{J}{\sqrt{2}}(1 - e^{\pm i\phi})$ , respectively.

Now we can finally apply second-order perturbation theory to our already perturbed Hamiltonian to obtain an effective model with quadratic form. Under PBC, the phase  $\phi$  must be commensurate with the lattice so

that  $\phi = 2\pi n/M$ . Then, we obtain

$$\hat{H}_{\text{eff}}^{(2)} = \begin{cases} -2\chi_\phi \hat{S}_x^2 & \text{if } \phi = \pi, \\ \chi_\phi \hat{S}_z^2 & \text{else,} \end{cases} \quad (6.4)$$

where

$$\chi_\phi = \frac{\Omega^2}{2J_{\text{SE}}(1 - \cos \phi)} \frac{1}{M-1}. \quad (6.5)$$

Interestingly, this means we can achieve not only a OAT model in different quantisation axis by tuning the phase  $\phi$ , but also generate TACT by including different SOC terms in our Hamiltonian through the use of multiple off-axis light sources.

While this is sufficiently remarkable on its own, we found the spin wave states change their form under OBC. This resulted in the unexpected realisation that, while our base Hamiltonian looks barely identical than under PBC, we obtain a much richer effective Hamiltonian for the same perturbation. After the appropriate phase shift, the effective Hamiltonian can be expressed as

$$\hat{H}_{\text{eff}} = \chi \left( \hat{S}^2 + \hat{S}_z^2 - \eta \hat{S}_x^2 + \eta \hat{S}_y^2 + \gamma \hat{S}_x \right), \quad (6.6)$$

where all parameters depend on  $\phi$ .

These new terms and coefficients with respect to PBC appear because we allow the phase  $\phi$  to be non-commensurate with the lattice,  $\phi \neq 2\pi q/M$ ;  $\forall q \in [1, M-1]$ . This means we excite a number, if not all, of the spin wave states with different fidelity, tuning the parameter  $\eta$  accordingly. This has the disadvantage that the energy gap condition can become more restrictive on these phases. However, this effect becomes less prominent with the system size. On the other hand,  $\eta$  allows us to obtain more squeezing than the OAT model, as it becomes closer to a TACT model.

The largest complication from these non-commensurate phases is the appearance of a linear term with coefficient  $\chi\gamma$  in eq. (6.6). This term acts as a fast rotation of the state in the Bloch sphere, suppressing the *twisting* effect of any term not aligned with its rotation axis. In any case, it will at most reduce the squeezing level to that of the OAT model if we choose an initial coherent state orthogonal to the given axis.

To better understand this effect, we may analyze the TACT-OAT transition in a simpler model, illustrated in fig. 6.3. If the Hamiltonian is given by

$$\hat{H} = \chi \left( \hat{S}_z^2 - \hat{S}_y^2 \right) + v \hat{S}_z, \quad (6.7)$$

we may wonder at which point the linear term  $v\hat{S}_z$  dominates the dynamics. We can estimate the magnitude of the terms from the maximal spin length of the system, which is  $S = N/2$ . In that case, the magnitude of the TACT term  $\hat{H}_{\text{TACT}} = \chi(\hat{S}_z^2 - \hat{S}_y^2)$  may have the ceiling  $\sim \chi(N/2)^2$ . Likewise, the linear



term  $v\hat{S}_z$  will have a magnitude  $\sim vN/2$ . When the linear term is negligible ( $v \ll \chi N/2$ ) the evolution is akin to the pure TACT model. However, when the linear term dominates ( $v \gg \chi N/2$ ) the state rotates around the Bloch sphere very fast. The squeezing effect produced on one side of the sphere is cancelled by immediately turning to the opposite side, where the *twisting* is executed in the opposite direction. Only the twisting along the  $z$ -axis remains, since its unaffected by the linear term. This effect is obscured in the mean-field portrait, as the linear term dominates the energy. A rotated frame treatment might help to recover more accurate streamplots.

In any case, for phases  $\phi \neq \pi$  but commensurate with the lattice, we do not obtain a OAT model like under PBC but an anisotropic TACT model with  $\eta = 1/2$ . This result does not vanish when  $M \rightarrow \infty$ , showing boundary conditions are critical for this system.

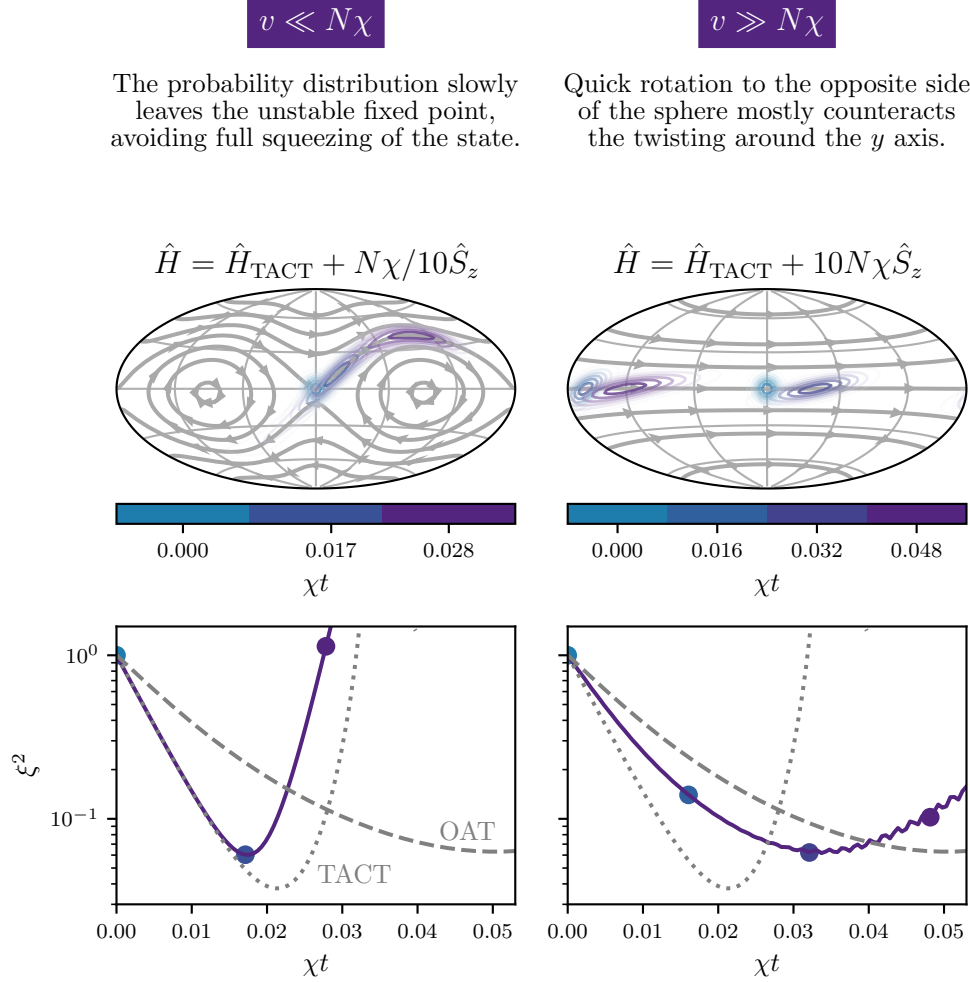


Figure 6.3: Illustrative example of transition from TACT dynamics,  $\hat{H}_{\text{TACT}} = \chi(\hat{S}_z^2 - \hat{S}_y^2)$ , to OAT dynamics,  $\hat{H}_{\text{OAT}} = \chi\hat{S}_z^2$ , through a linear term  $v\hat{S}_z$ . In the left column, we observe the effect of a linear term being smaller than the TACT model ( $v = N\chi/10$ ). In the right column, the linear term is larger than the TACT model ( $v = 10N\chi$ ). The top row briefly describes the corresponding effect of the linear term. The middle row shows Bloch spheres in Hammer projection where different colors identify different points in time. The bottom row compares the exact numerical results of the squeezing parameter to portray the transition from TACT-like dynamics to OAT-like dynamics. Colored points indicate the same moments in time as in the middle row panels.  $N = 100$ .



# One- and Two-Axis Squeezing via Laser Coupling in an Atomic Fermi-Hubbard Model

T. Hernández Yanes<sup>1</sup>, M. Płodzień<sup>2</sup>, M. Mackoīt Sinkevičienė<sup>3</sup>, G. Žlabys<sup>3</sup>, G. Juzeliūnas<sup>3</sup>, and E. Witkowska<sup>1</sup>

<sup>1</sup>*Institute of Physics PAS, Aleja Lotnikow 32/46, 02-668 Warszawa, Poland*

<sup>2</sup>*ICFO - Institut de Ciències Fotoniques, The Barcelona Institute of Science and Technology, Av. Carl Friedrich Gauss 3, 08860 Castelldefels (Barcelona), Spain*

<sup>3</sup>*Institute of Theoretical Physics and Astronomy, Vilnius University, Saulėtekio 3, LT-10257, Vilnius, Lithuania*



(Received 14 April 2022; revised 5 July 2022; accepted 28 July 2022; published 24 August 2022)

Generation, storage, and utilization of correlated many-body quantum states are crucial objectives of future quantum technologies and metrology. Such states can be generated by the spin-squeezing protocols, i.e., one-axis twisting and two-axis countertwisting. In this Letter, we show activation of these two squeezing mechanisms in a system composed of ultracold atomic fermions in the Mott insulating phase by a position-dependent laser coupling of atomic internal states. Realization of both the squeezing protocols is feasible in the current state-of-the-art experiments.

DOI: [10.1103/PhysRevLett.129.090403](https://doi.org/10.1103/PhysRevLett.129.090403)

**Introduction.**—The fundamental interest of emerging quantum technologies lies in many-body entangled and Bell correlated states, their production, and storage [1–4]. Spin-squeezing protocols, i.e., one-axis twisting (OAT) and two-axis countertwisting (TACT), represent such a resource [5,6] particularly useful for high-precision measurements, allowing one to overcome the shot-noise limit [7–9], and study many-body entanglement [10–14] and Bell correlations [15–22]. It applies to systems composed of  $N$  particles in two quantum states described by a spin of quantum number  $S = N/2$ , when the final measurement is performed by spectroscopic experiments. The uncertainty of such a measurement is  $\xi/\sqrt{N}$ , where  $\xi$  is the spin-squeezing parameter [6], and wherein the shot-noise limit is  $1/\sqrt{N}$ . Simulation of OAT by means of unitary evolution requires a nonlinear term in the Hamiltonian system. Such a term can be cast in the form  $\hat{S}_z^2$  with  $z$  being the twisting axis. TACT is a natural extension of the OAT model where the clockwise and counterclockwise twisting takes place around two orthogonal axes, such as  $z$  and  $x$ , and can be described by the term  $\hat{S}_z^2 - \hat{S}_x^2$ . The lowest value of the squeezing parameter is  $\xi_{\text{best}} \propto N^{-1/3}$  for OAT and  $\xi_{\text{best}} \propto N^{-1/2}$  for TACT.

From an experimental point of view an important aspect in simulation of OAT and TACT is a well-controlled quantum many-body system. Several methods were proposed with ultracold atoms, through the quantum non-demolition measurements [23], transfer of squeezing from light to atomic ensembles [24], or utilizing atom-atom interactions [25]. Proof-of-principle experiments were already performed to demonstrate spin squeezing via OAT with Bose-Einstein condensates utilizing atom-atom collisions [26–29] and atom-light interactions in cavity setups [30,31]. On the contrary, TACT was not

demonstrated experimentally yet, despite several methods having been proposed [32–38]. Currently, intensive research is carried out in lattice systems in the context of atomic lattice clocks [39–45]. The drawbacks of spin-squeezing generation with bosonic atoms are collision decoherence processes and losses [7]. An alternative is offered by spinful fermions in the Mott insulating phase where each lattice site is occupied by a single atom, and hence, the collision decoherence processes are reduced [46].

In this Letter, we study theoretically a scheme for the dynamical generation of both OAT and TACT by a position-dependent laser coupling of two atomic internal states, denoted by  $|\uparrow\rangle$  and  $|\downarrow\rangle$ , of  $N$  atomic fermions in a lattice, as illustrated in Fig. 1(a). We describe the system by the Fermi-Hubbard model (FHM). Additionally, there is a coupling between two internal states of atoms, i.e., Raman coupling or direct optical transitions, which effectively acts as the spin-orbit coupling in the momentum representation [47–56]. Generation of OAT due to such coupling was proposed for trapped ions [57] and ultracold fermions following additional site-dependent spin rotations [41,44]. Here, we show how not only the OAT but also TACT can be simulated directly from the FHM without any additional manipulation of individual spins.

We study the Ramsey-type spectroscopy scheme in which the coupling between atomic internal degrees of freedom is turned on during the interrogation time, as sketched in Fig. 1(c). The generation of spin squeezing starts after the preparation of an initial spin coherent state which subsequently undergoes a unitary evolution. The spin-squeezing parameter  $\xi^2 = N(\Delta S_\perp)_{\text{min}}^2 / \langle S \rangle^2$  [6] is then measured, where  $\langle S \rangle$  is the length of the mean collective spin and  $(\Delta S_\perp)_{\text{min}}^2$  is the minimal variance of the collective spin orthogonally to its direction. We show analytically that



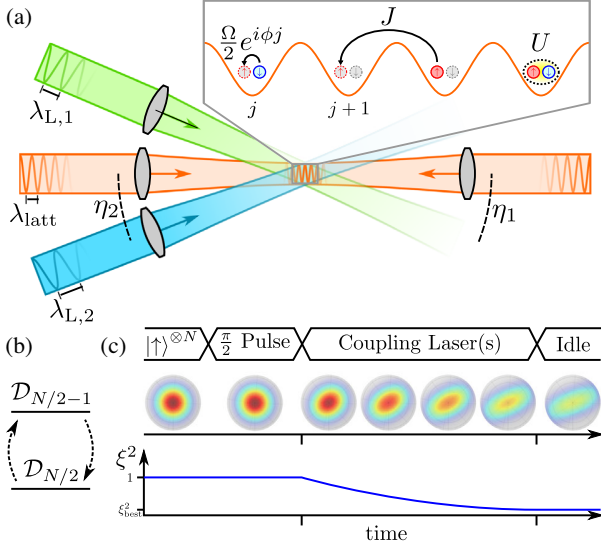


FIG. 1. (a) FHM for atoms in optical lattices with nearest-neighbor tunneling rate  $J$ , on site interaction  $U$ , and additional coupling between atomic internal degrees of freedom with position-dependent strength  $\Omega e^{i\phi j}$  realized with one or two off resonant laser beams. (b) The coupling causes the transition between the  $\mathcal{D}_{N/2}$  and  $\mathcal{D}_{N/2-1}$  spin manifolds (see main text). In the weakly coupling regime, the projection of the Hamiltonian onto the Dicke manifold  $\mathcal{D}_{N/2}$  leads to the OAT (single beam) and TACT (two beams) models. (c) The Ramsey-type spectroscopy for the spin-squeezing generation: (i) preparation of the initial spin coherent state in the  $\mathcal{D}_{N/2}$  manifold, (ii) unitary evolution with the FHM and nonzero coupling reduces the value of  $\xi^2$ , (iii) storing the spin squeezed state in the Mott phase for zero atom-light coupling.

the FHM in the Mott regime, supplied with the weak atom-light coupling, simulates both twisting models. Specifically, applying a single laser beam, the atom-light coupling induces OAT with a tunable axis of squeezing. This paves the way for the simulation of the famous TACT model [5,58] when two laser couplings are used during the interrogation time. To illustrate and demonstrate the validity of our analytical finding we perform full many-body calculations [59] for several atoms taking into account periodic and open boundary conditions.

**Model.**—We consider  $N$  fermionic ultracold atoms, each in two internal states  $|\uparrow\rangle$  and  $|\downarrow\rangle$  corresponding to a spin-1/2 degree of freedom, loaded into a one-dimensional optical lattice potential of  $M$  sites. The atoms are assumed to occupy the lowest Bloch band, interact through  $s$ -wave collisions, and hence can be described by the FHM. In addition, we include a laser driving term which induces a position-dependent spin-flip coupling (SFC) between atomic spin states. The Hamiltonian for such a system reads as

$$\hat{H} = \sum_{j=1}^{M'} \hat{H}_j^{\text{tunnel}} + \sum_{j=1}^M \hat{H}_j^{\text{int}} + \sum_{j=1}^M \hat{H}_j^L, \quad (1)$$

$$\hat{H}_j^{\text{tunnel}} = -J \sum_{s=\uparrow,\downarrow} (\hat{a}_{j,s}^\dagger \hat{a}_{j+1,s} + \text{H.c.}), \quad (2)$$

$$\hat{H}_j^{\text{int}} = U \hat{n}_{j,\uparrow} \hat{n}_{j,\downarrow}, \quad (3)$$

$$\hat{H}_j^L = \frac{\hbar\Omega}{2} (e^{i\phi j} \hat{a}_{j,\uparrow}^\dagger \hat{a}_{j,\downarrow} + e^{-i\phi j} \hat{a}_{j,\downarrow}^\dagger \hat{a}_{j,\uparrow}), \quad (4)$$

where the fermionic operators  $\hat{a}_{j,s}$  annihilate an atom in the  $j$ th lattice site in the state  $s \in \{\uparrow, \downarrow\}$ , and  $\hat{n}_{j,s} = \hat{a}_{j,s}^\dagger \hat{a}_{j,s}$  is the corresponding operator of the number of atoms. The upper limit of summation is  $M' = M$  under periodic boundary conditions (PBC), or  $M' = M - 1$  under the open ones (OBC). The terms  $\hat{H}_j^{\text{tunnel}}$  and  $\hat{H}_j^{\text{int}}$  describe the FHM including on site nearest-neighbor tunneling of fermions with rate  $J$  and on site repulsion of strength  $U$ . The term  $\hat{H}_j^L$  represents the on site laser coupling, with amplitude  $\hbar\Omega$  and position-dependent phase  $\phi j$ , where  $\phi = \pi \cos(\eta) \lambda_{\text{latt}} / \lambda_L$  can be tuned by properly choosing the angle  $\eta$  between laser beams producing the optical lattice and the direction of the laser field inducing the SFC. The wavelength of the latter field  $\lambda_L$  can differ from the underlying lattice wavelength  $\lambda_{\text{latt}}$ , as depicted in Fig. 1. The system has been realized experimentally using the optical clock transition between two electronic orbital states of  $^{87}\text{Sr}$  atoms [71,72]. The FHM can also be experimentally simulated using tweezer arrays [73,74].

We consider the system in the Mott insulating phase for  $U \gg J$ , with even  $N$  and at half filling,  $M = N$ , when double occupancy of a single site is energetically unfavorable. The second order processes, obtained by a projection of the Hamiltonian onto the low energy manifold by using the Schrieffer-Wolff transformation [44,75–78], lead to the nearest-neighbor spin exchange (SE) interaction [79] corrected by the atom-light coupling term:

$$\hat{H}_{\text{spin}} = \sum_{j=1}^{N'} \hat{H}_j^{\text{SE}} + \sum_{j=1}^N \hat{H}_j^{\uparrow\downarrow}, \quad (5)$$

$$\hat{H}_j^{\text{SE}} = J_{\text{SE}} \left( \hat{S}_j^x \hat{S}_{j+1}^x + \hat{S}_j^y \hat{S}_{j+1}^y + \hat{S}_j^z \hat{S}_{j+1}^z - \frac{1}{4} \right), \quad (6)$$

$$\hat{H}_j^{\uparrow\downarrow} = J_{\uparrow\downarrow} (e^{i\phi j} \hat{S}_j^+ + e^{-i\phi j} \hat{S}_j^-), \quad (7)$$

where the on site spin operators are  $\hat{S}_j^+ = \hat{a}_{j,\uparrow}^\dagger \hat{a}_{j,\downarrow}$ ,  $\hat{S}_j^- = \hat{a}_{j,\downarrow}^\dagger \hat{a}_{j,\uparrow}$ ,  $\hat{S}_j^\pm = \hat{S}_j^x \pm i\hat{S}_j^y$ , and  $\hat{S}_j^z = (\hat{n}_{j,\uparrow} - \hat{n}_{j,\downarrow})/2$ . The form of the spin Hamiltonian [Eq. (5)], with  $J_{\text{SE}} \approx 4J^2/U$  and  $J_{\uparrow\downarrow} \approx \hbar\Omega/2$ , is valid when  $U \gg \hbar\Omega$ . The spin Hamiltonian [Eq. (5)] can be obtained by making  $\hat{H}_j^L$  position independent via a  $j$ -dependent spin rotation [44] and returning to the original frame at the end of



calculations; see derivation and general form of Eq. (5) in Sec. I of the Supplemental Material [80].

*Simulation of the OAT model.*—If there is no atom-light coupling,  $\Omega = 0$ , the spin Hamiltonian reduces to the SE Hamiltonian  $\hat{H}_{\text{SE}} = \sum_j \hat{H}_j^{\text{SE}}$  whose eigenstates include Dicke states  $|N/2, m\rangle \propto \hat{S}_-^{N/2-m} \otimes_{j=1}^N |\uparrow\rangle_j$  characterized by zero eigenenergy [80]. Here,  $S = N/2$  is the spin quantum number and  $m = -S, -S+1, \dots, S$  is the spin projection quantum number, i.e.,  $\hat{S}^2|N/2, m\rangle = N/2(N/2+1)|N/2, m\rangle$  and  $\hat{S}_z|N/2, m\rangle = m|N/2, m\rangle$ , where  $\hat{S}^2 = \hat{S}_x^2 + \hat{S}_y^2 + \hat{S}_z^2$  and  $\hat{S}_w = \sum_{j=1}^N \hat{S}_j^w$  are the collective spin operators for  $w = x, y, z, \pm$ . Consequently, the initial spin coherent state  $|\theta, \varphi\rangle = e^{-i\hat{S}_z\varphi} e^{-i\hat{S}_y\theta} \otimes_{j=1}^N |\uparrow\rangle_j$  does not evolve in time, and no squeezing can be generated. A nontrivial evolution of the initial state appears when  $\Omega \neq 0$  due to the atom-light coupling term  $\hat{H}_{\uparrow\downarrow} = \sum_j \hat{H}_j^{\uparrow\downarrow}$ . In particular, the action of  $\hat{H}_{\uparrow\downarrow}$  onto the Dicke states gives  $\hat{H}_{\uparrow\downarrow}|N/2, m\rangle = J_{\uparrow\downarrow} c_{N/2, m+1}^{-1} |q; m+1\rangle - J_{\uparrow\downarrow} c_{N/2, m-1}^{-1} |q; m-1\rangle$ , where

$$|q; m\rangle \equiv \pm c_{N/2, \pm m} \sum_{j=1}^N e^{\pm i q j} \hat{S}_j^{\pm} |N/2, m \mp 1\rangle \quad (8)$$

are spin-wave states [82] for PBC, with  $c_{N/2, m} = \sqrt{N-1}/\sqrt{[(N/2)-m][(N/2)-m+1]}$ ,  $q = 2\pi n/N$ , and  $n = \pm 1, \pm 2, \dots, \pm(N/2-1), N/2$ . They are eigenstates of the total spin operator and its projection,  $\hat{S}^2|q; m\rangle = N/2(N/2+1)|q; m\rangle$  and  $\hat{S}_z|q; m\rangle = m|q; m\rangle$ , with  $-N/2+1 \leq m \leq N/2-1$ . The spin-wave states can be constructed starting with the state for maximal projection,  $|q; m = N/2-1\rangle \equiv (1/\sqrt{N}) \sum_l \hat{S}_l^- e^{i q l} \otimes_{j=1}^N |\uparrow\rangle_j$  [83]. Subsequently, applying the spin lowering operator  $\hat{S}_-$ , the state for any  $m$  is given by  $|q; m\rangle \propto \hat{S}_-^{N/2-1-m} |q; m = N/2-1\rangle$ . The spin-wave states [Eq. (8)] are eigenstates of  $\hat{H}_{\text{SE}}$  with eigenenergies  $E_q = J_{\text{SE}}(1 - \cos q)$  which do not depend on the spin projection  $m$  due to the spherical symmetry of the SE Hamiltonian.

The atom-light interaction thus couples the manifold of the Dicke states  $|N/2, m\rangle$  to that of the spin-wave states  $|q; m\rangle$  with  $q = \phi$ . The two manifolds, labeled  $\mathcal{D}_{N/2}$  and  $\mathcal{D}_{N/2-1}$ , are separated by the energy gap  $E_\phi = J_{\text{SE}}(1 - \cos \phi)$ . In the weak atom-light coupling regime,  $J_{\uparrow\downarrow} \ll E_\phi$ , the energy mismatch  $E_\phi$  suppresses the population transfer between the two manifolds. The effect of the spin-wave states on the Dicke states can thus be treated perturbatively. The first nonvanishing correction to an effective Hamiltonian for the Dicke manifold  $\mathcal{D}_{N/2}$  comes in the second order with respect to  $\hat{H}_{\uparrow\downarrow}$ , giving

$$\hat{H}_{\text{eff}}^{(2)} = \hat{I}_{N/2} \hat{H}_{\uparrow\downarrow} \hat{G}_{N/2-1} \hat{H}_{\uparrow\downarrow} \hat{I}_{N/2}, \quad (9)$$

where  $\hat{I}_{N/2} = \sum_m |N/2, m\rangle \langle N/2, m|$  is the unit projection operator onto the Dicke manifold, while  $\hat{G}_{N/2-1} = \sum_{q \neq 0, m} [|m, q\rangle \langle m, q| / (-E_q)]$  is an operator which sums projectors onto the  $\mathcal{D}_{N/2-1}$  manifold with the corresponding energy mismatch denominator  $-E_q$ . The Hamiltonian [Eq. (9)] can be expressed in terms of collective spin operators by relating its matrix elements  $\langle N/2, m | \hat{H}_{\text{eff}}^{(2)} | N/2, m' \rangle$  with the matrix elements of spin operators  $\hat{S}_x^2$  and  $\hat{S}_z^2$ , as explained in more details in Sec. II of the Supplemental Material [80]. The form of  $\hat{H}_{\text{eff}}^{(2)}$  depends on the value of the phase  $\phi$ . Specifically, one can distinguish two cases: (i) For  $\phi = \pi$  the effective Hamiltonian reads as

$$\hat{H}_{\text{eff}}^{(2)} = -\hbar \chi_\pi \hat{S}_x^2, \quad \text{with} \quad \hbar \chi_\pi = \frac{1}{2} \frac{J_{\uparrow\downarrow}^2}{J_{\text{SE}}} \frac{1}{N-1}, \quad (10)$$

and (ii) for  $\phi = 2\pi n/N$  with  $n = \pm 1, \pm 2, \dots, \pm(N/2-1)$  we obtain

$$\hat{H}_{\text{eff}}^{(2)} = \hbar \chi_\phi \hat{S}_z^2, \quad \text{with} \quad \hbar \chi_\phi = \frac{1}{2(1 - \cos \phi)} \frac{J_{\uparrow\downarrow}^2}{J_{\text{SE}}} \frac{1}{N-1}. \quad (11)$$

In both cases we omit the constant energy term proportional to  $\hat{S}^2$ . This shows that  $\hat{H}_{\text{eff}}^{(2)}$  has the form of the OAT model in which the axis of twisting is determined by the value of  $\phi$  while the direction of twisting is clockwise in Eq. (11) or counterclockwise in Eq. (10); for numerical demonstrations see Sec. IV of the Supplemental Material [80]. The dependence on  $\phi$  of the squeezing term will be used to develop a protocol for simulation of the TACT model. Before that, however, let us discuss the numerical results and a timescale for the best spin-squeezing generation.

In Figs. 2(a)–2(d) we present the time evolution of the spin-squeezing parameter  $\xi^2$  for the FHM with the atom-light coupling [Eq. (1)] and the spin model [Eq. (5)]. The results are obtained numerically by full many-body calculations, and compared to the solution of the OAT model for various values of the phase  $\phi$ . The state is spin squeezed whenever  $\xi^2 < 1$ . The level of the best squeezing (the minimal value of  $\xi^2$ ), as well as the best squeezing time, achieved by the FHM and the spin model agree with OAT as long as the energy gap is large compared with the strength of atom-light coupling  $E_\phi \gg J_{\uparrow\downarrow}$ , as required by the validity of the perturbation theory. The squeezing time diminishes when lowering the value of  $\phi$ , and it can be further shortened by optimizing parameters  $J$  and  $U$ . The best squeezing and the best squeezing time versus  $N$  for PBC (closed circles) and OBC (open squares) are shown in Figs. 2(e) and 2(f), respectively. Note, while the overall level of the best squeezing is similar for PBC and OBC for various values of  $N$ , the timescale for the best squeezing is shorter for OBC. In the limit of a large number of atoms,  $N \gg 1$ , the scaling of the best squeezing time with  $N$  is

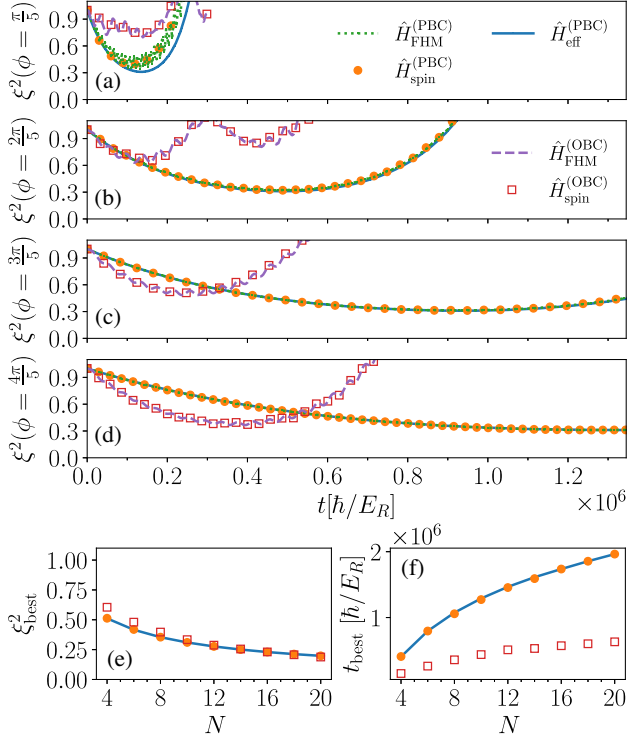


FIG. 2. Temporal dependence of the spin-squeezing parameter  $\xi^2$  for the initial state  $|\theta = \pi/2, \phi = \pi/2\rangle$  evolved with the FHM [Eq. (1)] (green dotted lines), the spin Hamiltonian [Eq. (5)] (orange circles), and the effective OAT model [Eq. (10)] (blue lines) under PBC for  $N = 10$ ,  $J/U = 0.04$ ,  $J_{SE} = 0.0032E_R$ ,  $J_{\uparrow\downarrow}/J_{SE} = 0.04$  (for  $U = 0.5E_R$ ,  $J = 0.02E_R$  where  $E_R = \hbar^2(2\pi)^2/(2m\lambda_{\text{latt}}^2)$  is the recoil energy), and (a)  $\phi = \pi/5$ ,  $J_{\uparrow\downarrow}/E_\phi \approx 0.21$ , (b)  $\phi = 2\pi/5$ ,  $J_{\uparrow\downarrow}/E_\phi \approx 0.06$ , (c)  $\phi = 3\pi/5$ ,  $J_{\uparrow\downarrow}/E_\phi \approx 0.03$ , and (d)  $\phi = 4\pi/5$ ,  $J_{\uparrow\downarrow}/E_\phi \approx 0.02$ . The results for the OBC are shown for the same parameters with the FHM (red squares) and the spin Hamiltonian (violet dashed lines). The panels (e) and (f) represent the best squeezing  $\xi_{\text{best}}^2$  and the best squeezing time  $t_{\text{best}}$ , respectively, versus the number of atoms  $N$  for the spin (orange circles) and OAT (blue line) models for  $\phi = \pi + 2\pi/N$ . Results for the OBC (red squares) are shown for comparison.

$\chi_\phi t_{\text{best}} \simeq N^{-2/3}$  [5] implying  $E_R t_{\text{best}}/\hbar \sim N^{1/3}$  for the fixed value of  $\phi$ , and this tendency is visible in Fig. 2(e).

We have also verified numerically that the unitary evolution governed by the FHM [Eq. (1)] gives rise to the existence of an Anderson's tower of states [45] corresponding to the Dicke manifold. This strongly indicates that the FHM with the atom-light coupling term features spin squeezing. It is also worth noting here that our derivation of Eq. (10) provides a rigorous mathematical confirmation of the quantum simulator arguments used to show the equivalence between the OAT and the XXX model with a staggered field [84].

*Simulation of TACT by means of two driving fields.*— Suppose now that our system is affected by two laser beams

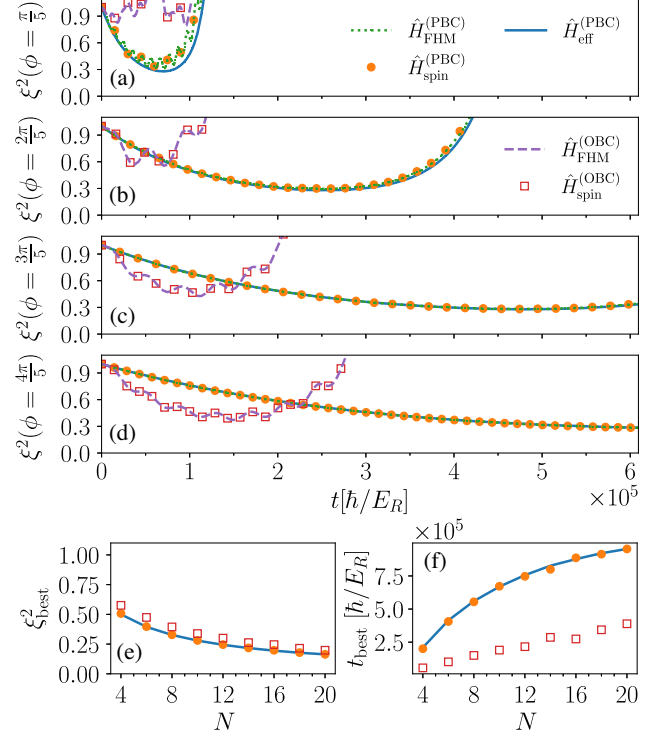


FIG. 3. Spin-squeezing parameter  $\xi^2$  in time when the system is coupled by two laser beams to simulate TACT from the initial state  $|\theta = \pi/2, \phi = \pi/2\rangle$ . The evolution with the FHM [Eq. (1)] (marked by green squares), the spin Hamiltonian [Eq. (5)] (orange circles), and the effective TACT model [Eq. (12)] (blue line) under PBC is shown for  $\phi_0 = \pi$ ,  $J_{\uparrow\downarrow}^{(1)}/J_{SE} = 0.04$ , and (a)  $\phi_1 = \pi/5$ , (b)  $\phi_1 = 2\pi/5$ , (c)  $\phi_1 = 3\pi/5$ , and (d)  $\phi_1 = 4\pi/5$ . The results for OBC are shown for the same parameters using the FHM (red squares) and the spin Hamiltonian (violet dashed lines). The best squeezing  $\xi_{\text{best}}^2$  (e) and the best squeezing time  $t_{\text{best}}$  (f) are shown versus the number of atoms  $N$  for the spin (orange circles for PBC and red squares for OBC) and TACT (blue line) models for  $\phi_1 = \pi + 2\pi/N$ . Other parameters are the same as in Fig. 2.

producing SFC characterized by two different phases  $\phi_0 = \pi$  and  $\phi_1 \neq \pi$ . Each beam corresponding to the phase  $\phi_l \equiv \phi_l$  (with  $l = 0, 1$ ) provides the spin-flip term  $\hat{H}^{\uparrow\downarrow}(\phi_l)$  with the amplitude  $J_{\uparrow\downarrow}^{(l)} \approx \hbar\Omega^{(l)}/2$ . The full SFC contribution is then described by the sum of the two terms  $\hat{H}^{\uparrow\downarrow} = \hat{H}^{\uparrow\downarrow}(\phi_0) + \hat{H}^{\uparrow\downarrow}(\phi_1)$ . In that case the second order effective Hamiltonian given by Eq. (9) provides two terms corresponding to contributions by both laser beams

$$\hat{H}_{\text{eff}}^{(2)} = \hbar\chi_{\phi_1} \left( \hat{S}_z^2 - \frac{\chi_\pi}{\chi_{\phi_1}} \hat{S}_x^2 \right), \quad (12)$$

where we omitted the constant energy shift. In general, the resulting model [Eq. (12)] represents a nonisotropic TACT. However, by taking carefully chosen spin-flip amplitudes





$J_{\uparrow\downarrow}^{(0)} = J_{\uparrow\downarrow}^{(1)} / \sqrt{1 - \cos(\phi_1)}$ , one has  $\chi_\pi = \chi_{\phi_1}$ , leading to the pure TACT model.

In Figs. 3(a)–3(d) we show the spin-squeezing dynamics with the FHM including the two atom-light coupling fields. The dynamics is seen to successfully simulate the TACT model for PBC. The use of OBC also supports the TACT generation, with a lower level of squeezing but a faster best squeezing time, as illustrated in Figs. 3(e) and 3(f). In the limit of a large number of atoms, the scaling of the best squeezing time for the TACT model is  $\chi_{\phi_1} t_{\text{best}} \sim N^{-1} \log(2N)$  [58] and for fixed  $\phi$  gives in our case  $t_{\text{best}} \sim \log(2N)$ .

**Conclusions.**—We considered Ramsey-type spectroscopy in the atomic Fermi-Hubbard model with the position-dependent atom-light coupling. We showed that the FHM and the corresponding Heisenberg spin model generate the same dynamics as the OAT and TACT in the weakly coupling regime. Such a regime corresponds to the system in a Mott insulating phase with sufficiently weak atom-light coupling which maintains single-site occupation at half filling and ensures that the generation of spin squeezing is protected by the energy gap  $E_\phi$ . Our analytical results are confirmed by the full many-body numerical simulations. The scheme is suitable for preparation of spin squeezed, many-body entangled and Bell correlated states [21,22] for state-of-the-art optical lattice clocks using either optical lattices [72] or tweezer arrays [74], a key resource for future quantum technologies.

We gratefully acknowledge discussions with Karol Gietka, Bruno Laburthe-Tolra, Alice Sinatra, Ana Maria Rey, and Martin Robert-de-Saint-Vincent. This work was supported by the DAINA project of the Polish National Science Center DEC-2020/38/L/ST2/00375 and Lithuanian Research Council S-LL-21-3. T. H. Y. acknowledge support from the Polish National Science Center DEC-2019/35/O/ST2/01873. M. P. acknowledges the support of the Polish National Agency for Academic Exchange, the Bekker Program No. PPN/BEK/2020/1/00317. M. P. also acknowledges support from Agencia Estatal de Investigación (the R&D Project No. CEX2019-000910-S, funded by MCIN/AEI/10.13039/501100011033, Plan National FIDEUA PID2019-106901 GB-I00, FPI), Fundació Privada Cellex, Fundació Mir-Puig, and from Generalitat de Catalunya (AGAUR Grant No. 2017 SGR 1341, CERCA program). E. W. was partially supported by the NCN Grant No. 2019/32/Z/ST2/00016 through the project MAQS under QuantERA, which has received funding from the European Union’s Horizon 2020 research and innovation program under Grant Agreement No. 731473. M. P. acknowledges the computer resources at MareNostrum and the technical support provided by BSC (RES-FI-2022-1-0042). Part of the computations were carried out at the Centre of Informatics Tricity Academic Supercomputer & Network.

- [1] A. Acín, I. Bloch, H. Buhrman, T. Calarco, C. Eichler, J. Eisert, D. Esteve, N. Gisin, S. J. Glaser, F. Jelezko, S. Kuhr, M. Lewenstein, M. F. Riedel, P. O. Schmidt, R. Thew, A. Wallraff, I. Walmsley, and F. K. Wilhelm, *New J. Phys.* **20**, 080201 (2018).
- [2] A. Kinos, D. Hunger, R. Kolesov, K. Mølmer, H. de Riedmatten, P. Goldner, A. Tallaire, L. Morvan, P. Berger, S. Welinski, K. Karrai, L. Rippe, S. Kröll, and A. Walther, Roadmap for rare-earth quantum computing, [arXiv:2103.15743](https://arxiv.org/abs/2103.15743).
- [3] C. Becher, W. Gao, S. Kar, C. Marciniak, T. Monz, J. G. Bartholomew, P. Goldner, H. Loh, E. Marcellina, K. E. J. Goh, T. S. Koh, B. Weber, Z. Mu, J.-Y. Tsai, Q. Yan, S. Gyger, S. Steinhauer, and V. Zwiller, 2022 roadmap for materials for quantum technologies, [arXiv:2202.07309](https://arxiv.org/abs/2202.07309).
- [4] J. Fraxanet, T. Salamon, and M. Lewenstein, The coming decades of quantum simulation, [arXiv:2204.08905](https://arxiv.org/abs/2204.08905).
- [5] M. Kitagawa and M. Ueda, *Phys. Rev. A* **47**, 5138 (1993).
- [6] D. J. Wineland, J. J. Bollinger, W. M. Itano, and D. J. Heinzen, *Phys. Rev. A* **50**, 67 (1994).
- [7] L. Pezzè, A. Smerzi, M. K. Oberthaler, R. Schmied, and P. Treutlein, *Rev. Mod. Phys.* **90**, 035005 (2018).
- [8] F. Wolfgang, A. Cerè, F. A. Beduini, A. Predojević, M. Koschorreck, and M. W. Mitchell, *Phys. Rev. Lett.* **105**, 053601 (2010).
- [9] K. Chabuda, J. Dziarmaga, T. J. Osborne, and R. Demkowicz-Dobrzański, *Nat. Commun.* **11**, 250 (2020).
- [10] M. Fadel, T. Zibold, B. Décamps, and P. Treutlein, *Science* **360**, 409 (2018).
- [11] A. Evrard, V. Makhalov, T. Chalopin, L. A. Sidorenkov, J. Dalibard, R. Lopes, and S. Nascimbene, *Phys. Rev. Lett.* **122**, 173601 (2019).
- [12] O. Hosten, N. J. Engelsen, R. Krishnakumar, and M. A. Kasevich, *Nature (London)* **529**, 505 (2016).
- [13] E. Pedrozo-Peñafiel, S. Colombo, C. Shu, A. F. Adiyatullin, Z. Li, E. Mendez, B. Braverman, A. Kawasaki, D. Akamatsu, Y. Xiao, and V. Vuletić, *Nature (London)* **588**, 414 (2020).
- [14] H. Bao, J. Duan, S. Jin, X. Lu, P. Li, W. Qu, M. Wang, I. Novikova, E. E. Mikhailov, K.-F. Zhao, K. Mølmer, H. Shen, and Y. Xiao, *Nature (London)* **581**, 159 (2020).
- [15] J. Tura, R. Augusiak, A. B. Sainz, T. Vértesi, M. Lewenstein, and A. Acín, *Science* **344**, 1256 (2014).
- [16] R. Schmied, J.-D. Bancal, B. Allard, M. Fadel, V. Scarani, P. Treutlein, and N. Sangouard, *Science* **352**, 441 (2016).
- [17] A. Aloy, J. Tura, F. Baccari, A. Acín, M. Lewenstein, and R. Augusiak, *Phys. Rev. Lett.* **123**, 100507 (2019).
- [18] F. Baccari, J. Tura, M. Fadel, A. Aloy, J.-D. Bancal, N. Sangouard, M. Lewenstein, A. Acín, and R. Augusiak, *Phys. Rev. A* **100**, 022121 (2019).
- [19] J. Tura, A. Aloy, F. Baccari, A. Acín, M. Lewenstein, and R. Augusiak, *Phys. Rev. A* **100**, 032307 (2019).
- [20] G. Müller-Rigat, A. Aloy, M. Lewenstein, and I. Frérôt, *PRX Quantum* **2**, 030329 (2021).
- [21] A. Niezgoda, M. Panfil, and J. Chwedeńczuk, *Phys. Rev. A* **102**, 042206 (2020).
- [22] M. Płodzień, M. Lewenstein, E. Witkowska, and J. Chwedeńczuk, [arXiv:2206.10542](https://arxiv.org/abs/2206.10542).
- [23] A. Kuzmich, L. Mandel, and N. P. Bigelow, *Phys. Rev. Lett.* **85**, 1594 (2000).

- [24] J. Hald, J. L. Sørensen, C. Schori, and E. S. Polzik, *Phys. Rev. Lett.* **83**, 1319 (1999).
- [25] M. H. Schleier-Smith, I. D. Leroux, and V. Vuletić, *Phys. Rev. A* **81**, 021804(R) (2010).
- [26] M. F. Riedel, P. Böhi, Y. Li, T. W. Hänsch, A. Sinatra, and P. Treutlein, *Nature (London)* **464**, 1170 (2010).
- [27] C. Gross, T. Zibold, E. Nicklas, J. Estève, and M. K. Oberthaler, *Nature (London)* **464**, 1165 (2010).
- [28] C. D. Hamley, C. S. Gerving, T. M. Hoang, E. M. Bookjans, and M. S. Chapman, *Nat. Phys.* **8**, 305 (2012).
- [29] A. Qu, B. Evrard, J. Dalibard, and F. Gerbier, *Phys. Rev. Lett.* **125**, 033401 (2020).
- [30] I. D. Leroux, M. H. Schleier-Smith, and V. Vuletić, *Phys. Rev. Lett.* **104**, 073602 (2010).
- [31] K. Maussang, G. E. Marti, T. Schneider, P. Treutlein, Y. Li, A. Sinatra, R. Long, J. Estève, and J. Reichel, *Phys. Rev. Lett.* **105**, 080403 (2010).
- [32] K. Mølmer and A. Sørensen, *Phys. Rev. Lett.* **82**, 1835 (1999).
- [33] W. Huang, Y.-L. Zhang, C.-L. Zou, X.-B. Zou, and G.-C. Guo, *Phys. Rev. A* **91**, 043642 (2015).
- [34] Y. C. Liu, Z. F. Xu, G. R. Jin, and L. You, *Phys. Rev. Lett.* **107**, 013601 (2011).
- [35] M. Wang, W. Qu, P. Li, H. Bao, V. Vuletić, and Y. Xiao, *Phys. Rev. A* **96**, 013823 (2017).
- [36] J. Kitzinger, M. Chaudhary, M. Kondappan, V. Ivannikov, and T. Byrnes, *Phys. Rev. Research* **2**, 033504 (2020).
- [37] J. Borregaard, E. J. Davis, G. S. Bentsen, M. H. Schleier-Smith, and A. S. Sørensen, *New J. Phys.* **19**, 093021 (2017).
- [38] L.-G. Huang, F. Chen, X. Li, Y. Li, R. Lü, and Y.-C. Liu, *npj Quantum Inf.* **7**, 168 (2021).
- [39] A. Sørensen and K. Mølmer, *Phys. Rev. Lett.* **83**, 2274 (1999).
- [40] D. Kajtoch, E. Witkowska, and A. Sinatra, *Europhys. Lett.* **123**, 20012 (2018).
- [41] P. He, M. A. Perlin, S. R. Muleady, R. J. Lewis-Swan, R. B. Hutson, J. Ye, and A. M. Rey, *Phys. Rev. Research* **1**, 033075 (2019).
- [42] M. Płodzień, M. Kościelski, E. Witkowska, and A. Sinatra, *Phys. Rev. A* **102**, 013328 (2020).
- [43] E. Pedrozo-Peñañiel, S. Colombo, C. Shu, A. F. Adiyatullin, Z. Li, E. Mendez, B. Braverman, A. Kawasaki, D. Akamatsu, Y. Xiao, and V. Vuletić, *Nature (London)* **588**, 414 (2020).
- [44] M. Mamaev, I. Kimchi, R. M. Nandkishore, and A. M. Rey, *Phys. Rev. Research* **3**, 013178 (2021).
- [45] T. Comparin, F. Mezzacapo, and T. Roscilde, *Phys. Rev. A* **105**, 022625 (2022).
- [46] S. Kolkowitz, S. L. Bromley, T. Bothwell, M. L. Wall, G. E. Marti, A. P. Koller, X. Zhang, A. M. Rey, and J. Ye, *Nature (London)* **542**, 66 (2017).
- [47] Y.-J. Lin, R. L. Compton, K. Jiménez-García, J. V. Porto, and I. B. Spielman, *Nature (London)* **462**, 628 (2009).
- [48] Y.-J. Lin, K. Jiménez-García, and I. B. Spielman, *Nature (London)* **471**, 83 (2011).
- [49] Z. Fu, P. Wang, S. Chai, L. Huang, and J. Zhang, *Phys. Rev. A* **84**, 043609 (2011).
- [50] J.-Y. Zhang, S.-C. Ji, Z. Chen, L. Zhang, Z.-D. Du, B. Yan, G.-S. Pan, B. Zhao, Y.-J. Deng, H. Zhai *et al.*, *Phys. Rev. Lett.* **109**, 115301 (2012).
- [51] P. Wang, Z.-Q. Yu, Z. Fu, J. Miao, L. Huang, S. Chai, H. Zhai, and J. Zhang, *Phys. Rev. Lett.* **109**, 095301 (2012).
- [52] L. W. Cheuk, A. T. Sommer, Z. Hadzibabic, T. Yefsah, W. S. Bakr, and M. W. Zwierlein, *Phys. Rev. Lett.* **109**, 095302 (2012).
- [53] J. Struck, C. Ölschläger, M. Weinberg, P. Hauke, J. Simonet, A. Eckardt, M. Lewenstein, K. Sengstock, and P. Windpassinger, *Phys. Rev. Lett.* **108**, 225304 (2012).
- [54] K. Jiménez-García, L. J. LeBlanc, R. A. Williams, M. C. Beeler, A. R. Perry, and I. B. Spielman, *Phys. Rev. Lett.* **108**, 225303 (2012).
- [55] S. Kolkowitz, S. L. Bromley, T. Bothwell, M. L. Wall, G. E. Marti, A. P. Koller, X. Zhang, A. M. Rey, and J. Ye, *Nature (London)* **542**, 66 (2017).
- [56] J. Dalibard, F. Gerbier, G. Juzeliūnas, and P. Öhberg, *Rev. Mod. Phys.* **83**, 1523 (2011).
- [57] K. Mølmer and A. Sørensen, *Phys. Rev. Lett.* **82**, 1835 (1999).
- [58] D. Kajtoch and E. Witkowska, *Phys. Rev. A* **92**, 013623 (2015).
- [59] Our numerical calculations are based on the exact diagonalization method in the full Fock state basis for total number of atoms  $N \leq 10$ , without fixed magnetization. For larger number of atoms we employed a standard density matrix renormalization group (DMRG) technique for calculating initial spin coherent state [60–64]. Time evolution was prepared within algorithm for time evolution where one-site time-dependent variational principle (TDVP) scheme [65–68] is combined with a global basis expansion [69]. To perform both DMRG and time evolution we use ITensor C++ library [70].
- [60] S. R. White, *Phys. Rev. Lett.* **69**, 2863 (1992).
- [61] S. R. White, *Phys. Rev. B* **48**, 10345 (1993).
- [62] U. Schollwöck, *Rev. Mod. Phys.* **77**, 259 (2005).
- [63] U. Schollwöck, *Ann. Phys. (Amsterdam)* **326**, 96 (2011), january 2011 Special Issue.
- [64] R. Orús, *Ann. Phys. (Amsterdam)* **349**, 117 (2014).
- [65] P. Kramer, *J. Phys.* **99**, 012009 (2008).
- [66] J. Haegeman, J. I. Cirac, T. J. Osborne, I. Pižorn, H. Verschelde, and F. Verstraete, *Phys. Rev. Lett.* **107**, 070601 (2011).
- [67] T. Koffel, M. Lewenstein, and L. Tagliacozzo, *Phys. Rev. Lett.* **109**, 267203 (2012).
- [68] J. Haegeman, C. Lubich, I. Oseledets, B. Vandereycken, and F. Verstraete, *Phys. Rev. B* **94**, 165116 (2016).
- [69] M. Yang and S. R. White, *Phys. Rev. B* **102**, 094315 (2020).
- [70] M. Fishman, S. R. White, and E. M. Stoudenmire, *arXiv*: 2007.14822.
- [71] S. Campbell, R. Hutson, E. Marti, A. Goban, D. Oppong, R. McNally, L. Sonderhouse, J. Robinson, W. Zhang, B. Bloom, and J. Ye, *Science* **358**, 90 (2017).
- [72] S. L. Bromley, S. Kolkowitz, T. Bothwell, D. Kedar, A. Safavi-Naini, M. L. Wall, C. Salomon, A. M. Rey, and J. Ye, *Nat. Phys.* **14**, 399 (2018).
- [73] A. W. Young, W. J. Eckner, W. R. Milner, D. Kedar, M. A. Norcia, E. Oelker, N. Schine, J. Ye, and A. M. Kaufman, *Nature (London)* **588**, 408 (2020).
- [74] B. M. Spar, E. Guardado-Sanchez, S. Chi, Z. Z. Yan, and W. S. Bakr, *Phys. Rev. Lett.* **128**, 223202 (2022).



- [75] K. A. Chao, J. Spalek, and A. M. Oles, *J. Phys. C* **10**, L271 (1977).
- [76] K. A. Chao, J. Spalek, and A. M. Oleś, *Phys. Rev. B* **18**, 3453 (1978).
- [77] J. R. Schrieffer and P. A. Wolff, *Phys. Rev.* **149**, 491 (1966).
- [78] S. Bravyi, D. P. DiVincenzo, and D. Loss, *Ann. Phys. (Amsterdam)* **326**, 2793 (2011).
- [79] L.-M. Duan, E. Demler, and M. D. Lukin, *Phys. Rev. Lett.* **91**, 090402 (2003).
- [80] See Supplemental Materials at <http://link.aps.org/supplemental/10.1103/PhysRevLett.129.090403> for details of analytical calculations, which includes Refs. [75,81].
- [81] K. Husimi, *Proc. Phys.-Math. Soc. Jpn. 3rd Ser.* **22**, 264 (1940).
- [82] M. D. Swallows, M. Bishof, Y. Lin, S. Blatt, M. J. Martin, A. M. Rey, and J. Ye, *Science* **331**, 1043 (2011).
- [83] D. D. Stancil and A. Prabhakar, *Spin Waves. Theory and Applications* (Springer Science, New York, 2009).
- [84] K. Gietka, A. Usui, J. Deng, and T. Busch, *Phys. Rev. Lett.* **126**, 160402 (2021).

## Spin squeezing in open Heisenberg spin chains

T. Hernández Yanes,<sup>1</sup> G. Żlabys<sup>2,3</sup>, M. Płodzień<sup>4</sup>, D. Burba<sup>2</sup>, M. Mackoitis Sinkevičienė<sup>2</sup>,  
E. Witkowska<sup>1</sup>, and G. Juzeliūnas<sup>2</sup>

<sup>1</sup>*Institute of Physics, PAS, Aleja Lotnikow 32/46, 02-668 Warszawa, Poland*

<sup>2</sup>*Institute of Theoretical Physics and Astronomy, Vilnius University, Saulėtekio 3, 10257 Vilnius, Lithuania*

<sup>3</sup>*Quantum Systems Unit, Okinawa Institute of Science and Technology Graduate University, Onna, Okinawa 904-0495, Japan*

<sup>4</sup>*Institut de Ciències Fotoniques, Barcelona Institute of Science and Technology, Avenida Carl Friedrich Gauss 3, 08860 Castelldefels (Barcelona), Spain*



(Received 27 June 2023; revised 19 August 2023; accepted 21 August 2023; published 5 September 2023)

Spin squeezing protocols successfully generate entangled many-body quantum states, the key pillars of the second quantum revolution. In our recent work [Phys. Rev. Lett. **129**, 090403 (2022)] we showed that spin squeezing described by the one-axis twisting model can be generated in the Heisenberg spin-1/2 chain with periodic boundary conditions when accompanied by a position-dependent spin-flip coupling induced by a single laser field. In this work, we show analytically that the change in boundary conditions from the periodic to the open ones significantly modifies spin squeezing dynamics. A broad family of twisting models can be simulated by the system in the weak-coupling regime, including one- and two-axis twisting under specific conditions, providing the Heisenberg level of squeezing and acceleration of the dynamics. Our analytical findings are confirmed by full numerical simulations.

DOI: [10.1103/PhysRevB.108.104301](https://doi.org/10.1103/PhysRevB.108.104301)

### I. INTRODUCTION

Neutral atom arrays have recently emerged as promising platforms for realizing programmable quantum systems [1–3]. Based on individually trapped cold atoms in optical lattices [4] and tweezers with strong interactions between Rydberg states [5], atom arrays have been utilized to explore physics involving Hubbard and Heisenberg models [6–10]. It has been shown that indistinguishable Hubbard bosons serve as a platform for the generation and storage of metrologically useful many-body quantum states [11–15]. In some regime of parameters, arrays of ultracold atoms simulate chains of distinguishable spins (qubits) which are perfectly suitable for quantum information tasks and the generation of massive nonclassical correlations, including Bell correlations and nonlocality [16–19]. These quantum many-body systems are crucial resources for emerging quantum technologies [20,21].

Systems composed of ultracold fermions in optical lattices are also attracting a lot of attention currently in the context of the generation of nonclassical states (see, e.g., [22–24]). In particular, in our recent work [25], we showed that in a lattice of strongly interacting ultracold fermionic atoms involving two internal states, it is possible to generate nonclassical correlations when adding position-dependent atom-light coupling. The Fermi-Hubbard model describing the system under periodic boundary conditions (PBCs) can be cast onto an isotropic spin-1/2 Heisenberg chain in a deep Mott regime, while the atom-light coupling can be considered a position-dependent spin flipping. To generate spin squeezing the Ramsey-type spectroscopy scheme is considered [25], as illustrated in Fig. 1. As soon as the atoms are put in a coherent superposition of two internal states by an electromagnetic pulse, an additional weak atom-laser coupling is turned on. This coupling activates the general mechanism in the PBC

case: it induces excitation of a pair of spin waves with opposite quasimomenta. These spin waves extend over the entire system, allowing individual atoms to interact “effectively” and establish nontrivial quantum correlations [22,23,25–27]. When the desired level of spin squeezing is established, the spin-flip coupling is turned off, but the quantum correlations survive and are stored deep in the Mott insulating phase. We

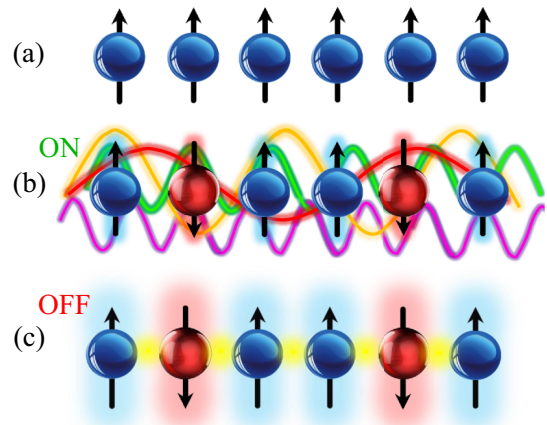


FIG. 1. Illustration of the Ramsey-type spectroscopy scheme. (a) Preparation of the initial spin coherent state. (b) The excitation of spin-wave states (different colored lines) by the spin-flip coupling serves as an intermediate state to induce “effective” interaction and establish correlations between elementary spins. (c) Turning off the coupling freezes the dynamics, and the spin-squeezed states are stored in the Mott insulating phase. (b) and (c) illustrate an example of a configuration of spins. Yet the resulting state during and at the end of evolution is a superposition of various possible configurations, including the initial one presented in (a).





showed that an isotropic Heisenberg spin-1/2 chain with weak position-dependent spin-flip coupling generates spin squeezing dynamics given by the one-axis twisting (OAT) model. Furthermore, we numerically observed that open boundary conditions (OBCs) change the spin squeezing dynamics. Depending on the coupling parameters, an acceleration of squeezing generation was observed with the same or a similar level of squeezing [25].

In this paper, we provide a detailed analytical and numerical analysis of the impact of OBCs on the spin squeezing dynamics in Heisenberg spin chains. To this end, we develop a spin-wave theory for OBCs by modifying the coordinate Bethe ansatz [28]. Next, by using the Schrieffer-Wolf transformation [23,29–32] we derive the effective model in terms of collective spin operators to describe the squeezing dynamics generated in the weak-coupling regime. For OBCs the coupling leads to the excitation of a superposition of spin waves with different energies and amplitudes rather than a pair of spin waves with opposite quasimomenta, as is the case for PBCs. This still allows individual atoms to correlate and generate squeezing. However, the excitation of a superposition of spin waves complicates the form of the effective model. We analyze this unconventional model in detail, identifying the initial conditions and the coupling parameters for spin squeezing generation with the level given by the OAT and two-axis counter twisting (TACT) models [25,33,34]. Consequently, we show that it is possible to generate a Heisenberg level of squeezing in spin-1/2 Heisenberg chains under OBCs. In addition, we show that the corresponding timescale of the best squeezing is reduced with respect to PBCs while keeping the same perturbation level. Our analytical findings are confirmed by full numerical simulations. The results obtained can be used in current state-of-the-art experiments with ultracold atoms in optical lattices [35–37] and tweezer arrays [38,39].

## II. HEISENBERG MODEL AND SPIN-WAVE STATES FOR OBCs

Let us concentrate on a specific physical system composed of a total even number  $N$  of fermionic ultracold atoms loaded into a one-dimensional optical lattice potential with  $N$  sites. Each atom has two internal states,  $|\uparrow\rangle$  and  $|\downarrow\rangle$ , corresponding to a spin-1/2 degree of freedom. The atoms are assumed to occupy the lowest Bloch band, interact through  $s$ -wave collisions, and hence can be described by the Fermi-Hubbard model.

We assume the interaction dominates over the tunneling and the system is in the Mott insulating phase at half filling when double occupancy of a single site is energetically unfavorable. The second-order processes, obtained with a projection onto the manifold of single occupancy of lattice sites, lead to the nearest-neighbor spin-exchange interactions [23,25,29–32]. The spin dynamics of this system is well captured by the isotropic Heisenberg (spin-exchange) model [40,41],

$$\hat{H}_{\text{SE}} = J_{\text{SE}} \sum_{j=1}^{N-1} \left( \hat{S}_j^x \hat{S}_{j+1}^x + \hat{S}_j^y \hat{S}_{j+1}^y + \hat{S}_j^z \hat{S}_{j+1}^z - \frac{1}{4} \right), \quad (1)$$

where  $J_{\text{SE}}$  represents the spin-exchange energy;  $\hat{S}_j^+ = \hat{a}_{j,\uparrow}^\dagger \hat{a}_{j,\downarrow}$ ,  $\hat{S}_j^- = \hat{a}_{j,\downarrow}^\dagger \hat{a}_{j,\uparrow}$ ,  $\hat{S}_j^\pm = \hat{S}_j^x \pm i\hat{S}_j^y$ , and  $\hat{S}_j^z = (\hat{n}_{j,\uparrow} - \hat{n}_{j,\downarrow})/2$  are on-site spin operators; and we take  $\hbar = 1$ . The fermionic operators  $\hat{a}_{j,s}$  annihilate an atom in the  $j$ th lattice site in the state  $s \in \{\uparrow, \downarrow\}$ , and  $\hat{n}_{j,s} = \hat{a}_{j,s}^\dagger \hat{a}_{j,s}$  is the corresponding on-site operator of the number of atoms. We also introduce the collective spin operators  $\hat{S}_\sigma = \sum_j \hat{S}_j^\sigma$ , with  $\sigma = x, y, z, \pm$ . The analytical form of the energy spectrum of the Hamiltonian (1) and corresponding eigenstates for PBCs are known from 1931 due to the famous work of Bethe [28]. Their counterpart for OBCs is less explored, to our knowledge.

The Hamiltonian (1) is spherically symmetric with respect to spin rotation. Thus, eigenstates of  $\hat{H}_{\text{SE}}$  can also be taken to be eigenstates of the square of the total spin  $\hat{S}^2 = \hat{S}_x^2 + \hat{S}_y^2 + \hat{S}_z^2$  and its  $z$  projection  $\hat{S}_z$  with eigenvalues  $S(S+1)$  and  $m$ , respectively. To understand the spin squeezing dynamics let us first recall the analytical form of two energy manifolds of  $\hat{H}_{\text{SE}}$  characterized by the largest values of the total spin.

The first energy manifold corresponding to the total spin quantum number  $S = N/2$  is spanned by Dicke states  $|m\rangle \equiv |N/2, m\rangle$ , which are zero-energy eigenstates of  $\hat{H}_{\text{SE}}$ . They can be represented in terms of the all-spin-up state affected  $N/2 - m$  times by the collective spin lowering operator  $\hat{S}_-$ :

$$|m\rangle = \sqrt{\frac{(N/2 + m)!}{(N/2 - m)!(N)!}} \hat{S}_-^{N/2-m} \bigotimes_{j=1}^N |\uparrow\rangle_j, \quad (2)$$

where the quantization axis is chosen to be along the  $z$  direction:  $\hat{S}_j^z |\uparrow\rangle_j = 1/2 |\uparrow\rangle_j$  and  $\hat{S}_j^z |\downarrow\rangle_j = -1/2 |\downarrow\rangle_j$ . Alternatively, the Dicke states  $|m\rangle$  can be defined by using the rising operator  $\hat{S}_+ \equiv (\hat{S}_-)^^\dagger$  in the place of  $\hat{S}_-$  when replacing  $m$  and  $|\uparrow\rangle_j$  with  $-m$  and  $|\downarrow\rangle_j$ , respectively, on the right-hand side of (2). The Dicke states are eigenstates of  $\hat{H}_{\text{SE}}$  with zero eigenenergies for both PBCs and OBCs. Altogether, there are  $N+1$  Dicke states corresponding to different values of  $m \in (-N/2, -N/2+1, \dots, N/2)$ .

The second energy manifold to be considered is spanned by the spin-wave states [23,25,42,43] containing one spin excitation and characterized by the total spin quantum number  $S = N/2 - 1$ . In the case of OBCs one can analytically solve the eigenproblem of these states for the Hamiltonian (1) by using the coordinate Bethe ansatz modified appropriately to account for the difference arising from the two boundary points; see Appendix A for a derivation. This leads to the following form of the spin-wave states:

$$|m, q\rangle = \pm \sqrt{N} c_{N/2, \pm m} \sum_{j=1}^N p_j^{(q)} \hat{S}_j^\pm |m \mp 1\rangle, \quad (3)$$

where

$$c_{N/2, \pm m} = \sqrt{\frac{N-1}{(N/2 \mp m)(N/2 \mp m + 1)}}. \quad (4)$$

The sign  $\pm$  in Eq. (3) for  $|m, q\rangle$  corresponds to two equivalent definitions of the spin waves in terms of the on-site spin raising and lowering operators  $\hat{S}_j^\pm$  acting on the Dicke states.



Furthermore, the coefficients featured in Eq. (3) are

$$p_j^{(q)} = \sqrt{\frac{2}{N}} \cos \left[ \frac{\pi}{N} \left( j - \frac{1}{2} \right) q \right]. \quad (5)$$

Altogether, there are  $(N-1)^2$  different spin-wave states corresponding to various combinations of quantum numbers  $m \in (-N/2 + 1, -N/2 + 2, \dots, N/2 - 1)$  and  $q = 1, 2, \dots, N-1$ . The corresponding eigenenergies  $E_q$  do not depend on the spin projection quantum number  $m$  and read

$$E_q = J_{SE} \left[ \cos \left( \frac{\pi}{N} q \right) - 1 \right]. \quad (6)$$

Note that for OBCs the amplitudes  $p_j^{(q)}$  given by Eq. (5) represent standing waves. They thus differ from the solution for PBCs, where the amplitudes  $p_j^{(q)} = N^{-1/2} e^{i2\pi qj/N}$  are plane waves [43]. This has substantial consequences for the coupling mechanism and the spin squeezing dynamics analyzed in Secs. IV and V.

### III. PROTOCOL FOR DYNAMICAL GENERATION OF SPIN SQUEEZING

In order to generate spin squeezing in this Heisenberg spin-1/2 chain with OBCs described by Hamiltonian (1) we add an atom-light coupling which induces position-dependent spin flipping. The resulting system Hamiltonian  $\hat{H}_{\text{spin}}$  reads

$$\begin{aligned} \hat{H}_{\text{spin}} &= \hat{H}_{SE} + \hat{H}_{\uparrow\downarrow}, \\ \hat{H}_{\uparrow\downarrow} &= \frac{\Omega}{2} \sum_{j=1}^N (e^{i(\phi j - \phi_0)} \hat{S}_j^+ + e^{-i(\phi j - \phi_0)} \hat{S}_j^-), \end{aligned} \quad (7)$$

where the extra term  $\hat{H}_{\uparrow\downarrow}$  represents the sum over the on-site spin-flip coupling with amplitude  $\Omega$  and position-dependent phase  $\phi j$ , where  $\phi = \pi \cos(\alpha) \lambda_{\text{latt}} / \lambda_L$  can be tuned by properly choosing an angle  $\alpha$  between laser beams producing the optical lattice and the direction of the laser field inducing the coupling. The two beams are characterized by the wavelengths  $\lambda_{\text{latt}}$  and  $\lambda_L$ , respectively (see, e.g., [25]). Here,  $\phi_0 \in [0, 2\pi)$  is the global offset phase of the coupling lasers, which can be interpreted as the transformation of  $\hat{H}_{\uparrow\downarrow}$  due to the global spin rotation around the  $z$  axis by the angle  $\phi_0$ . Equivalently, it can also be interpreted as the spin rotation for the initial state around the same  $z$  axis and by the same angle  $\phi_0$ , but in the opposite direction.

In the case of PBCs, the coupling phase  $\phi$  should be commensurate with  $2\pi/N$ , namely,  $\phi = 2\pi n/N$ , where  $n = 1, 2, \dots, N-1$ , to ensure the periodicity of  $\hat{H}_{\uparrow\downarrow}$  [25]. Here, however, we are interested in OBCs, and therefore,  $\phi$  can take any real values apart from the trivial one  $\phi = 0$  or  $\phi = 2\pi$ , for which  $\hat{H}_{\uparrow\downarrow}$  does not provide coupling between the Dicke and spin-wave state manifolds needed for the generation of spin squeezing.

The initial state that is convenient to start the evolution is the spin coherent state

$$|\theta, \varphi\rangle = e^{-i\hat{S}_z\varphi} e^{-i\hat{S}_y\theta} \bigotimes_{j=1}^N |\uparrow\rangle_j, \quad (9)$$

where all the spins point in the same direction parameterized by the spherical angles  $\theta$  and  $\varphi$ . In general, the spin coherent state (9) belongs to the Dicke manifold of the total spin  $S = N/2$  and hence can be expressed in the basis of the Dicke states (2) as

$$|\theta, \varphi\rangle = \sum_{m=-N/2}^{N/2} a_m |m\rangle, \quad (10)$$

where

$$a_m = \sqrt{\binom{N}{\frac{N}{2} + m}} \cos^{\frac{N}{2} + m} \left( \frac{\theta}{2} \right) \sin^{\frac{N}{2} - m} \left( \frac{\theta}{2} \right) e^{i(\frac{N}{2} - m)\varphi} \quad (11)$$

are coefficients of decomposition.

The subsequent evolution of the initial state is defined by the unitary operator  $\hat{U} = e^{-i\hat{H}_{\text{spin}}}$ . To quantify the level of squeezing generated in time we use the spin squeezing parameter

$$\xi^2 = \frac{N(\Delta\hat{S}_\perp)_{\min}^2}{\langle\hat{S}\rangle^2}, \quad (12)$$

where the length of the mean collective spin is  $\langle\hat{S}\rangle$  and the minimal variance of the collective spin orthogonal to its direction is  $(\Delta\hat{S}_\perp)_{\min}^2$  [44].

Nontrivial quantum correlations are produced in the weak-coupling regime, where the characteristic energy of the coupling Hamiltonian  $\hat{H}_{\uparrow\downarrow}$  is smaller than that of the spin-exchange term  $\hat{H}_{SE}$ . In the next section, we derive the effective model describing the spin squeezing dynamics in terms of collective spin operators.

### IV. EFFECTIVE MODEL

When the spin-flip coupling is weak compared to the energy of the spin exchange, the dynamics of the initial spin coherent state  $|\theta, \varphi\rangle$  governed by the spin Hamiltonian  $\hat{H}_{\text{spin}}$  within the Dicke manifold can be well approximated using perturbation theory. Therefore, the coupling term  $\hat{H}_{\uparrow\downarrow}$  can be treated as a perturbation. For reasons that will be explained later, let us rephrase this operator in the following way:

$$\hat{H}_{\uparrow\downarrow} = \hat{\hat{H}}_{\uparrow\downarrow} + v_x \hat{S}_x + v_y \hat{S}_y, \quad (13)$$

where

$$\hat{\hat{H}}_{\uparrow\downarrow} = \frac{\Omega}{2} \sum_{j=1}^N (\alpha_j^+ \hat{S}_j^+ + \alpha_j^- \hat{S}_j^-). \quad (14)$$

Here,  $\alpha_j^\pm = e^{\pm i(\phi j - \phi_0)} - A^\pm$ , with  $A^\pm = \frac{1}{N} \sum_j e^{\pm i(\phi j - \phi_0)}$ , and  $v_x = \Omega \text{Re}[A^+]/2$ , and  $v_y = -\Omega \text{Im}[A^+]/2$ . The separation of the two last terms in (13) is made in such a way that  $\alpha_j^\pm$  sum up to zero. Note that  $v_x$  and  $v_y$  are nonzero only for phases  $\phi$  incommensurate with  $2\pi/N$ .

#### A. First- and second-order contributions

The operator  $\hat{\hat{H}}_{\uparrow\downarrow}$  on the right-hand side of (13) induces the coupling between the Dicke and spin-wave state manifolds, while the remaining ones directly couple the Dicke states and represent the first-order perturbation term

$$\hat{H}_{\text{eff}}^{(1)} = v_x \hat{S}_x + v_y \hat{S}_y. \quad (15)$$



To generate spin squeezing one needs to take into account the second-order contribution induced by  $\hat{H}_{\uparrow\downarrow}$ . It can be obtained via the Schrieffer-Wolf transformation [23,23,25,29–32], leading to

$$\hat{H}_{\text{eff}}^{(2)} = \hat{I}_{N/2} \hat{H}_{\uparrow\downarrow} \hat{G}_{N/2-1} \hat{H}_{\uparrow\downarrow} \hat{I}_{N/2}, \quad (16)$$

where  $\hat{I}_{N/2} = \sum_m |m\rangle\langle m|$  is the unit operator for projection onto the Dicke manifold and  $\hat{G}_{N/2-1} = \sum_{q \neq 0, m} \frac{|m, q\rangle\langle m, q|}{-E_q}$  is an operator which sums projectors onto the spin-wave state manifold with the corresponding energy mismatch denominator  $-E_q$ . The matrix elements of (16) are

$$\langle m' | \hat{H}_{\text{eff}}^{(2)} | m \rangle = - \sum_{m'', q} \frac{\langle m' | \hat{H}_{\uparrow\downarrow} | m'', q \rangle \langle m'', q | \hat{H}_{\uparrow\downarrow} | m \rangle}{E_q}. \quad (17)$$

The details of the transformation and its application to the Heisenberg spin-1/2 chain with spin-flip coupling can be found in the Supplemental Material of Ref. [25]. In the following, we focus on the derivation of the effective Hamiltonian  $\hat{H}_{\text{eff}}^{(2)}$  and its representation in terms of the collective spin operators.

Let us start by expressing the action of  $\hat{H}_{\uparrow\downarrow}$  on Dicke states, namely,

$$\hat{H}_{\uparrow\downarrow} |m\rangle = \frac{\Omega}{2} |\Psi, m+1\rangle^+ + \frac{\Omega}{2} |\Psi, m-1\rangle^-, \quad (18)$$

where states  $|\Psi, m \pm 1\rangle^\pm = \sum_j \alpha_j^\pm \hat{S}_j^\pm |m\rangle$  can be expanded in terms of the spin-wave states  $|m \pm 1, q\rangle$  as

$$|\Psi, m \pm 1\rangle^\pm = \sqrt{N} c_{N/2, \pm m+1} \sum_q f_q^\pm |m \pm 1, q\rangle. \quad (19)$$

Here,  $c_{N/2, \pm m+1}$  are given by Eq. (4), and

$$f_q^\pm = \sum_j p_j^{(q)} \alpha_j^\pm = \sum_j p_j^{(q)} e^{\pm i(\phi j - \phi_0)}, \quad (20)$$

with  $f_q^+ = (f_q^-)^*$  because  $p_j^{(q)}$  is real. Note that the spin-flip term  $\hat{H}_{\uparrow\downarrow}$  couples each Dicke state  $|m\rangle$  with a superposition of spin-wave states (19) characterized by energies  $E_q$ . This is different from the PBC case, where  $\hat{H}_{\uparrow\downarrow}$  couples each Dicke state with a pair of spin-wave states of well-defined quantum numbers  $q = \pm \phi N / (2\pi)$  set by the coupling phase  $\phi$  [25]. An example of the amplitude of elementary couplings  $f_q^+$  to the  $|m, q\rangle$  states is presented in Fig. 2. We can see that, indeed, the coupling could be non-negligible even to the lowest state  $|m, q = 1\rangle$ . Therefore, the perturbative regime is defined by the smallest energy gap, namely,  $\Omega \ll |E_{q=1}| = J_{\text{SE}} |\cos(\pi/N) - 1|$ .

The relevant matrix elements of the second-order contribution can be written as

$$\begin{aligned} \langle m'', q | \hat{H}_{\uparrow\downarrow} | m \rangle &= \frac{\Omega}{2} N^{-1/2} c_{N/2, m+1}^{-1} f_q^+ \delta_{m'', m+1} \\ &+ \frac{\Omega}{2} N^{-1/2} c_{N/2, -m+1}^{-1} f_q^- \delta_{m'', m-1}, \end{aligned} \quad (21)$$

where the coefficients  $N^{-1/2} c_{N/2, \pm m+1}^{-1}$  come from the scalar product between the Dicke state  $|m\rangle$  and states  $|\Psi, m \pm 1\rangle^\pm$ .

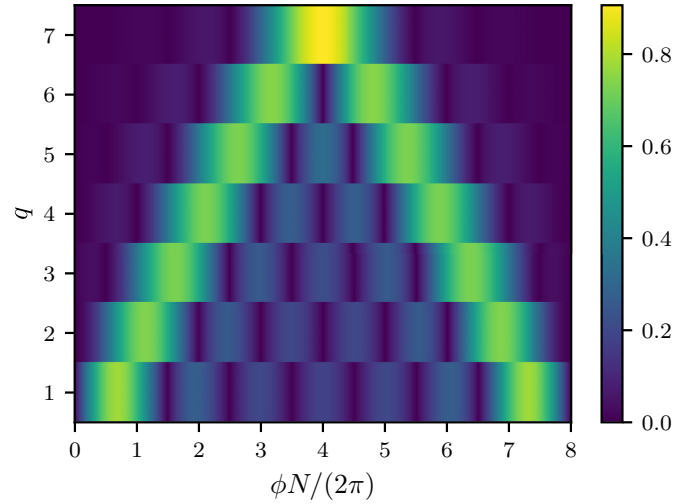


FIG. 2. The absolute values of the normalized coefficients  $|f_q^+| N^{-1/2}$  are shown by color versus the coupling phase  $\phi \in \mathbb{R}$  and the spin-wave quantum number  $q \in \mathbb{Z}$  for an arbitrary  $\phi_0$  when  $N = 8$ .

The nonzero matrix elements of the second-order term (17), namely,  $H_{m', m} = \langle m' | \hat{H}_{\text{eff}}^{(2)} | m \rangle$ , read

$$H_{m, m} = -(c_{N/2, m}^{-2} + c_{N/2, -m}^{-2}) (N-1) \chi_z, \quad (22)$$

$$H_{m, m-2} = c_{N/2, m-1}^{-1} c_{N/2, -(m-1)}^{-1} (N-1) \chi_x, \quad (23)$$

$$H_{m, m+2} = c_{N/2, m+1}^{-1} c_{N/2, -(m+1)}^{-1} (N-1) \chi_x, \quad (24)$$

where

$$\chi_z = \frac{\Omega^2}{4N J_{\text{SE}} (N-1)} \sum_{q=1}^{N-1} \frac{f_q^+ f_q^-}{\cos(\frac{\pi}{N} q) - 1}, \quad (25)$$

$$\chi_x = \frac{\Omega^2}{4N J_{\text{SE}} (N-1)} \sum_{q=1}^{N-1} \frac{(f_q^-)^2}{\cos(\frac{\pi}{N} q) - 1}. \quad (26)$$

Comparing the matrix elements presented in Eqs. (22)–(24) with the matrix elements of the appropriate collective spin operators, the second-order perturbation contribution can be represented in operator form as

$$\begin{aligned} \hat{H}_{\text{eff}}^{(2)} &= -2\chi_z (\hat{S}_z^2 + \hat{S}_z^2) + \text{Re}[\chi_x] (\hat{S}_+^2 + \hat{S}_-^2) \\ &+ i\text{Im}[\chi_x] (\hat{S}_+^2 - \hat{S}_-^2), \end{aligned} \quad (27)$$

as explained in Appendix B. The full effective Hamiltonian is a sum of the first- and second-order contributions:

$$\hat{H}_{\text{eff}}^{(\phi_0)} = \hat{H}_{\text{eff}}^{(1)} + \hat{H}_{\text{eff}}^{(2)}. \quad (28)$$

## B. Choosing the offset phase $\phi_0 = \phi(N+1)/2$

In what follows, we will take the value of the global coupling phase to be  $\phi_0 = \phi(N+1)/2$ , so that  $v_y$  entering Eqs. (13) and (15) and the imaginary part of  $\chi_x$  vanish, i.e.,  $v_y = \text{Im}[\chi_x] = 0$  (see Appendix C). This simplifies the form of the effective model, leading to

$$\hat{H}_{\text{eff}}^{(\phi_0)} = -2\chi_z (\hat{S}_z^2 + \hat{S}_z^2 - \eta \hat{S}_x^2 + \eta \hat{S}_y^2 + \gamma \hat{S}_x), \quad (29)$$

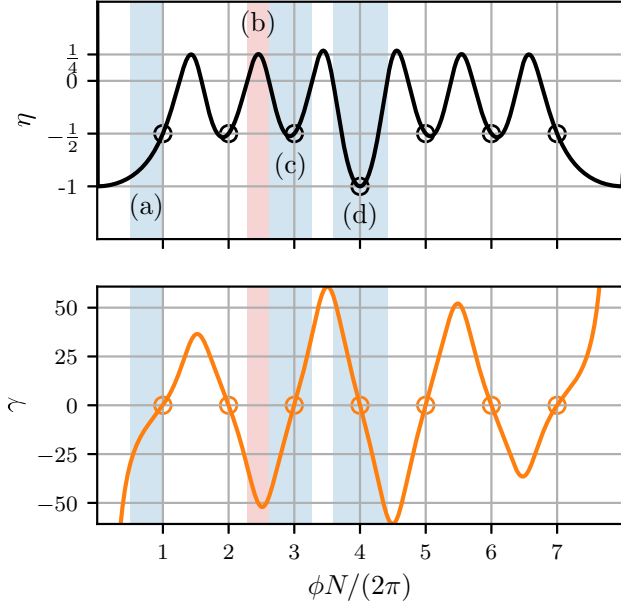


FIG. 3. The parameters  $\eta$  (top panel) and  $\gamma$  (bottom panel) of the effective model (29) versus the coupling phase  $\phi$  are marked by black and orange lines, respectively, for  $N = 8$ ,  $\Omega = |E_{q=1}|/10$ , and  $\phi_0 = \phi(N+1)/2$ . The values of  $\eta$  and  $\gamma$  for commensurate phases are marked by open circles. The regions shaded in blue present examples when  $\eta < 0$ , while the one shaded in red shows an example when  $\eta > 0$ .

where  $\eta = \chi_x/\chi_z$  and  $\gamma = v_x/\chi_z$ . This specific choice of phase  $\phi_0$  does not involve a loss of generality because the full effective Hamiltonian (28) containing  $\hat{H}_{\text{eff}}^{(1)}$  and  $\hat{H}_{\text{eff}}^{(2)}$  in Eqs. (15) and (27) is related to that given by Eq. (29) via a unitary transformation set by the global rotation around the  $z$  axis through the angle  $\phi_0$ .

In Fig. 3 we show the variation of the two parameters of the effective model (29), namely,  $\eta$  and  $\gamma$ , versus  $\phi$ . The commensurate phases corresponding to  $\phi = 2\pi n/N$ , with  $n \in [1, N-1]$ , are marked by open points in Fig. 3, for which we have  $\gamma = 0$ . In this case, we numerically observe that  $\eta = -1/2$  for  $\phi \neq \pi$  and  $\eta = -1$  for  $\phi = \pi$ . In addition, we have also analytically found that

$$\chi_z = -\frac{\Omega^2}{4J_{\text{SE}}(N-1)\cos(\phi)-1}, \quad (30)$$

$$\chi_x = \frac{\Omega^2}{4J_{\text{SE}}(N-1)\cos(\phi)-1} \quad (31)$$

for commensurate phases  $\phi = 2\pi n/N$ , apart from  $\phi = \pi$ , where

$$\chi_z = -\chi_x = -\frac{\Omega^2}{4J_{\text{SE}}(N-1)}. \quad (32)$$

The derivation is presented in Appendix E. The noncommensurate coupling phases  $\phi$  result in both positive and negative values of the parameter  $\eta$ , which is independent of  $J_{\text{SE}}$ ,  $\Omega$ , and  $N$ . On the contrary, the coefficient  $\gamma$  depends on the system parameters and scales as  $\gamma \propto NJ_{\text{SE}}/\Omega$ .

In this way, we derive the second-order contribution (27) and, consequently, the effective model (29), showing that the boundaries significantly modify the spin squeezing

Hamiltonian with respect to PBCs, in which one arrives at the effective Hamiltonian in the form of the OAT model, namely,  $\hat{H}_{\text{eff}} = -\chi_\pi \hat{S}_x^2$  for  $\phi = \pi$  and  $\hat{H}_{\text{eff}} = \chi_\phi \hat{S}_z^2$  for  $\phi \neq \pi$  [25]. Therefore, it is not only the timescale that is changed due to the OBCs but the entire dynamics as well. This is a counterintuitive result because, usually, the PBC describes well the system in the limit of large  $N$ .

## V. SPIN SQUEEZING FOR OBCs

In this section, we analyze the unitary evolution of the spin squeezing parameter governed by the effective spin Hamiltonian (29). We distinguish two cases depending on the commensurability of the coupling phase  $\phi$ . We demonstrate that if the coupling phase is commensurate, the resulting model (29) can be either OAT for  $\phi = \pi$  or nonisotropic TACT for  $\phi \neq \pi$ . However, the most general case of noncommensurate phases gives rise to a squeezing dynamics not simulated by the conventional OAT and TACT twisting models.

### A. Spin squeezing with commensurate phase

Tuning the value of the coupling phase  $\phi$  to the integer multiple of  $2\pi/N$  simplifies the problem. In particular, by taking  $\phi = \pi$  we have  $\eta = -1$ , and the effective Hamiltonian (29) acquires the form of the OAT one, namely,

$$\hat{H}_{\text{eff}} = 4\chi_z \hat{S}_y^2, \quad (33)$$

where we omitted a term proportional to  $\hat{S}^2$ , as it only shifts the origin of energy. The convenient initial spin coherent states are the ones polarized in the  $x$ - $z$  plane, namely,  $|\theta, \varphi = 0\rangle$  for any  $\theta$ . The best level of squeezing  $\xi_{\text{best}}^2 \approx N^{-2/3}$  is achievable for times  $t_{\text{best}} \approx N^{-2/3}|4\chi_z|^{-1}$  in the large- $N$  limit according to the OAT dynamics [33,45]. Next, taking the analytical expression (32) for  $\chi_z$ , we obtain  $t_{\text{best}} \approx N^{1/3}J_{\text{SE}}/\Omega^2$ . Therefore, the twisting dynamics is essentially the same as for PBCs [25]. The only difference is that for OBCs the resulting timescale is four times shorter than in the PBC case for the same perturbation level  $\Omega$ . Acceleration of the best squeezing time takes place because of a broader range of amplitudes  $p_j^{(q)}$  contributing to the generation of spin squeezing.

In another situation, when the coupling phase is not equal to  $\pi$ , we have  $\eta = -1/2$ , and  $\gamma = 0$ , so the effective Hamiltonian (29) reduces to

$$\hat{H}_{\text{eff}} = 2\chi_z(\hat{S}_y^2 - \hat{S}_z^2/2), \quad (34)$$

where we omitted the term proportional to  $\hat{S}^2$ . Equation (34) represents the anisotropic TACT with the anisotropy equal to  $1/2$ . It is worth stressing here that the OBC provides anisotropic TACT without adding an extra atom-light coupling characterized by two different phases. In the case of the PBC it was necessary to include two spin-flipping terms in order to simulate TACT [25]. Let us again consider the initial state for spin squeezing generation to be the spin coherent state polarized in the  $x$ - $z$  plane,  $|\theta, \varphi = 0\rangle$ . The anisotropic TACT given by (34) generates the Heisenberg limited level of squeezing  $\xi_{\text{best}}^2 \approx N^{-1}$  on the timescale  $t_{\text{best}} \approx (2\chi_z N \sqrt{2})^{-1} \ln(N/2)$  [12]. Therefore, taking into account the system parameters and the relation for  $\chi_z$  given



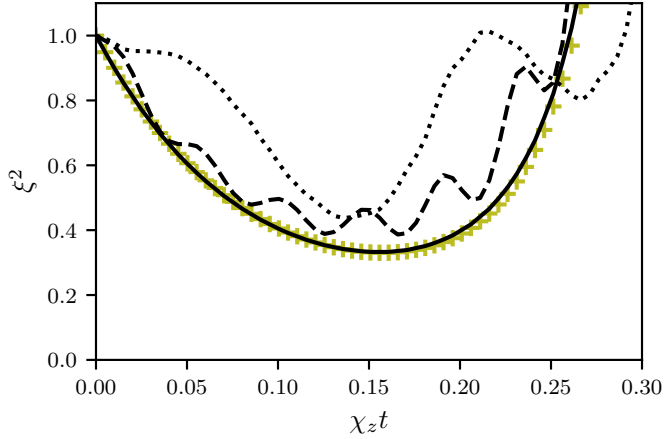


FIG. 4. Variation of spin squeezing parameter (12) in time for different values of  $\Omega$  when the initial state is  $|\theta = \pi/2, \phi = 0\rangle$ ,  $N = 8$ ,  $\phi = \pi - 2\pi/N$ , and  $\phi_0 = \phi(N + 1)/2$ . The result for the effective model (29) is marked by olive crosses, while results for the coupled Heisenberg model (7) are shown by black lines for  $\Omega = |E_{q=1}|/10$  (solid),  $\Omega = |E_{q=1}|$  (dashed) and  $\Omega = 2|E_{q=1}|$  (dotted).

by (30), we have  $t_{\text{best}} \approx J_{\text{SE}} \ln(N/2) |\cos \phi - 1|/(\sqrt{2}\Omega^2)$ . In Fig. 4 we show examples of spin squeezing dynamics for different values of  $\Omega$  obtained from exact many-body numerical simulations, using single occupied Fock states, of the spin-exchange model  $\hat{H}_{\text{SE}}$  with coupling  $\hat{H}_{\uparrow\downarrow}$ . Perfect agreement with the effective model (29) is observed in the perturbative regime when  $\Omega \ll |E_{q=1}|$ . Significant spin squeezing can also be generated beyond this regime, yet large discrepancies arise with respect to the TACT dynamics.

It is also worth commenting here on the importance of the coupling strength  $\Omega$  and phase  $\phi$  to the best squeezing time. Due to the perturbation regime condition,  $\Omega$  scales as  $\sim N^{-2}$ . This leads to a very long squeezing time, in principle. However, dependence on  $\phi$ , which is hidden in the function  $\chi_z$ , leads to a twofold modification of the time scaling. For  $\phi$  close to 0 or  $2\pi$  the timescale is reduced by  $N^{-2}$ . On the other hand,  $\phi \sim \pi$  does not provide an improvement directly, but the coupling to the lowest spin-wave states is smaller, increasing the perturbation regime condition and allowing it to increase the value of  $\Omega$ . In Fig. 5 we plot the variation of the best squeezing time with the phase  $\phi$  for a fixed value of the total number of spins  $N = 100$  obtained from the numerical simulations of the effective two-ordered model (29). We can see the timescale increases by orders of magnitude for values of the coupling phase from  $\phi = 2\pi/N$  to  $\phi = \pi$  and then decreases symmetrically to  $\phi = 2\pi(N - 1)/N$ . Thus, in practical applications, the optimization of the system parameters  $J_{\text{SE}}$ ,  $\Omega$ , and  $\phi$  will be necessary to have the shortest possible timescale.

### B. Spin squeezing with noncommensurate phases

The resulting effective model (29) simulated by the coupled Heisenberg model (7) also gives rise to the spin squeezing generation for noncommensurate coupling phases  $\phi$ , i.e., the one which is not equal to integer multiplications of  $2\pi/N$ . In general, the results depend strongly on the chosen initial spin coherent state  $|\theta, \phi\rangle$  and parameters  $\eta$  and  $\gamma$ .

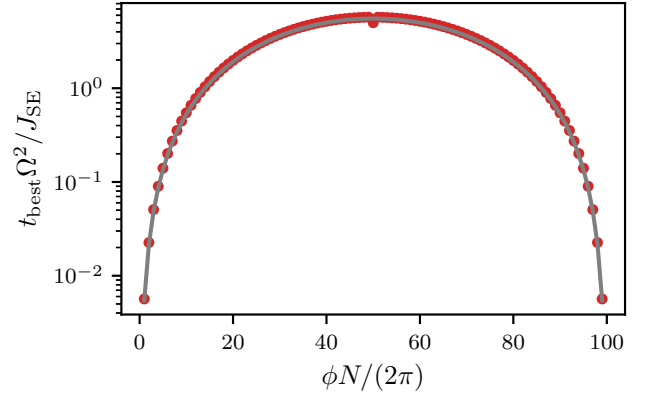


FIG. 5. The best squeezing time  $t_{\text{best}}$  multiplied by  $\Omega^2/J_{\text{SE}}$  for  $N = 100$  to isolate the dependence on the coupling phase  $\phi$ . The numerically evaluated values of the best squeezing time using unitary evolution according to (29) are shown by red points. The corresponding behavior  $t_{\text{best}} \Omega^2/J_{\text{SE}} = \ln(N/2) |\cos \phi - 1|/(\sqrt{2})$  for  $\phi \neq \pi$  and  $\phi_0 = \phi(N + 1)/2$  is shown with by the solid gray line; see text for more details.

Let us discuss the situation when the initial spin coherent state is polarized along the  $z$  axis:  $|0, 0\rangle = \bigotimes_{j=1}^N |\uparrow\rangle_j$ . Examples of the best squeezing and the best squeezing times are shown in Figs. 6(a)–6(d) for  $N = 100$  from the full numerical simulations of the effective model (29) using Dicke states basis (2). A characteristic behavior is the OAT level of best squeezing for positive values of  $\eta$ , which is demonstrated in Fig. 6(b). In other cases, when  $\eta$  is negative, the OAT level is also achieved mainly with  $\eta$  close to zero [see, e.g., Figs. 6(c) and 6(d)]. It is possible to exceed the OAT level of squeezing when  $\eta$  approaches the local minimum [see Figs. 6(a), 6(c) and 6(d)]. Interestingly, the last term in the effective model (29), namely,  $\gamma \hat{S}_x$ , does not dominate the dynamics even if  $\gamma$  is orders of magnitude larger than  $\eta$ . In Appendix D we show the corresponding results for two different initial states. The OAT level of squeezing can be achieved when the initial state is polarized along the  $y$  axis,  $|\theta = \pi/2, \phi = \pi/2\rangle$ . The best squeezing and times are of the same level as the ones presented in Fig. 6. On the other hand, if the evolution starts with the state polarized along the  $x$  axis,  $|\theta = \pi/2, \phi = 0\rangle$ , the dominant Zeeman-like term  $\gamma \hat{S}_x$  in (29) freezes the dynamics of the spin state, and only weak spin squeezing is generated for noncommensurate phases.

## VI. CONCLUSIONS AND SUMMARY

We studied in detail the effect of OBCs on the generation of spin squeezing in one-dimensional isotropic Heisenberg spin-1/2 chains induced by position-dependent spin-flip coupling with the offset phase  $\phi_0$  (8). We extended the spin-wave theory for the case of OBCs using the coordinate Bethe ansatz. We analytically derived the effective model in terms of the collective spin operators which describe the squeezing dynamics in the weak-coupling regime. The resulting effective model obtained differs significantly from the one under PBCs and therefore provides an example in which the boundaries significantly modify the dynamics of the system. To classify the squeezing scenarios, we distinguished two cases depending



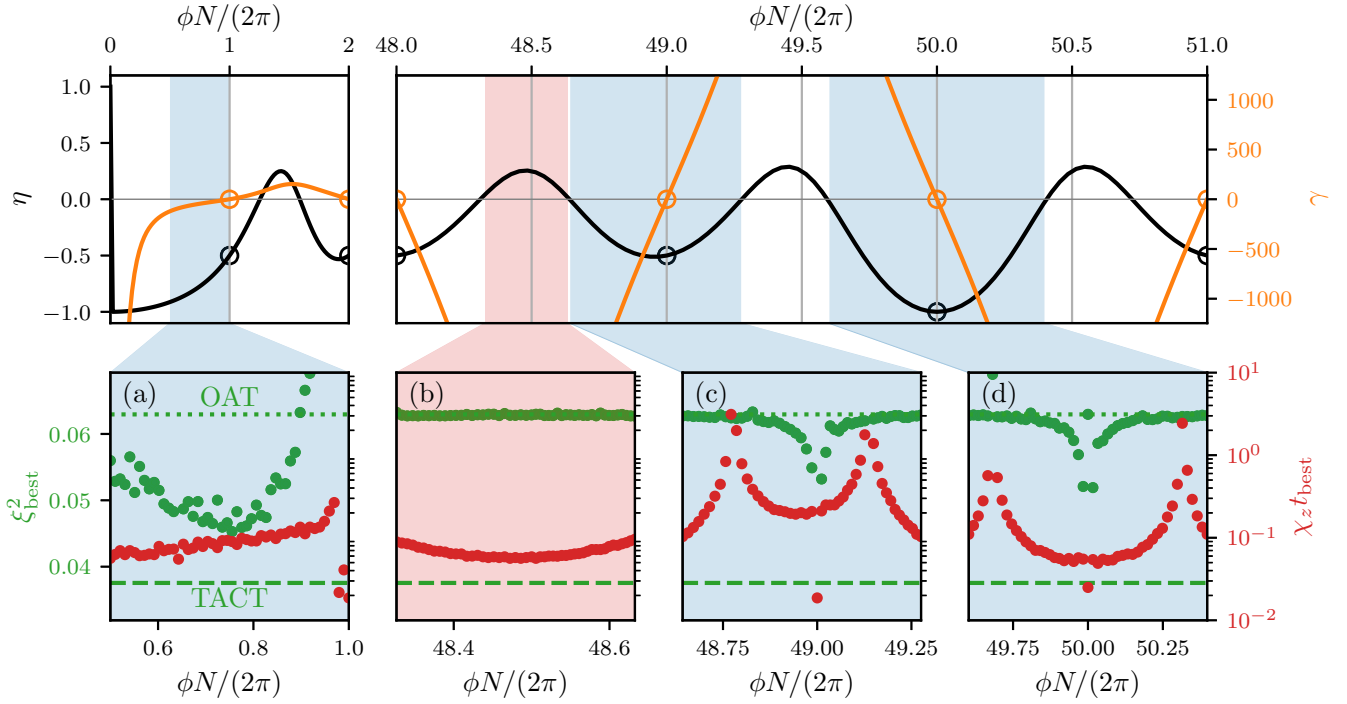


FIG. 6. The best squeezing  $\xi_{\text{best}}^2$  (green points) and the best squeezing time  $t_{\text{best}}$  (red points) are shown in (a)–(d) for different regions of  $\phi$ . The numerical results for the effective model (29) with  $N = 100$ ,  $J_{\text{SE}} = 1$ ,  $\Omega = |E_{q=1}|/10$ ,  $\phi_0 = \phi(N+1)/2$ , and  $\eta > 0$  (red shaded areas) or  $\eta < 0$  (blue shaded areas). The numerical values of  $\eta$  and  $\gamma$  used in the simulations are shown in the top panels. The two limit cases for the values of  $\xi_{\text{best}}^2$ , namely, OAT and TACT for  $N = 100$ , are marked by horizontal green dotted and dashed lines, respectively.

on the commensurability of the coupling phase  $\phi$  for a well-defined offset phase  $\phi_0 = \phi(N+1)/2$ . When the coupling phase is commensurate, the dynamics of spin squeezing is well captured by the nonisotropic TACT if  $\phi \neq \pi$  and OAT for  $\phi = \pi$ . The most general case of the noncommensurate phase  $\phi$  and arbitrary offset phase  $\phi_0$  still gives rise to the simulation of a squeezing model, although not a conventional one. This is in contrast to the PBC case, where the OAT model is simulated by the system independently of  $\phi$ . Our analytical predictions were confirmed by the full many-body numerical simulations.

The results presented here show how to produce entangled states in the isotropic spin-1/2 Heisenberg chains with nearest-neighbor interactions. This is possible through the addition of the position-dependent spin-flip coupling that is weak enough to maintain the dynamics within the Dicke manifold and strong enough to excite spin waves that are extended over the entire system, allowing effective all-to-all interaction between the individual spins. It is also worth adding that the dynamics of generated spin-squeezed states can be frozen at a desired time just by turning off the spin-flipping term. The results obtained can be verified experimentally by current state-of-the-art experiments with ultracold atoms.

#### ACKNOWLEDGMENTS

We gratefully acknowledge discussions with B. B. Laburthe-Tolra, M. R. de Saint-Vincent, and A. Sinatra. We thank O. Stachowiak for discussions and providing Fig. 7. This work was supported by the European Social Fund (Project No. 09.3.3-LMT-K-712-23-0035)

under a grant agreement with the Research Council of Lithuania (M.M.S.), Polish National Science Centre Project No. DEC-2019/35/O/ST2/01873 (T.H.Y.), and Grant No. 2019/32/Z/ST2/00016 through the project MAQS under QuantERA, which has received funding from the European Union's Horizon 2020 research and innovation program under Grant Agreement No. 731473 (E.W.). M.P. acknowledges the support of the Polish National Agency for Academic Exchange, Bekker Program Grants No. PPN/BEK/2020/1/00317, and No. ERC AdG NOQIA; Ministerio de Ciencia y Innovación Agencia Estatal de Investigaciones (PGC2018-097027-B-I00/10.13039/501100011033, CEX2019-000910-S/10.13039/501100011033, Plan National FIDEUA PID2019-106901GB-I00, FPI, QUANTERA MAQS PCI2019-111828-2, QUANTERA DYNAMITE PCI2022-132919, Proyectos de I+D+I Retos Colaboración QUSPIN RTC2019-007196-7); MICIIN with funding from European Union NextGenerationEU (PRTR-C17.I1) and from Generalitat de Catalunya; Fundació Cellex; Fundació Mir-Puig; Generalitat de Catalunya (European Social Fund FEDER and CERCA program, AGAUR Grant No. 2021 SGR 01452, QuantumCAT & U16-011424, cofunded by the ERDF Operational Program of Catalonia 2014–2020); the Barcelona Supercomputing Center MareNostrum (FI-2022-1-0042); EU Horizon 2020 FET-OPEN OPTologic (Grant No. 899794); the EU Horizon Europe Program (Grant Agreement No. 101080086 NeQST); the National Science Centre, Poland (Symfonia Grant No. 2016/20/W/ST4/00314); the ICFO Internal QuantumGaudi project; and the European Union's Horizon 2020 research and innovation program under



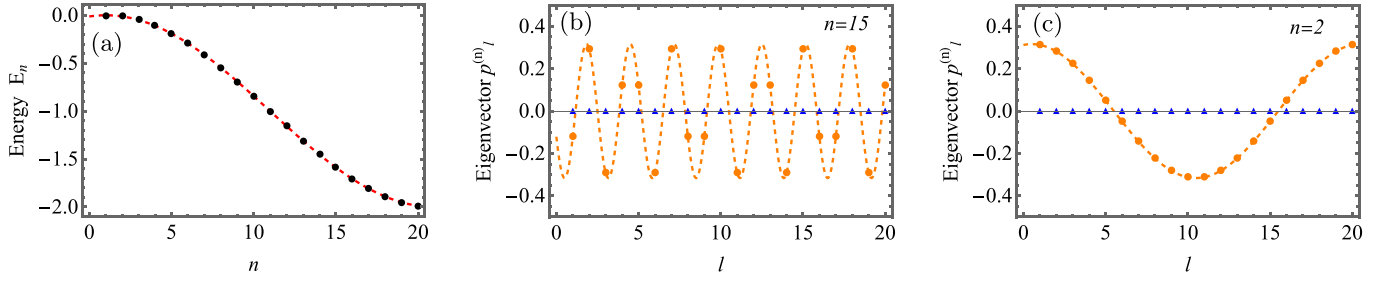


FIG. 7. (a) Energy spectrum  $E_q$  of the spin-wave states for open boundary conditions for numerical (black points) and analytical (red dashed line) results. (b) and (c) Eigenvectors  $p_l$ , which are solutions of (A10)–(A12), for open boundary conditions when  $q = 15$  and  $q = 2$ , respectively. Analytical results are marked by lines, while the numerical one are marked by points (the orange dashed lines mark the real parts of  $p_l$ , while the blue solid lines show the imaginary parts of  $p_l$ ).  $N = 20$ .

Marie-Skodowska-Curie Grant Agreements No. 101029393 (STREDCH) and No. 847648 (La Caixa Junior Leaders fellowships ID100010434: LCF/BQ/PI19/11690013, LCF/BQ/PI20/11760031, LCF/BQ/PR20/11770012, and LCF/BQ/PR21/11840013). The views and opinions expressed in this work are those of the author(s) and do not necessarily reflect those of the European Union, European Climate, the Infrastructure and Environment Executive Agency (CINEA), or any other granting authority. Neither the European Union nor any granting authority can be held responsible for them. Some of the computations were carried out at the Centre of Informatics Tricity Academic Supercomputer and Network.

T.H.Y. performed check-in numerical simulations and provided all numerical results presented in the paper. M.P. performed preliminary many-body numerical calculations. T.H.Y., E.W., and G.J. provided the spin-wave states for OBCs presented in Appendix A. T.H.Y., G.Ž., and E.W. contributed to a derivation of the effective Hamiltonian (29). T.H.Y. and G.Ž. analytically calculated the offset phase  $\phi_0$ , as discussed in Appendix C. G.Ž., D.B., and G.J. contributed to calculations of  $\eta$  for commensurate phases, as shown in Appendix E. E.W. and G.J. conceived the idea and guided the research. T.H.Y. and E.W. wrote the first draft. All the authors contributed to the discussion of the results and the manuscript preparation and revision.

## APPENDIX A: SPIN-WAVE STATES FOR OBCs

In this Appendix, we are interested in spin-wave states which are eigenstates of the isotropic Heisenberg model,

$$\hat{H}_{\text{SE}} = J_{\text{SE}} \sum_{j=1}^{N-1} \left( S_j^z S_{j+1}^z + S_j^y S_{j+1}^y + S_j^x S_{j+1}^x - \frac{1}{4} \right), \quad (\text{A1})$$

for  $N$  spins and open boundary conditions. In the following, we will show that the spin-wave states are given by Eq. (3) of the main text, namely,

$$|m, q\rangle = \pm \sqrt{N} c_{N/2, \pm m} \sum_{j=1}^N p_j^{(q)} \hat{S}_j^{\pm} |m \mp 1\rangle. \quad (\text{A2})$$

In the above equation, the states  $|m \mp 1\rangle$  are Dicke states, while the usage of the on-site rising and lowering operators  $\hat{S}_j^{\pm}$  corresponds to the two ways to define spin-wave states. Note

that  $S_z |m, q\rangle = m |m, q\rangle$ , as each term comprising the state vector (A2) is characterized by the same spin projection  $m$ . Furthermore,  $\hat{S}^2 |m, q\rangle = S(S+1) |m, q\rangle$ , with  $S = N/2 - 1$ . To see this we notice that the states (A2) are constructed in such a way that

$$|m, q\rangle \propto \hat{S}_{\pm}^{N/2-1 \pm m} |q\rangle^{\pm}, \quad (\text{A3})$$

where the state vector  $|q\rangle^{\pm} \equiv |\mp(N/2 - 1), q\rangle$  corresponds to the minimum and maximum values of the spin projection  $m = \mp(N/2 - 1)$ . Since  $[\hat{S}^2, \hat{S}_{\pm}] = 0$ ,

$$\hat{S}^2 |m, q\rangle \propto \hat{S}_{\pm}^{N/2-1 \pm m} \hat{S}^2 |q\rangle^{\pm}. \quad (\text{A4})$$

Therefore, one needs to find the action of the operator  $\hat{S}^2$  on the state vector  $|q\rangle^{\pm}$ , which is

$$\begin{aligned} \hat{S}^2 |q\rangle^{\pm} &= (\hat{S}_z^2 + \hat{S}_z + \hat{S}_- \hat{S}_+) |q\rangle^{\pm} \\ &= \left[ \left( \frac{N}{2} \right)^2 - \frac{N}{2} \right] |q\rangle^{\pm} + \left( \sum_j p_j^{(q)} \right) \hat{S}_{\pm} |N/2, \mp N/2\rangle. \end{aligned} \quad (\text{A5})$$

One can see that the state vectors  $|q\rangle^{\pm}$  are eigenstates of the  $\hat{S}^2$  operator with the spin quantum number  $S = N/2 - 1$  if the last term in (A5) is zero, i.e.,

$$\sum_j p_j^{(q)} = 0. \quad (\text{A6})$$

In that case the state vectors  $|m, q\rangle$  with an arbitrary  $m$  are also the eigenstates of  $\hat{S}^2$  with quantum number  $S = N/2 - 1$ . Note that the explicit form of the coefficients  $p_j^{(q)}$  presented later in Eq. (A16) does obey the condition (A6).

We are looking for the spin-wave states  $|m, q\rangle$  which are eigenstates of the Hamiltonian (A1). Since  $[\hat{H}_{\text{SE}}, \hat{S}_{\pm}] = 0$ , using Eq. (A3), one can see that the eigenstates  $|m, q\rangle$  of the Hamiltonian  $\hat{H}_{\text{SE}}$  have eigenenergies  $E_q$  which do not depend on the quantum number  $m$ . Therefore, by choosing the amplitudes  $p_j^{(q)}$  in such a way that  $|q\rangle^{\pm}$  are eigenstates of the spin-exchange Hamiltonian (A1), the states  $|m, q\rangle$  for any magnetization  $m$  are also its eigenstates with the same eigenenergies  $E_q$ .

Below we show how to derive the form of  $p_j^{(q)}$  for  $|q\rangle^{+}$  using OBCs. The equations for  $|q\rangle^{-}$  give the same expansion coefficients  $p_j^{(q)}$  and the same eigenenergies  $E_q$ . Using the

coordinate basis vectors

$$|\tilde{l}\rangle \equiv \hat{S}_l^+ | -N/2 \rangle = \hat{S}_l^+ \bigotimes_{j=1}^N |\downarrow\rangle_j, \quad (\text{A7})$$

the spin-wave states  $|q\rangle^+$  can be represented as

$$|q\rangle^+ = \sum_{l=1}^N p_l |\tilde{l}\rangle. \quad (\text{A8})$$

The coefficients  $p_l$  are evaluated by considering the eigenvalue problem

$$(H - EI)\vec{p} = 0, \quad (\text{A9})$$

where  $I$  is the identity matrix,  $\vec{p} = (p_1, p_2, \dots)$  and the matrix elements of  $H$  are  $H_{l',l} = \langle \tilde{l}' | \hat{H}_{\text{SE}} | \tilde{l} \rangle$ .

The matrix form of eigenproblem (A9) leads to the set of equations

$$-\frac{J_{\text{SE}}}{2} p_1 + \frac{J_{\text{SE}}}{2} p_2 = E p_1, \quad (\text{A10})$$

$$\frac{J_{\text{SE}}}{2} p_{l-1} - J_{\text{SE}} p_l + \frac{J_{\text{SE}}}{2} p_{l+1} = E p_l \text{ for } l \in [2, N-1], \quad (\text{A11})$$

$$-\frac{J_{\text{SE}}}{2} p_N + \frac{J_{\text{SE}}}{2} p_{N-1} = E p_N, \quad (\text{A12})$$

where (A10) and (A12) are for the boundary sites of the lattice. We use Puzskarski's idea [46] and add two virtual lattice sites  $p_0$  and  $p_{N+1}$  subject to the boundary constraints  $p_0 = p_1$  and  $p_{N+1} = p_N$ . In that case, the set of equations (A10)–(A12) becomes equivalent to the following set of bulk equations valid for any  $l$ :

$$\frac{J_{\text{SE}}}{2} p_{l-1} - J_{\text{SE}} p_l + \frac{J_{\text{SE}}}{2} p_{l+1} = E p_l. \quad (\text{A13})$$

The solution to Eq.(A13) can be represented as

$$p_l = p \cos[k(l+u)], \quad (\text{A14})$$

with the corresponding eigenenergies  $E = J_{\text{SE}}(\cos k - 1)$ . The boundary constraint  $p_0 = p_1$  requires  $\cos(uk) = \cos(uk+k)$ , which is fulfilled for  $u = -1/2$ . The second constraint,  $p_{N+1} = p_N$ , leads to the requirement

$$\cos(kN+k+uk) = \cos(kN+uk), \quad (\text{A15})$$

which is fulfilled when  $k = q\pi/N$ , with  $q = 1, 2, \dots, N-1$  being an integer. Therefore, we arrive at the required expansion coefficients and the corresponding eigenenergies:

$$p_l^{(q)} = \sqrt{\frac{2}{N}} \cos\left[\frac{\pi}{N}\left(l - \frac{1}{2}\right)q\right], \quad (\text{A16})$$

$$E_q = J_{\text{SE}}\left[\cos\left(\frac{\pi}{N}q\right) - 1\right]. \quad (\text{A17})$$

Note that the value  $q = 0$  is not included here, as in that case, the coefficients  $p_l^{(q)}$  do not depend on  $l$  and thus do not obey the condition (A6). Although such a state with  $q = 0$  is an eigenstate of the Hamiltonian  $\hat{H}_{\text{SE}}$ , it belongs to the Dicke manifold and is characterized by the spin quantum number  $S = N/2$  and zero eigenenergy.

In Fig. 7 we show a comparison of the numerical solution of (A10)–(A12) with the analytical results. Perfect agreement can be seen.

## APPENDIX B: MATRIX REPRESENTATION OF SPIN OPERATORS NEEDED FOR EFFECTIVE MODEL

In the following, we will present the matrix representation of various spin operators  $\hat{S}_\sigma$  with  $\sigma = z, \pm$  by using  $\hat{S}_- |S, m\rangle = A_-^{S,m} |S, m-1\rangle$ ,  $A_-^{S,m} = \sqrt{(S+m)(S-m+1)}$ ,  $\hat{S}_+ |S, m\rangle = A_+^{S,m} |S, m+1\rangle$ , and  $A_+^{S,m} = \sqrt{(S-m)(S+m+1)}$ .

The nonzero elements relevant for the relation of the matrix representation to the corresponding spin operators are

$$\langle N/2, m | \hat{S}_-^2 | N/2, m+2 \rangle = \sqrt{\left(\frac{N}{2} + m + 2\right) \left(\frac{N}{2} - m - 1\right) \left(\frac{N}{2} + m + 1\right) \left(\frac{N}{2} - m\right)}, \quad (\text{B1})$$

$$\langle N/2, m | \hat{S}_+^2 | N/2, m-2 \rangle = \sqrt{\left(\frac{N}{2} + m\right) \left(\frac{N}{2} - m + 1\right) \left(\frac{N}{2} + m - 1\right) \left(\frac{N}{2} - m + 2\right)}. \quad (\text{B2})$$

One can show that the right-hand side of Eq. (B1) equals  $(N-1)c_{N/2,m+1}^{-1}c_{N/2,-(m+1)}^{-1}$  and the right-hand side of Eq. (B2) equals  $(N-1)c_{N/2,m-1}^{-1}c_{N/2,-(m-1)}^{-1}$ . In addition,  $\langle N/2, m | \hat{S}_z^2 | N/2, m \rangle = m^2$ , and  $\langle N/2, m | \hat{S}^2 | N/2, m \rangle = \frac{N}{2}(\frac{N}{2} + 1)$ , while  $(c_{N/2,m}^{-2} + c_{N/2,-m}^{-2}) = \frac{2}{N-1}(m^2 + \frac{N}{2} + \frac{N^2}{4})$ .

## APPENDIX C: EFFECTIVE MODEL AND OFFSET PHASE

The general form of the effective model including the first- and second-order perturbation terms is

$$\begin{aligned} \hat{H}_{\text{eff}} = & 2\chi_z(\hat{S}_z^2 + \hat{S}_z^2) - \text{Re}[\chi_x](\hat{S}_+^2 + \hat{S}_-^2) \\ & - i\text{Im}[\chi_x](\hat{S}_+^2 - \hat{S}_-^2) + v_x\hat{S}_x + v_y\hat{S}_y, \end{aligned} \quad (\text{C1})$$

which for  $\phi_0 = \phi(M+1)/2$  leads to (29).

While the general form of the effective Hamiltonian (C1) includes the mixed term  $\hat{S}_+^2 - \hat{S}_-^2 \propto \hat{S}_x\hat{S}_y + \hat{S}_y\hat{S}_x$  that complicates the effective model, it can be removed in general by a proper choice of the global phase factor in the atom-light coupling term. This is done by choosing a phase shift  $\phi_0$  so that  $\text{Im}[\chi_x] = 0$ . In fact, it is sufficient to fulfill  $\text{Im}[(f_q^\pm)^2] = 0 \forall q$  since  $\text{Im}[\chi_x] \propto \sum_q \{\text{Im}[(f_q^\pm)^2]/E_q\}$ . By explicitly calculating

$$f_q^\pm = \sum_{j=1}^N p_j(q) \alpha_j^\pm = \frac{\sqrt{2}}{N} \sum_{j=1}^N \cos\left[\frac{\pi}{N}q\left(j - \frac{1}{2}\right)\right] e^{i(\phi_j - \phi_0)}, \quad (\text{C2})$$



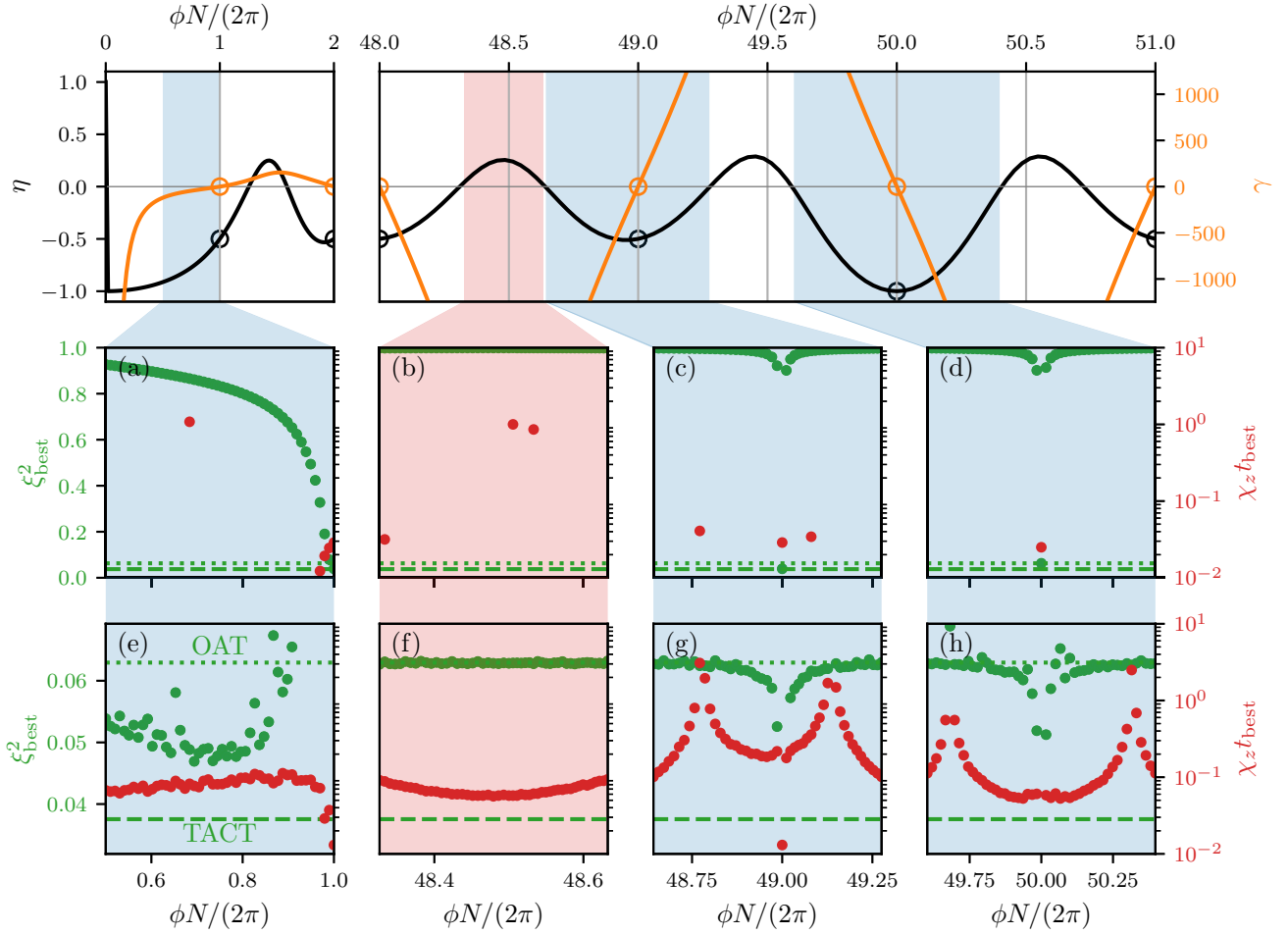


FIG. 8. The best squeezing  $\xi_{\text{best}}^2$  (green points) and the best squeezing time  $t_{\text{best}}$  (red points) are shown in (a)–(d) for initial state  $|\theta = \pi/2, \phi = 0\rangle$  and in (e)–(h) for initial state  $|\theta = \pi/2, \phi = \pi/2\rangle$ . The numerical results for the effective model (29) with  $N = 100$ ,  $J_{\text{SE}} = 1$ ,  $\Omega = |E_{q=1}|/10$ ,  $\phi_0 = \phi(N+1)/2$ , and  $\eta > 0$  (red shaded areas) or  $\eta < 0$  (blue shaded areas). The numerical values of  $\eta$  and  $\gamma$  used in the simulations are shown in the top panels. The two limit cases for the values of  $\xi_{\text{best}}^2$ , namely, OAT and TACT for  $N = 100$ , are marked by horizontal green dotted and dashed lines, respectively.

using the geometric series result

$$\sum_{j=1}^N r^j = \begin{cases} \frac{1-r^{N+1}}{1-r} & \text{if } r \neq 1, \\ N & \text{if } r = 1, \end{cases} \quad (\text{C3})$$

we obtain

$$f_q^\pm = \begin{cases} \frac{e^{i(\frac{\phi}{2} - \phi_0)}}{\sqrt{2}} \left[ \frac{e^{-in(\frac{q}{2} - \frac{N\phi}{2\pi})}}{N} g(q, -\phi) + \frac{e^{in(\frac{q}{2} + \frac{N\phi}{2\pi})}}{N} g(q, \phi) \right] & \text{if } \phi \neq \pm \frac{\pi}{N}q, \\ \frac{e^{i(\frac{\phi}{2} - \phi_0)}}{\sqrt{2}} & \text{if } \phi = \pm \frac{\pi}{N}q, \end{cases} \quad (\text{C4})$$

where  $g(q, \phi) = \frac{\sin \pi(\frac{q}{2} + \frac{N\phi}{2\pi})}{\sin \frac{\pi}{N}(\frac{q}{2} + \frac{N\phi}{2\pi})}$ . This can also be written as

$$f_q^\pm = \begin{cases} \frac{e^{i(\frac{N+1}{2}\phi - \phi_0)}}{\sqrt{2}} \frac{1}{N} \left[ (-1)^q g(q, -\phi) + g(q, \phi) \right], & \text{if } \phi \neq \pm \frac{\pi}{N}q, \\ \frac{e^{i(\frac{\phi}{2} - \phi_0)}}{\sqrt{2}}, & \text{if } \phi = \pm \frac{\pi}{N}q. \end{cases} \quad (\text{C5})$$

Then

$$\text{Im}[(f_q^\pm)^2] \propto \begin{cases} \sin[(N+1)\phi - 2\phi_0] & \text{if } \phi \neq \pm \frac{\pi}{N}q, \\ \sin(\phi - 2\phi_0) & \text{if } \phi = \pm \frac{\pi}{N}q, \end{cases} \quad (\text{C6})$$

for  $\text{Im}[(f_q^\pm)^2] = 0$ ; for all  $q$  it follows that

$$\phi_0 = \begin{cases} \frac{N+1}{2}\phi + \frac{\pi}{2}n & \text{if } \phi \neq \pm \frac{\pi}{N}q, \\ \frac{\phi}{2} + \frac{\pi}{2}n & \text{if } \phi = \pm \frac{\pi}{N}q, \end{cases} \quad (\text{C7})$$

$\forall n \in \mathbb{Z}$ . Notice we can write the second case result as the first one without any loss of generality by changing the variable  $n = q + n'$ . As such,  $\text{Im}[\chi_x] = 0$  when

$$\phi_0 = \frac{N+1}{2}\phi + \frac{\pi}{2}n; \quad \forall n \in \mathbb{Z}. \quad (\text{C8})$$

#### APPENDIX D: SPIN SQUEEZING FOR THE INCOMMENSURATE PHASE

We showcased the best squeezing results for the initial coherent state  $|\theta = 0, \phi = 0\rangle = \bigotimes_j |\uparrow\rangle_j$  in Sec. VB (Fig. 6).



Here, we show that other choices for the initial state can provide different results. They are shown in Fig. 8 for the initial states  $|\theta = \pi/2, \varphi = 0\rangle$  [Figs. 8(a)–8(d)] and  $|\theta = \pi/2, \varphi = \pi/2\rangle$  [Figs. 8(e)–8(h)]. The unitary evolution with the initial state being the eigenstate of  $\hat{S}_x$ ,  $|\theta = \pi/2, \varphi = 0\rangle$ , shows practically no squeezing except very close to the commensurate phases or when  $\gamma$  is very small [see Fig. 8(a)–8(d)]. On the other hand, when the initial state is the eigenstate of  $\hat{S}_y$ ,  $|\theta = \pi/2, \varphi = \pi/2\rangle$ , the squeezing dynamics is the same as for the initial state  $|\theta = 0, \phi = 0\rangle$ , which is presented in Fig. 6. This is shown in Figs. 8(e)–8(h).

#### APPENDIX E: CALCULATION OF $\eta$ FOR COMMENSURATE PHASES

For commensurate phase  $\phi = 2\pi n/N$ , it is possible to calculate  $\chi_z$  and  $\chi_x$  analytically. Consequently, one can obtain  $\eta$ .

We make use of a method originally used in the study of random walks on lattices [47,48] and also employed to study excitons in molecular aggregates [49].

For convenience, let us represent Eqs. (25) and (26) in the following way:

$$\chi_z = \frac{\Omega^2}{4J_{SE}(N-1)} F_{\text{diag}}^{(\phi)}, \quad (\text{E1})$$

$$\chi_x = \frac{\Omega^2}{4J_{SE}(N-1)} F_{\text{off}}^{(\phi)}, \quad (\text{E2})$$

where we have defined the dimensionless sums  $F_{\text{diag}}^{(\phi)}$  and  $F_{\text{off}}^{(\phi)}$ :

$$F_{\text{diag}}^{(\phi)} = \frac{1}{N} \sum_{j,l=1}^N E_{j,l} e^{i\phi(j-l)}, \quad (\text{E3})$$

$$F_{\text{off}}^{(\phi)} = \frac{1}{N} \sum_{j,l=1}^N E_{j,l} e^{i\phi(j+l)-i2\phi_0}, \quad (\text{E4})$$

where

$$E_{j,l} = \frac{2}{N} \sum_{q=1}^N \frac{\cos\left[\frac{\pi q}{N}\left(j - \frac{1}{2}\right)\right] \cos\left[\frac{\pi q}{N}\left(l - \frac{1}{2}\right)\right]}{\cos(\pi q/N) - p}. \quad (\text{E5})$$

Here, we added the  $q = N$  term, which is zero, and introduced  $p = 1 + \epsilon$  to avoid divergences. The limit  $\epsilon \rightarrow 0^+$  will be taken at the end of calculations.

The main idea in finding this sum is to expand the denominator into a geometric series. To achieve this, we rewrite the denominator in the following way:

$$\cos(\pi q/N) - p = -\frac{b}{2} [1 - b^{-1} e^{i\pi q/N}] [1 - b^{-1} e^{-i\pi q/N}], \quad (\text{E6})$$

where

$$b = p + \sqrt{p^2 - 1}. \quad (\text{E7})$$

By using the symmetry of the summand to expand the summation limits, we can rewrite  $E_{j,l}$  as

$$E_{j,l} = -C_{j+l-1} - C_{j-l} - \frac{1}{N} \frac{1}{1-p}, \quad (\text{E8})$$

where

$$C_n = \frac{1}{bN} \sum_{q=1-N}^N \frac{e^{i\pi qn/N}}{[1 - b^{-1} e^{i\pi q/N}] [1 - b^{-1} e^{-i\pi q/N}]}, \quad (\text{E9})$$

with  $C_{-n} = C_n^*$ . Note that the last term in Eq. (E8) cancels the added  $q = 0$  term in the summation.

Representing the denominator in terms of the geometric series, we have

$$C_n = \frac{1}{bN} \sum_{q=1-N}^N \sum_{r=0}^{\infty} \sum_{s=0}^{\infty} e^{i\pi q(n+r-s)/N} b^{-(r+s)}. \quad (\text{E10})$$

Using

$$\frac{1}{N} \sum_{q=1-N}^N e^{i\pi q(n+r-s)/N} = 2 \sum_{m=-\infty}^{\infty} \delta_{n+r-s, 2Nm}, \quad (\text{E11})$$

we obtain

$$C_n = \frac{2}{b} \sum_{m=-\infty}^{\infty} \sum_{r=0}^{\infty} \sum_{s=0}^{\infty} b^{-(r+s)} \delta_{n+r-s, 2Nm}.$$

Due to the Kronecker delta, the terms in the summation are nonzero only if  $s = r + n - 2Nm$  or, equivalently, if  $r = s - n + 2Nm$ . Assuming that  $0 \leq n < 2N$ , the integer  $s = r + n - 2Nm$  is  $s \geq 0$  if  $m \leq 0$ , whereas the integer  $r = s - n + 2Nm$  is  $r \geq 0$  if  $m \geq 1$ . Therefore, it is convenient to split the summation over  $m$  into a part with  $m < 1$  and one with  $m > 0$ , giving

$$C_n = 2b^{-1} \sum_{m=0}^{\infty} \sum_{r=0}^{\infty} b^{-(2r+2Nm+n)} + 2b^{-1} \sum_{m=1}^{\infty} \sum_{s=0}^{\infty} b^{-(2s+2Nm-n)}. \quad (\text{E12})$$

After evaluating the geometric sums, we arrive at

$$C_n = \frac{2}{b - b^{-1}} \frac{b^{-|n|} + b^{-2N+|n|}}{1 - b^{-2N}}, \quad (\text{E13})$$

where we have used the relation  $C_{-n} = C_n^*$ .

Taking the limit  $\epsilon \rightarrow 0^+$ , we obtain

$$-3NE_{j,l} = 1 - 3j + 3j^2 - 3l + 3l^2 + 3N - 6 \max(j, l)N + 2N^2. \quad (\text{E14})$$

Therefore, we can rewrite Eq. (E3) in terms of a double summation over  $j > l$  and a single summation for  $j = l$ :

$$F_{\text{diag}}^{(\phi)} = \frac{2}{N} \sum_{j=1}^N \sum_{l=1}^{j-1} E_{j,l} e^{i\phi(j-l)} + \frac{1}{N} \sum_{j=1}^N E_{j,j}. \quad (\text{E15})$$

Performing this summation, we obtain

$$F_{\text{diag}}^{(\phi)} = -\csc^2\left(\frac{\pi n}{N}\right). \quad (\text{E16})$$

Remembering that  $\phi = 2\pi n/N$ , we can rewrite this as

$$F_{\text{diag}}^{(\phi)} = \frac{2}{\cos \phi - 1}, \quad (\text{E17})$$

thus proving the identity mentioned in the main text.



As for  $F_{\text{off}}^{(\phi)}$ , the steps are analogous; first, we rewrite the sum (E4):

$$F_{\text{off}}^{(\phi)} = \frac{2}{N} \sum_{j=1}^N \sum_{l=1}^{j-1} E_{j,l} e^{i\phi(j+l)-i2\phi_0} + \frac{1}{N} \sum_{j=1}^N E_{j,j} e^{i2\phi j-i2\phi_0}. \quad (\text{E18})$$

For the initial phase  $\phi_0 = \phi(N+1)/2$ , the summation yields

$$F_{\text{off}}^{(\phi)} = \frac{1}{2} \csc^2\left(\frac{\pi n}{N}\right), \quad (\text{E19})$$

or, equivalently,

$$F_{\text{off}}^{(\phi)} = -\frac{1}{\cos \phi - 1}, \quad (\text{E20})$$

as expected.

Having both  $F_{\text{diag}}^{(\phi)}$  and  $F_{\text{off}}^{(\phi)}$ , we can confirm that

$$\eta = \frac{\text{Re}[F_{\text{off}}^{(\phi)}]}{F_{\text{diag}}^{(\phi)}} = -\frac{1}{2}, \quad (\text{E21})$$

as clearly seen in Fig. 3.

The exceptional case of  $\phi = \pi$  must be considered separately for  $\phi_0 = \phi(N+1)/2$ :

$$F_{\text{diag}}^{(\pi)} = -F_{\text{off}}^{(\pi)} = 1. \quad (\text{E22})$$

In general, for any  $\phi_0$  we have the following identities:

$$F_{\text{off}}^{(\pi)} = \frac{1}{2} e^{i(\frac{2\pi n}{N}-2\phi_0)} \csc^2\left(\frac{\pi n}{N}\right), \quad (\text{E23})$$

or, equivalently,

$$F_{\text{off}}^{(\pi)} = -\frac{e^{i(\phi-2\phi_0)}}{\cos \phi - 1}. \quad (\text{E24})$$

- 
- [1] H. Bernien, S. Schwartz, A. Keesling, H. Levine, A. Omran, H. Pichler, S. Choi, A. S. Zibrov, M. Endres, M. Greiner, V. Vuletić, and M. D. Lukin, *Nature (London)* **551**, 579 (2017).
- [2] A. Browaeys and T. Lahaye, *Nat. Phys.* **16**, 132 (2020).
- [3] C. Gross and I. Bloch, *Science* **357**, 995 (2017).
- [4] D. Jaksch, C. Bruder, J. I. Cirac, C. W. Gardiner, and P. Zoller, *Phys. Rev. Lett.* **81**, 3108 (1998).
- [5] A. M. Kaufman and K.-K. Ni, *Nat. Phys.* **17**, 1324 (2021).
- [6] I. Bloch, J. Dalibard, and W. Zwerger, *Rev. Mod. Phys.* **80**, 885 (2008).
- [7] R. Jördens, N. Strohmaier, K. Günter, H. Moritz, and T. Esslinger, *Nature (London)* **455**, 204 (2008).
- [8] R. A. Hart, P. M. Duarte, T.-L. Yang, X. Liu, T. Paiva, E. Khatami, R. T. Scalettar, N. Trivedi, D. A. Huse, and R. G. Hulet, *Nature (London)* **519**, 211 (2015).
- [9] J. Simon, W. S. Bakr, R. Ma, M. E. Tai, P. M. Preiss, and M. Greiner, *Nature (London)* **472**, 307 (2011).
- [10] S. Murmann, F. Deuretzbacher, G. Zürn, J. Bjerlin, S. M. Reimann, L. Santos, T. Lompe, and S. Jochim, *Phys. Rev. Lett.* **115**, 215301 (2015).
- [11] M. Płodzień, M. Kościelski, E. Witkowska, and A. Sinatra, *Phys. Rev. A* **102**, 013328 (2020).
- [12] M. Dziurawiec, T. Hernández Yanes, M. Płodzień, M. Gajda, M. Lewenstein, and E. Witkowska, *Phys. Rev. A* **107**, 013311 (2023).
- [13] M. Płodzień, M. Lewenstein, E. Witkowska, and J. Chwedeńczuk, *Phys. Rev. Lett.* **129**, 250402 (2022).
- [14] M. Płodzień, T. Wasak, E. Witkowska, M. Lewenstein, and J. Chwedeńczuk, *arXiv:2306.06173*
- [15] G. Müller-Rigat, A. Aloy, M. Lewenstein, and I. Frérot, *PRX Quantum* **2**, 030329 (2021).
- [16] A. Acín, I. Bloch, H. Buhrman, T. Calarco, C. Eichler, J. Eisert, D. Esteve, N. Gisin, S. J. Glaser, F. Jelezko, S. Kuhr, M. Lewenstein, M. F. Riedel, P. O. Schmidt, R. Thew, A. Wallraff, I. Walmsley, and F. K. Wilhelm, *New J. Phys.* **20**, 080201 (2018).
- [17] J. Eisert, D. Hangleiter, N. Walk, I. Roth, D. Markham, R. Parekh, U. Chabaud, and E. Kashefi, *Nat. Rev. Phys.* **2**, 382 (2020).
- [18] A. Kinos, D. Hunger, R. Kolesov, K. Mā, lmer, H. de Riedmatten, P. Goldner, A. Tallaie, L. Morvan, P. Berger, S. Welinski, K. Karrai, L. Rippe, S. Kröll, and A. Walther, Roadmap for rare-earth quantum computing, *arXiv:2103.15743* [quant-ph] (2021).
- [19] A. Laucht *et al.*, *Nanotechnology* **32**, 162003 (2021).
- [20] C. Becher, W. Gao, S. Kar, C. Marciniak, T. Monz, J. G. Bartholomew, P. Goldner, H. Loh, E. Marcellina, K. E. J. Goh, T. S. Koh, B. Weber, Z. Mu, J.-Y. Tsai, Q. Yan, S. Gyger, S. Steinhauer, and V. Zwiller, *Materials Quantum Techno.* **3**, 012501 (2023).
- [21] J. Fraxanet, T. Salamon, and M. Lewenstein, *arXiv:2204.08905*.
- [22] P. He, M. A. Perlin, S. R. Muleady, R. J. Lewis-Swan, R. B. Hutson, J. Ye, and A. M. Rey, *Phys. Rev. Res.* **1**, 033075 (2019).
- [23] M. Mamaev, I. Kimchi, R. M. Nandkishore, and A. M. Rey, *Phys. Rev. Res.* **3**, 013178 (2021).
- [24] T. Comparin, F. Mezzacapo, M. Robert-de-Saint-Vincent, and T. Roscilde, *Phys. Rev. Lett.* **129**, 113201 (2022).
- [25] T. Hernández Yanes, M. Płodzień, M. Mackoite Sinkevičienė, G. Žilabys, G. Juzeliūnas, and E. Witkowska, *Phys. Rev. Lett.* **129**, 090403 (2022).
- [26] K. Mølmer and A. Sørensen, *Phys. Rev. Lett.* **82**, 1835 (1999).
- [27] K. Gietka, A. Usui, J. Deng, and T. Busch, *Phys. Rev. Lett.* **126**, 160402 (2021).
- [28] H. Bethe, *Z. Phys.* **71**, 205 (1931).
- [29] K. A. Chao, J. Spalek, and A. M. Oles, *J. Phys. C* **10**, L271 (1977).
- [30] K. A. Chao, J. Spalek, and A. M. Oleś, *Phys. Rev. B* **18**, 3453 (1978).
- [31] J. R. Schrieffer and P. A. Wolff, *Phys. Rev.* **149**, 491 (1966).
- [32] S. Bravyi, D. P. DiVincenzo, and D. Loss, *Ann. Phys. (NY)* **326**, 2793 (2011).
- [33] M. Kitagawa and M. Ueda, *Phys. Rev. A* **47**, 5138 (1993).
- [34] D. Kajtoch and E. Witkowska, *Phys. Rev. A* **92**, 013623 (2015).

- [35] S. Campbell, R. Hutson, E. Marti, A. Goban, D. Oppong, R. McNally, L. Sonderhouse, J. Robinson, W. Zhang, B. Bloom, and J. Ye, *Science* **358**, 90 (2017).
- [36] S. L. Bromley, S. Kolkowitz, T. Bothwell, D. Kedar, A. Safavi-Naini, M. L. Wall, C. Salomon, A. M. Rey, and J. Ye, *Nat. Phys.* **14**, 399 (2018).
- [37] P. Bataille, A. Litvinov, I. Manai, J. Huckans, F. Wiotte, A. Kaladjian, O. Gorceix, E. Maréchal, B. Laburthe-Tolra, and M. Robert-de-Saint-Vincent, *Phys. Rev. A* **102**, 013317 (2020).
- [38] A. W. Young, W. J. Eckner, W. R. Milner, D. Kedar, M. A. Norcia, E. Oelker, N. Schine, J. Ye, and A. M. Kaufman, *Nature (London)* **588**, 408 (2020).
- [39] B. M. Spar, E. Guardado-Sanchez, S. Chi, Z. Z. Yan, and W. S. Bakr, *Phys. Rev. Lett.* **128**, 223202 (2022).
- [40] W. Heisenberg, *Z. Phys.* **49**, 619 (1928).
- [41] L.-M. Duan, E. Demler, and M. D. Lukin, *Phys. Rev. Lett.* **91**, 090402 (2003).
- [42] J. Lamers, in *Proceedings of 10th Modave Summer School in Mathematical Physics — PoS(Modave2014)* (Sissa Medialab, 2015).
- [43] M. Gaudin, *The Bethe Wavefunction*, edited by J.-S. Caux (Cambridge University Press, Cambridge, 2014).
- [44] D. J. Wineland, J. J. Bollinger, W. M. Itano, F. L. Moore, and D. J. Heinzen, *Phys. Rev. A* **46**, R6797 (1992).
- [45] Y. Baamara, A. Sinatra, and M. Gessner, *Comptes Rendus. Phys.* **23**, 1 (2022).
- [46] H. Puzskarski, *Surf. Sci.* **34**, 125 (1973).
- [47] E. W. Montroll, *J. Math. Phys.* **10**, 753 (1969).
- [48] K. Lakatos-Lindenberg, R. P. Hemenger, and R. M. Pearlstein, *J. Chem. Phys.* **56**, 4852 (1972).
- [49] G. Juzeliūnas and P. Reineker, *J. Chem. Phys.* **109**, 6916 (1998).





## Chapter 7

# Spin Squeezing under Imperfections and Holes

We have found a very successful scheme when extending the Fermi–Hubbard model with spin orbit coupling in the Mott insulating phase. We achieve OAT and TACT under both PBC and OBC while reducing the risk of particle losses. We can also obtain very similar results for bosons, for which the derivation of the effective models is almost identical. However, spin orbit coupling can be difficult to engineer in the lab when looking for a very precise value of the phase, more so for a geometry that respects PBC. In this chapter, we explore spin squeezing in the Mott insulating phase using bosons by studying two different sources of OAT models: inhomogeneous magnetic fields and anisotropic contact interactions. We work under OBC whenever possible to produce more realistic results with respect to experimental conditions. To validate the robustness of these implementations, we also consider the effects of occupation defects in the form of site vacancies or holes.

The results shown in this chapter are the result of our own research and have been published as:

T. Hernández Yanes, A. Niezgoda, and E. Witkowska, “Exploring spin squeezing in the Mott insulating regime: Role of anisotropy, inhomogeneity, and hole doping”, *Physical Review B* **109**, 214310 (2024).

### 7.1 Squeezing via Contact Interactions in the Mott Insulating Phase

We already made use of anisotropic contact interactions in the superfluid regime to generate squeezing in chapter 5, but it also has a relevant effect in the Mott insulating regime. In this scenario, as explained in section 3.3, in the presence of anisotropy  $\Delta \neq 1$  we obtain the Heisenberg XXZ model as an



effective model of the base Bose–Hubbard model.

$$\hat{H}_{\text{XXZ}} = -J_{\perp} \sum_{i=1}^M \left( \hat{S}_i^x \hat{S}_{i+1}^x + \hat{S}_i^y \hat{S}_{i+1}^y + \Delta \hat{S}_i^z \hat{S}_{i+1}^z \right). \quad (7.1)$$

While this is a well known fact, the key insight becomes apparent when we take into account some of our previous observations while developing our effective models:

- Local spin excitations build up the magnon states, which are excited states of the XXX model.
- If the perturbation does not match with a particular magnon excitation, it might couple to a number of them, if not all.
- These excitations can be produced along any axis, not only perpendicular to the spin quantisation axis.

Given these observations, what would happen if we have a perturbation in our Hamiltonian that excites two spins instead of a single one? The natural conclusion would be the coupling to two-magnon excitations. These states give us an even higher energy manifold than single magnon excitations that can also be exploited to obtain squeezing.

To study the anisotropy as a perturbation at the level of the Heisenberg model, we simply add and subtract terms in our Hamiltonian to recover the XXX model with an extra term  $-J_{\perp}(1-\Delta) \sum_j \hat{S}_j^z \hat{S}_{j+1}^z$ . This term acts as our perturbation.

While two-magnon states are more complicated to solve and in most cases their solution is not exact [105], their eigenenergies are well defined and are sufficient for our purposes. This is because, while we need to be in the perturbative regime, the perturbation already generates a zero-order term that results in an effective OAT model by itself.

$$\hat{H}_{\text{eff}}^{(1)} = \chi^{(1)} \hat{S}_z^2, \quad (7.2)$$

with  $\chi^{(1)} = J_{\perp}(1-\Delta)/(M-1)$ . As we excite all the two-magnon states, we need to fulfil the energy gap condition for the smallest of them or we risk getting out of the perturbative regime. As the smallest energy gap depends on the inverse of the system size, this effect will vanish when  $M \rightarrow \infty$ .

Contribution from second-order processes can be largely ignored as they are much smaller in principle and provides squeezing around the same axis. It can be found that they provide terms  $\propto \hat{S}_z^2$  and  $\propto \hat{S}_z^4$ , but the specific coefficients are difficult to derive.

While this method to generate squeezing disappears when  $M \rightarrow \infty$ , any slight difference in contact interactions will have a relevant effect in the system. Moreover, the smaller this difference is, the faster the squeezing process will

be. This is a relevant effect that needs to be taken into account for realistic setups and also a strong contender in terms of implementation simplicity.

## 7.2 Squeezing via Inhomogeneous Magnetic Field in the Mott Insulating Phase

Another way to experimentally engineer the spin orbit coupling term is to produce a spatially varying magnetic field across the lattice, polarised perpendicularly to the spin quantisation axis. This scheme still suffers from the same problem of achieving a commensurate phase with the lattice, but it gives us an insight on how to make our proposed model more robust: magnon excitations also happen if we polarise the magnetic field along the spin quantisation axis as

$$\hat{H}_B = \sum_{j=1}^M \beta_j \hat{S}_j^z. \quad (7.3)$$

While this might be a soft conceptual realisation, it makes mathematical derivations much more straightforward.

As the spin excitation term is now diagonal in the Fock state basis, there is no need to use the rotated frame to study the virtual transitions. We can instead directly apply perturbation theory to the Hubbard model with eq. (7.3) to retrieve the first effective Hamiltonian for the Mott insulating phase condition, with  $J \ll U_{\sigma,\sigma'}, |\beta_j - \beta_{j+1}|/2 \ll U_{\sigma,\sigma'}; \forall j, \sigma, \sigma'$ . We refer to  $U_{\sigma,\sigma'}$  as the magnitudes of the contact interactions depending on the internal states of the bosons. After that, we obtain the Heisenberg XXZ model with a perturbation in the form of the inhomogeneous magnetic field.

$$\hat{H} = \hat{H}_{\text{XXZ}} + \hat{H}_B. \quad (7.4)$$

To remove the contribution from the two magnon excitations that comes from the anisotropic contact interactions, we choose  $\Delta = 1$  so that our Hamiltonian becomes

$$\hat{H} = \hat{H}_{\text{XXX}} + \hat{H}_B. \quad (7.5)$$

As we discussed, single magnon states can be defined along any axis and in turn this results in an easier derivation of the effective OAT model with respect to the Heisenberg model.

$$\hat{H}_{\text{eff}}^{(2)} = \chi \hat{S}_z^2 + v \hat{S}_z, \quad (7.6)$$

where  $\chi = \sum_q |f_q|^2 / E_q$  with  $f_q$  being the fidelity to the single magnon states with the perturbation and  $v = \sum_j \beta_j / M$ .

If we excite a single magnon of quasi-momenta  $q$ , the perturbative condition will be  $|\beta_j| \ll E_q; \forall j$ . In general, we might be exciting to more single magnon states, so the energy gap can become smaller. However, this also depends



on the exact shape of the inhomogeneous magnetic field, as it might have negligible fidelity with magnon excitations of lower  $q$ .

This guarantees the existence of squeezing for any sufficiently small inhomogeneous magnetic field. For instance, we can even use a random magnetic field and obtain squeezing if the magnitude of the field is, at worst,  $\ll E_{q=1}$ . The setup we propose is both very resilient and sufficiently easy to construct. We thus conclude the inhomogeneous magnetic field is a strong candidate to obtain scalable spin squeezing in the lab.

### 7.3 Effect of hole doping

In this chapter, we have derived effective models under two scenarios, inhomogeneous magnetic field or anisotropy in contact interactions for the Bose-Hubbard model. Both of them yield an effective OAT model with or without a linear term, respectively. However, both results rely on the half-filling condition to fix particles in place. The corresponding  $t$ - $J$  model in the presence of holes

$$\hat{H}_{t-J} = -t \sum_{\langle j,i \rangle} \hat{P}_0^\dagger \left( \hat{a}_j^\dagger \hat{a}_i + \hat{b}_j^\dagger \hat{b}_i \right) \hat{P}_0 + \hat{H}_{\text{XXZ}} + \hat{H}_{\text{B}}, \quad (7.7)$$

where  $t \in \{0, J\}$  and  $\hat{P}_0$  projects into the single occupied states, is difficult to study analytically. We can nevertheless find limiting cases that are easier to analyse to obtain an estimation of the squeezing level we will obtain. In this section we explore such a case where position and number of holes are fixed over time. We will see how they make the dynamics separable into partial chains. The opposite limiting case is when holes move infinitely fast across the lattice and the system acts as if fully filled.

As discussed in previous chapters, when holes are present in the system in the Mott insulating phase, the system maps into a  $t$ - $J$  model, where tunnelling processes are still possible among single occupied states. While the tunnelling rate is the same as before applying perturbation theory, this rate will be larger than the magnitude of the spin exchange term by virtue of the approximation itself. In other words, since  $J \ll U_{\sigma,\sigma'}$ , we obtain  $J \gg J_\perp$ . If we express the evolution of a coherent state in units of  $J_\perp$ , the tunnelling processes will be very quick in comparison. We can picture particles moving across neighbour vacancies, while the spin exchange processes will occur as if no holes were present in the system, up to a filling factor correction. Of course, this does not mean particles move across the lattice without friction like in the superfluid regime. Particles will still block each other from tunnelling to their respective sites as  $U_{\sigma,\sigma'} \gg J$ , but when a particle finds a hole next to its position, it will immediately travel to the next site. This approximation makes sense in the limit where  $U_{\sigma,\sigma'}/J \rightarrow \infty$ .

The opposite limiting case, which is reached due to the perturbation condition, is the case where holes are fixed in certain locations across the lattice



in time. This is a relevant limit of the system, even if idealised, which gives us insight into the dynamics of the  $t$ - $J$  model.

Let us then focus on this particular limiting case of fixed holes. If we look at the Heisenberg model described in previous chapters, we will notice the correlations are nearest neighbour only. If a hole is present in the system, it will simply cancel the effect of any term that interacts with it, isolating the sub-systems bounded by these holes from any other part of the system. We will refer to these sub-systems as partial chains, as illustrated in figs. 7.1 and 7.2. We found these partial chains evolve independently from one another, as the Dicke states or the one and two magnon excitations can all be defined independently for each chain, as explained in section 3.3.

The second moments of the spin operators can introduce problems to this realisation, as they are needed to calculate the co-variances present in the spin squeezing parameter  $\xi^2$  and might account for correlations among partial chains. Nevertheless, the co-variances recover this independent behaviour, so the study of the squeezing parameter can be done within this framework.

Let us now focus on the possible effective models for each partial chain. If the model is generated through anisotropic contact interactions, we obtain a pure OAT model (7.2). The probability distributions of the partial chain represented on the Bloch sphere will mostly overlap in time, with small discrepancies due to the spin length of each partial chain and the coefficient  $\chi$  of each partial chain, which also depends on its length, as illustrated in fig. 7.1.

However, when the model appears as a result of an inhomogeneous magnetic field, a linear term  $v\hat{S}_z$  is present in the partial chain Hamiltonian, as described in eq. (7.6). This implies the mean spin direction will rotate along the equator of the Bloch sphere at a rate  $\propto \cos 2\pi/v$ . As  $v$  changes on each partial chain, the partial chain mean spin directions will rotate at different rates with respect to each other. This is detrimental for squeezing as it inevitably lowers  $\langle \hat{S}_n \rangle$  unless they overlap. Another effect of the magnetic field is that the coefficient  $\chi$  of each sub-system might be different depending on both the partial chain length and the magnetic field itself. In any case, the largest contribution to the loss of squeezing is the misalignment of the mean spin directions, as we demonstrate in fig. 7.2.

In any case, this gives us a semi-analytical model, as each partial chain evolution is analytical but adding them up can be non-trivial.

## 7.4 Movement of holes

In the previous section we mentioned the limiting cases of the model when tunnelling is allowed in the presence of holes: frozen holes during dynamics and infinite effective tunnelling. In this section, we explore numerical results of the corresponding  $t$ - $J$  models, for which we tune the effective tunnelling



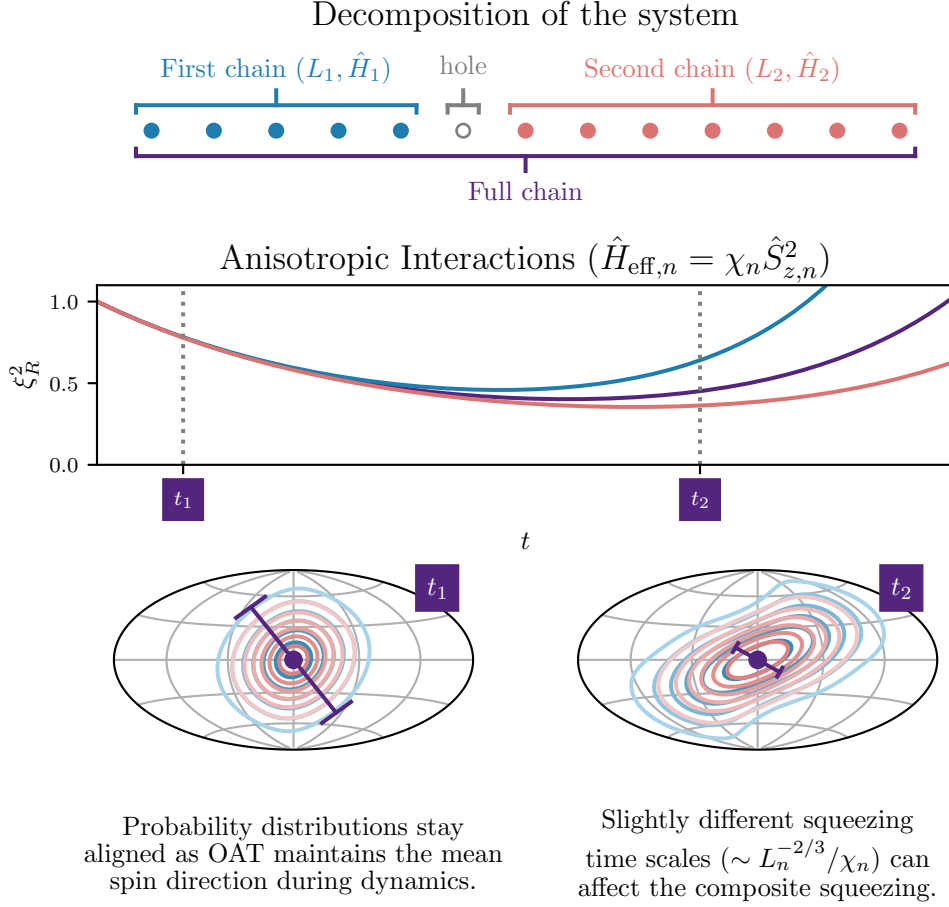


Figure 7.1: Spin squeezing dynamics induced by anisotropy of the contact interactions in the presence of a hole in the system. When the hole is fixed at a given site, we can decompose the system as two independent spin chains. Results for independent chains as well as for the full chain are indicated by different colors, as in the upper diagram. The purple point in the Bloch spheres indicate the mean spin direction of the full chain. The purple brackets that accompany the point indicate the minimal variance  $(\Delta \hat{S}_{\min})^2$  direction and magnitude. We label the partial chains by numbers 1 and 2.  $M = 13, N = 12$ .  $L_1 = N_1 = 5, L_2 = N_2 = 7$ .  $\Delta = 0.98, \beta_j = 0$ .

$t/J_\perp$  from zero (fixed holes) to a large value with respect to the energy scale of the system.

Let us imagine we perform an experiment where we have a fixed number of sites  $M$  and a number of particles  $N$  such that  $N \leq M$ , but the location of the particles in the lattice is completely random for each realisation. After

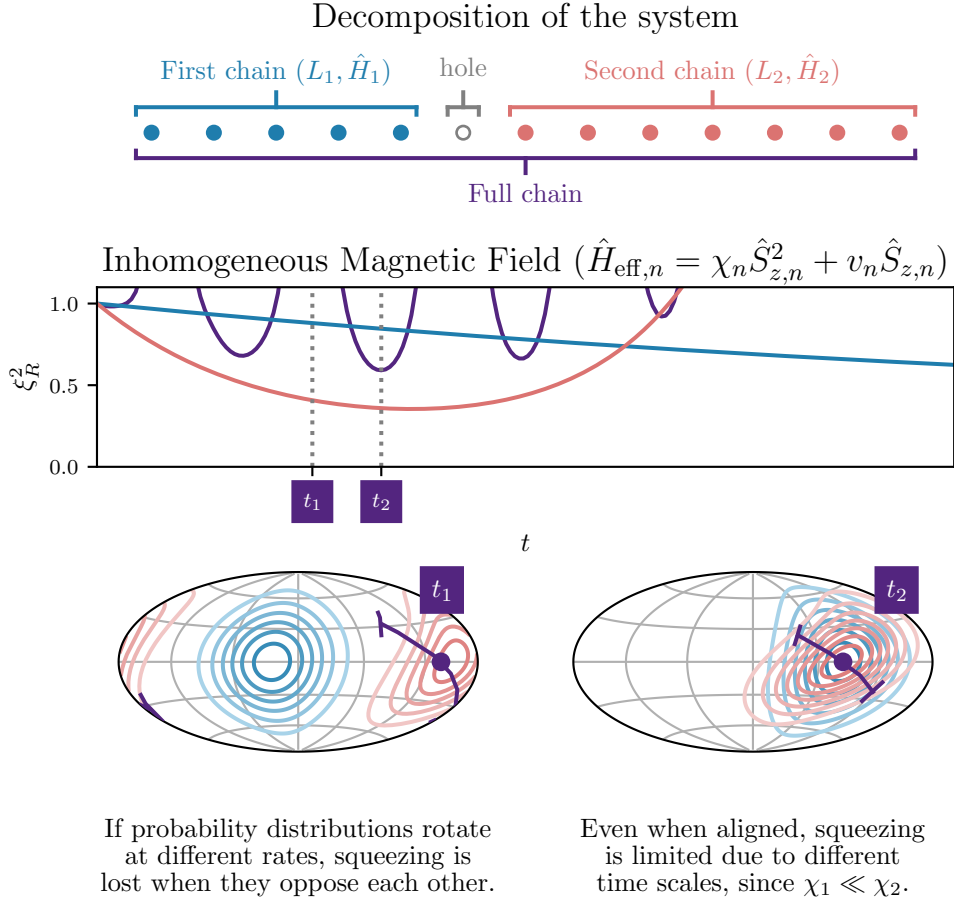


Figure 7.2: Spin squeezing dynamics induced by an inhomogeneous magnetic field in the presence of a hole in the system. When the hole is fixed at a given site, we can decompose the system as two independent spin chains. Results for independent chains as well as for the full chain are indicated by different colors, as in the upper diagram. The purple point in the Bloch spheres indicate the mean spin direction of the full chain. The purple brackets that accompany the point indicate the minimal variance  $(\Delta \hat{S}_{\min})^2$  direction and magnitude. We label the partial chains by numbers 1 and 2.  $M = 13, N = 12$ .  $L_1 = N_1 = 5$ ,  $L_2 = N_2 = 7$ .  $\Delta = 1, \beta_j = E_M^{(M-1)}/50 \cos(\frac{\pi}{M}(M-1)(j-1/2))$ .

averaging over many of them, we will obtain an initial density matrix like

$$\hat{\rho}(0) = \frac{1}{N_{\mathcal{P}}} \mathcal{P} \left( \bigotimes_{j=1}^N |\uparrow_j\rangle\langle\uparrow_j| \bigotimes_{k=M-N}^M |0_k\rangle\langle 0_k| \right), \quad (7.8)$$

where  $\mathcal{P}$  stands for the sum of all possible permutations of  $N$  particles in  $M$



sites and  $N_{\mathcal{P}}$  is the total number of said permutations.

In fig. 7.3 we can see how, in the case of the spin squeezing induced by the inhomogeneous magnetic field, the squeezing is quickly suppressed with the reduction of particles in the system of fixed size  $M$ . Moreover, the time scale of the squeezing seems to grow with the effective tunnelling. These effects can be traced to the presence of a linear term in the effective Hamiltonian, which makes the coherent evolution of the partial chains difficult, even when correlations between them due to tunnelling appear.

On the contrary, the coherent squeezing for the scenario of anisotropic contact interactions is remarkable even in the case where the effective tunnelling is suppressed. The different configurations add up coherently, since the absence of a linear term in the effective Hamiltonian allows for the alignment of the probability distributions of the partial chains. In the cases where effective tunnelling is allowed, the squeezing level immediately jumps very close to the idealised scenario of infinite tunnelling, even for small values. Also, the squeezing is much more resilient to the reduction of the particle number.

Similar conclusions can be drawn from the results reflected in the publication, where we employ a more involved density matrix related to the on-site filling factor. In that case, time scales seem to adhere better to the proposed estimations, but the conclusions about the drastic change for the magnetic field scenario and the resilience of the anisotropic scenario are the same.

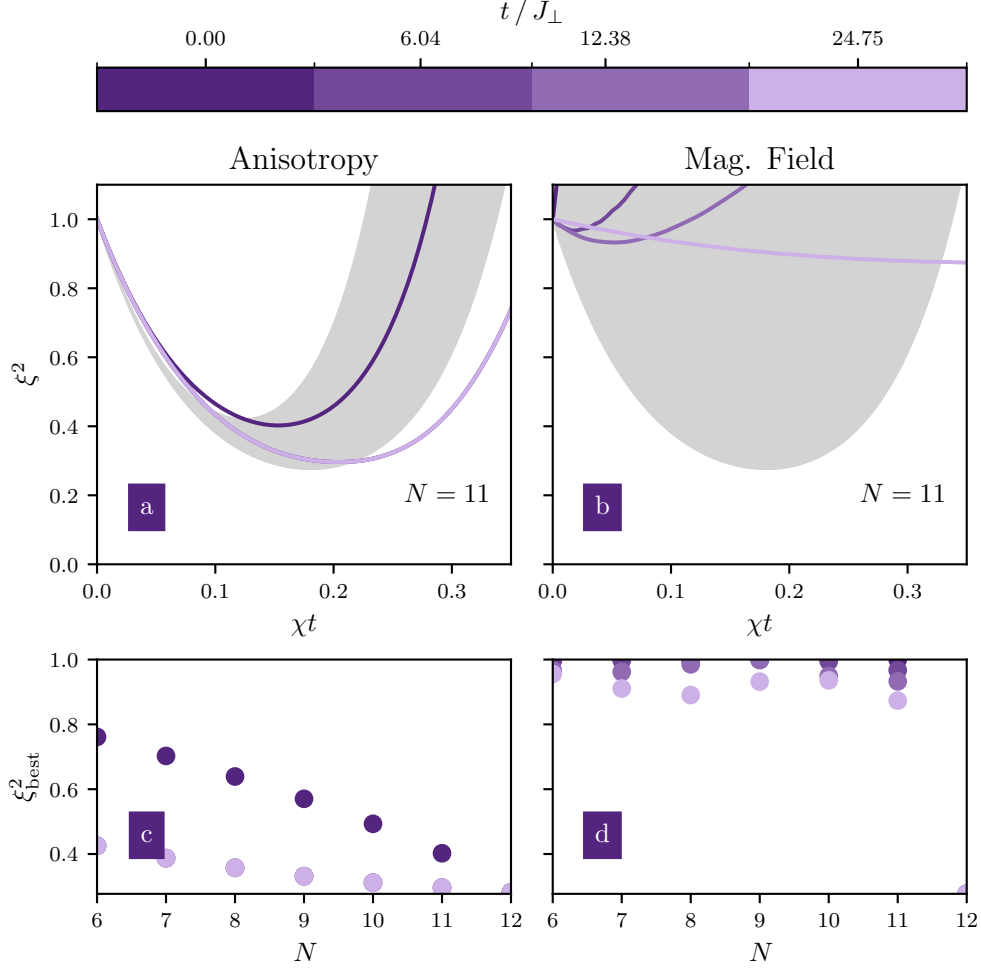


Figure 7.3: Evolution of spin squeezing parameter induced by anisotropy (a) and inhomogeneous magnetic field (b) for different values of the tunnelling rate  $t \in \{0, J\}$  and filling factor  $f$ . In each instance,  $\chi$  is estimated from the corresponding effective models when  $N = M = 12$ . In all cases, the initial state is characterized by the density matrix in eq. (7.8). Grey areas indicate the regions between the semi-analytical upper and lower bounds. The best squeezing  $\xi^2_{\text{best}}$  with respect to  $N$  is shown in (c) and (d) when its generation is governed by anisotropy and inhomogeneous magnetic field, respectively. To tune the effective tunnelling, we fix  $J = 1$  but change  $2U_{ab}/(1 + \Delta) \in \{24.4J, 50J, 100J\}$ , with  $J_{\perp} = J^2/(4U_{ab})$ ,  $U_{aa} = U_{bb} = 2U_{ab}/(1 + \Delta)$ . For the anisotropic case  $\Delta = 0.98, \beta_j = 0$ , while for the magnetic field case  $\Delta = 1, \beta_j = E_M^{(M-1)}/50 \cos(\frac{\pi}{M}(M-1)(j-1/2))$ .



# Exploring spin squeezing in the Mott insulating regime: Role of anisotropy, inhomogeneity, and hole doping

Tanausú Hernández Yanes<sup>1,2,\*</sup>, Artur Niezgoda<sup>3</sup>, and Emilia Witkowska<sup>1</sup>

<sup>1</sup>*Institute of Physics PAS, Aleja Lotnikow 32/46, 02-668 Warszawa, Poland*

<sup>2</sup>*Universität Innsbruck, Fakultät für Mathematik, Informatik und Physik, Institut für Experimentalphysik, 6020 Innsbruck, Austria*

<sup>3</sup>*ICFO - Institut de Ciències Fòniques, The Barcelona Institute of Science and Technology, 08860 Castelldefels, Barcelona, Spain*



(Received 8 May 2024; revised 10 June 2024; accepted 11 June 2024; published 24 June 2024)

Spin squeezing in systems with single-particle control is a well-established resource of modern quantum technology. Applied in an optical lattice clock it can reduce the statistical uncertainty of spectroscopic measurements. Here, we consider dynamic generation of spin squeezing with ultra-cold bosonic atoms with two internal states loaded into an optical lattice in the strongly interacting regime as realized with state-of-the-art experiments using a quantum gas microscope. We show that anisotropic interactions and inhomogeneous magnetic fields generate scalable spin squeezing if their magnitudes are sufficiently small, but not negligible. The effect of nonuniform filling caused by hole doping, nonzero temperature, and external confinement is studied at a microscopic level demonstrating their limiting role in the dynamics and scaling of spin squeezing.

DOI: [10.1103/PhysRevB.109.214310](https://doi.org/10.1103/PhysRevB.109.214310)

## I. INTRODUCTION

Quantum technology is an emerging interdisciplinary field of study that combines the areas of physics, mathematics, and computer science. A prominent resource fueling emergent technologies like quantum simulators, computers and sensing is entanglement [1–4], a concept originating from the quantum mechanics formalism to explain correlations that cannot be reproduced classically. A plethora of useful entanglement-enhanced approaches are examined and spin squeezing is a well-established one [5].

Spin squeezing applies to a system composed of  $N$  qubits, further described by the collective spin with the corresponding quantum number  $S = N/2$ . The uncertainty of spectroscopic measurements of unknown phase  $\varphi$  for a given state is  $\Delta\varphi = \xi/\sqrt{N}$ , where

$$\xi^2 = \frac{N\Delta^2\hat{S}_{\perp\min}}{|\langle\mathbf{S}\rangle|^2} \quad (1)$$

is the spin squeezing parameter while  $\Delta^2\hat{S}_{\perp\min}$  is the minimal variance in the plane orthogonal to the direction of the mean collective spin  $\langle\mathbf{S}\rangle$ , where  $\mathbf{S} = (\hat{S}_x, \hat{S}_y, \hat{S}_z)$  [6,7]. If  $\xi^2 < 1$ , the corresponding state is spin squeezed. However, a remarkable metrological gain is obtained with scalable spin squeezing when its level decreases significantly with the total number of spins.

The archetypal model undergoing such desired scalability is the famous one-axis twisting (OAT) protocol (all-to-all interactions) where the best squeezing scales with the system size as  $\xi_{\text{best}}^2 \propto N^{-2/3}$  [8]. It was simulated with pioneering experiments using bimodal Bose-Einstein [9,10] and spinor

[11–14] condensates utilizing atom-atom collisions and atom-light interactions in cavity setups [15,16]. These platforms, however, weakly support a single-spin addressing and control required very often by quantum technology tasks. There is an increasing interest in generation of spin squeezed states using platforms where individual addressing of spins is possible [17–24]. Recent experiments using an array of trapped ions [25] and Rydberg atoms [26,27] have demonstrated the generation of such scalable squeezing with tens of spins. Ultracold atoms in optical lattices offer yet another platform for scalable spin squeezing generation in a system composed of tens of thousands of spins. It was already considered for spin squeezing generations by utilizing atom-atom collisions for bosons in superfluid regime [18,19,23] and spin-orbit coupling in the Mott phase [20,28,29].

In this paper, we study dynamical generation of scalable spin squeezing with ultracold bosonic atoms in two internal states loaded into a one-dimensional optical lattice. We consider the strongly interacting regime with one atom per lattice site, where the system forms a ferromagnetic Heisenberg XXZ spin chain with nearest-neighbor interactions [30,31]. This is the Mott insulating regime. The anisotropy of the corresponding XXZ spin model is set by intra- and interspecies interactions. When interaction strengths equal each other, the model reduces to the isotropic XXX Heisenberg spin chain. We concentrate on the system and parameters as in the recent experiments with rubidium-87 atoms in the optical lattice, which can be diagnosed using the quantum gas microscope when the nearly single-atom control and resolution were obtained [32].

However, our analytical theory is general and can be applied to trapped ions and molecules when they simulate the same models [33,34].

Even for the simple system considered by us, experimental imperfections may arise such as slight anisotropy of the

\*Contact author: hdez@ifpan.edu.pl

interactions, residual local magnetic fields, hole doping, external trapping effects, or nonzero temperature. They could negatively affect the dynamics of the system. Throughout this work, we found that in most cases, not only these different effects can be accurately accounted for, but in most cases, they are beneficial for spin squeezing generation.

We show analytically, and confirmed numerically, that a weak anisotropy of interactions allows generating scalable spin squeezing from the initial spin coherent state, and the OAT model approximates the dynamics well. While recent work [23] also demonstrates spin squeezing generation through anisotropy, here we strictly define the weak anisotropy regime where scalable spin squeezing can be observed. Beyond that, we evaluate analytically the timescale of the best squeezing showing its experimental feasibility. We show that adding a weak inhomogeneous magnetic field generates scalable spin squeezing by itself, similarly. The coexistence of weak anisotropy and inhomogeneous field does not destroy squeezing generation but smoothly changes the timescale.

We address the problem of hole doping on the generation of spin squeezing. We develop a microscopic theory to explain the change in the variation of the spin squeezing parameter in time due to hole doping. While the squeezing due to anisotropic interactions is weakly affected, the inhomogeneous field introduces subsystem rotations that modulate squeezing over time. This result is proven analytically for the case when holes are fixed in place. We also explore the  $t$ - $J$  model, where tunneling is allowed and identify the upper and lower bounds for the generation of squeezing at a given filling factor. We find in the anisotropy case that squeezing immediately converges to the lower bound result if tunneling is allowed. On the other hand, in the inhomogeneous magnetic field case the squeezing level hardly changes with the effective tunneling. In both cases, the movement of holes facilitates the correlation between individual atoms initially belonging to different partial chains separated by these holes.

The effect of harmonic trapping is also taken into account and even beneficial acceleration of dynamics is observed. Lastly, we explore the effects of nonzero temperature on the squeezing generation of our model. We illustrate our results for the parameters of experiments [32] demonstrating they can be realized with state-of-the-art techniques.

## II. MODEL

We consider  $N$  rubidium-87 atoms in two internal states  $|a\rangle$  and  $|b\rangle$  loaded in an optical lattice potential having  $M$  lattice sites. For simplicity, we consider a one-dimensional lattice with open boundary conditions. The system is described by the two-component Bose-Hubbard model

$$\begin{aligned} \hat{\mathcal{H}}_{\text{BH}} = & -J \sum_{j,i=j\pm 1} (\hat{a}_j^\dagger \hat{a}_i + \hat{b}_j^\dagger \hat{b}_i) \\ & + \frac{U_{aa}}{2} \sum_j \hat{n}_j^a (\hat{n}_j^a - 1) \\ & + \frac{U_{bb}}{2} \sum_j \hat{n}_j^b (\hat{n}_j^b - 1) + U_{ab} \sum_j \hat{n}_j^a \hat{n}_j^b, \end{aligned} \quad (2)$$

in the lowest Bloch band and under the tight-binding approximation [35].  $\hat{a}_j$  ( $\hat{b}_j$ ) is the annihilation operator of an atom in internal state  $a$  ( $b$ ) in the  $j$ th site of the lattice, and  $\hat{n}_j^a = \hat{a}_j^\dagger \hat{a}_j$ ,  $\hat{n}_j^b = \hat{b}_j^\dagger \hat{b}_j$  are the corresponding number operators.  $J$  is the tunneling rate, the same for bosons in the states  $a$  and  $b$ .  $U_{aa}$ ,  $U_{bb}$ , and  $U_{ab}$  are specific intraspecies and interspecies interaction strengths. The model (2) can be realized using a quantum gas microscope [32,36]. We assume interaction dominates over the tunneling strength leaving the system in the Mott insulating regime. In the case of unit filling, one atom per lattice site, the effective Hamiltonian reduces to the Heisenberg XXZ model

$$\hat{H}_{\text{XXZ}} = -J_\perp \sum_{j=1}^{M-1} \left( \hat{S}_j^x \hat{S}_{j+1}^x + \hat{S}_j^y \hat{S}_{j+1}^y + \Delta \hat{S}_j^z \hat{S}_{j+1}^z - \frac{1}{4} \right), \quad (3)$$

where the couplings  $J_\perp = 4J^2 U_{ab}^{-1}$  and anisotropy parameter  $\Delta = U_{ab}/U_{aa} + U_{ab}/U_{bb} - 1$  are derived by second-order perturbation theory in the tunneling [30]. When  $\Delta = 1$  the Hamiltonian takes the form of isotropic Heisenberg XXX model. Here,  $\hat{S}_j^x = (\hat{S}_j^+ + \hat{S}_j^-)/2$ ,  $\hat{S}_j^y = (\hat{S}_j^+ - \hat{S}_j^-)/(2i)$ ,  $\hat{S}_j^z = (\hat{a}_j^\dagger \hat{a}_j - \hat{b}_j^\dagger \hat{b}_j)/2$  with  $\hat{S}_j^+ = \hat{a}_j^\dagger \hat{b}_j$ ,  $\hat{S}_j^- = (\hat{S}_j^+)^\dagger$ . The collective spin operators are just a summation over the individual ones,  $\hat{S}_\sigma = \sum_{j=1}^M \hat{S}_j^\sigma$  for  $\sigma = x, y, z, \pm$ .

The generation of spin squeezing starts with the initial spin coherent state  $|\theta, \varphi\rangle = e^{-i\varphi \hat{S}_z} e^{-i\theta \hat{S}_y} \bigotimes_{j=1}^M |a\rangle_j$  for  $\varphi = 0$  and  $\theta = \pi/2$  followed by unitary evolution with the Hamiltonian (3). Note that the state for  $\varphi = \theta = 0$  is the Dicke state  $|S, m\rangle = \bigotimes_{j=1}^M |a\rangle_j$  for maximal spin quantum number  $S = N/2$  and magnetization  $m = N/2$ . In our numerical simulations, we consider open boundary conditions [29] and use the parameters as in the recent experiment of A. Rubio-Abadal *et al.* [32] with  $^{87}\text{Rb}$  atoms, lattice spacing  $d = 532$  nm, tunneling amplitude  $J = \hbar \times 2\pi \times 24.8$  Hz and almost equal inter- and intraspecies interactions  $U_{aa} \sim U_{bb} \sim U_{ab} = U$  [37] with  $U = 24.4J$ . For the sake of simplicity, timescales will be expressed in tunneling units. The initial state is prepared as a coherent state along the  $x$  direction in the Bloch sphere, namely,  $|\theta = \pi/2, \varphi = 0\rangle$ . Finally, the spin squeezing parameter (1) is evaluated for collective spin operators.

## III. ROLE OF ANISOTROPY

The dynamical generation of spin squeezing is possible by anisotropic interactions, that is when  $\Delta \neq 1$ . We demonstrate this feature in Fig. 1(c) by plotting the best spin squeezing, see also Fig. 3 in Ref. [23]. This numerical observation is confirmed by our perturbative analysis of the system Hamiltonian (3) when the term  $\hat{H}_z = -J_\perp (\Delta - 1) \sum_{j=1}^{M-1} \hat{S}_j^z \hat{S}_{j+1}^z$  is treated as a perturbation to the isotropic XXX model. This leads to the zero-order dominant term of the form

$$\hat{H}_{\text{eff}}^{(0)} = \chi_M^{(0)} \hat{S}_z^2, \quad \text{with} \quad \chi_M^{(0)} = J_\perp \frac{1 - \Delta}{M - 1}, \quad (4)$$

where we omitted constant energy terms. Details of derivation are described in Appendix B. The resulting Hamiltonian (4) is the famous OAT model [8] which dynamics is solvable analytically for any  $N$ . The effective model approximates





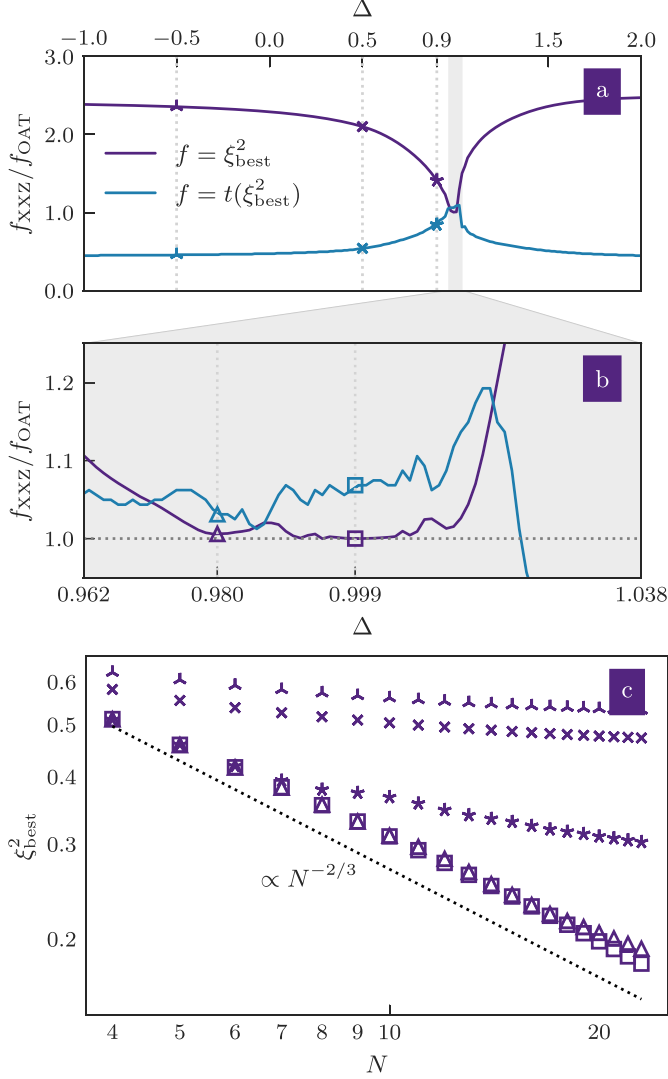


FIG. 1. (a) The ratio  $f$  between results of the XXZ model (3) and the effective one (4) for the best spin squeezing  $\xi_{\text{best}}^2$  (first minima of  $\xi^2$ ) and the best spin squeezing time marked by purple and blue lines, respectively, when  $M = N = 16$  and  $\Delta \in (-1, 1) \cup (1, 2]$ . (b) The same as in (a) but in the perturbative regime enlarged for  $\Delta \in [2 \cos(\pi/N) - 1, 1) \cup (1, 3 - 2 \cos(\pi/N)]$ . (c) The best spin squeezing generated dynamically with the XXZ model (3) for different values of  $\Delta$  (see markers in upper and middle panels) vs  $N$ . A scalable level of squeezing is possible in the perturbative regime marked by triangles and squares.

the dynamics of spin squeezing in the perturbative regime when  $2 \cos(\pi/M) - 1 \ll \Delta \ll 3 - 2 \cos(\pi/M)$  and  $\Delta \neq 1$ . In Appendix D we collect specific analytical expressions for the first and second moments of spin components governed by OAT.

The validity of our analytical finding is demonstrated in Figs. 1(a) and 1(b) by showing the relative level of best squeezing and best squeezing time obtained numerically from the full XXZ model (3) and the effective one (4). Notice the comparison of timescales (blue line) is slightly different than unity in the perturbation regime since we calculate  $\chi_M^{(0)}$  only up to first order. However, the comparison of squeezing level (purple line) is less sensitive to this constraint of

the approximation. For the considered set of parameters, the characteristic timescale for the best squeezing  $\xi_{\text{best}}^2$  is close to the one predicted by the OAT model, namely,  $Jt/\hbar \simeq 3^{1/6}(M-1)N^{-2/3}U_{ab}/(4|1-\Delta|J)$ . It is  $Jt/\hbar \simeq 850$  for  $M = N = 16$ ,  $\Delta = 0.98$ , and  $U_{ab} = 22.2J(\Delta + 1)$ . We found numerically for this set of parameters that the spin squeezing parameter for the OAT model reaches the minima at  $Jt/\hbar \simeq 692$  while for the XXZ model at  $Jt/\hbar \simeq 713$ .

#### IV. INHOMOGENEOUS MAGNETIC FIELD

The addition of an external homogenous magnetic field  $B\hat{S}_z$  to the XXZ model does not spoil spin squeezing generation as long as  $N$  is fixed. It contributes in the same form to the effective Hamiltonian (4) leading to the model  $\hat{H}_{\text{eff}} = \chi_M^{(0)}\hat{S}_z^2 + B\hat{S}_z$  which dynamics is solvable analytically as shown in Appendix D.

Similarly, even a weak inhomogeneous magnetic field

$$\hat{H}_B = \sum_{j=1}^M \beta_j \hat{S}_j^z \quad (5)$$

does not destroy spin squeezing generation but changes the timescale of dynamics. To demonstrate this effect, let us consider the isotropic case when  $\Delta = 1$  with an addition of a weak inhomogeneous magnetic field (5). The second-order correction obtained by using the Schrieffer-Wolff (SW) transformation [28] takes the OAT form

$$\hat{H}_{\text{eff}}^{(2)} = -\chi_M^{(2)}\hat{S}_z^2 + v_M\hat{S}_z, \quad (6)$$

when  $\hat{H}_B$  is treated as a perturbation to the XXX model and where

$$\chi_M^{(2)} = \frac{1}{M-1} \sum_{q=1}^{M-1} \frac{|c_M^{(q)}|^2}{E_M^{(q)}}, \quad (7)$$

$$v_M = \frac{1}{M} \sum_{j=1}^M \beta_j, \quad (8)$$

with

$$c_M^{(q)} = \sum_{j=1}^M p_j^{(q,M)} (\beta_j - v_M), \quad (9)$$

$$p_j^{(q,M)} = \sqrt{\frac{2}{M}} \cos \left[ \frac{\pi}{M} \left( j - \frac{1}{2} \right) q \right], \quad (10)$$

$$E_M^{(q)} = J_{\perp} \left[ 1 - \cos \left( \frac{\pi}{M} q \right) \right], \quad (11)$$

for  $q \in [1, M-1]$ . The derivation is explained in Appendix C. We omitted constant energy terms in (6). The validity of (6) for the dynamical generation of spin squeezing via an inhomogeneous field (5) when  $\Delta = 1$  is demonstrated in Fig. 2. This is an interesting example of when spin squeezing, and therefore two-body correlations between elementary spins, are induced by inhomogeneity. In this case, the mechanism of spin squeezing generation is caused by spin wave excitations which are extended over the entire system allowing individual spin to correlate [29]. It is the same mechanism as for the dynamical generation of spin squeezing via spin-orbit coupling



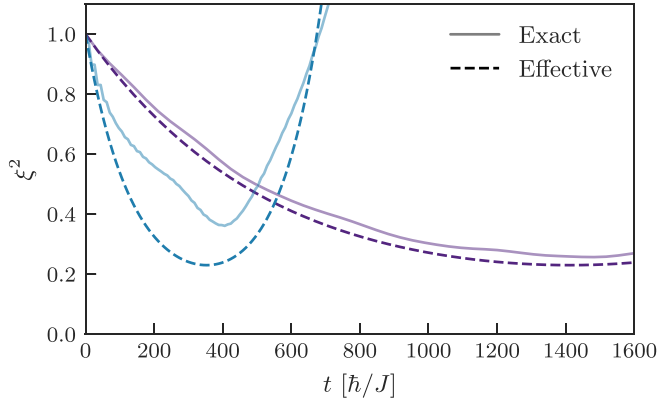


FIG. 2. The spin squeezing parameter  $\xi^2$  for isotropic XXX Heisenberg model with inhomogeneous field  $\hat{H}_B$  and the effective one (6) are marked by solid and dashed lines, respectively. The amplitudes of magnetic field are  $\beta_l = \sqrt{2/M} \cos[\pi(l-1/2)(M-1)/M]$ . Here,  $N = M = 16$ ,  $J = 1$ ,  $U_{aa} = U_{bb} = U_{ab} = U = 24.4J$ ,  $J_\perp = 4\frac{J^2}{U}$ ,  $\Omega = E_M^{(M-1)}/10$  (purple lines) and  $\Omega = E_M^{(M-1)}/5$  (blue lines) with  $E_M^{(M-1)} = J_\perp(1 - \cos(\pi\frac{M-1}{M}))$ .

[20,29]. This means any kind of inhomogeneous magnetic field (constant from shot to shot) will couple to the spin wave states, generating squeezing under the appropriate perturbation conditions. We discuss this point in more detail in Appendix C where we also show other examples when the magnetic field takes a random value on each lattice site. This random potential also leads to the generation of two-body correlations and spin squeezing in the perturbative regime.

## V. DOPING OF HOLES

In this section, we consider an important effect coming from the nonoccupied sites which we call holes. In general, the dynamics is then captured by the  $t$ - $J$  model [38,39] which is the XXZ model with the additional tunneling term. The tunneling leads to the hole movement along the chain. Here, we assume that positions of holes are fixed during unitary dynamics. The approximation is valid in the regime of parameters where the tunneling is strongly suppressed as compared to  $J_\perp$ . The system dynamics can be then approximated by the XXZ model. This allows an understanding of the role of holes at a microscopic level.

Let us first consider the simplest situation with one hole located somewhere in the middle of the chain (not at the borders) as illustrated in Fig. 3. Since the hole is not moving, the configuration can be identified as two independent spin chains with open boundary conditions.

In this case, the collective Dicke state for maximal magnetization containing the hole reads

$$|N/2, N/2\rangle_h = |\uparrow\rangle_{j=1} \cdots |0\rangle_{j=j_h} \cdots |\uparrow\rangle_{j=M}. \quad (12)$$

It can be represented as the product state of two partial Dicke states separated by the empty site,

$$|N/2, N/2\rangle_h = |N_L/2, N_L/2\rangle \otimes |0\rangle_{j_h} \otimes |N_R/2, N_R/2\rangle, \quad (13)$$

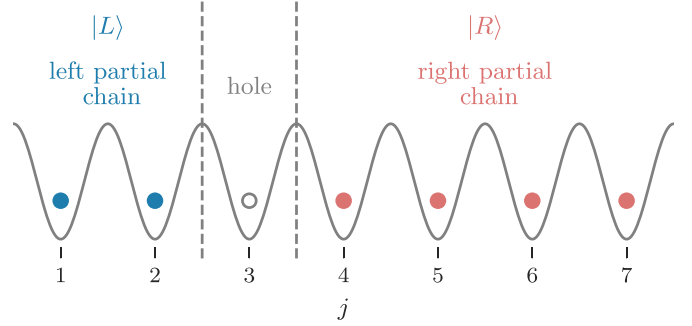


FIG. 3. An example of a configuration with the position of a hole fixed. The hole located at the third lattice site  $j_h = 3$  separates the chain in two parts. The left (right) partial chain consists of two (four) spins. The two partial chains are independent Heisenberg spin chains with open boundary conditions. Their dynamics are independent of each other.

where  $N_L$  is the number of spins on the left-hand side of the hole and  $N_R$  is the number of spins on the right-hand side. The empty site does not contribute to the unitary dynamics driven by the XXZ Hamiltonian with nearest-neighbors interactions. Therefore we will omit the term  $|0\rangle_{j_h}$  when writing the states in the remaining part of the paper.

The initial spin coherent state for  $\varphi = 0$  and  $\theta = \pi/2$  reads  $|t=0\rangle_h = e^{-i\hat{S}_y\pi/2}|N/2, N/2\rangle_h$ . It can be formulated in the following way:

$$|t=0\rangle_h = |L\rangle \otimes |R\rangle, \quad (14)$$

where we have introduced

$$|L\rangle = e^{-i\hat{S}_{y,L}\pi/2}|N_L/2, N_L/2\rangle \quad (15)$$

$$|R\rangle = e^{-i\hat{S}_{y,R}\pi/2}|N_R/2, N_R/2\rangle, \quad (16)$$

and used  $\hat{S}_y = \hat{S}_{y,L} + \hat{S}_{y,R}$  with  $L(R)$  summing up over the left(right)-hand part of the chain.<sup>1</sup>

The dynamics of each partial chain (left and right) is independent of each other, and therefore the evolution of the initial state of the system can be considered as

$$|\psi(t)\rangle_h = \hat{U}_L|L\rangle \otimes \hat{U}_R|R\rangle, \quad (17)$$

where the unitary operators are  $\hat{U}_L = \hat{P}_L e^{i\hat{H}_L t/\hbar} \hat{P}_L$  and  $\hat{U}_R = \hat{P}_R e^{i\hat{H}_R t/\hbar} \hat{P}_R$  with  $\hat{P}_L$  ( $\hat{P}_R$ ) being the projector operator on the left (right) partial chain for a given Hamiltonian  $\hat{H}$  containing nearest-neighbors interactions only.

The dynamics of partial chains is well approximated by effective OAT-like models for a weak anisotropy (4) and inhomogeneous magnetic field (6) as we discussed in two previous sections. However, evolution operators acting on the left and right partial spin chains need to be constructed appropriately.

<sup>1</sup>Here,  $\hat{S}_{\sigma,L} = \sum_{j=1}^{N_L} \hat{S}_j^\sigma$  and  $\hat{S}_{\sigma,R} = \sum_{j=1}^{N_R} \hat{S}_{N_L+1+j}^\sigma$ .



### A. Unitary evolution for partial chains for weak anisotropic interactions

The effective model in the weak anisotropy limit when  $2\cos(\pi/M) - 1 \ll \Delta \ll 3 - 2\cos(\pi/M)$  and  $\Delta \neq 1$  reads

$$\hat{H}_{\text{eff},L}^{(0)} = -\chi_L^{(0)} \hat{S}_{z,L}^2, \quad (18)$$

for the left partial chain with  $\chi_L^{(0)} = J_\perp(\Delta - 1)/(N_L - 1)$  and the same for the right partial chain when  $L$  is replaced with  $R$ . Therefore the unitary operator describing the dynamics with the hole for the left partial chains is  $\hat{U}_L = e^{-i\hat{H}_{\text{eff},L}^{(0)}t/\hbar}$  and similarly for the right partial chain when  $L$  is replaced with  $R$ .

### B. Unitary evolution for partial chains for weak inhomogeneous magnetic fields

On the other hand, if spin squeezing is generated entirely by the inhomogeneous magnetic field (5) for  $\Delta = 1$  the following effective model can well approximate the dynamics of the left partial chain

$$\hat{H}_{\text{eff},L} = \chi_L \hat{S}_{z,L}^2 + v_L \hat{S}_{z,L}, \quad (19)$$

with

$$\chi_L = \frac{1}{N_L - 1} \sum_{q=1}^{N_L-1} \frac{|c_L^{(q)}|^2}{E_L^{(q)}}, \quad (20)$$

$$v_L = \frac{1}{N_L} \sum_{l=1}^{N_L} \beta_l, \quad (21)$$

where

$$c_L^{(q)} = \frac{\sqrt{2}}{N_L} \sum_{l=1}^{N_L} p_l^{(q,L)} (\beta_l - v_L). \quad (22)$$

For convenience, we have redefined

$$p_j^{(q,k)} = \sqrt{\frac{2}{L_k}} \cos \left[ \frac{\pi}{L_k} \left( j - \left( l_k - \frac{1}{2} \right) \right) q \right], \quad (23)$$

$$E_k^{(q)} = J_\perp \left[ 1 - \cos \left( \frac{\pi}{L_k} q \right) \right], \quad (24)$$

where  $k$  is the index of the partial chain,  $l_k$  is its starting site,  $L_k$  is its length and  $q \in [1, L_k - 1]$ .

The form of the effective model (19) for the right partial chain is the same when one replaces  $L$  with  $R$  and where

$$v_R = \frac{1}{N_R} \sum_{l=N_L+2}^{N_R} \beta_l \quad (25)$$

$$c_R^{(q)} = \frac{\sqrt{2}}{N_R} \sum_{l=1}^{N_R} p_l^{(q,R)} (\beta_{N_L+1+l} - v_R). \quad (26)$$

The corresponding unitary operator describing the system dynamics of the initial state (14) is  $\hat{U}_{L(R)} = e^{-i\hat{H}_{\text{eff},L(R)}t/\hbar}$ .

### C. Evaluation of spin squeezing parameter

To calculate the evolution of the spin squeezing parameter (1) one can use the approximated effective models as long as the system parameters are in the perturbative regime. This simplifies the calculations and enables the simulation

of large systems unattainable by exact many-body numerical simulations.

To demonstrate the validity of our treatment of the system dynamics with hole doping, let us start with a general treatment of the first and second moments of spin operators that are necessary for calculations of  $\xi^2$ . The unitary evolution of first moments separates into two parts, e.g., if  $\hat{X} = \hat{X}_L + \hat{X}_R$ , we have

$$\langle \hat{X}(t) \rangle_h = \langle \hat{X} \rangle_L + \langle \hat{X} \rangle_R, \quad (27)$$

where subscript  $L$  ( $R$ ) refers to the left (right) partial chain.  $\langle \hat{X}(t) \rangle_h$  is a sum over the two partial chains, each evolved with the corresponding unitary operator. On the other hand, an expectation value of second moments is separated into four parts, e.g.,  $\hat{X}\hat{Y} = (\hat{X}_L + \hat{X}_R)(\hat{Y}_L + \hat{Y}_R)$ , and reads

$$\langle \hat{X}\hat{Y}(t) \rangle_h = \langle \hat{X}\hat{Y} \rangle_L + \langle \hat{X}\hat{Y} \rangle_R + \langle \hat{X} \rangle_L \langle \hat{Y} \rangle_R + \langle \hat{X} \rangle_R \langle \hat{Y} \rangle_L. \quad (28)$$

Each term in  $\langle \hat{X}\hat{Y}(t) \rangle_h$  evolves with the unitary operator marked by the subscript  $L$  or  $R$ . While (28) shows an apparent interconnection between partial chains, the covariance  $\Delta(\hat{X}\hat{Y})_h^2 = \langle \hat{X}\hat{Y} \rangle_h^2 - \langle \hat{X} \rangle_h \langle \hat{Y} \rangle_h$  turns out to be simply additive

$$\Delta(\hat{X}\hat{Y})_h^2 = \Delta(\hat{X}\hat{Y})_L^2 + \Delta(\hat{X}\hat{Y})_R^2. \quad (29)$$

According to the definition (1), this means that spin squeezing is immediately reduced when the system is broken into partial chains, however, the minimal variance can be optimal when the probability distributions of the partial chains add up appropriately.

We illustrate this observation in Fig. 4. One can observe a good agreement between full many-body numerical calculations (solid lines) and approximated effective dynamics (dashed lines) as described in Secs. VA and VB. In the anisotropy case, shown in Fig. 4(b), the partial chains obey Hamiltonian (18) which maintains the mean spin direction across the short time dynamics. Thus the main effect in the suppression of squeezing is due to the reduction of the collective mean spin. There is a secondary effect in the broadening of the minimal variance when the squeezing timescales of the partial chains differ (i.e.,  $\chi_L^{(0)} \neq \chi_R^{(0)}$ ).

On the other hand, the results for spin squeezing in the presence of an inhomogeneous magnetic field (19) includes a linear term that makes the probability distribution of each partial chain rotate around the  $\hat{S}_z$  axis at different velocities. This creates oscillations in the squeezing parameter due to the misalignment of the partial mean spin directions, as illustrated in Fig. 5. This feature is further discussed in Appendix F.

Generalization of these results to any number and configurations of fixed holes is straightforward, as detailed explained in Appendix E.

### D. Effective bounds when movement of holes is allowed

In the previous sections, we assumed the positions of particles and holes were fixed. However, a realistic scenario includes particle movement as stated in this section's beginning. The dynamics is then well captured by the  $t$ - $J$  model:

$$\hat{H}_{t-J} = -t \sum_{i,j=i\pm 1} \hat{P}_0(\hat{a}_i^\dagger \hat{a}_j + \hat{b}_i^\dagger \hat{b}_j) \hat{P}_0 + \hat{H}_{\text{XXZ}}, \quad (30)$$

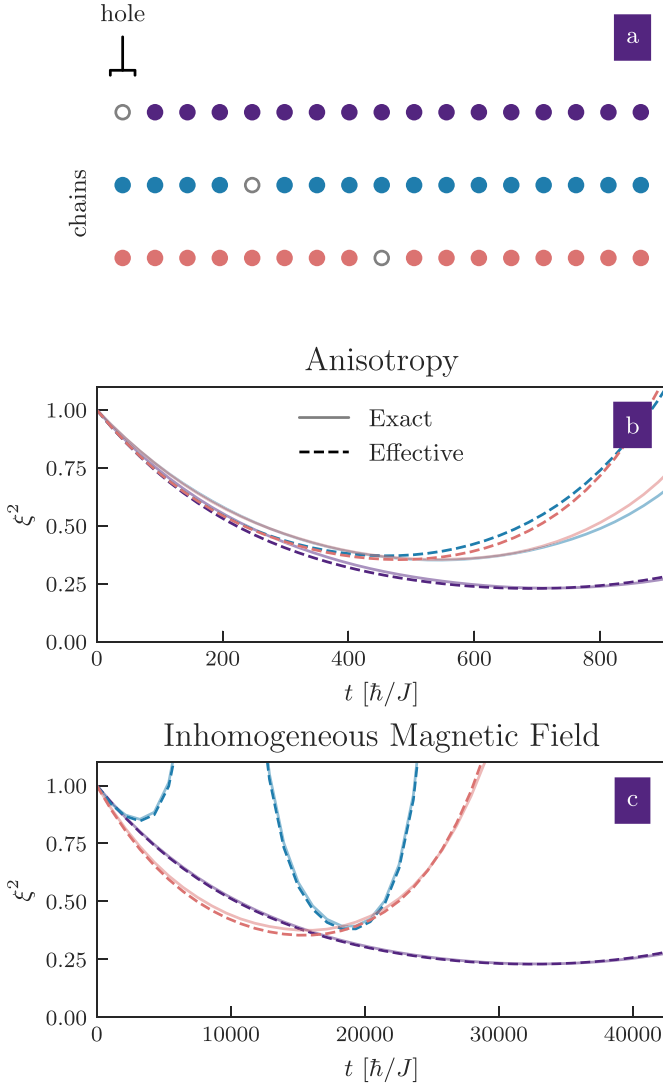


FIG. 4. (a) Configuration of holes for results shown in bottom panels. The spin squeezing parameter induced by anisotropy (b) and inhomogeneous magnetic field (c) for the system with  $N = 16$  atoms and a single hole ( $M = 17$ ) at different sites as indicated by color. The results from the exact many-body simulation are depicted in solid lines while the ones given by the effective models are depicted in dashed lines, respectively. In the anisotropic case,  $U_{aa} = U_{bb} = 24.4J$ ,  $U_{ab} = 0.99U_a$  ( $\Delta = 0.98$ ),  $\beta_j = 0; \forall j$ . In the inhomogeneous magnetic field case,  $U_a = U_b = U_{ab} = 24.4J$ ,  $\beta_j = \Omega \cos(\frac{\pi}{M}(M-1)(j-1/2))$ , where  $\Omega = E_M^{(M-1)}/50 = J_{\perp}(1 - \cos(\frac{\pi}{M}(M-1)))/50$ .

where  $\hat{P}_0$  is a projector operator over the manifold's ground states (i.e., single occupancy). We define  $t \in [0, J]$  to maintain the usual notation of the  $t$ - $J$  model. The evolution of a system is constrained to single occupied states but where particles can tunnel will be trivially bounded by two scenarios: no tunneling and infinite tunneling. The absence of tunneling,  $t = 0$  in (30), is equivalent to a system where the holes are pinned down in fixed sites. Meanwhile, when tunneling is effectively infinite, the system will behave as if fully occupied with a certain filling factor  $f$  per site. Tunneling is effectively infinite for a given timescale when the rest of the terms are energetically much smaller. For instance, an increase in contact interactions in Eq. (3) will in turn decrease  $J_{\perp}$ , increasing

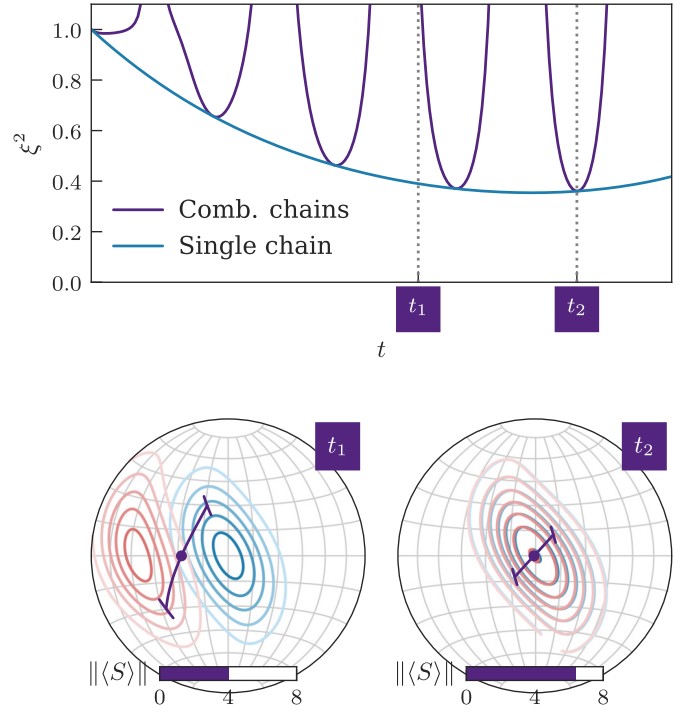


FIG. 5. Modulation of spin squeezing dynamics for two partial chains, each with  $N = 8$ , due to asynchronous rotation around the  $\hat{S}_z$  axis. Both partial chains  $L$  and  $R$  obey the Hamiltonian (19) where  $\chi_L^{(0)} = \chi_R^{(0)} = \chi$  but  $v_R - v_L = 100\chi$ . ( $t_1$ ) The Husimi distribution with respect to coherent states of the partial chains ( $Q(\theta, \phi) = |\langle \psi_{L(R)}(t) | \theta, \phi \rangle|^2$ ) is drawn over the Bloch sphere in different colors at time  $t_1$ . The collective mean spin (lower bar) is reduced and the minimal variance (purple bracket) increases when the probability distributions separate. ( $t_2$ ). At times  $t \propto 2\pi/(v_R - v_L)$ , the probability distributions overlap, maximizing the mean spin and reducing the minimal variance.

the timescale of the effective OAT model but making the tunneling more prevalent.

As a result, an increase in effective tunneling will transform the evolution from the fixed holes scenario to the infinite tunneling scenario. We examined the scenario of fixed holes in previous sections. The analytical result for the infinite tunneling scenario is exactly the OAT model but expectation values are modulated by the filling factor. This is the lower bound for spin squeezing. In any intermediate cases with the holes tunneling spin squeezing would be worse, depending on the energy scales ratio  $t/J_{\perp}$ .

To illustrate this process, we consider a simple statistical ensemble of  $N_r$  realizations where the initial state has a fixed number of particles  $N$  in a lattice of  $M$  sites with  $N < M$ ,

$$\hat{\rho}(0) = \frac{1}{N_r} \sum_{r=1}^{N_r} \left[ \bigotimes_{j=1}^M |\Psi_x\rangle \langle \Psi_x|_j \right], \quad (31)$$

where over set of on-site random numbers  $r \in \{x_1, x_2, \dots, x_{N_r}\}$ . Each state in (31) is

$$|\Psi_x\rangle_j = \bar{\theta}(f - x_j) |\uparrow\rangle_j + (1 - \bar{\theta}(f - x_j)) |0\rangle_j, \quad (32)$$

where  $\bar{\theta}(x)$  is the Heaviside step function and  $x_j \in (0, 1]$  is an independent random number different for each lattice site. If



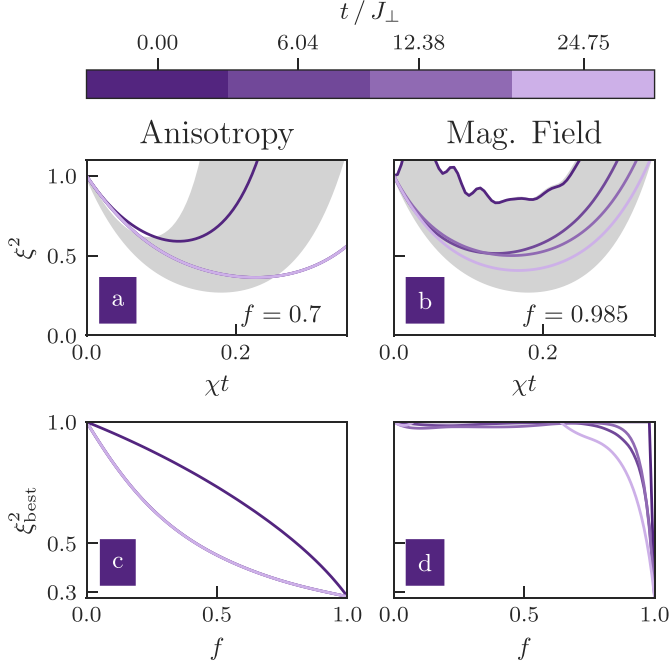


FIG. 6. The evolution of spin squeezing parameter on the  $t$ - $J$  model (30) induced by anisotropy (a) and inhomogeneous magnetic field (b) for different values of  $t/J_{\perp}$  indicated in the colorbar and fixed filling factor  $f$  indicated in the panels. For each instance,  $\chi$  is estimated as the corresponding parameter of effective models (4), (6) when  $N = M = 12$ . Grey areas indicate the regions between the semianalytical upper and lower bounds, as explained in the text. The best squeezing  $\xi_{\text{best}}^2$  versus filling factor  $f$  is shown in (c) and (d) when its generation is governed by anisotropy and inhomogeneous magnetic field, respectively. To tune the effective tunneling, we fix  $J = 1$  but change  $2U_{ab}/(1 + \Delta) \in \{24.4J, 50J, 100J\}$ , with  $J_{\perp} = J^2/(4U_{ab})$ ,  $U_{aa} = U_{bb} = 2U_{ab}/(1 + \Delta)$ . For the anisotropic case,  $\Delta = 0.98$ ,  $\beta_j = 0$ , while for the magnetic field case,  $\Delta = 1$ ,  $\beta_j = E_M^{(M-1)}/50 \cos(\frac{\pi}{M}(M-1)(j-1/2))$ .

$x_j \leq f$ , then the site is occupied by an atom while if  $x_j > f$  the site is empty resulting in a hole at that lattice site. In this way, we represented the presence of holes within the lattice by the filling factor  $f$ . Next, the state corresponding to each realization  $r$  is rotated to form the spin coherent state for  $\varphi = 0$  and  $\theta = \pi/2$ ,  $|t=0\rangle_r = e^{-i\delta_y \pi/2} [\bigotimes_{j=1}^M |\Psi_x\rangle \langle \Psi_x|_j]$ , and unitary evolution is applied with the  $t$ - $J$  model. To tackle the dynamics, we employ a semianalytical approach. We analytically determine the dynamics of individual realizations using microscopic models developed in previous sections but we treat the statistical ensemble numerically. This set the upper bound for spin squeezing at a given filling factor.

In Fig. 6, we compare the results for spin squeezing generation using anisotropy and inhomogeneous magnetic field when  $M = 12$ . Since the effective model for the anisotropic case (4) lacks a linear term, the addition of multiple configurations of partial chains does not destroy squeezing and the inclusion of effective tunneling immediately provides results close to the theoretical bound given by the OAT model.<sup>2</sup>

<sup>2</sup>In the infinite tunneling limit, the effective model describing the dynamics is the OAT one with expectation values modulated by the

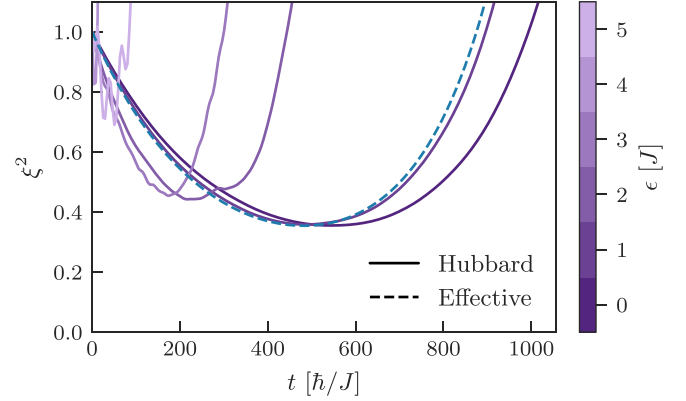


FIG. 7. The effect of external harmonic trapping potential  $\hat{V}_{\text{ext}}$  on the spin squeezing dynamics obtained by numerical simulations from the two-component Bose-Hubbard model (2) in the Mott insulating phase compared to the effective model (4).  $M = N = 8$ ,  $J = 1$ ,  $U_{aa} = U_{bb} = 24.4J$ , and  $U_{ab} = 0.99U_a$  ( $\Delta = 0.98$ ). Solid line colors correspond to different values of  $\epsilon$ . The perturbation condition in this case is  $\epsilon < 1.86J$ .

This contrasts with the inhomogeneous magnetic field case, where presence of a linear term in its effective model (6) illustrates the difficulty in achieving the infinite tunneling limit in this case. Since each configuration of holes returns a different velocity, we can picture an overlap between probability distributions as in Fig. 5, but many of them move at different speeds.

## VI. EFFECT OF EXTERNAL CONFINEMENT

Up to now, we considered a homogeneous system with open boundary conditions. In this section, we show how the best squeezing time is tuned by an external harmonic potential without compromising the squeezing level, up to a certain threshold. To be specific, we focus our attention on the simplest case with weak anisotropy,  $\Delta \neq 1$ , without a magnetic field or holes.

The external trapping potential can be described in the second quantization form as

$$\hat{V}_{\text{ext}} = \epsilon \sum_{j=1}^M \left( j - \frac{M+1}{2} \right)^2 (\hat{n}_j^a + \hat{n}_j^b), \quad (33)$$

where  $\epsilon = m\omega^2/2$  is the strength of the effective harmonic confinement with  $m$  being the particle mass and  $\omega$  the trapping frequency. Typically, the harmonic confinement is much smaller than the hopping rate,  $\epsilon/J \lesssim 0.01$  [40].

In fact, as long as  $J \ll U_{\sigma\sigma'}$ ,  $\epsilon < \min(U_{\sigma\sigma'}/2 - J, U_{ab} - J)/(M-2)$ , double occupancy is unlikely and the effective OAT model (4) well approximates the dynamics. In Fig. 7, we illustrate the regimes above and below this threshold for a given set of parameters. For small values of  $\epsilon$  the influence of the trapping potential is weak and only accelerates slightly the squeezing dynamics. On the other hand, a large  $\epsilon$  means

filling factor  $f$ . This is an itinerant bosons limit where lattice barriers lose their role and atoms move freely along the system.



a promotion of double or larger occupied states, affecting the squeezing level as well. In the limit case of trapping potential frequency of the order of individual lattice sites, the indistinguishability of individual spins is lost (all bosons located in a single lattice site), and our description is not valid. In this limit, the system is effectively bimodal. It is relevant to remark that at such a trapping strength, the system might actually also promote particles to higher bands outside the lattice [41].

## VII. NONZERO TEMPERATURE

Thermal fluctuations limit the best squeezing achievable in two-component Bose-Einstein condensates [42,43]. The same can be expected in the lattice system. To illustrate the effect we performed exact many-body numerical simulations. We consider the isotropic Heisenberg XXX model,  $\Delta = 1$ , exposed to the weak inhomogeneous field with  $\hat{H}_B = \Omega/2 \sum_{j=1}^M (e^{i\phi_j} \hat{S}_j^+ + e^{-i\phi_j} \hat{S}_j^-)$ ,  $\phi = 2\pi/M$  and periodic boundary conditions as in Ref. [28]. To observe spin squeezing, we choose the Gibbs state characterized by temperature  $T$  as the initial state of the dynamics:

$$\rho_T = \sum_{q=0}^{N-1} \frac{e^{-E_q/k_B T}}{Z} |q\rangle \langle q| \quad (34)$$

next rotated with  $\hat{R} = e^{-i\hat{S}_y \pi/2}$ , namely,

$$\hat{\rho}_R = \hat{R}^\dagger \hat{\rho}_T \hat{R} \quad (35)$$

to create the initial spin coherent state with  $\varphi = 0$  and  $\theta = \pi/2$ . In (34), the ground state is the Dicke state  $|q=0\rangle = |N/2, N/2\rangle$  with  $E_0 = 0$ , and higher energy states are spin wave states  $|q\rangle$  given by

$$|q\rangle = \frac{1}{\sqrt{N}} \sum_{l=1}^N e^{iqj2\pi/N} \hat{S}_l^- |N/2, N/2\rangle, \quad (36)$$

with periodic boundary conditions considered for this specific calculation, and where  $q = 2\pi n/N$  and  $n = \pm 1, \pm 2, \dots, \pm(N/2 - 1), N/2$ . The states  $|q\rangle$  are eigenstates of the total spin operator and its projection with the energy  $E_q = J_\perp [1 - \cos(2\pi q/N)]$ . The thermally populated states are the lowest energy states of the  $\hat{H}_{XXX}$  Hamiltonian which are spin-wave states. The form (34) is justified for  $k_B T \ll |E_{q=N/2}|$  when the temperature is much smaller than the largest energy gap when the occupations of the higher energy states are negligible.

In Fig. 8, we show numerical results for various temperatures. Admixture of higher energy states influences spin squeezing dynamics and lowers the best squeezing generated in the system while the best squeezing time is shortened. However, as long as the temperature is much smaller than the smallest energy gap,  $k_B T \ll E_{q=1}$  the effect is negligible as demonstrated in Fig. 8. However, a detailed description of this effect goes beyond this work.

## VIII. SUMMARY AND CONCLUSIONS

We study the generation of scalable spin squeezing with ultra-cold bosonic atoms in optical lattices in the Mott regime. This is possible through two main mechanisms related to

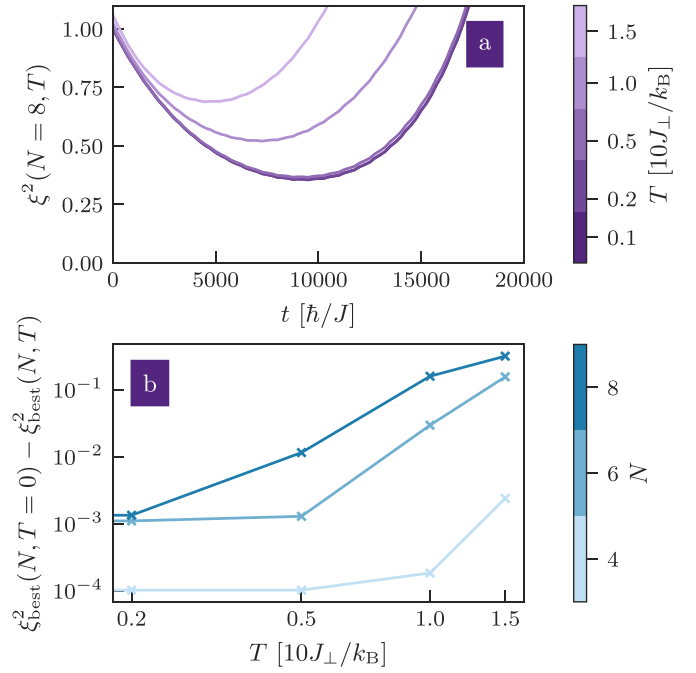


FIG. 8. An illustration of the effect of nonzero temperature on the spin squeezing parameter. (a) The variation of the spin squeezing parameter in time for various temperatures is indicated in the legend. The smallest energy gap is  $J_\perp(1 - \cos(2\pi/N)) \approx 0.29J_\perp$  and  $\Omega = 0.01J_\perp$ . (b) A difference between the best spin squeezing for zero and nonzero temperatures.

imperfections in the system: anisotropy of contact interactions and inhomogeneous magnetic fields.

We develop the microscopic theory to predict the dynamics of the spin squeezing parameter in the presence of hole doping in the simplified scenario when the positions of holes are fixed. In the more general  $t-J$  model, where a hole moves freely along the chain, the correlations in the system are bounded between the cases of zero and infinite effective tunneling. The first case was considered by us in this paper at the microscopic level. In the second case, the movement of holes allows correlation of individual spins and, hence, the system behaves as fully occupied but the expectation values are modulated by the filling factor  $f$ . Additionally, we address numerically the question of the effect of external confinement and thermal fluctuations. While external trapping potential accelerates spin squeezing dynamics, nonzero temperature diminishes the level of squeezing. However, in the latter case, the effect is negligible as long as the temperature value is much smaller than the smallest energy gap.

We believe our analysis sheds more light on the practical limitations of spin squeezing strategy for quantum technology tasks with ultracold atomic systems using a quantum gas microscope, or even trapped ions or molecules. However, we are aware that a transition from science to technology takes time and would happen when the quantum advantage outweighs the complexity of the experiments which are still under very extensive development. For example in the case of squeezed light, it took more than forty years for the successful application of entanglement-enhanced detection of gravitational waves [44,45].



## ACKNOWLEDGMENTS

We gratefully acknowledge discussions with Bruno Laburthe-Tolra, Martin Robert-de-Saint-Vincent, Alice Sinatra, Youcef Bamaara and Manfred Mark. This work was supported by the Polish National Science Center DEC-2019/35/O/ST2/01873. T.H.Y acknowledges support from the Polish National Agency for Academic Exchange through the Foreign Doctoral Internship Grant NAWA Preludium BIS 1 No. PPN/STA/2021/1/00080. A part of the computations was carried out at the Centre of Informatics Tricity Academic Supercomputer & Network. A. N. was supported by Government of Spain (Severo Ochoa CEX2019-000910-S, TRANQI, European Union NextGenerationEU PRTR-C17.II), European Union (PASQuanS2.1, 101113690) and the ERC AdG CERQUITE.

### APPENDIX A: DERIVATION OF THE XXZ MODEL IN THE PRESENCE OF ANISOTROPY AND INHOMOGENEOUS MAGNETIC FIELD

We start our derivation from the two-component Bose-Hubbard Model for open boundary conditions with the addition of an inhomogeneous magnetic field

$$\hat{H} = \hat{H}_{\text{BH}} + \hat{H}_{\text{B}}, \quad (\text{A1})$$

where

$$\begin{aligned} \hat{H}_{\text{BH}} = & -J \sum_{j,i=j\pm 1} (\hat{a}_j^\dagger \hat{a}_i + \hat{b}_j^\dagger \hat{b}_i) + \frac{U_{aa}}{2} \sum_j \hat{n}_j^a (\hat{n}_j^a - 1) \\ & + \frac{U_{bb}}{2} \sum_j \hat{n}_j^b (\hat{n}_j^b - 1) + U_{ab} \sum_j \hat{n}_j^a \hat{n}_j^b, \end{aligned} \quad (\text{A2})$$

$$\hat{H}_{\text{B}} = \sum_{j=1}^M \beta_j \hat{S}_j^z. \quad (\text{A3})$$

In fact, it does not have to be a magnetic field, it can be any other coupling that leads to the position-dependent external potential. Notice  $\hat{S}_j^z = (\hat{n}_j^a - \hat{n}_j^b)/2$ , so the local magnetic field is diagonal with respect to the Fock states.

The Bose-Hubbard Hamiltonian commutes with the total number of particles in each component  $[\hat{H}_{\text{BH}}, \hat{N}_\sigma] = 0$ , where  $\hat{N}_\sigma = \sum_j \hat{n}_{\sigma,j}$  with  $\sigma = a, b$ , but it does not commute with the occupation numbers  $\hat{n}_{a,j}$ ,  $\hat{n}_{b,j}$  of the  $j$ th site, due to the presence of the hopping terms. We address the case where the total filling is commensurate with the lattice.

We consider the system in the Mott phase when interaction dominates over the tunneling strength. In the Mott regime, the system Hamiltonian is well described by the following model:

$$\begin{aligned} \hat{H} = & - \sum_{j=1}^{N-1} \left[ J_{aa} \hat{n}_j^a \hat{n}_{j+1}^a + J_{bb} \hat{n}_j^b \hat{n}_{j+1}^b + J_{ab} \hat{n}_j^a \hat{n}_{j+1}^b \right. \\ & \left. + J_{ab}^+ \hat{n}_j^b \hat{n}_{j+1}^a + J_\perp \frac{1}{2} (\hat{S}_j^+ \hat{S}_{j+1}^- + \hat{S}_j^- \hat{S}_{j+1}^+) \right] + \hat{H}_{\text{B}}, \end{aligned} \quad (\text{A4})$$

where

$$J_{aa} = \frac{4J^2 U_{aa}}{U_{aa}^2 - (\beta_j - \beta_{j+1})^2}, \quad (\text{A5})$$

$$J_{bb} = \frac{4J^2 U_{bb}}{U_{bb}^2 - (\beta_j - \beta_{j+1})^2}, \quad (\text{A6})$$

$$J_{ab}^- = \frac{2J^2}{U_{ab} - (\beta_j - \beta_{j+1})}, \quad (\text{A7})$$

$$J_{ab}^+ = \frac{2J^2}{U_{ab} + (\beta_j - \beta_{j+1})}, \quad (\text{A8})$$

$$J_\perp = \frac{4J^2 U_{ab}}{U_{ab}^2 - (\beta_j - \beta_{j+1})^2}, \quad (\text{A9})$$

when taking into account the inhomogeneous field and after performing a SW transformation with the tunneling term as a perturbation. The resulting system Hamiltonian can also be rephrased as

$$\begin{aligned} \hat{H} = & - \sum_{j=1}^{N-1} \left[ J_z \hat{S}_j^z \hat{S}_{j+1}^z + J_\perp \frac{1}{2} (\hat{S}_j^+ \hat{S}_{j+1}^- + \hat{S}_j^- \hat{S}_{j+1}^+) - \frac{J_N}{4} \right] \\ & + B \hat{S}_z + \sum_j h_j \hat{S}_j^z - \bar{h} (\hat{S}_1^z - \hat{S}_N^z) + \hat{H}_{\text{B}}, \end{aligned} \quad (\text{A10})$$

where

$$J_z = J_{aa} + J_{bb} - J_{ab}^- - J_{ab}^+, \quad (\text{A11})$$

$$J_N = J_{aa} + J_{bb} + J_{ab}^- + J_{ab}^+, \quad (\text{A12})$$

$$B = J_{bb} - J_{aa}, \quad (\text{A13})$$

$$h_j = - \frac{J^2 (\beta_j - \beta_{j+1})}{U_{ab}^2 - \frac{1}{4} (\beta_j - \beta_{j+1})^2} + \frac{J^2 (\beta_{j-1} - \beta_j)}{U_{ab}^2 - \frac{1}{4} (\beta_{j-1} - \beta_j)^2}, \quad (\text{A14})$$

$$\bar{h} = - \frac{J^2 (\beta_N - \beta_1)}{U_{ab}^2 - \frac{1}{4} (\beta_N - \beta_1)^2}. \quad (\text{A15})$$

We found numerically the influence of the  $\bar{h}$ ,  $h_j$  terms is negligible if the difference  $\beta_j - \beta_{j+1} \ll U_{ab}$  and  $\hat{H}_{\text{B}}$  dominates the perturbation of the XXZ model. In numerical calculations, we will keep using Eq. (A10) but in a further analysis, we simplify the model in two main scenarios while also discarding these contributions and the homogeneous magnetic field  $B \hat{S}_z$ .

In the first case, we can take  $\beta_j = 0$ ;  $\forall j$ , leading to the simple XXZ model in (3),

$$\hat{H} = \hat{H}_{\text{XXZ}} = -J_\perp \sum_{j=1}^{M-1} \left( \hat{S}_j^x \hat{S}_{j+1}^x + \hat{S}_j^y \hat{S}_{j+1}^y + \Delta \hat{S}_j^z \hat{S}_{j+1}^z - \frac{1}{4} \right), \quad (\text{A16})$$

where  $J_\perp = 4J^2/U_{ab}$  and the anisotropy parameter  $\Delta = 4J^2(U_{aa}^{-1} + U_{bb}^{-1} - U_{ab}^{-1})/J_\perp$ . This can be further decomposed into an XXX model with perturbative term such that

$$\hat{H} = \hat{H}_{\text{XXX}} + \hat{H}_z, \quad (\text{A17})$$

where

$$\hat{H}_{\text{XXX}} = -J_{\perp} \sum_{j=1}^{M-1} \left( \hat{S}_j^x \hat{S}_{j+1}^x + \hat{S}_j^y \hat{S}_{j+1}^y + \hat{S}_j^z \hat{S}_{j+1}^z - \frac{1}{4} \right), \quad (\text{A18})$$

$$\hat{H}_z = -J_{\perp} (\Delta - 1) \sum_{j=1}^N \hat{S}_j^z \hat{S}_{j+1}^z. \quad (\text{A19})$$

The calculation of the resulting effective model is described in Appendix B.

On the other hand, by choosing  $U = U_{aa} = U_{bb} = U_{ab}$  and  $U \gg (\beta_j - \beta_{j+1})$ ;  $\forall j$  one easily obtains an XXX model with the inhomogeneous magnetic field.

$$\hat{H} = \hat{H}_{\text{XXX}} + \hat{H}_B. \quad (\text{A20})$$

Excited states of the XXX model are given by the spin wave states [29], for which the  $\hat{H}_B$  term is a generator of. This leads to the effective model in (6). See Appendix C for more details.

## APPENDIX B: DERIVATION OF THE EFFECTIVE MODEL FROM ANISOTROPY

The initial state for unitary evolution is the phase state

$$|\theta, \varphi\rangle = e^{-i\varphi \hat{S}_z} e^{-i\theta \hat{S}_y} \bigotimes_{j=1}^N |a\rangle_j, \quad (\text{B1})$$

which can be conveniently expressed in terms of the Dicke basis for maximal spin  $S = N/2$ , namely,

$$|\theta, \varphi\rangle = \sum_{m=-N/2}^{N/2} \binom{N}{m+N/2}^{1/2} (\cos \theta/2)^{N/2-m} \times (e^{i\varphi} \sin \theta/2)^{N/2+m} |m\rangle. \quad (\text{B2})$$

In the above representation,  $|m\rangle$  is the Dicke state as  $\hat{S}^2|m\rangle = S(S+1)|m\rangle$  and  $\hat{S}_z|m\rangle = m|m\rangle$ , and  $\hat{S}^2$  and  $\hat{S}_z$  are collective operators.

We consider the effective model describing the dynamics in the Dicke manifold where the initial state is localized. We derive the effective model in a perturbative way. The unperturbed Hamiltonian is the XXX model (A18) and it is weakly coupled to the anisotropy term  $\hat{H}_z$  (A19).

When the coupling is weak compared to the energy of the spin exchange  $J_{\perp}$ , the dynamics of the initial spin coherent state  $|\theta, \varphi\rangle$  governed by the full Hamiltonian  $\hat{H} = \hat{H}_{\text{XXX}} + \hat{H}_z$  projected over the Dicke manifold can be well approximated using SW transformation [28,29] where the coupling  $\hat{H}_z$  is treated as a perturbation.

The dominant zero-order term  $\hat{H}_{\text{eff}}^{(0)}$  is determined by a projection of the coupling term over the Dick states and gives the following matrix representation:

$$\langle m' | \hat{H}_z | m \rangle = -J_{\perp} (\Delta - 1) \left( -\frac{N}{4(N-1)} + \frac{m^2}{N-1} \right) \delta_{m',m}. \quad (\text{B3})$$

Using the representation of the  $\hat{S}_z$  operator, we obtain

$$\hat{H}_{\text{eff}}^{(0)} = -J_{\perp} \frac{\Delta - 1}{N - 1} \hat{S}_z^2 + \text{const.} \quad (\text{B4})$$

## APPENDIX C: DERIVATION OF THE EFFECTIVE MODEL FROM INHOMOGENEOUS MAGNETIC FIELD

A weak inhomogeneous magnetic field  $\hat{H}_B$  (A3) can generate spin squeezing when added to the isotropic XXX Heisenberg model (A18). In fact it can be any other coupling which leads to the above form, also in different directions, e.g.,  $x$  or  $y$ .

To see this, one needs to calculate the second-order term  $\hat{H}_{\text{eff}}^{(2)}$  in perturbation, which matrix elements are defined as

$$\langle m' | \hat{H}_{\text{eff}}^{(2)} | m \rangle = - \sum_{m'',q} \frac{\langle m' | \hat{H}_B | m'', q \rangle \langle m'', q | \hat{H}_B | m \rangle}{E_q}. \quad (\text{C1})$$

Details about the SW transformation and its application to the Heisenberg XXX model with the coupling can be found in Ref. [28]. In the above equation states  $|m, q\rangle$  are spin-wave states which are eigenstates of the isotropic Heisenberg model (A18) for open boundary conditions [29], namely,

$$|m, q\rangle = \pm \sqrt{N} c_{N/2, \pm m} \sum_{j=1}^N p_j^{(q)} \hat{S}_j^{\pm} |m \mp 1\rangle, \quad (\text{C2})$$

where  $c_{N/2, \pm m} = \sqrt{\frac{N-1}{(N/2 \mp m)(N/2 \mp m + 1)}}$ . The sign  $\pm$  in Eq. (C2) for  $|m, q\rangle$  corresponds to two equivalent definitions of the spin waves in terms of the on-site spin raising and lowering operators  $\hat{S}_j^{\pm}$  acting on the Dicke states  $|m\rangle$ . Furthermore, the coefficients featured in Eq. (C2) are  $p_j^{(q)} = \sqrt{\frac{2}{N}} \cos[\frac{\pi}{N}(j - \frac{1}{2})q]$ , with  $q = 1, \dots, N-1$ . The corresponding eigenenergies  $E_q$  of the isotropic model (A18) read  $E_q = J_{\perp} [\cos(\frac{\pi}{N}q) - 1]$ .

To calculate the form of the second-order term  $\hat{H}_{\text{eff}}^{(2)}$ , it is useful to use the following commutation relations  $[\hat{S}_j^z, \hat{S}_j^n] = -n \hat{S}_j^- \hat{S}_j^{n-1}$ , and  $[\hat{S}_j^z \hat{S}_{j+1}^z, \hat{S}_j^n] = -n(\hat{S}_{j+1}^- \hat{S}_j^{n-1} \hat{S}_j^z + \hat{S}_j^- \hat{S}_{j+1}^{n-1} \hat{S}_{j+1}^z) + n(n-1) \hat{S}_j^- \hat{S}_{j+1}^- \hat{S}_j^{n-2}$ . They allow writing the action of  $\hat{H}_B$  on the Dick state  $|m\rangle$  in the convenient form

$$\hat{H}_B |m\rangle = \sum_j \beta_j \hat{S}_j^z |m\rangle = -\sqrt{\frac{S-m}{S+m+1}} \sum_j \beta_j \hat{S}_j^- |m+1\rangle, \quad (\text{C3})$$

to get the matrix elements in (C1).

A term coupling directly the Dicke states with the spin wave states of  $q = 0$  proportional to  $\sum_j \beta_j$  will appear in  $\langle m' | \hat{H}_B | m'', q \rangle$ . However,  $E_{q=0} = 0$ , meaning we would have an infinite term. To correct this, we simply have to make this sum zero by adding and subtracting a term to  $\hat{H}_B$  so that

$$\hat{H}_B = \sum_{j=1}^N (\beta_j - v) \hat{S}_j^z + v \hat{S}_z = \hat{H}_{B'} + v \hat{S}_z, \quad (\text{C4})$$

where  $v = 1/N \sum_j \beta_j$ . This guarantees  $\sum_j (\beta_j - v) = 0$ , so if in the previous analysis we substitute  $\hat{H}_B$  by  $\hat{H}_{B'}$  we can correctly calculate (C1).



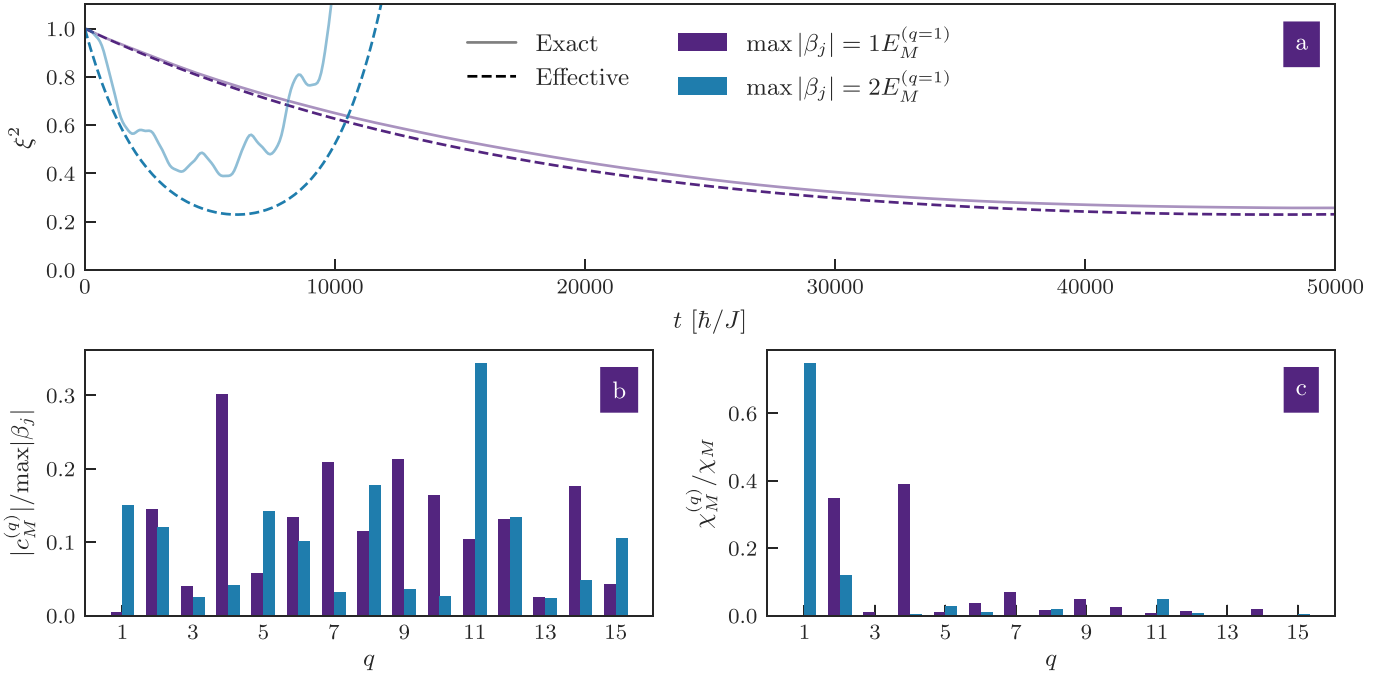


FIG. 9. (a) Variation of spin squeezing parameter  $\xi^2$  dynamically generated using the XXX model with a randomly generated inhomogeneous magnetic field (A18) (solid lines) and the effective model (6) (dashed lines). Colors indicate the maximal magnitude of the magnetic field with respect to the smallest energy gap of the spin wave states. Since  $\chi_M \propto \max |\beta_j|^2$ , the best squeezing time  $t_{\text{best}} \propto 1/|\chi_M|$  will be faster the larger this value is, in principle. (b) The perturbation condition for each spin wave state is  $\max |\beta_j| \ll E_M^{(q)}$ . The effective model approximates the exact dynamics more accurately if the fidelity with spin wave states of quasi-momenta  $q$  ( $|c_M^{(q)}|/\max |\beta_j|$ ) is negligible when the perturbation condition is not fulfilled (compare with (a)). (c) Due to the functional form of the energy gap, the contributions of smaller  $q$  in  $\chi_M = \sum_q \chi_M^{(q)}$  tend to dominate the squeezing timescale.  $N = M = 16$ ,  $J = 1$ ,  $U_{aa} = U_{bb} = U_{ab} = U = 24.4J$ , and  $J_{\perp} = 4\frac{J^2}{U}$ ,  $E_M^{(q)} = J_{\perp}(1 - \cos(\pi q/M))$ .

The final expression for the effective Hamiltonian  $\hat{H}_{\text{eff}}^{(2)}$  will then be

$$\hat{H}_{\text{eff}}^{(2)} = \chi (\hat{S}^2 - \hat{S}_z^2) + v \hat{S}_z, \quad (C5)$$

where  $\chi = \frac{1}{N-1} \sum_{q=1}^{N-1} \frac{|\sum_l p_l^{(q)} (\beta_l - v)|^2}{E_q}$ .

This effective model can even be generated using a random magnetic field which excites many spin wave states, as demonstrated in Fig. 9.

#### APPENDIX D: DYNAMICS DRIVEN BY $\chi \hat{S}_z^2 + v \hat{S}_z$

Consider the unitary evolution of the initial state

$$|\Psi(t=0)\rangle = \sum_m c_m |S, m\rangle \quad (D1)$$

with the Hamiltonian

$$H = \chi (\hat{S}^2 - \hat{S}_z^2) + v \hat{S}_z, \quad (D2)$$

namely,

$$|\Psi(t)\rangle = \sum_m c_m e^{i\chi m^2 t - i v m t} |S, m\rangle \quad (D3)$$

where we omitted the constant phase factor.

One can express the evolution of spin operators in terms of evolution given by the pure OAT model when  $v = 0$ . Simple

algebra shows that the first moments read

$$\langle \hat{S}_+ \rangle = e^{i v t / \hbar} \langle \hat{S}_+ \rangle_{\text{OAT}}, \quad (D4)$$

$$\langle \hat{S}_- \rangle = e^{-i v t / \hbar} \langle \hat{S}_- \rangle_{\text{OAT}}, \quad (D5)$$

$$\langle \hat{S}_x \rangle = \cos(v t / \hbar) \langle \hat{S}_x \rangle_{\text{OAT}} - \sin(v t / \hbar) \langle \hat{S}_y \rangle_{\text{OAT}}, \quad (D6)$$

$$\langle \hat{S}_y \rangle = \cos(v t / \hbar) \langle \hat{S}_y \rangle_{\text{OAT}} + \sin(v t / \hbar) \langle \hat{S}_x \rangle_{\text{OAT}}, \quad (D7)$$

$$\langle \hat{S}_z \rangle = \langle \hat{S}_z \rangle_{\text{OAT}} = 0, \quad (D8)$$

where for OAT, we have

$$\langle \hat{S}_x \rangle_{\text{OAT}} = S \cos^{2S-1}(\chi t / \hbar), \quad (D9)$$

$$\langle \hat{S}_y \rangle_{\text{OAT}} = \langle \hat{S}_z \rangle_{\text{OAT}} = 0. \quad (D10)$$

On the other hand, the second moments are

$$\langle \hat{S}_+^2 \rangle = e^{i 2 v t / \hbar} \langle \hat{S}_+^2 \rangle_{\text{OAT}}, \quad (D11)$$

$$\langle \hat{S}_-^2 \rangle = e^{-i 2 v t / \hbar} \langle \hat{S}_-^2 \rangle_{\text{OAT}}, \quad (D12)$$

$$\langle \hat{S}_+ \hat{S}_- \rangle = \langle \hat{S}_+ \hat{S}_- \rangle_{\text{OAT}}, \quad (D13)$$

$$\begin{aligned} \langle \hat{S}_y \hat{S}_z \rangle &= \cos(v t / \hbar) \langle \hat{S}_y \hat{S}_z \rangle_{\text{OAT}} + \sin(v t / \hbar) \langle \hat{S}_x \hat{S}_z \rangle_{\text{OAT}} \\ &= \cos(v t / \hbar) \langle \hat{S}_y \hat{S}_z \rangle_{\text{OAT}}, \end{aligned} \quad (D14)$$



$$\begin{aligned}\langle \hat{S}_x \hat{S}_z \rangle &= \cos(vt/\hbar) \langle \hat{S}_x \hat{S}_z \rangle_{\text{OAT}} - \sin(vt/\hbar) \langle \hat{S}_y \hat{S}_z \rangle_{\text{OAT}} \\ &= -\sin(vt/\hbar) \langle \hat{S}_y \hat{S}_z \rangle_{\text{OAT}},\end{aligned}\quad (\text{D15})$$

$$\langle \hat{S}_x^2 \rangle = \frac{1}{2}(1 + \cos(2vt)) \langle \hat{S}_x^2 \rangle_{\text{OAT}} + \frac{1}{2}(1 - \cos(2vt)) \langle \hat{S}_y^2 \rangle_{\text{OAT}}, \quad (\text{D16})$$

$$\langle \hat{S}_y^2 \rangle = \frac{1}{2}(1 + \cos(2vt)) \langle \hat{S}_y^2 \rangle_{\text{OAT}} + \frac{1}{2}(1 - \cos(2vt)) \langle \hat{S}_x^2 \rangle_{\text{OAT}}, \quad (\text{D17})$$

$$\langle \hat{S}_z^2 \rangle = \langle \hat{S}_z^2 \rangle_{\text{OAT}}, \quad (\text{D18})$$

$$\begin{aligned}\langle \hat{S}_x \hat{S}_y \rangle &= \cos 2vt \langle \hat{S}_x \hat{S}_y \rangle_{\text{OAT}} + \frac{1}{2} \sin 2vt (\langle \hat{S}_x^2 \rangle_{\text{OAT}} - \langle \hat{S}_y^2 \rangle_{\text{OAT}}) \\ &= \frac{1}{2} \sin 2vt (\langle \hat{S}_x^2 \rangle_{\text{OAT}} - \langle \hat{S}_y^2 \rangle_{\text{OAT}}),\end{aligned}\quad (\text{D19})$$

while the ones derived for the OAT model are

$$\langle \hat{S}_x^2 \rangle_{\text{OAT}} = S/4[(2S-1)\cos^{2S-2}(2\chi t) + (2S+1)], \quad (\text{D20})$$

$$\langle \hat{S}_y^2 \rangle_{\text{OAT}} = -S/4[(2S-1)\cos^{2S-2}(2\chi t) - (2S+1)], \quad (\text{D21})$$

$$\langle S_+ S_- + S_- S_+ \rangle_{\text{OAT}} = 2(\langle \hat{S}_x^2 \rangle_{\text{OAT}} + \langle \hat{S}_y^2 \rangle_{\text{OAT}}), \quad (\text{D22})$$

$$\langle S_+^2 + S_-^2 \rangle_{\text{OAT}} = 2(\langle \hat{S}_x^2 \rangle_{\text{OAT}} - \langle \hat{S}_y^2 \rangle_{\text{OAT}}), \quad (\text{D23})$$

$$\langle S_+^2 - S_-^2 \rangle_{\text{OAT}} = 4i \langle S_x S_y \rangle_{\text{OAT}} = 0, \quad (\text{D24})$$

$$\langle S_x S_z \rangle_{\text{OAT}} = 0, \quad (\text{D25})$$

$$\langle \hat{S}_z^2 \rangle_{\text{OAT}} = S/2, \quad (\text{D26})$$

$$\langle S_y S_z \rangle_{\text{OAT}} = S(2S-1)/2 \cos^{2S-2}(\chi t) \sin(\chi t). \quad (\text{D27})$$

## APPENDIX E: GENERALIZATION TO ANY NUMBER OF HOLES AND CONFIGURATIONS

The generalization of the two-hole analysis to an arbitrary number of holes and their configurations is straightforward. In general, holes are located between occupied sites that constitute partial chains. All partial chains are independent as long as the positions of holes are fixed.

Let us start with the Dicke state for maximal magnetization written as the product state

$$|N/2, N/2\rangle_{\{h\}} = \bigotimes_n |L_n/2, L_n/2\rangle \bigotimes_{k \in \{h\}} |0\rangle_k, \quad (\text{E1})$$

where  $\{h\}$  describes the set of fixed locations of  $N_h$  holes in the chain having  $M$  sites,  $n$  is the index numerating individual partial chains in the system and  $L_n$  is the corresponding number of spins. The total number of spins in the whole chain is  $N = M - N_h = \sum_n L_n$ . We will omit the empty sites  $|0\rangle_k$  when describing the states in the further part of the text.

The initial spin coherent state is a product of coherent states of partial chains

$$|t=0\rangle_{\{h\}} = \bigotimes_n |n\rangle, \quad (\text{E2})$$

where

$$|n\rangle = e^{-i\pi \hat{S}_{y,n}/2} |L_n/2, L_n/2\rangle, \quad (\text{E3})$$

for  $\theta = \pi/2$  and  $\phi = 0$ .

The further unitary dynamics is separable and each partial chain evolves independently

$$|\psi(t)\rangle_{\{h\}} = \bigotimes_n \hat{U}_n |n\rangle, \quad (\text{E4})$$

meaning the state at any point in time can be described as a separable state of partial chains.

In the case of spin squeezing generation by anisotropy, the Hamiltonian described in Sec. V A extends, and for each partial chain  $n$  reads

$$\hat{H}_{\text{eff},n}^{(0)} = -\chi_n^{(0)} \hat{S}_{z,n}^2, \quad (\text{E5})$$

with  $\chi_n^{(0)} = J_\perp(\Delta - 1)/(L_n - 1)$ . When the spin squeezing is generated via the inhomogeneous field with  $\Delta = 1$ , as discussed in Sec. V B, the effective OAT-like model for each partial chain is described effectively by the following Hamiltonian:

$$\hat{H}_{\text{eff},n} = \chi_n \hat{S}_{z,n}^2 + v_n \hat{S}_{z,n}, \quad (\text{E6})$$

where

$$\chi_n = \frac{1}{L_n - 1} \sum_{q=1}^{L_n-1} \frac{|c_n^{(q)}|^2}{E_n^{(q)}}, \quad (\text{E7})$$

$$v_n = \frac{1}{L_n} \sum_{l=l_n}^{l_n+L_n-1} \beta_l, \quad (\text{E8})$$

$$c_n^{(q)} = \frac{\sqrt{2}}{L_n} \sum_{l=l_n}^{l_n+L_n-1} p_l^{(q,n)} (\beta_l - v_n), \quad (\text{E9})$$

where  $l_n$  is the location of the first spin in the partial chain and  $E_n^{(q)} = J_\perp(1 - \cos(\pi q/L_n))$ .

Finally, to calculate the spin squeezing parameter  $\xi^2$  one needs to calculate the first and second moments of the spin operators to obtain their covariances. Expectation values of an on-site linear operator can be described as a sum over all partial chains,  $\langle \hat{X} \rangle_{\{h\}} = \sum_n \langle \hat{X} \rangle_n$  while for a product of two linear operators reads  $\langle \hat{X} \hat{Y} \rangle_{\{h\}} = \sum_n \langle \hat{X} \hat{Y} \rangle_n + \sum_n \sum_{n' \neq n} \langle \hat{X} \rangle_n \langle \hat{Y} \rangle_{n'}$ . From these results, one obtains  $\Delta(\hat{X} \hat{Y})_{\{h\}}^2 = \sum_n \Delta(\hat{X} \hat{Y})_n^2$ . The effective models for partial chains, as well as their separation, allow approximation of the dynamics of spin squeezing parameter by using analytical expressions shown in Appendix D valid for any  $N$  and  $M$ .

## APPENDIX F: SWS WITH HOLES

One can construct the spin-wave states about these spin states separated by holes for maximal spin. When considered in the Bethe basis:

$$|l\rangle_h = \hat{S}_l^- |S = N/2, m = N/2\rangle_h \quad (\text{F1})$$

the spin wave states can be defined in the following way for the  $N_h$  holes

$$|n, q_n\rangle = \sum_{l=1}^M p_l^{(q_n)} |l\rangle_h, \quad (\text{F2})$$



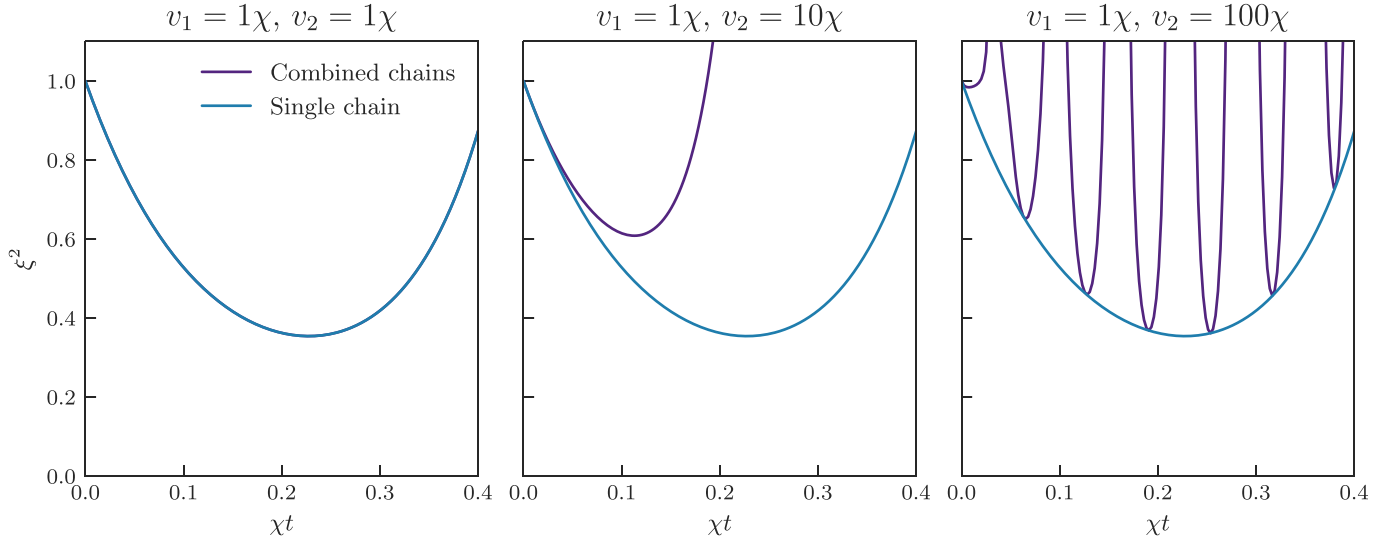


FIG. 10. Comparison of spin squeezing parameter dynamics among combinations two of chains of  $M = N = 8$  particles with Hamiltonian (F6) with same value of  $\chi_n$  ( $\chi_1 = \chi_2 = \chi$ ) but different values of  $v_n$ , indicated in the title of each panel.

where  $n$  numerates partial chains, and they are eigenstates of the  $\hat{H}_{XXX}$  Hamiltonian when

$$p_l^{(q_n)} = \sqrt{\frac{2}{L_n}} \cos \left[ \frac{\pi}{L_n} (l - (l_n - 1/2)) q_n \right],$$

$$l \in (l_n, l_n + L_n - 1) \quad (\text{F3})$$

$$p_l^{(q_n)} = 0 \quad \text{otherwise} \quad (\text{F4})$$

with  $l_n$  being the position of the first spin in the partial chain.

One can show that eigenenergies are

$$E_{q_n} = J_{\perp} \left[ 1 - \cos \left( \frac{\pi}{L_n} q_n \right) \right], \quad (\text{F5})$$

where  $L_n$  is the length of individual sub-chain (number of spins constituting the partial chains), while the corresponding quantum number of quasi-momentum  $q_n \in [1, L_n - 1]$ .

Thus  $\hat{H}_{XXX} + \hat{H}_B$  leads through the second-order processes to the effective pure OAT model in each partial chain

$$\hat{H}_{\text{eff},n}^{(2)} = -\chi_n (\hat{S}_n^2 - \hat{S}_{z,n}^2) + v_n \hat{S}_{z,n}, \quad (\text{F6})$$

where

$$\chi_n = \frac{1}{L_n - 1} \sum_{q_n=1}^{L_n-1} \frac{|c_n^{(q)}|^2}{E_n^{(q)}},$$

$$c_n^{(q)} = \frac{\sqrt{2}}{L_n} \sum_{l=l_n}^{l_n+L_n-1} p_l^{(q,n)} (\beta_l - v_n),$$

$$v_n = \frac{1}{L_n} \sum_{l=l_n}^{l_n+L_n-1} \beta_l,$$

and one needs to set  $l_n = 1$  in  $p_l^{(q,n)}$ . Examples of various dynamics are presented in Fig. 10.

- 
- [1] V. Giovannetti, S. Lloyd, and L. Maccone, Quantum metrology, *Phys. Rev. Lett.* **96**, 010401 (2006).
  - [2] C. L. Degen, F. Reinhard, and P. Cappellaro, Quantum sensing, *Rev. Mod. Phys.* **89**, 035002 (2017).
  - [3] D. Leibfried, M. D. Barrett, T. Schaetz, J. Britton, J. Chiaverini, W. M. Itano, J. D. Jost, C. Langer, and D. J. Wineland, Toward Heisenberg-limited spectroscopy with multiparticle entangled states, *Science* **304**, 1476 (2004).
  - [4] L. Pezzè, A. Smerzi, M. K. Oberthaler, R. Schmied, and P. Treutlein, Quantum metrology with nonclassical states of atomic ensembles, *Rev. Mod. Phys.* **90**, 035005 (2018).
  - [5] A. Sinatra, Spin-squeezed states for metrology, *Appl. Phys. Lett.* **120**, 120501 (2022).
  - [6] D. J. Wineland, J. J. Bollinger, W. M. Itano, F. L. Moore, and D. J. Heinzen, Spin squeezing and reduced quantum noise in spectroscopy, *Phys. Rev. A* **46**, R6797(R) (1992).
  - [7] D. J. Wineland, J. J. Bollinger, W. M. Itano, and D. J. Heinzen, Squeezed atomic states and projection noise in spectroscopy, *Phys. Rev. A* **50**, 67 (1994).
  - [8] M. Kitagawa and M. Ueda, Squeezed spin states, *Phys. Rev. A* **47**, 5138 (1993).
  - [9] M. F. Riedel, P. Böhi, Y. Li, T. W. Hänsch, A. Sinatra, and P. Treutlein, Atom-chip-based generation of entanglement for quantum metrology, *Nature (London)* **464**, 1170 (2010).
  - [10] C. Gross, T. Zibold, E. Nicklas, J. Estève, and M. K. Oberthaler, Nonlinear atom interferometer surpasses classical precision limit, *Nature (London)* **464**, 1165 (2010).
  - [11] C. D. Hamley, C. S. Gerving, T. M. Hoang, E. M. Bookjans, and M. S. Chapman, Spin-nematic squeezed vacuum in a quantum gas, *Nat. Phys.* **8**, 305 (2012).
  - [12] A. Qu, B. Evard, J. Dalibard, and F. Gerbier, Probing spin correlations in a bose-einstein condensate near the single-atom level, *Phys. Rev. Lett.* **125**, 033401 (2020).

- [13] A. Evrard, V. Makhlov, T. Chalopin, L. A. Sidorenkov, J. Dalibard, R. Lopes, and S. Nascimbene, Enhanced magnetic sensitivity with non-gaussian quantum fluctuations, *Phys. Rev. Lett.* **122**, 173601 (2019).
- [14] T.-W. Mao, Q. Liu, X.-W. Li, J.-H. Cao, F. Chen, W.-X. Xu, M. K. Tey, Y.-X. Huang, and L. You, Quantum-enhanced sensing by echoing spin-nematic squeezing in atomic Bose–Einstein condensate, *Nat. Phys.* **19**, 1585 (2023).
- [15] I. D. Leroux, M. H. Schleier-Smith, and V. Vuletić, Implementation of cavity squeezing of a collective atomic spin, *Phys. Rev. Lett.* **104**, 073602 (2010).
- [16] K. Maussang, G. E. Marti, T. Schneider, P. Treutlein, Y. Li, A. Sinatra, R. Long, J. Estève, and J. Reichel, Enhanced and reduced atom number fluctuations in a BEC splitter, *Phys. Rev. Lett.* **105**, 080403 (2010).
- [17] P. Richerme, Z.-X. Gong, A. Lee, C. Senko, J. Smith, M. Foss-Feig, S. Michalakakis, A. V. Gorshkov, and C. Monroe, Non-local propagation of correlations in quantum systems with long-range interactions, *Nature (London)* **511**, 198 (2014).
- [18] D. Kajtoch, E. Witkowska, and A. Sinatra, Spin-squeezed atomic crystal, *Europhys. Lett.* **123**, 20012 (2018).
- [19] M. Płodzień, M. Kościelski, E. Witkowska, and A. Sinatra, Producing and storing spin squeezed states and Greenberger-Horne-Zeilinger states in a one-dimensional optical lattice, *Phys. Rev. A* **102**, 013328 (2020).
- [20] P. He, M. A. Perlin, S. R. Muleady, R. J. Lewis-Swan, R. B. Hutson, J. Ye, and A. M. Rey, Engineering spin squeezing in a 3D optical lattice with interacting spin-orbit-coupled fermions, *Phys. Rev. Res.* **1**, 033075 (2019).
- [21] T. Comparin, F. Mezzacapo, and T. Roscilde, Multipartite entangled states in dipolar quantum simulators, *Phys. Rev. Lett.* **129**, 150503 (2022).
- [22] T. Comparin, F. Mezzacapo, M. Robert-de-Saint-Vincent, and T. Roscilde, Scalable spin squeezing from spontaneous breaking of a continuous symmetry, *Phys. Rev. Lett.* **129**, 113201 (2022).
- [23] M. Mamaev, D. Barberena, and A. M. Rey, Spin squeezing in mixed-dimensional anisotropic lattice models, *Phys. Rev. A* **109**, 023326 (2024).
- [24] J. C. Pelayo, K. Gietka, and T. Busch, Distributed quantum sensing with optical lattices, *Phys. Rev. A* **107**, 033318 (2023).
- [25] J. Franke, S. R. Muleady, R. Kaubruegger, F. Kranzl, R. Blatt, A. M. Rey, M. K. Joshi, and C. F. Roos, Quantum-enhanced sensing on optical transitions through finite-range interactions, *Nature (London)* **621**, 740 (2023).
- [26] G. Bornet, G. Emperauger, C. Chen, B. Ye, M. Block, M. Bintz, J. A. Boyd, D. Barredo, T. Comparin, F. Mezzacapo, T. Roscilde, T. Lahaye, N. Y. Yao, and A. Browaeys, Scalable spin squeezing in a dipolar Rydberg atom array, *Nature (London)* **621**, 728 (2023).
- [27] W. J. Eckner, N. Darkwah Oppong, A. Cao, A. W. Young, W. R. Milner, J. M. Robinson, J. Ye, and A. M. Kaufman, Realizing spin squeezing with Rydberg interactions in an optical clock, *Nature (London)* **621**, 734 (2023).
- [28] T. Hernández Yanes, M. Płodzień, M. Mackoīt Sinkevičienė, G. Žlabys, G. Juzeliūnas, and E. Witkowska, One- and two-axis squeezing via laser coupling in an atomic Fermi-Hubbard model, *Phys. Rev. Lett.* **129**, 090403 (2022).
- [29] T. H. Yanes, G. Žlabys, M. Płodzień, D. Burba, M. M. Sinkevičienė, E. Witkowska, and G. Juzeliūnas, Spin squeezing in open Heisenberg spin chains, *Phys. Rev. B* **108**, 104301 (2023).
- [30] E. Altman, W. Hofstetter, E. Demler, and M. D. Lukin, Phase diagram of two-component bosons on an optical lattice, *New J. Phys.* **5**, 113 (2003).
- [31] A. Chu, J. Will, J. Arlt, C. Klempt, and A. M. Rey, Simulation of XXZ spin models using sideband transitions in trapped bosonic gases, *Phys. Rev. Lett.* **125**, 240504 (2020).
- [32] A. Rubio-Abadal, J.-Y. Choi, J. Zeiher, S. Hollerith, J. Rui, I. Bloch, and C. Gross, Many-body delocalization in the presence of a quantum bath, *Phys. Rev. X* **9**, 041014 (2019).
- [33] J. Dobrzyniecki and M. Tomza, Quantum simulation of the central spin model with a Rydberg atom and polar molecules in optical tweezers, *Phys. Rev. A* **108**, 052618 (2023).
- [34] A. Micheli, G. K. Brennen, and P. Zoller, A toolbox for lattice-spin models with polar molecules, *Nat. Phys.* **2**, 341 (2006).
- [35] I. Bloch, J. Dalibard, and W. Zwerger, Many-body physics with ultracold gases, *Rev. Mod. Phys.* **80**, 885 (2008).
- [36] D. Wei, A. Rubio-Abadal, B. Ye, F. Machado, J. Kemp, K. Srakaew, S. Hollerith, J. Rui, S. Gopalakrishnan, N. Y. Yao, I. Bloch, and J. Zeiher, Quantum gas microscopy of Kardar-Parisi-Zhang superdiffusion, *Science* **376**, 716 (2022).
- [37] T. Fukuhara, P. Schauß, M. Endres, S. Hild, M. Cheneau, I. Bloch, and C. Gross, Microscopic observation of magnon bound states and their dynamics, *Nature (London)* **502**, 76 (2013).
- [38] P. A. Lee, N. Nagaosa, and X.-G. Wen, Doping a Mott Insulator: Physics of high-temperature superconductivity, *Rev. Mod. Phys.* **78**, 17 (2006).
- [39] F. Grusdt, Z. Zhu, T. Shi, and E. Demler, Meson formation in mixed-dimensional t-J models, *SciPost Phys.* **5**, 057 (2018).
- [40] F. Meinert, M. J. Mark, E. Kirilov, K. Lauber, P. Weinmann, M. Gröbner, A. J. Daley, and H.-C. Nägerl, Observation of many-body dynamics in long-range tunneling after a quantum quench, *Science* **344**, 1259 (2014).
- [41] P. L. Pedersen, M. Gajdacz, N. Winter, A. J. Hilliard, J. F. Sherson, and J. Arlt, Production and manipulation of wave packets from ultracold atoms in an optical lattice, *Phys. Rev. A* **88**, 023620 (2013).
- [42] A. Sinatra, E. Witkowska, J.-C. Dornstetter, Y. Li, and Y. Castin, Limit of spin squeezing in finite-temperature Bose-Einstein condensates, *Phys. Rev. Lett.* **107**, 060404 (2011).
- [43] A. Sinatra, E. Witkowska, and Y. Castin, Spin squeezing in finite temperature Bose-Einstein condensates: Scaling with the system size, *Eur. Phys. J.: Spec. Top.* **203**, 87 (2012).
- [44] M. Tse *et al.*, Quantum-enhanced advanced ligo detectors in the era of gravitational-wave astronomy, *Phys. Rev. Lett.* **123**, 231107 (2019).
- [45] F. Acernese *et al.* (Virgo Collaboration), Increasing the astrophysical reach of the advanced virgo detector via the application of squeezed vacuum states of light, *Phys. Rev. Lett.* **123**, 231108 (2019).





## Chapter 8

# Entanglement of squeezed states under occupation defects

The schemes we have shown involving the Mott insulating phase where we excite spin wave states via a small perturbation are very effective at reproducing models akin to OAT and TACT. The absence of double occupied states in this mapping prevents particle losses due to collisions. Moreover, the proposed schemes do not involve complicated setups and are sufficiently resilient to small changes in the system parameters. In the previous chapter we also developed a model for the case of holes pinned in different locations of the lattice. We also explored the  $t$ - $J$  model in the context of spin squeezing, where we allowed particles to move in the lattice. The study of dynamics in the presence of holes is relevant since, in an experiment, we might have little control on the number of particles that survive the preparation stage. An aspect of the spin squeezing parameter which we have yet to explore is its utility as an entanglement witness. We may then question how holes affect correlations and entanglement in the context of spin squeezing. In this work we propose a two-site Bell correlator to certify entanglement, which can be conveniently expressed in terms of the normalized mean spin and the spin squeezing parameter. The correlator accounts for occupation defects and is well bounded by limiting cases obtained through a toy model. The occupation defects under study appear either at the state preparation stage or the measurement stage.

The results shown in this chapter are the result of our own research and the pre-print of the research article is available as:

T. H. Yanes, Y. Bamaara, A. Sinatra, and E. Witkowska, *Bounds on detection of Bell correlations with entangled ultra-cold atoms in optical lattices under occupation defects*, (Sept. 4, 2024) <http://arxiv.org/abs/2409.02873> (visited on 09/08/2024), pre-published.



## 8.1 Two-body Bell Correlator

While we could use standard definitions of the spin squeezing parameter to detect negative pairwise correlations [9] or rely on a set of generalized spin squeezing inequalities [72], we instead opt for a data-driven approach to construct Bell correlators based on local measurements [37]. Bell inequality violation represents the most robust scheme for entanglement certification, avoiding assumptions on physical nature and degrees of freedom to be measured or calibration of measurement.

We consider the  $M$  sites of our lattice as separate subsystems where at least two observables  $\alpha$  are measured, each having  $d$  possible outcomes. A Bell experiment checks if correlations can be provided through a local hidden variable theory, meaning the obtained results depend on local correlations from the past. To check this, we may choose an arbitrary observable for each of the  $M$  subsystems  $\alpha = \{\alpha_j\}_{j=1}^M$  to calculate probabilities of the measurement outcomes  $r = \{r^{(j)}\}_{j=1}^M$ . The expected pair probability distribution is given by

$$P_M^{(\text{LV})}(r|\alpha) = \int d\lambda q(\lambda) \prod_{j=1}^M P^{(j)}(r^{(j)}|\alpha_j, \lambda). \quad (8.1)$$

Instead of working with eq. (8.1), we equivalently consider one- and two-body correlations summed over the permutations of the subsystems as

$$M_\alpha = \sum_{j=1}^M \langle r_\alpha^{(j)} \rangle, \quad (8.2)$$

$$C_{\alpha\beta} = \sum_{i,j \neq i} \langle r_\alpha^{(i)} r_\beta^{(j)} \rangle, \quad (8.3)$$

$$\tilde{C}_{\alpha\beta} = C_{\alpha\beta} - M_\alpha M_\beta. \quad (8.4)$$

We can use these correlations to build up a vector  $\vec{M}$  and matrix  $\tilde{C}$  to represent the non-locality condition as a convex optimization problem. Then, given a positive-semi-definite matrix  $A \succeq 0$  and a vector  $\vec{h}$ , we find

$$L(A, h) = \text{tr}(A\tilde{C}) + \vec{h} \cdot \vec{M} + E_{\text{max}} \geq 0, \quad (8.5)$$

where  $E_{\text{max}}$  is the classical limit, as long as  $\vec{M}, \tilde{C}$  are compatible with a local hidden variable theory. If we introduce data corresponding to a spin-squeezed state in the proposed convex optimization problem, we may obtain [37]

$$L = \tilde{C}_{00} + \tilde{C}_{11} - \tilde{C}_{01} - \tilde{C}_{10} - M_0 - M_1 + M \geq 0, \quad (8.6)$$

While this inequality was originally proposed for systems with two possible measurement outcomes, we numerically found the convex optimization that

yields eq. (8.6) from eq. (8.5) is also satisfied with our proposed three possible measurement outcomes  $r_j \in \{-1/2, 0, +1/2\}$ .

To recover the collective character of the spin squeezing parameter in the Bell correlators, we choose all local measurements to be along the same directions, retrieving coherent measurement expressions. Our two chosen measurement settings  $\alpha \in \{0, 1\}$  are

$$\hat{S}_j^{0,1} = \cos \theta \hat{S}_j^n \pm \sin \theta \hat{S}_j^{\min}, \quad (8.7)$$

where  $n$  is the mean spin direction and  $\min$  is the minimal variance direction of the state. While some local measurements survive this choice of settings, they can be effectively replaced with basic information about the initial state of the system, as we show later. Moreover, we implicitly assume that any local measurement outcome outside the eigensubspace of eigenvalues  $r^{(j)} = \pm 1/2$  is treated as if the site was empty.

We can introduce eq. (8.7) into eq. (8.6) and optimize over the change of variable  $x = \cos \theta$ , as the inequality takes the form of a simple quadratic polynomial. Through this approach we derive a general two-site Bell correlator which only depends on first and second moment results of the form

$$L_{\text{opt}}^{(1)} = M - \frac{\mathcal{M}_n^2}{4(\mathcal{M}_{\min}^2 - \mathcal{C}_{\min,\min})} - 4(\mathcal{M}_{\min}^2 - \mathcal{C}_{\min,\min}), \quad (8.8)$$

where we considered the averages along the mean spin and squeezing directions,

$$\mathcal{M}_n = \sum_{j=1}^M \langle \hat{S}_j^n \rangle, \quad (8.9)$$

$$\mathcal{M}_{\min} = \sum_{j=1}^M \langle \hat{S}_j^{\min} \rangle, \quad (8.10)$$

as well as the two-site correlations along the squeezing direction

$$\mathcal{C}_{\min,\min} = \sum_{i,j \neq i}^M \langle \hat{S}_i^{\min} \hat{S}_j^{\min} \rangle. \quad (8.11)$$

We can rewrite this definition with collective expectation values by introducing the average number of unit-filled site  $\bar{M} \equiv \sum_i \text{Tr}(\rho_i)$ , which is a time-independent on-site measurement. This is because we do not consider the generation of occupation defects during dynamics, meaning the Hamiltonian maintains the different occupation sectors separated. In such case, we obtain

$$L_{\text{opt}}^{(1)} = M - \frac{\langle \hat{S}_n \rangle^2}{\bar{M} - 4(\Delta \hat{S}_{\min})^2} - (\bar{M} - 4(\Delta \hat{S}_{\min})^2), \quad (8.12)$$

where  $|\langle \hat{S}_n \rangle| \leq |\bar{M} - 4(\Delta \hat{S}_{\min})^2|$ ; otherwise we have  $L_{\text{opt}}^{(1)} = M - 2|\langle \hat{S}_n \rangle|$ .



The result can be expressed in terms of the spin squeezing parameter  $\xi^2$  and the normalized mean spin direction  $v = 2\langle\hat{S}_n\rangle/N$  as

$$L_{\text{opt}}^{(1)} = M - \frac{N}{4} \frac{Nv^2}{\bar{M} - N\xi^2 v^2} - (\bar{M} - N\xi^2 v^2). \quad (8.13)$$

## 8.2 Occupation defects and toy model

This data-driven approach to derive our target Bell correlator becomes relevant when we include measurement conditions in our experiment. In particular, we explore the effects of occupation defects on the system. To demonstrate the usefulness of the proposal, we assume two possible scenarios which provide two different sources of occupation defects: particle losses at the preparation stage and double occupations at the measurement stage. In the former scenario, state preparation is imperfect and we loose particles with a given probability before the start of the dynamics. In the latter scenario, preparation and dynamics are as expected but we loose single occupancy per site at the measurement stage.

To have a reference of the entanglement limit in these different scenarios, we develop a toy model that assumes complete decoupling between the internal degrees of freedom (spin) and the external ones (spatial distribution). While this is a broad simplification, we observe the toy model closely benchmarking the correlation limit of our models under occupation defects. This treatment requires an adaptation of the Bell correlator to each of the scenarios with the toy model, based on the particular constraints on entanglement they impose.

For instance, the particle losses scenario yields the toy model two-site Bell correlator

$$\frac{L^{(V)}}{M} = 1 - \frac{p(N-1)}{N-p} \frac{\langle\hat{S}_n\rangle_{\text{SS}}^2}{N \left[ N - 4(\Delta\hat{S}_{\text{min}})_{\text{SS}}^2 \right]} - \frac{p(N-p)}{N-1} \left[ 1 - \frac{4(\Delta\hat{S}_{\text{min}})_{\text{SS}}^2}{N} \right], \quad (8.14)$$

where SS signifies expectation values of a purely squeezed state of  $N$  particles,  $p$  is the probability of finding a given site at unit-filling, and  $N = pM$ . Equation (8.14) can be obtained from eq. (8.12) by introducing

$$\begin{aligned} N &= pM, \\ \bar{M} &= pM = N \\ \langle\hat{S}_n\rangle &= \langle\hat{S}_n\rangle_{\text{SS}}, \\ (\Delta\hat{S}_m)^2 &= \frac{N-p}{N-1} \left[ (\Delta\hat{S}_m)_{\text{SS}}^2 - \frac{N}{4} \right] + \frac{N}{4}. \end{aligned}$$

Equation (8.14) holds when  $N \leq M$ , that is  $p \leq 1$ . The asymptotic behaviour in the large particle limit,  $N \rightarrow \infty$ , sets a fixed limit on the Bell correlations



with respect to the probability  $p$ . Values above the critical probability  $p_c$  are unable to provide non-local correlations. In this case,  $\lim_{N \rightarrow \infty} p_c = 5/4$ .

Instead, the measurement defects scenario yields the following result

$$\frac{L^{(\text{VI})}}{M} = 1 - \frac{\langle \hat{S}_n \rangle_{\text{SS}}^2}{N \left[ N - 4(\Delta \hat{S}_{\min})_{\text{SS}}^2 \right]} - p^2 \left[ 1 - \frac{4(\Delta \hat{S}_{\min})_{\text{SS}}^2}{N} \right], \quad (8.15)$$

where  $N = M$ . Equation (8.15) can be obtained from eq. (8.12) by introducing

$$\begin{aligned} N &= M, \\ \bar{M} &= pM \\ \langle \hat{S}_n \rangle &= p \langle \hat{S}_n \rangle_{SS}, \\ (\Delta \hat{S}_m)^2 &= \sum_{i,j} \langle \hat{s}_{im} \hat{s}_{jm} \rangle + \langle \hat{S}_m \rangle^2 = \sum_{i \neq j} \langle \hat{s}_{im} \hat{s}_{jm} \rangle_{SS} + \frac{\bar{M}}{4} + \langle \hat{S}_m \rangle^2 \\ &= p^2 \left[ (\Delta \hat{S}_m)_{SS}^2 - \frac{M}{4} \right] + p \frac{M}{4}, \end{aligned}$$

In this case,  $\lim_{N \rightarrow \infty} p_c = \sqrt{3}/2$ .

### 8.3 Realistic implementations

We exemplify the particle losses scenario in the Mott insulating phase through two different sources of squeezing given an average filling factor. As seen in chapter 7, we can generate OAT dynamics through a weak anisotropy of the contact interactions such that the effective Hamiltonian of a partial chain  $n$  isolated by empty sites is given by

$$\hat{H}_{\text{eff},n}^{(0)} = -\chi_n^{(0)} \hat{S}_{z,n}^2. \quad (8.16)$$

Alternatively, if we implement a weak inhomogeneous magnetic field, we may obtain the effective Hamiltonian

$$\hat{H}_{\text{eff},n} = \chi_n \hat{S}_{z,n}^2 + v_n \hat{S}_{z,n}. \quad (8.17)$$

We demonstrate numerically that the presence of a linear term in the effective Hamiltonian, usually negligible in the unit-filling regime, greatly affects the generation of non-local correlations, as we showed previously with spin squeezing in chapter 7.

We also compare the obtained two-site correlator with an M-site correlator capable of detecting GHZ states [77] to benchmark its usefulness. While the M-site correlator is sensitive to non-local correlations up to  $p > p_c = 1/\sqrt{2}$  in the large particle number limit, it requires larger time scales ( $\chi t = \pi/2$ ) and experimentally challenging correlation measurements involving all sites of the lattice. On the contrary, the two-site correlator shows optimal detection at the best squeezing time scale ( $\chi t \ll \pi/2$ ) and the correlation measurements are only two-body collective measurements.



# Bounds on detection of Bell correlations with entangled ultra-cold atoms in optical lattices under occupation defects

T. Hernández Yanes\*,<sup>1,2</sup> Y. Bamaara\*,<sup>3</sup> A. Sinatra,<sup>3</sup> and E. Witkowska<sup>1</sup>

<sup>1</sup>*Institute of Physics PAS, Aleja Lotnikow 32/46, 02-668 Warszawa, Poland*

<sup>2</sup>*Universität Innsbruck, Fakultät für Mathematik, Informatik und Physik, Institut für Experimentalphysik, 6020 Innsbruck, Austria*

<sup>3</sup>*Laboratoire Kastler Brossel, ENS-Université PSL, CNRS, Sorbonne Université, Collège de France, 24 rue Lhomond, 75005 Paris, France*

(Dated: September 11, 2024)

Bell non-locality stems from quantum correlations effectively identified using inequalities. Spin chains, simulated with ultra-cold atoms in optical lattices, Rydberg atoms in tweezer arrays, trapped ions, or molecules, allow single-spin control and measurement. Therefore, they are suitable for studying fundamental aspects of these correlations and non-locality. Occupation defects, such as vacancies or multiple atoms occupying a single site due to imperfect system preparation, limit the detection of Bell correlations. We investigate their impact using a simplified toy model parameterized by the probability of a site being singly occupied. We derive the corresponding Bell inequality and identify the smallest probability that establishes a lower bound for detecting Bell correlations. We relate the bound to two physical parameters leading to defects in occupations: non-zero temperature and filling factor, focusing on entangled ultra-cold atoms in optical lattices. Finally, we numerically validate the predictions of the toy model by full many-body simulations.

## I. INTRODUCTION

Quantum mechanics introduced groundbreaking concepts of non-local correlations and entanglement that challenged well-established principles of classical physics, including realism, causality and locality [1]. A classical picture can be recovered at the price of introducing local hidden variables, and the corresponding local hidden variable (LV) theories are shown to satisfy Bell inequalities [2]. Quantum correlations that violate Bell inequalities are inconsistent with LV theory and are, therefore, referred to as non-local [3].

The most robust method for entanglement certification is provided by violating Bell's inequalities, as it avoids assumptions about the physical nature and degrees of freedom to be measured or the calibration of measurements [4]. This is known as the device-independent scenario, which is a powerful resource in many quantum information tasks, such as self-testing [5], randomness amplification and expansion [6, 7], quantum key distribution [8–10], and quantum sensing and metrology [11, 12]. Recent experimental demonstrations have employed various platforms, including entangled photons [13–15], spins in nitrogen-vacancy centers [16], superconducting circuits [17], pairs of Josephson phase qubits [18], and neutral and ultra-cold atoms [19, 20]. Many studies have concentrated on few-particle scenarios; however, non-local correlations also naturally emerge in quantum many-body systems [21].

Atom assembly in optical lattices and optical tweezer arrays [22–24], as well as trapped ions and molecules [25, 26], offer excellent approaches for studying many-body

entanglement, with capabilities for single-atom preparation, control, and detection. In the above-mentioned platforms, entanglement can be generated dynamically from the initial coherent state well approximated by the one-axis twisting (OAT) model [27] where spin-squeezed and GHZ states are produced. Given the control and local measurements possible in such architectures and their scalability, the systems offer the powerful setup to generate and study fundamental aspects of Bell correlations and non-locality, enabling the exploration of quantum information concepts. Imperfections, however, e.g. in system preparation, may introduce occupation defects, limiting Bell inequalities' application and entanglement certification.

In this paper, we study the role of occupation defects in detecting Bell correlations focusing on  $N$  two-level bosonic atoms in a spin-entangled state distributed among  $M$  sites of an optical lattice, such that  $N \leq M$ . In the Bell scenario, we consider the measurement of two local collective spin observables at each lattice site where 0, 1 or 2 atoms are present. For each measurement result there are three possible outcomes:  $\pm 1/2$  when the site is singly occupied, and 0 whenever a defect such as an empty or doubly occupied site is present, as illustrated in Fig. 1. We introduce a simplified toy model where the atoms' internal and external degrees of freedom are decoupled. The dynamics of the internal spin degrees of freedom, including possible entanglement among the spins, is assumed to be given by the OAT model with  $N$  atoms. The external degrees of freedom are parameterized by the probability  $p$  of having a single occupied site allowing vacant, double, etc. occupancy sites when  $p < 1$ . We derive the corresponding  $p$ -parameterized Bell inequalities based on  $M$ - and two-sites Bell correlations [28, 29]. We analytically estimate the lowest (critical) value of the probability  $p$  for violation of Bell

---

\* These authors contributed equally to this work

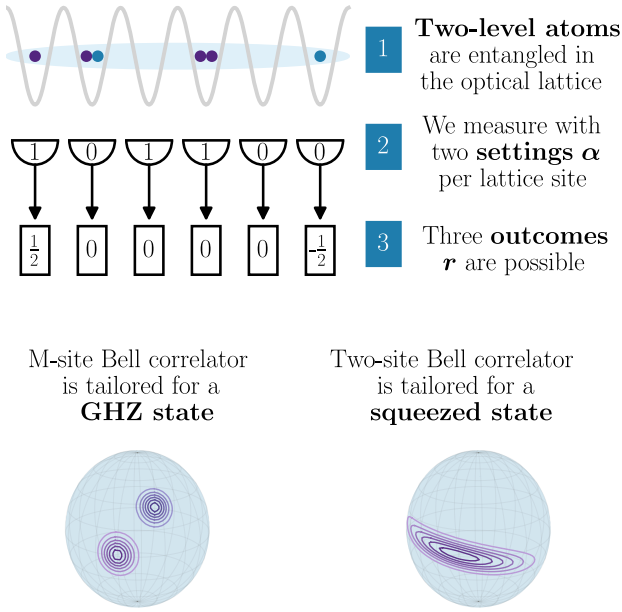


FIG. 1. A chain of  $M$  spins is created by two-level ultra-cold atoms loaded into an optical lattice. Bell scenario considered: on each of  $M$  subsystems (sites) two different measurement are performed  $\hat{s}_\alpha^{(j)}$ , with  $\alpha = 0, 1$ , locally leading to three measurement outcomes  $r_1^{(j)}, r_2^{(j)}, r_3^{(j)} \in \{-1/2, +1/2, 0\}$ . The M-site Bell correlator is tailored for GHZ states, while the two-site Bell correlator is tailored for spin-squeezed states.

inequality. We obtain  $p_c \approx 1/\sqrt{2}$  for the  $M$ -site Bell correlations. For the two-site Bell correlations, we obtain  $p_c = 4/5$  and  $p_c = \sqrt{3}/2$  when  $N = pM < M$  and  $N = M$ , respectively. These results are general and can be relevant for any platform where individual addressing of spins is possible [30–37], for example as in recent experiments using an array of trapped ions [38] and Rydberg atoms [39, 40] demonstrating generation of entanglement in terms of scalable spin-squeezing with tens of spins.

We explore the predictions of the toy model by performing full many-body numerical simulations of ultra-cold atoms in an optical lattice. We consider two distinct protocols for Bell correlations generation, which differ by the source of the occupation defects.

In the first one, Bell correlations between individual atoms are generated in the Mott insulating regime via a weak inhomogeneous magnetic field or interaction anisotropy [41, 42], and the considered occupation defects are vacant sites (holes). The probability  $p$  of single occupancy sites is the filling factor  $f = N/M$ . Our numerical simulations confirm predictions of the toy model of the lower bound on the filling factor concerning the detection of the  $M$ -sites Bell correlations. However, the detection of the two-site Bell correlations in the lattice system is hindered whenever  $f < 1$  for fixed positions of holes. The movement of holes turned out to be crucial

to lower the numerical bound on the filling factor, allowing for the detection of two-site Bell correlations up to  $f \approx p_c$ , as predicted by the toy model.

In the second protocol, entanglement is generated in the superfluid regime using atom-atom interactions [28, 32, 43] and next is transferred to the Mott phase by increasing the lattice height. The main source of defects is imposed by non-zero temperature  $T$  of an initial sample when  $N = M$ . We relate analytically the probability  $p$  with the initial temperature  $T$  of the system in the limit of an isoentropic transformation that leaves the system in thermal equilibrium at each moment. In this case, we determine analytically the upper bound for the initial temperature corresponding to  $p_c$  below which  $M$ - and two-site Bell correlations can be detected.

The paper is organized as follows: In Secs. II and III, we provide the theoretical framework for the Bell scenario and toy model. This is applied to the system composed of ultra-cold atoms in an optical lattice presented in Sec. IV via analytical and numerical approaches. In Secs. V and VI we present the results for the first and second protocols, respectively, discussing the role of defects introduced by holes and non-zero initial temperature of the system. We conclude with further discussion and outlook in Sec. VII.

## II. BELL SCENARIO

We consider  $M$  spatially separated subsystems labelled  $i = 1, \dots, M$ , sharing a quantum  $M$ -partite state described by the density operator  $\hat{\rho}$ . In each subsystem,  $k$  observables labeled  $\alpha = 0, \dots, k-1$ , can be measured, each having  $d$  possible outcomes. A Bell experiment, as shown in Fig. 1, involves choosing an arbitrary observable for each of the  $M$  subsystems  $\alpha = \{\alpha_i\}_{i=1}^M$ , and recording the measurement results  $r = \{r^{(i)}\}_{i=1}^M$ . The goal is to determine the  $M$ -partite probability distribution  $P_M(r|\alpha)$  for the outcomes  $r$  given the settings  $\alpha$  for all possible choices of settings  $\alpha$ . In the LV theory [44], any probability distribution  $P_M(r|\alpha)$  can be written as

$$P_M^{(LV)}(r|\alpha) = \int d\lambda q(\lambda) \prod_{i=1}^M P^{(i)}(r^{(i)}|\alpha_i, \lambda). \quad (1)$$

The local nature of this equation resides in the fact that the probability distribution of the outcomes for any given subsystem  $i$  depends only on the setting within that same subsystem  $i$ . The correlations between different subsystems here take their origin from a dependence relation that was established in the past, when the state  $\hat{\rho}$  was generated. This dependence can be fully described by some variable  $\lambda$ , which may be random with a probability distribution  $q(\lambda)$ , affecting simultaneously all the  $M$  subsystems. Furthermore, if we consider a local realistic model where the measurement result  $r^{(i)}$  is deterministically determined by the setting  $\alpha_i$  and the variable  $\lambda$  in



each subsystem  $i$ , we have

$$P^{(i)}(r^{(i)}|\alpha_i, \lambda) = \delta_{r^{(i)}, r^{(i)}(\lambda)}. \quad (2)$$

In the Bell experiment described above, the possibility of decomposing the measured probability distribution  $P_M(r|\alpha)$  into the form (1) constitutes the locality condition for correlations between the  $M$  subsystems under study. Conversely, if the measured probability distribution  $P_M(r|\alpha)$  cannot be written in the form (1), the correlations present in the system are non-local. This decomposition corresponds to the most general locality condition, as defined by Bell. In practice, as we will see later, this condition is often formulated as a Bell inequality.

In this paper, we consider an optical lattice with  $M$  sites, each containing zero, one or two two-level atoms. Each atom with two internal states  $a$  and  $b$  is an effective spin  $1/2$ , and we can express local collective spins in the quantized form as  $\hat{s}_x^{(j)} = (\hat{s}_+^{(j)} + \hat{s}_-^{(j)})/2$ ,  $\hat{s}_y^{(j)} = (\hat{s}_+^{(j)} - \hat{s}_-^{(j)})/(2i)$ ,  $\hat{s}_z^{(j)} = (\hat{a}_j^\dagger \hat{a}_j - \hat{b}_j^\dagger \hat{b}_j)/2$  with  $\hat{s}_+^{(j)} = \hat{a}_j^\dagger \hat{b}_j$ ,  $\hat{s}_-^{(j)} = (\hat{s}_+^{(j)})^\dagger$ .

Within the Bell scenario, we consider in each site  $j$ , the measurement of two local collective spin observables  $\hat{s}_\alpha^{(j)}$  on the  $j$ -th site, with  $\alpha = 0, 1$ , each giving  $d = 3$  possible results

$$r_0^{(j)} = 0, -\frac{1}{2}, +\frac{1}{2} \quad ; \quad r_1^{(j)} = 0, -\frac{1}{2}, +\frac{1}{2}, \quad (3)$$

as illustrated in Fig. 1, where the result  $r = 0$  is assigned to any measurement result different from  $\pm 1/2$ . The probability distribution  $P_M(r|\alpha)$  to obtain the results  $r$  given the settings  $\alpha$  can be theoretically calculated, in terms of the density operator  $\hat{\rho}$  describing the system's state, as

$$P_M(r|\alpha) = \text{tr} \left[ \hat{\rho} \bigotimes_{j=1}^M \hat{\Pi}_{\alpha_j, r^{(j)}} \right], \quad (4)$$

where  $\hat{\Pi}_{\alpha_j, r^{(j)}=\pm 1/2}$  projects onto the eigensubspace of  $\hat{s}_{\alpha_j}^{(j)}$  with eigenvalue  $r^{(j)} = \pm 1/2$ , and  $\hat{\Pi}_{\alpha_j, r^{(j)}=0} = \hat{1} - \sum_{r=\pm 1/2} \hat{\Pi}_{\alpha_j, r}$  projects onto the subspace perpendicular to both eigensubspaces of  $\hat{s}_{\alpha_j}^{(j)}$  corresponding to the eigenvalues  $r^{(j)} = +1/2$  and  $r^{(j)} = -1/2$ .

In the next Section, we derive two Bell inequalities using this framework. The first one, relying on  $M$ -site correlations, is mainly useful for highly entangled states with a small number of lattice sites (see, e.g., Fig. 1). The second one, relying on two-site correlations, is more applicable to spin-squeezed states with a large number of lattice sites (see, e.g., Fig. 1-(c)). For both cases, we introduce a simplified toy model accounting for occupation defects that result in measurements outcomes  $r^{(j)} \neq \pm 1/2$ .

### III. TOY MODEL

In the lattice system considered one starts from a product state  $|x\rangle^{\otimes N}$  where each atom is in a coherent superposition of two internal states, i.e. coherent spin state (CSS) along the  $x$  direction. The entanglement between spins is dynamically obtained using many-body interactions by different protocols (see e.g., Sec. V and Sec. VI) that can be effectively described, in some limit, by the OAT model

$$\hat{H}_{\text{OAT}} = \hbar \chi \hat{S}_z^2, \quad (5)$$

where  $\chi$  quantifies the strength of interactions and  $\hat{S}_\sigma$  represents the collective spin operator of  $N$  two-level atoms with  $\sigma = x, y, z$ . In (5) we have  $\sigma = z$ . The OAT model generates spin-squeezed states as well as non-Gaussian entangled states, including the GHZ state [45].

In order to study the role of occupation defects in the detection of Bell correlations, we introduce an approximate toy model where the internal and external degrees of freedom of the atoms are decoupled

$$\hat{\rho} = \hat{\rho}_{\text{ext}} \otimes \hat{\rho}_{\text{SS}}. \quad (6)$$

Here  $\hat{\rho}_{\text{SS}}$  describes the internal degrees of freedom of the atoms including entanglement among the spins. In particular, we consider the OAT evolution (5)

$$\hat{\rho}_{\text{SS}} = |\psi_t\rangle\langle\psi_t| \quad \text{with} \quad |\psi_t\rangle = e^{-i\hat{H}_{\text{OAT}}t/\hbar} |x\rangle^{\otimes N}, \quad (7)$$

and  $\hat{\rho}_{\text{ext}}$  describes the external degrees of freedom, which we assume to be factorized over the different lattice sites

$$\hat{\rho}_{\text{extern}} = \bigotimes_{j=1}^M \hat{\rho}_j \quad \text{with} \quad \hat{\rho}_j = p|1\rangle_{jj}\langle 1| + (1-p)\hat{\rho}_j^\perp, \quad (8)$$

where  $|1\rangle_j$  is the Fock state with one spin at site  $j$  and  $p$  is the probability of having a single occupancy state. The probability of having an empty, double, etc., occupied site, as described by  $\hat{\rho}_j^\perp$ , is given by  $(1-p)$ . In practice, in  $\hat{\rho}_j^\perp$  we only consider empty sites or doubly occupied sites. In this framework, when measuring a local spin observable, we assign the value  $r^{(j)} = 0$  to any measurement result different from  $\pm 1/2$ .

#### A. $M$ -site Bell correlations

We now derive a Bell inequality whose violation allows the detection of non-local correlations. For this, from the measurement outcomes, in the two settings  $\alpha = 0, 1$ , in each subsystem we introduce the complex quantity

$$r_+^{(j)} = r_0^{(j)} + i r_1^{(j)} \quad (9)$$

and we consider the product

$$c_M = \prod_{j=1}^M r_+^{(j)}, \quad (10)$$

In a local realistic theory, where the probability distribution  $P_M(r|\alpha)$  has the form of (1) and (2), the average of  $c_M$  over many Bell experiment realizations is given by

$$\langle c_M \rangle = \int d\lambda q(\lambda) \prod_{j=1}^M r_+^{(j)}(\lambda). \quad (11)$$

By introducing the functions  $f(\lambda) = 1$  and  $g(\lambda) = \prod_{j=1}^M r_+^{(j)}(\lambda)$ , and the scalar product  $\langle f, g \rangle = \int d\lambda q(\lambda) f^*(\lambda) g(\lambda)$ , the application of the Cauchy-Schwarz inequality to the functions  $f(\lambda)$  and  $g(\lambda)$ , gives

$$|\langle f, g \rangle|^2 \leq \langle f, f \rangle \langle g, g \rangle. \quad (12)$$

This leads to the following Bell inequality

$$\mathcal{E}_M \equiv |\langle c_M \rangle|^2 \leq \int d\lambda q(\lambda) \prod_{j=1}^M |r_+^{(j)}(\lambda)|^2 \leq 2^{-M}, \quad (13)$$

and  $\mathcal{E}_M$  is the  $M$ -site Bell correlator. We choose, in each site  $j$ , the settings  $\alpha = 0$  and  $\alpha = 1$  corresponding to  $\hat{s}_y^{(j)}$  and  $\hat{s}_z^{(j)}$  respectively [28], to form

$$\hat{s}_+^{(j)} = \hat{s}_y^{(j)} + i \hat{s}_z^{(j)}. \quad (14)$$

It is worth stressing here, that the above setting is optimal for the GHZ state and is less effective for other entangled states generated by the OAT dynamics. The Bell inequality (13) takes the form

$$\mathcal{E}_M = |\langle \hat{s}_+^{(1)} \hat{s}_+^{(2)} \dots \hat{s}_+^{(M)} \rangle|^2 \leq 2^{-M}. \quad (15)$$

When considering the toy model (6), the only nonzero contribution to  $\mathcal{E}_M$  (15) comes from the sites occupied by a single spin. We have

$$\mathcal{E}_M^{(p \neq 1)} = p^{2M} \mathcal{E}_M^{(p=1)}, \quad (16)$$

where  $p^M$  represents the probability that the  $M$  sites are occupied with a single atom. In the non-Gaussian regime of the OAT dynamics (7), a macroscopic superposition of coherent states is created at some particular instants  $\chi\tau = \pi/q$  labelled by an even integer  $q = 2, 4, 6, \dots, M$ , with  $q = 2$  for the GHZ state [28, 45]. The  $M$ -site Bell correlator corresponding to these non-Gaussian spin states, for  $p = 1$ , reads  $\mathcal{E}_M^{(p=1)} \approx 1/q^2$ , see Eq.(17) in [28]. By replacing in (16), one can derive a critical value of  $p$  below which the  $M$ -site Bell correlations present in the states generated at  $\chi\tau = \pi/q$  cannot be detected

$$p_c = \frac{q^{1/M}}{\sqrt{2}}, \quad (17)$$

i.e. for which  $\mathcal{E}_M^{(p=p_c)} = 2^{-M}$ . We note that in the large  $M$  limit we have  $p_c \approx 1/\sqrt{2}$  for all  $q$ .

## B. Two-sites Bell correlations

In the case of the two-sites Bell correlations, we introduce the vector  $\vec{M}$  and the matrix  $\tilde{C}$ , whose elements, for  $\alpha, \beta = 0, 1$ , are respectively given by

$$M_\alpha = \sum_{j=1}^M \langle r_\alpha^{(j)} \rangle \quad (18)$$

$$C_{\alpha\beta} = \sum_{i,j \neq i} \langle r_\alpha^{(i)} r_\beta^{(j)} \rangle, \quad \tilde{C}_{\alpha\beta} = C_{\alpha\beta} - M_\alpha M_\beta. \quad (19)$$

It can be shown [29] that for any input data  $\vec{M}$  and  $\tilde{C}$  compatible with a LV theory (1), any  $2 \times 2$  positive semi-definite matrix  $A$  and any  $2 \times 1$  vector  $\vec{h}$ , the following Bell inequality holds

$$L(A, h) = \text{tr}(A\tilde{C}) + \vec{h} \cdot \vec{M} + E_{\max} \geq 0, \quad (20)$$

where the classical limit is

$$E_{\max} = \max_{\vec{r}} \left[ \vec{r}^T A \vec{r} - \vec{h} \cdot \vec{r} \right], \quad (21)$$

with  $\vec{r} = (r_0, r_1)^T$  being the vector of all possible pairs of outcomes corresponding to the two settings  $\alpha = 0$  and  $\alpha = 1$  for a single subsystem. The positive semi-definite matrix  $A$  and the vector  $\vec{h}$  that minimize  $L(A, h)$  can be found using a data-driven method as in Ref. [29]. We find that the Bell inequality <sup>2</sup>

$$L = \tilde{C}_{00} + \tilde{C}_{11} - \tilde{C}_{01} - \tilde{C}_{10} - M_0 - M_1 + M \geq 0, \quad (22)$$

first established in Ref. [29] for spin-squeezed states in the case of only two possible measurement outcomes, is optimal also in our case with the three possible outcomes (3) and under occupation defects.

For the case of two-sites Bell correlations, we choose  $\alpha = 0$  and  $\alpha = 1$  corresponding to the measurement, at each site  $j$ , of the spin components [29]

$$\hat{s}_0^{(j)} = \hat{s}_{\vec{n}}^{(j)} \cos(\theta) + \hat{s}_{\vec{m}}^{(j)} \sin(\theta), \quad (23)$$

$$\hat{s}_1^{(j)} = \hat{s}_{\vec{n}}^{(j)} \cos(\theta) - \hat{s}_{\vec{m}}^{(j)} \sin(\theta), \quad (24)$$

where the unit vector  $\vec{n}$  is in the spin direction and  $\vec{m}$ , perpendicular to the spin direction, is in the best squeezing direction. The choice of the two settings (23)-(24) is dictated by the geometry of the spin-squeezed states. Non-zero expectation values come from the averages calculated in the plane spanned by the  $\vec{n}$  and  $\vec{m}$  vectors.

<sup>2</sup> Alternatively, the Bell inequality (22) can be represented using the  $C$  matrix, namely  $L = C_{00} + C_{11} - C_{01} - C_{10} - (M_0 - M_1)^2 - M_0 - M_1 + M \geq 0$ .



The averages (18) and the correlations (19) for  $\alpha, \beta \in \{0, 1\}$ , that form the Bell inequality (22), take respectively the form

$$M_\alpha = \sum_{j=1}^M \sum_{r=\pm 1/2} r \operatorname{tr} [\hat{\rho} \hat{\Pi}_{\alpha_j, r}] \quad (25)$$

$$\tilde{C}_{\alpha\beta} = \sum_{i,j \neq i}^M \left( \sum_{r,s=\pm 1/2} r s \operatorname{tr} [\hat{\rho} \hat{\Pi}_{\alpha_i, r} \otimes \hat{\Pi}_{\beta_j, s}] \right) - M_\alpha M_\beta. \quad (26)$$

To account for the occupation defects, we evaluate  $M_\alpha$  and  $\tilde{C}_{\alpha\beta}$  to determine the form of the Bell inequality using the toy model density matrix (6) under the two scenarios investigated in the physical systems presented in Secs. V and VI when  $N \leq M$  and  $N = M$ , respectively.

### 1. Non-unit filling

The first scenario, relevant to the system described in Sec. V, assumes that  $N = pM \leq M$ . Under this condition,  $p < 1$  indicates a non-unit filling of the lattice whose sites are empty or singly occupied. The density matrix  $\hat{\rho}_j^\perp$  in (8), in this scenario, becomes

$$\hat{\rho}_j^\perp = |0\rangle_{jj}\langle 0|. \quad (27)$$

The averages (18) and the correlations (19) for  $\alpha, \beta \in \{0, 1\}$  are in this case

$$M_\alpha = \langle \hat{S}_{\vec{n}} \rangle_{\text{SS}} \cos(\theta), \quad (28)$$

$$\tilde{C}_{\alpha\beta} = \frac{N-p}{N-1} \left\{ (\Delta \hat{S}_{\vec{n}})_{\text{SS}}^2 \cos^2(\theta) - (-1)^{\delta_{\alpha\beta}} (\Delta \hat{S}_{\vec{m}})_{\text{SS}}^2 \sin^2(\theta) - \frac{N}{4} \cos[2\theta(1 - \delta_{\alpha\beta})] \right\} + \frac{1-p}{N-1} \langle \hat{S}_{\vec{n}} \rangle_{\text{SS}}^2 \cos^2(\theta). \quad (29)$$

The Bell inequality (22) is given, for this scenario, by

$$\frac{L_\theta^{(V)}}{M} = \frac{p(N-p)}{N-1} \sin^2(\theta) \left( \frac{4(\Delta \hat{S}_{\vec{m}})_{\text{SS}}^2}{N} - 1 \right) - 2p \frac{\langle \hat{S}_{\vec{n}} \rangle_{\text{SS}}}{N} \cos(\theta) + 1 \geq 0. \quad (30)$$

The minimization of  $L_\theta^{(V)}$  with respect to  $\theta$  gives

$$\frac{L^{(V)}}{M} = 1 - \frac{p(N-1)}{N-p} \frac{\langle \hat{S}_{\vec{n}} \rangle_{\text{SS}}^2}{N [N - 4(\Delta \hat{S}_{\vec{m}})_{\text{SS}}^2]} - \frac{p(N-p)}{N-1} \left[ 1 - \frac{4(\Delta \hat{S}_{\vec{m}})_{\text{SS}}^2}{N} \right], \quad (31)$$

for an optimal  $\theta$  such that  $\cos \theta_{\text{opt}} = \frac{N-1}{N-p} \frac{\langle \hat{S}_{\vec{n}} \rangle_{\text{SS}}}{N - 4(\Delta \hat{S}_{\vec{m}})_{\text{SS}}^2}$ <sup>3</sup>. The equation (31) is represented in Fig. 2 as a function

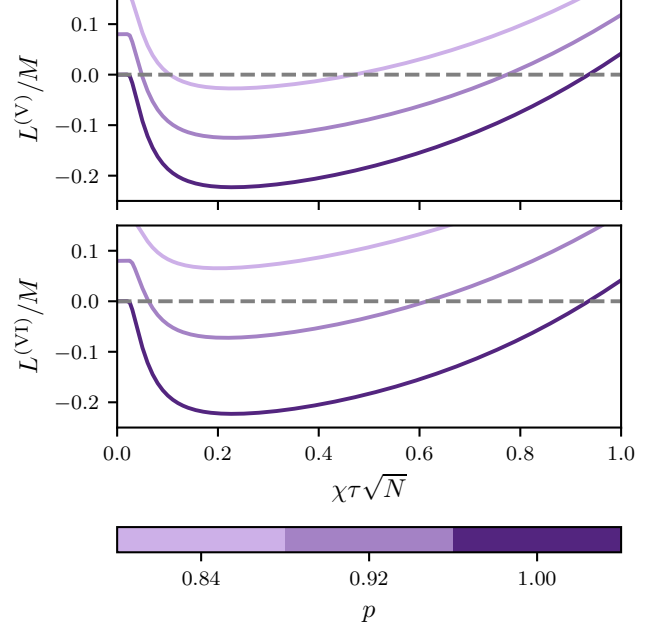


FIG. 2. Variation of the non-locality witness  $L_{\text{opt}}/M$ , given by (39) in the upper panel and (31) in the lower panel, during the one-axis twisting dynamics with  $N = 10^3$  for different values of  $p$  (probability of single occupation of a given site). The flat behaviour at short times happens because of the optimization condition.

of time of the OAT dynamics for a given  $N$  and for different values of the occupation probability  $p$ . This reveals that for a given  $N$  and at each moment of time  $\tau$ , there is a critical value of  $p$  below which, the two-site Bell correlations present in the system cannot be detected. This critical probability  $p = p_c$  is the value for which, the following 3<sup>rd</sup> order equation holds

$$p^3 - 2N \left( 1 - \frac{4(\Delta \hat{S}_{\vec{m}})_{\text{SS}}^2}{N} \right) p^2 + [N^2 + N - 1] p + \left[ 4N(\Delta \hat{S}_{\vec{m}})_{\text{SS}}^2 + \frac{(N-1)^2 \langle \hat{S}_{\vec{n}} \rangle_{\text{SS}}^2}{N [N - 4(\Delta \hat{S}_{\vec{m}})_{\text{SS}}^2]} \right] p - N(N-1) = 0. \quad (33)$$

In the limit of large atom number  $N$ , the minimal value

the restriction  $p \leq N - (N-1) \frac{\langle \hat{S}_{\vec{n}} \rangle_{\text{SS}}}{[N - 4(\Delta \hat{S}_{\vec{m}})_{\text{SS}}^2]}$ . Here,  $L^{(V)}$  can be written in terms of the squeezing parameter  $\xi^2 = N(\Delta \hat{S}_{\vec{m}})_{\text{SS}}^2 / \langle \hat{S}_{\vec{n}} \rangle_{\text{SS}}^2$  and the normalized mean spin  $v = \langle \hat{S}_{\vec{n}} \rangle_{\text{SS}} / (N/2)$  as

$$\frac{L^{(V)}}{M} = 1 - \frac{p(N-1)}{N-p} \frac{v^2/4}{1 - \xi^2 v^2} - \frac{p(N-p)}{N-1} (1 - \xi^2 v^2). \quad (32)$$

<sup>3</sup> This solution should verify  $|\cos(\theta_{\text{opt}})| \leq 1$ , which introduces



of (31), over  $\chi\tau$ , converges to the  $p$ -dependent constant

$$\frac{L_{\min}^{(\text{V})}}{M} \approx 1 - \frac{5}{4}p, \quad (34)$$

and the corresponding critical value of the occupation probability tends to  $p_c = 4/5$ .

## 2. Doubly occupied sites

In this scenario, relevant to the system described in Sec. VI, we assume that  $N = M$ . Under this condition,  $p < 1$  indicates a redistribution of the  $N$  atoms among the  $M$  lattice sites resulting in the emergence of both empty and doubly occupied sites. The filling factor is one,  $f = 1$ . Thus, the density matrix  $\hat{\rho}_j^\perp$  in (8) can be written as

$$\hat{\rho}_j^\perp = \frac{|0\rangle_{jj}\langle 0| + |2\rangle_{jj}\langle 2|}{2}. \quad (35)$$

The calculation of the averages (18) and the correlations (19) for  $\alpha, \beta \in \{0, 1\}$  gives

$$M_\alpha = p\langle \hat{S}_{\vec{n}} \rangle_{\text{SS}} \cos(\theta), \quad (36)$$

$$\begin{aligned} \tilde{C}_{\alpha\beta} &= p^2(\Delta\hat{S}_{\vec{n}})_{\text{SS}}^2 \cos^2(\theta) - (-1)^{\delta_{\alpha\beta}} p^2(\Delta\hat{S}_{\vec{m}})_{\text{SS}}^2 \sin^2(\theta) \\ &\quad - p^2 \frac{N}{4} \cos[2\theta(1 - \delta_{\alpha\beta})], \end{aligned} \quad (37)$$

where the subscript SS refers to an expectation calculated in the  $\hat{\rho}_{\text{SS}}$  state (7), and the Bell inequality (22) reads

$$\begin{aligned} \frac{L_\theta^{(\text{VI})}}{M} &= p^2 \sin^2(\theta) \left( \frac{4(\Delta\hat{S}_{\vec{m}})_{\text{SS}}^2}{N} - 1 \right) \\ &\quad - 2p \frac{\langle \hat{S}_{\vec{n}} \rangle_{\text{SS}}}{N} \cos(\theta) + 1 \geq 0. \end{aligned} \quad (38)$$

By minimizing  $L_\theta^{(\text{VI})}$  with respect to  $\theta$  we obtain

$$\frac{L^{(\text{VI})}}{M} = 1 - \frac{\langle \hat{S}_{\vec{n}} \rangle_{\text{SS}}^2}{N [N - 4(\Delta\hat{S}_{\vec{m}})_{\text{SS}}^2]} - p^2 \left[ 1 - \frac{4(\Delta\hat{S}_{\vec{m}})_{\text{SS}}^2}{N} \right], \quad (39)$$

for an optimal  $\theta$  such that  $\cos\theta_{\text{opt}} = \frac{1}{p} \frac{\langle \hat{S}_{\vec{n}} \rangle_{\text{SS}}}{N - 4(\Delta\hat{S}_{\vec{m}})_{\text{SS}}^2}$ .<sup>4,5</sup>

The equation (39) is represented in Fig. 2 as a function of time  $\tau$  of the OAT dynamics for a given  $N$  and for

different values of  $p$ . We note that for a given  $N$  and at each moment of time, there is a critical value of  $p$  below which, the two-site Bell correlations present in the system cannot be detected, from (39) we obtain

$$p_c = \frac{\sqrt{N [N - 4(\Delta\hat{S}_{\vec{m}})_{\text{SS}}^2] - \langle \hat{S}_{\vec{n}} \rangle_{\text{SS}}^2}}{N - 4(\Delta\hat{S}_{\vec{m}})_{\text{SS}}^2}. \quad (41)$$

In the limit of large atom number  $N$ , the minimal value of (39), over  $\chi t$ , approaches a  $p$ -dependent constant value

$$\frac{L_{\min}^{(\text{VI})}}{M} \approx \frac{3}{4} - p^2, \quad (42)$$

and the corresponding critical probability  $p_c$  approaches  $p_c = \sqrt{3}/2$ . A lower value of  $p$  can be obtained with a Bell inequality including onsite and two-site correlations up to the fourth-order. In the limit of large  $N$ , this leads to a critical occupation probability of  $p_c = 1/2$  [46].

## IV. APPLICATION WITH ULTRA-COLD ATOMS IN OPTICAL LATTICES

We test the predictions of our toy model using a system consisting of  $N$  ultra-cold bosonic atoms confined in an optical lattice. We focus on rubidium-87 atoms occupying two internal states, labelled  $a$  and  $b$ , and loaded into an optical lattice potential, akin to recent experiments employing quantum gas microscopes [47, 48]. The optical lattice comprises  $M$  lattice sites and is considered to be in one dimension.

The system, in the lowest energy band, is conveniently considered in the Wannier functions basis [49]. In the tight-binding limit, where the lattice potential exceeds the recoil energy  $E_R = \hbar^2 k^2 / (2m)$ , the system can be conveniently described by the Bose-Hubbard model,

$$\begin{aligned} \hat{H}_{\text{BH}} &= -t \sum_{i,j=i\pm 1} \left( \hat{a}_i^\dagger \hat{a}_j + \hat{b}_i^\dagger \hat{b}_j \right) + \frac{U_{aa}}{2} \sum_{i=1}^M \hat{n}_i^a (\hat{n}_i^a - 1) \\ &\quad + \frac{U_{bb}}{2} \sum_{i=1}^M \hat{n}_i^b (\hat{n}_i^b - 1) + U_{ab} \sum_{i=1}^M \hat{n}_i^a \hat{n}_i^b, \end{aligned} \quad (43)$$

where  $t$  and  $U_{\sigma\sigma'}$  are the tunneling and interaction parameters.  $\hat{a}_i$  ( $\hat{b}_i$ ) is the annihilation operator of an atom in internal state  $a$  ( $b$ ) in the  $i$ -th site of the lattice, and  $\hat{n}_i^a = \hat{a}_i^\dagger \hat{a}_i$ ,  $\hat{n}_i^b = \hat{b}_i^\dagger \hat{b}_i$  are the corresponding number operators.

We explore two protocols for the dynamical generation of Bell correlations within this system as detailed in Sections V and VI, both resulting in Mott entangled states where atoms exhibit spin entanglement and are evenly distributed across the lattice. In both cases, the initial state  $\hat{\rho}_a$  with all atoms in the internal state  $|a\rangle$  is turned into a coherent superposition of  $|a\rangle$  and  $|b\rangle$  by applying a  $\pi/2$ -pulse, which is equivalent to

$$\hat{\rho}_{\text{ini}} = e^{-i\hat{S}_y\pi/2} \hat{\rho}_a e^{i\hat{S}_y\pi/2}. \quad (44)$$

<sup>4</sup> This solution should verify  $|\cos(\theta_{\text{opt}})| \leq 1$  which introduces the restriction  $p \geq |\langle \hat{S}_{\vec{n}} \rangle_{\text{SS}}| / [N - 4(\Delta\hat{S}_{\vec{m}})_{\text{SS}}^2]$ .

<sup>5</sup> An alternative formula of  $L^{(\text{VI})}$  can be obtained by introducing the spin squeezing parameter  $\xi^2$  and the normalized mean spin  $v$  as

$$\frac{L^{(\text{VI})}}{M} = 1 - \frac{v^2/4}{1 - \xi^2 v^2} - p^2(1 - \xi^2 v^2). \quad (40)$$



The two protocols differ in their specific mechanisms for inducing entanglement in the system and hence in the relevant source of occupation defects.

In the first protocol, Bell correlations are generated directly in the strongly interacting Mott regime  $U_{\sigma\sigma'} \gg t$  where individual spins interact via spin-exchange interactions between neighbouring spins (46). These interactions allow for the generation of entanglement within the system either through weak anisotropy or by coupling with an inhomogeneous field. The mechanism for generating entanglement was explained and demonstrated in prior works such as [41, 42, 50]. In the second protocol, Bell correlations are induced by atom-atom interactions in the superfluid regime  $t \gg U_{\sigma\sigma'}$  with all-to-all individual spin connections. Subsequently, these correlations are transferred to the Mott phase by an adiabatic increase of the optical lattice depth, a process described in detail in previous studies [28, 31, 32].

The final state of both protocols allows measuring spin components at a specific lattice site. In the Bell scenario, the outcomes of local measurements across all lattice sites can be collected, and used for the detection of Bell correlations using inequalities (15) and (22). In the ideal realization of the Mott phase protocol, when  $\hat{\rho}_a$  is the ground state where each lattice site hosts precisely one atom, two distinct measurement outcomes are possible. However, imperfections introduce non-unit filling throughout the lattice, leading to additional measurement outcomes, such as when a site is either empty or double occupied. These failures arise from imperfect preparation of initial state  $\hat{\rho}_a$  or to non-zero temperature.

In the following sections, we consider the role of imperfections and we establish a connection between the factor  $p$  of the toy model (6) and the filling factor  $f = N/M$  or the initial temperature  $T$  for these two protocols.

## V. ENTANGLEMENT GENERATION IN THE MOTT PHASE

In the strongly interacting limit  $U_{\sigma\sigma'} \gg t$  and in the ground state manifold with at most one atom per lattice site, the system (43) is approximately described by the  $t$ - $J$  model

$$\hat{H}_{t-J} = -t \sum_{i,j=\pm 1} \hat{P}_0 \left( \hat{a}_i^\dagger \hat{a}_j + \hat{b}_i^\dagger \hat{b}_j \right) \hat{P}_0 + \hat{H}_{\text{XXZ}}, \quad (45)$$

where  $\hat{P}_0$  is a projector operator over the manifold of at most single occupancy states, and where

$$\hat{H}_{\text{XXZ}} = -J \sum_{j=1}^{M-1} \left( \hat{s}_x^{(j)} \hat{s}_x^{(j+1)} + \hat{s}_y^{(j)} \hat{s}_y^{(j+1)} + \Delta \hat{s}_z^{(j)} \hat{s}_z^{(j+1)} - \frac{1}{4} \right), \quad (46)$$

is the Heisenberg XXZ model with the spin-exchange interaction parameter  $J = 4t^2/U_{ab}$  and the anisotropy parameter  $\Delta = U_{ab}/U_{aa} + U_{ab}/U_{bb} - 1$  [51]. When  $\Delta = 1$

the Hamiltonian takes the form of the isotropic Heisenberg XXX model and it is a natural case for rubidium-87 where  $U_{aa} \approx U_{bb} \approx U_{ab}$ . The anisotropy parameter  $\Delta$  can be tuned by changing the values of interaction strengths using either Feshbach resonances or by shifting optical lattice potentials for states  $a$  and  $b$ . The collective spin operators are just a summation over the individual ones,  $\hat{S}_\sigma = \sum_{j=1}^M \hat{s}_\sigma^{(j)}$  for  $\sigma = x, y, z, \pm$ . The tunnelling term in (45) is relevant whenever the filling factor  $f = N/M$  is not one, meaning there are holes (empty sites) in the system and  $N \leq M$ .

Let us consider the case of zero temperature when the initial state  $\hat{\rho}_a$  is in the Mott regime. In the ideal case, we have  $\hat{\rho}_a = \bigotimes_{j=1}^M |a\rangle\langle a|_j$ , indicating that at each lattice site there is an atom in the internal state  $|a\rangle$ . However, in the presence of holes, the on-site state can be  $|0\rangle\langle 0|_j$  if it is not occupied. In the given experimental realisation, the number of holes can be arbitrary as well as their positions. In our simulations, we evolve single realizations with initially each site being empty or singly occupied, and then average over many realizations to evaluate expectation values. Specifically, we generate a random number  $x_j \in (0, 1]$  for each lattice site, obtaining

$$|\Psi_x\rangle_j = \bar{\theta}(f - x_j)|a\rangle_j + (1 - \bar{\theta}(f - x_j))|0\rangle_j, \quad (47)$$

where  $\bar{\theta}(x)$  is the Heaviside step function. The density matrix  $\hat{\rho}_a$  describing  $N_r$  realizations is obtained through a simple averaging,

$$\hat{\rho}_a = \frac{1}{N_r} \sum_{r=1}^{N_r} \left[ \bigotimes_{j=1}^M |\Psi_x\rangle\langle\Psi_x|_j \right], \quad (48)$$

over the set of on-site random numbers  $r = \{x_j^1, x_j^2, \dots, x_j^{N_r}\}$  for all  $j \in \{1, \dots, M\}$ . One can show, that in the continuous limit, we obtain

$$\hat{\rho}_a = \bigotimes_{j=1}^M (f|a\rangle\langle a|_j + (1 - f)|0\rangle\langle 0|_j), \quad (49)$$

given that all the sites are equivalent. Therefore, the filling factor  $f$  can be identified with the parameter  $p$  of the external state of the toy model (6) provided that  $\hat{\rho}_j^\perp = |0\rangle\langle 0|_j$ . Owing to the presence of holes, the average number of atoms  $N$  differs from the number of lattice sites  $M$  when  $f \neq 1$ , namely  $N = fM$ .

It is worth noting here, that the density matrix  $\rho_a$



in (49) can also be cast in the following way

$$\begin{aligned}\hat{\rho}_a = & f^M \bigotimes_{j=1}^M |a\rangle\langle a|_j \\ & + f^M \left(\frac{1-f}{f}\right)^1 \left( |0\rangle\langle 0|_1 \bigotimes_{j=1}^{M-1} |a\rangle\langle a|_j + \mathcal{P}_1 \right) \\ & + f^M \left(\frac{1-f}{f}\right)^2 \left( |0\rangle\langle 0|_1 \otimes |0\rangle\langle 0|_2 \bigotimes_{j=1}^{M-2} |a\rangle\langle a|_j + \mathcal{P}_2 \right) \\ & + \dots, \end{aligned} \quad (50)$$

where  $\mathcal{P}_\sigma$  are all other configurations with  $\sigma$  holes. The state (50) can be written using the shorter notation

$$\hat{\rho}_a = f^M \left[ \bigotimes_{j=1}^M |a\rangle\langle a|_j + \sum_{\sigma=1}^M \left(\frac{1-f}{f}\right)^\sigma \Sigma_\sigma [\hat{\rho}_\sigma] \right], \quad (51)$$

where  $\hat{\rho}_\sigma$  is the product state of a given configuration having  $\sigma$  holes and  $1-\sigma$  occupied sites while  $\Sigma_\sigma$  represents summation over permutations of all possible configurations.

Having the above expression, the initial spin coherent state (44) can be expressed as follows:

$$\hat{\rho}_{\text{ini}} = f^M \left[ \hat{\rho}_{\text{ini}}^{(0)} + \sum_{\sigma=1}^M \left(\frac{1-f}{f}\right)^\sigma \Sigma_\sigma [\hat{\rho}_{\text{ini}}^{(\sigma)}] \right], \quad (52)$$

where the rotations act on the density matrix corresponding to specific configurations of  $\sigma$  holes

$$\hat{\rho}_{\text{ini}}^{(\sigma)} = e^{-i\hat{S}_y\pi/2} \hat{\rho}_\sigma e^{i\hat{S}_y\pi/2}, \quad (53)$$

and  $\hat{\rho}_{\text{ini}}^{(0)} = e^{-i\hat{S}_y\pi/2} \left( \bigotimes_{j=1}^M |a\rangle\langle a|_j \right) e^{i\hat{S}_y\pi/2}$ . Therefore, any expectation values of the operator  $\hat{O}$  can be evaluated as

$$\langle \hat{O} \rangle = f^M \left[ \text{Tr}[\hat{\rho}_{\text{ini}}^{(0)} \hat{O}] + \sum_{\sigma=1}^M \left(\frac{1-f}{f}\right)^\sigma \langle \hat{O} \rangle_\sigma \right], \quad (54)$$

where  $\langle \hat{O} \rangle_\sigma = \Sigma_\sigma \text{Tr}[\hat{\rho}_{\text{ini}}^{(\sigma)} \hat{O}]$ , and where summation runs over all configurations of  $\sigma$  holes on  $M$  lattice sites.

In Subsections VB and VC, we employ the above-discussed approach for the numerical evaluation of Bell correlations and the critical value of the filling factor allowing for their detection. Before, however, let us discuss the mechanism responsible for generating entanglement within the system in the Mott phase.

### A. Effective microscopic description

To generate entanglement from the initial spin coherent states (52) driven by the  $t$ - $J$  Hamiltonian (45) we

consider two methods. Both of them were thoroughly investigated in [41].

The first (A) uses a weak anisotropy  $\Delta \neq 1$  in (46), such that  $\Delta \ll 3 - 2\cos(\pi/M)$  and  $\Delta \gg 2\cos(\pi/M) - 1$ , to generate entanglement in the system. Under an ideal scenario with  $N = M$ , the system can be represented by a single spin chain whose dynamics is described by the OAT model [41]. The presence of holes divides the spin chain into partial chains separated by holes whose configurations are included in (52). For instance, if a single hole is located somewhere in the middle of the chain (not at the borders), the system can be effectively viewed as two partial chains. The system dynamics composed of the partial chains separate only when the positions of holes are fixed. The microscopic model describing the dynamics of each specific configuration involved in (50) is effectively approximated by the OAT model when the positions of holes are pinned to the lattice. The model describing each of  $n$  partial chains for a given configuration of  $\sigma$  holes reads

$$\hat{H}_{\text{eff},n}^{(0)} = -\chi_n^{(0)} \hat{S}_{z,n}^2, \quad \text{with } \chi_n^{(0)} = \frac{J(\Delta - 1)}{(L_n - 1)}, \quad (55)$$

where  $L_n$  is the number of atoms consisting of the partial chain.

The second method (B) uses a weak inhomogeneous magnetic field

$$\hat{H}_B = \sum_j \beta_j \hat{s}_z^{(j)}, \quad (56)$$

with  $\beta_j \ll J[\cos(\frac{\pi}{N}) - 1]$ , for the isotropic case  $\Delta = 1$  to generate entanglement in the system. In this case, when  $\sigma$  holes are pinned into the lattice, the effective model describing each of the  $n$  partial chains is described effectively by the following Hamiltonian

$$\hat{H}_{\text{eff},n} = \chi_n \hat{S}_{z,n}^2 + v_n \hat{S}_{z,n}, \quad (57)$$

where we omitted constant energy terms, and where

$$\chi_n = \frac{1}{L_n - 1} \sum_{q=1}^{L_n-1} \frac{|c_n^{(q)}|^2}{E_n^{(q)}}, \quad (58)$$

$$v_n = \frac{1}{L_n} \sum_{l=l_n}^{l_n+L_n-1} \beta_l, \quad (59)$$

$$c_n^{(q)} = \frac{\sqrt{2}}{L_n} \sum_{l=l_n}^{l_n+L_n-1} p_l^{(q,n)} (\beta_l - v_n), \quad (60)$$

with  $l_n$  being the location of the first spin in the partial chain and  $E_n^{(q)} = J(1 - \cos(\pi q/L_n))$ .

The effective models for the (A) and (B) methods are derived and explained in detail in [41]. Their validity for describing spin-squeezing generation was also demonstrated.

Therefore, one can employ the effective models based on the OAT dynamics for partial chains when evaluating expectation values as given by (54) when considering



fixed positions of holes (effectively  $t = 0$  in the  $t$ - $J$  model (45)). We employ them to calculate the upper bound on the filling factor required for the Bell correlations detection as demonstrated in V C. However, the effective models become inaccurate when the tunnelling of holes occurs. In such a case, we perform full numerical many-body calculations by the exact diagonalization method of the  $t$ - $J$  model (45) when demonstrating Bell correlations and validity of the Toy model.

In the next subsections, we demonstrate the generation of Bell correlations in the system using scenarios A and B. In our numerical simulations, we consider open boundary conditions [41] and use the parameters as in the recent experiment of A. Rubio-Abadal et al [47] with  $^{87}\text{Rb}$  atoms, lattice spacing  $d = 532$  nm, and inter- and intraspecies interactions  $U_{aa} \sim U_{bb} \sim U_{ab} = U$  [52] with  $U = 24.4t$ .

### B. $M$ -site Bell correlations

We numerically evaluate the many-body Bell correlator  $\mathcal{E}_M = |\langle \hat{s}_{1,+} \dots \hat{s}_{M,+} \rangle|^2$  as defined in (15) for the initial spin coherent state given by (52).

In the upper panel of Fig. 3 we show the evolution of the  $M$ -site Bell correlator  $\mathcal{E}_M$  with  $M = 12$  and for the two proposed methods, A and B. The small shift in time scale and lower magnitude of the correlator maxima in the anisotropic case result from its effective model being approximated to the first order [41]. The only relevant contribution comes from the part of the system state describing all sites occupied, as already discussed in Section III. The tunnelling of holes cannot change the value of this correlator.

In the lower panel of Fig. 3 we check the scaling of the correlator with the filling factor  $f$  for relevant instances in time using a logarithmic scale. We see good agreement with the scaling of the toy model result in Eq. (16) when identifying  $p$  with  $f$ . Likewise, we see the GHZ state result crossing the classical limit at the value obtained in Eq. (17) for  $q = 2$ , identified by the edge of the grey area.

### C. Two-sites Bell correlations

In the short-time dynamics, where spin squeezing is generated, the two-site Bell correlator  $L$  given by (22) is more relevant.

In Fig. 4 we demonstrate the variation of the two-sites Bell correlations generated using the method A (interactions anisotropy, left column) and B (inhomogeneous magnetic field, right column) for different filling factors and effective tunnelling rates  $t/J$ . The color bar indicates the magnitude of effective tunnelling when holes are present in the system relative to the relevant energy scale  $J$ . While in all instances  $t \neq 0$  to have a non-zero value of  $J$ , we assume for the effective tunnelling  $t/J = 0$

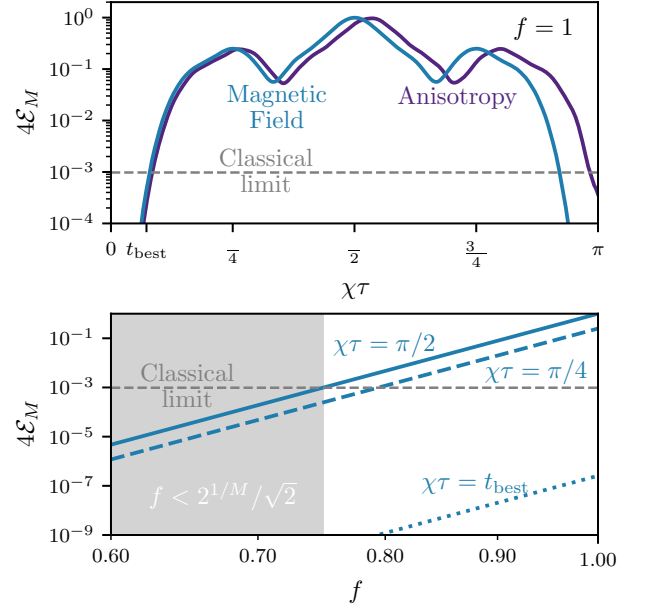


FIG. 3.  $M$ -sites Bell correlator  $\mathcal{E}_M = |\langle \otimes_j^M \hat{s}_j^+ \rangle|^2$  for the Hamiltonian (45) with  $M = 12$  sites under scenario A (Anisotropy) with  $\Delta = 0.98, \beta_j = 0$  (blue line) and scenario B (Magnetic Field) with  $\Delta = 1, \beta_j = J/50 \cos[\pi(M-1)/M(j-1/2)]$  (orange lines). Upper panel shows the evolution of the correlator for  $f = 1$ . Lower panel shows the scaling at a particular moment in time with the filling factor  $f$  for scenario B. The solid line corresponds to the GHZ state, the dashed line to a superposition of  $q = 4$  coherent states, and the dotted line to the best spin-squeezing time  $t_{\text{best}}$ . The logarithmic scale has been used to illustrate the power-law influence of  $f$  and the classical limit  $2^{-M}$ .

that positions of spins are fixed for those particular numerical simulations. Shaded areas indicate the upper and lower boundaries set by the results of holes fixed in place and holes moving infinitely fast, respectively. The upper bound is calculated numerically for the case of the fixed position of holes by using effective models as described in [41]. The lower bound is given by the toy model and the corresponding Bell inequality (31) where expectation values  $\langle \cdot \rangle_{\text{SS}}$  are replaced with the one given by the corresponding OAT model. We also observe the generation of Bell correlations requires a larger filling factor in the inhomogeneous magnetic field scenario; both when the movement of holes is allowed and when not. Nevertheless, the numerical results demonstrate the effectiveness of the proposed toy model (31) in the estimation of the lower bound in the detection of two-sites Bell correlations.

Note, the microscopic effective models (55) and (57) differ by the presence of a linear term, such that their results will be bounded by different limits as illustrated in Fig. 5. The critical value for the lower bound in this figure is obtained by solving the corresponding cubic equation by setting (31) to zero, for which only one

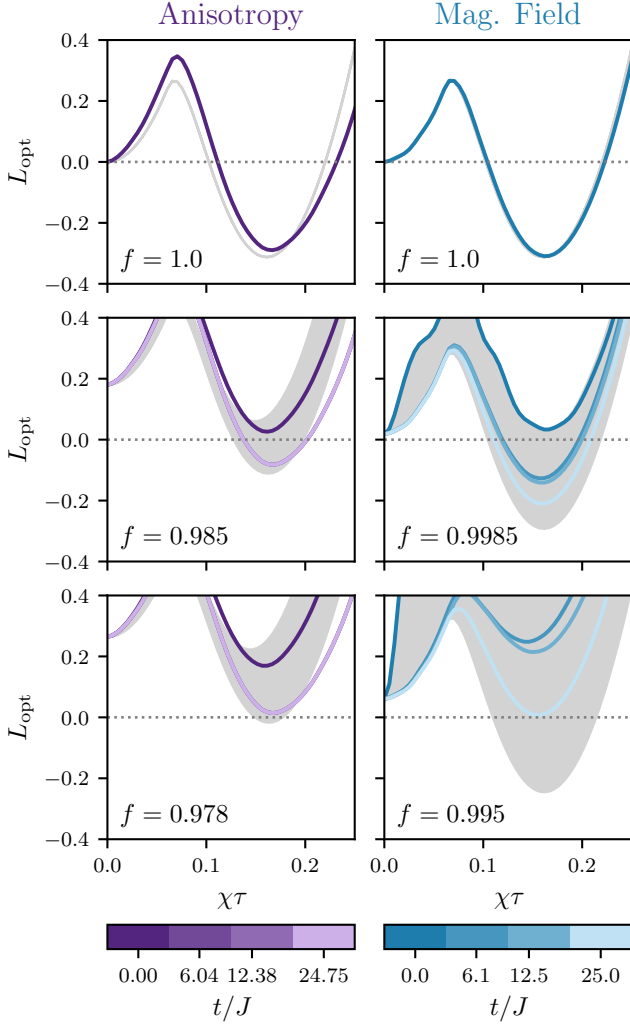


FIG. 4. Evolution of the two-sites Bell correlator (22) optimized over  $\theta$  for the Hamiltonian (45) with  $M = 12$  sites under the scenario A (Anisotropy) with  $\Delta = 0.98, \beta_j = 0$  (left column) and scenario B (Mag. Field) with  $\Delta = 1, \beta_j = J/50 \cos[\pi(M-1)/M(j-1/2)]$  (right column). Each panel corresponds to a given filling factor  $f$ , as indicated in their lower left corners. Lines of different colours show different values of  $t/J$  (see colour bars). Grey areas indicate the regions between the lower and upper bounds as explained in the text, where  $\chi$  is calculated with (55) or (58) assuming a single chain of size  $M$ .

real root exists. The anisotropy scenario A, while less accurately described by the corresponding effective OAT model (55) as explained in [41], achieves lower bound results predicted by the toy model (31) when tunnelling processes happen. This is much harder to achieve in the inhomogeneous magnetic field scenario B since the linear term in (57) changes at each configuration of holes and makes the dynamics largely incoherent. This is a stark contrast with the M-site Bell correlator presented in Fig. 3 where we find the lower bound set by the toy

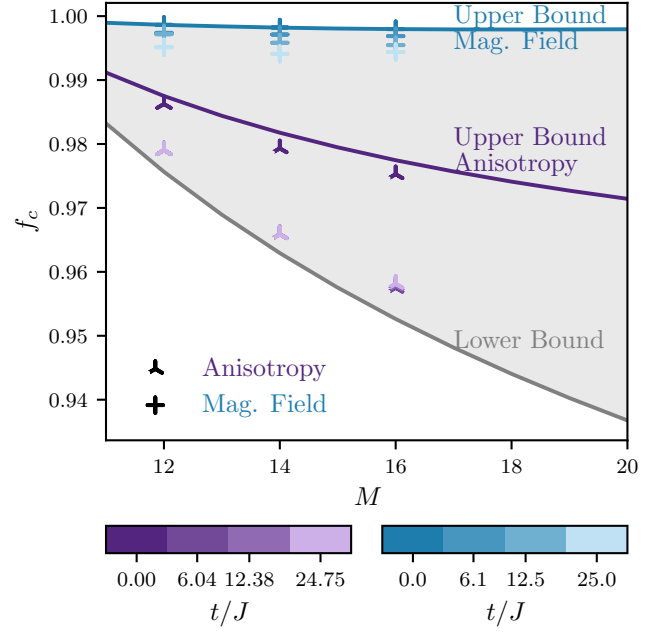


FIG. 5. Critical value of filling factor  $f_c$  with respect to system size  $M$  for the Hamiltonian (45) under scenario A (Anisotropy) with  $\Delta = 0.98, \beta_j = 0$  (triangular markers) and scenario B (Mag. Field) with  $\Delta = 1, \beta_j = J/50 \cos[\pi(M-1)/M(j-1/2)]$  (cross markers). The lower and upper bounds are shown in solid lines, with the area between them filled in grey. We use a first passage algorithm with similar data to the one used in Fig. 4 to obtain these values. Due to numerical calculation costs, results for  $M = 12$  include configurations of all possible numbers of holes in the initial state, while results for  $M = 14, 16$  include configurations with, at least, up to three holes.

model (16) to be equally accurate.

## VI. ENTANGLEMENT GENERATION IN THE SUPERFLUID PHASE

We consider here the protocol where the quantum correlations are generated using atom-atom interactions within the superfluid phase and then stored in the Mott phase through adiabatic increasing of the lattice height [43, 53]. The tunnelling parameter  $t$  and interaction parameters  $U_{\sigma\sigma'}$  are then approximated as [53]

$$t \approx \frac{4}{\sqrt{\pi}} \left( \frac{V_0}{E_r} \right)^{3/4} e^{-2\sqrt{V_0/E_r}}, \quad (61)$$

$$U_{\sigma\sigma'} \approx \sqrt{\frac{32}{\pi}} \frac{a_{\sigma\sigma'} d}{L_{\perp}^2} \left( \frac{V_0}{E_r} \right)^{1/4}, \quad (62)$$

where  $a_{\sigma\sigma'}$  are the s-wave scattering lengths,  $V_0$  is the lattice potential depth and  $L_{\perp}$  is characteristic length of the wave-function perpendicular to the lattice direction. In this protocol, initially, all atoms occupy the internal



state  $a$ , and at zero temperature, they are in the ground state of the Bose-Hubbard Hamiltonian  $|\psi_0^{(a)}\rangle$  in the superfluid regime. Subsequently, a  $\pi/2$  pulse is applied to put the atoms in a coherent spin state where the collective spin is along the  $x$ -axis. During the dynamics, the lattice height  $V_0$  linearly increases as

$$V_0(\tau) = V_{\text{ini}} + (V_{\text{fin}} - V_{\text{ini}}) \frac{\tau}{\tau_{\text{ramp}}}, \quad (63)$$

such that, at  $\tau = \tau_{\text{ramp}}$ , for an adiabatic evolution and initially zero temperature, the system reaches the Mott-squeezed state where the atoms are spatially distributed with one atom per lattice site and show entanglement in their internal degree of freedom (from spin squeezed state up to a GHZ state according to the chosen ramp duration  $\tau_{\text{ramp}}$ ). This corresponds to a state of the form (6) with  $\hat{\rho}_{\text{ext}} = \bigotimes_{i=1}^M |1\rangle_{jj}\langle 1|$ . At finite temperature  $T$ , the system exhibits initial thermal fluctuations described by the density operator

$$\hat{\rho}_T = \frac{1}{Z} \sum_n e^{-E_n^{(0)}/k_B T} |\psi_n^{(a)}\rangle \langle \psi_n^{(a)}|, \quad (64)$$

where  $k_B$  is the Boltzmann constant,  $E_n^{(0)}$  are the eigenenergies of the initial Hamiltonian (in the superfluid phase), all atoms are in the internal mode  $a$  so  $|\psi_n^{(a)}\rangle$  are the corresponding eigenstates, and  $Z = \sum_n e^{-E_n^{(0)}/k_B T}$  is the normalization constant. These initial thermal fluctuations lead, at the end of the ramp, to a non-zero probability of having holes and double occupations of the lattice sites. In this section, we explore the effect of these initial thermal fluctuations on the detection of the  $M$ -site and two-sites non-local Bell correlations present in the final state. We first note that numerical observations performed in small 1D lattices reveal that when  $U_{aa} = U_{bb} \gtrsim U_{ab} > 0$ , which is relevant to our purposes, the external dynamics is weakly affected by the internal dynamics up to the Mott transition. Consequently, we estimate the occupation statistics of different lattice sites in the final state by restricting the Bose-Hubbard model to a single internal state  $a$ . In this case, the spectrum of the Hamiltonian in the deep Mott phase with  $t \rightarrow 0$ , is simple: a non-degenerate ground state  $|\psi_0^{\text{MI}}\rangle$ , with one atom per lattice site, and gapped excited states  $|\psi_n^{\text{MI}}\rangle$  showing holes and doubly occupied sites. The ground state  $|\psi_0^{\text{MI}}\rangle$  is obtained, from the initial ground superfluid state  $|\psi_0^{(a)}\rangle$ , by a unitary evolution with the time dependent Bose-Hubbard Hamiltonian

$$|\psi_0^{\text{MI}}\rangle = \hat{U} |\psi_0^{(a)}\rangle. \quad (65)$$

### A. $M$ -site Bell correlations

Since the excited states  $|\psi_n^{\text{MI}}\rangle$  have at least one hole and one doubly occupied lattice site, they give no contribution to the  $M$ -site Bell correlator (16) whose value at

non-zero temperature is given by

$$\mathcal{E}_M^{(T \neq 0)} = P_0^2 \mathcal{E}_M^{(T=0)}, \quad (66)$$

where  $P_0 = e^{-E_0^{(0)}/k_B T}/Z$  represents the probability of occupying the ground state in (64)<sup>6</sup>. The upper panel of Fig. 6 illustrates this relationship for  $N = M = 4$  over varying temperatures, revealing the existence of a critical temperature  $T_c$  below which  $M$ -site Bell correlations are detectable. In the weakly interacting regime, the probability  $P_0$  can be analytically determined using the Bogoliubov theory, where, in the initial superfluid regime, when all the atoms occupy the internal state  $a$ , the system can be approximately described by the Hamiltonian

$$\hat{H}_{\text{Bog}} = E_0 + \sum_{j \neq 0} \hbar \omega_j \hat{d}_j^\dagger \hat{d}_j. \quad (67)$$

In equation (67),  $E_0$  is the ground state energy of the system,  $\hat{d}_j$  is the annihilation operator of a Bogoliubov quasi-particle associated with the quasi-momentum  $q_j$ , and  $\hbar \omega_j$  is given in terms of the tunneling parameter  $t$  and the interaction parameter  $U = U_{aa}$ , by

$$\hbar \omega_j = 4t \sqrt{\sin^2(\frac{\pi}{N} j) \left( \sin^2(\frac{\pi}{N} j) + \frac{U}{2t} \frac{N}{M} \right)}. \quad (68)$$

At non-zero temperature  $T$ , the probability  $P_0$  of being in the ground state is given by

$$P_0 = \prod_{j \neq 0} p_j(n_j = 0), \quad (69)$$

where,  $p_j(n_j = n) = e^{-n \hbar \omega_j / k_B T} / Z_j$  with  $Z_j = (1 - e^{-\hbar \omega_j / k_B T})^{-1}$ . By replacing in (69), one obtains

$$P_0 = \prod_{j \neq 0} \left( 1 - e^{-\hbar \omega_j / k_B T} \right). \quad (70)$$

The critical temperature  $T_c$ , below which Bell correlations in states generated at times  $\chi\tau = \pi/q$  of OAT dynamics are detectable, can be determined by setting  $P_0$  (70) equal to the critical probability  $p_c^M$ , where  $p_c$  is given by (17). The lower panel of Fig. 6 illustrates this critical temperature for a GHZ state (i.e.  $q = 2$ ) as a function of the atom number  $N$ . We also find the critical temperature for  $N \rightarrow \infty$  by taking the continuous limit in (70), which yields

$$\begin{aligned} \ln P_0 &\simeq \int_{-\infty}^{\infty} dj \ln \left( 1 - e^{-\hbar \omega_j / k_B T} \right) \\ &\simeq -\frac{\pi k_B T N}{6\sqrt{2tU}}. \end{aligned} \quad (71)$$

<sup>6</sup> It is important to note that in general, the final external configuration of the system does not consist of a factorized state over lattice sites, as in (8), in particular the probability  $P_0$  is not of the form  $P_0 = p^M$ .

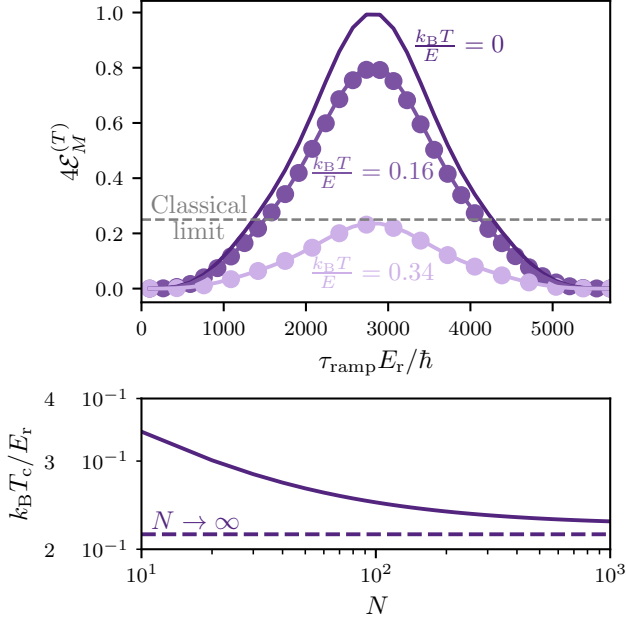


FIG. 6. Upper panel:  $M$ -sites Bell correlator  $\mathcal{E}_M^{(T)}$  at zero and nonzero temperature as a function of the ramp duration  $\tau_{\text{ramp}}$  for  $N = M = 4$  with initial lattice height  $V_{\text{ini}}/E_r = 3$  and final lattice height  $V_{\text{fin}}/E_r = 20$ . Parameters used here are:  $a_a = a_b = 100.4a_B$  and  $a_{ab} = 0.95a_a$ , with  $a_B$  being the Bohr radius,  $d = 431$  nm,  $L_\perp = d/\sqrt{2\pi}$ . Colored points represent the exact numerical results, including the  $\pi/2$  pulse and the dynamical raising of the lattice, and continuous lines represent Equation (66) where  $P_0$  was calculated using exact numerical simulations. The horizontal grey dashed line represents the non-locality bound. Lower panel: Critical temperature  $T_c$ , below which the non-local Bell correlations associated to the GHZ state can be detected, as a function of atom number  $N$ . The dashed line corresponds to the limit found in (72).

We again take  $P_0 = p_c^M$  for  $q = 2$  to obtain the critical temperature

$$k_B T_c = \frac{3 \ln 2}{\pi} \sqrt{2tU}, \quad (72)$$

which is illustrated as a dashed line in the lower panel of Fig. 6.

### B. Two-sites Bell correlations

In large systems, studying  $M$ -site Bell correlations can be challenging both theoretically and experimentally. Therefore, for such systems, we focus on two-site Bell correlations. In this context, we assume that the system is brought to the Mott phase through a transformation that leaves the system in thermal equilibrium at each moment and conserves the entropy. Under such conditions, one can explicitly write an approximate external density matrix  $\hat{\rho}_{\text{ext}}$  of the system in the final Mott phase and thus analytically determine the probability  $p(T_i)$  of having ex-

actly one atom in a given lattice site as a function of the initial temperature  $T_i$ . We first calculate the initial entropy  $S_{\text{SF}}$  as a function of  $T_i$ . We then determine the final temperature  $T_f$  of the system in Mott using entropy conservation [54–56]

$$S_{\text{SF}}(T_i)|_{V_0=V_{\text{ini}}} = S_{\text{Mott}}(T_f)|_{V_0=V_{\text{fin}}}. \quad (73)$$

In the weakly interacting regime, in the superfluid phase, the entropy can be calculated using the Bogoliubov theory. Indeed, By using the Bogoliubov spectrum (68), the system partition function at temperature  $T$  can be written as (non interacting bosons)

$$Z_{\text{Bog}}(T) = \prod_j \left( 1 - e^{-\frac{\hbar\omega_j}{k_B T}} \right)^{-1}. \quad (74)$$

The free energy defined as  $F_{\text{Bog}} = -k_B T \ln Z_{\text{Bog}}$  is given by

$$F_{\text{Bog}}(T) = k_B T \sum_j \ln \left( 1 - e^{-\frac{\hbar\omega_j}{k_B T}} \right). \quad (75)$$

We thus deduce the entropy of the system as

$$\begin{aligned} \frac{S_{\text{SF}}^{(\text{Bog})}(T)}{k_B} &\equiv -\partial_T F/k_B \\ &= -\sum_j \left[ \ln \left( 1 - e^{-\frac{\hbar\omega_j}{k_B T}} \right) + \frac{\hbar\omega_j}{k_B T} \frac{e^{-\frac{\hbar\omega_j}{k_B T}}}{1 - e^{-\frac{\hbar\omega_j}{k_B T}}} \right]. \end{aligned} \quad (76)$$

We now calculate the entropy of the system in the Mott phase by considering the limit  $t = 0$  and small temperatures. In this case, the partition function, when  $N = M$ , can be estimated using a two particles-holes excitation approximation, where, we take into account only the states with at most two holes and two doubly occupied lattice sites, with  $U = U_{aa}$

$$\begin{aligned} Z_{\text{Mott}}(T) &= 1 + M(M-1)e^{-\frac{U}{k_B T}} \\ &\quad + M(M-1)(M-2)(M-3)e^{-\frac{2U}{k_B T}}. \end{aligned} \quad (77)$$

By using the free energy, in the Mott phase, one can obtain the system entropy

$$\begin{aligned} \frac{S_{\text{Mott}}(T)}{k_B} &= \ln Z_{\text{Mott}} + \frac{1}{Z_{\text{Mott}}} \frac{U}{k_B T} \left[ M(M-1)e^{-\frac{U}{k_B T}} \right. \\ &\quad \left. + M(M-1)(M-2)(M-3)e^{-\frac{2U}{k_B T}} \right]. \end{aligned} \quad (78)$$

After determining  $T_f$  using (73), we approximate the external density matrix of the system at the end of the





ramp as

$$\begin{aligned} \hat{\rho}_{\text{ext}} \approx & \frac{1}{Z_{\text{Mott}}(T_f)} \left[ |\psi_0^{0h}\rangle \langle \psi_0^{0h}| \right. \\ & + e^{-\frac{U}{k_B T_f}} \sum_{j=1}^M \sum_{k \neq j}^M |\psi_{jk}^{1h}\rangle \langle \psi_{jk}^{1h}| \\ & \left. + e^{-\frac{2U}{k_B T_f}} \sum_{j=1}^M \sum_{k \neq j}^M \sum_{l \neq j,k}^M \sum_{m \neq j,k,l}^M |\psi_{jklm}^{2h}\rangle \langle \psi_{jklm}^{2h}| \right], \end{aligned} \quad (79)$$

where  $|\psi_0^{0h}\rangle$  is the state with exactly one atom per lattice site (zero holes),  $|\psi_{jk}^{1h}\rangle$  is the state with only one hole in the  $j^{\text{th}}$  site and a single double occupancy in the  $k^{\text{th}}$  site and  $|\psi_{jklm}^{2h}\rangle$  is the state with two holes in the  $j^{\text{th}}$  and  $k^{\text{th}}$  sites respectively and two double occupancies in the  $l^{\text{th}}$  and  $m^{\text{th}}$  sites respectively. This approximation enables us to analytically calculate, as a function of the initial temperature, the probability  $p$  of having a Fock state with one atom in a given lattice site

$$\begin{aligned} p &\equiv \text{tr} [|1\rangle_{ii} \langle 1| \hat{\rho}_{\text{ext}}] \\ &= \frac{1}{Z_{\text{Mott}}(T_f)} \left[ 1 + (M-1)(M-2)e^{-\frac{U}{k_B T_f}} \right. \\ &\quad \left. + (M-1)(M-2)(M-3)(M-4)e^{-\frac{2U}{k_B T_f}} \right] \end{aligned} \quad (80)$$

In numerical simulations of the exact dynamics,  $p$  can be calculated as the trace of the projection of the density matrix of the system on the eigenspace of the observable  $\hat{n}_i$  associated with the eigenvalue  $n_i = 1$ . Equation (80) is represented in the upper panel of Fig. 7 as a function of the initial temperature, compared to exact results using both one- and two-component Bose-Hubbard Hamiltonian. This reveals that at sufficiently low temperatures in small systems, the probability  $p(T_i)$  can be accurately approximated using (80) and the entropy conservation condition (73). By equating  $p(T_i)$  with the critical probability (41) from the toy model, one can determine an upper bound, dependent on the ramp duration  $\tau_{\text{ramp}}$ , for the initial temperature  $T_c$  above which two-sites non-local Bell correlations cannot be detected. Lower panel of Fig. 7 shows the critical temperature associated to the minimal (critical)  $p$ , over the ramp duration  $\tau_{\text{ramp}}$ , as a function of the atom number  $N$ <sup>7</sup>.

## VII. SUMMARY AND CONCLUSIONS

In this paper, we considered the detection of Bell correlations using two-level ultra-cold bosonic atoms loaded

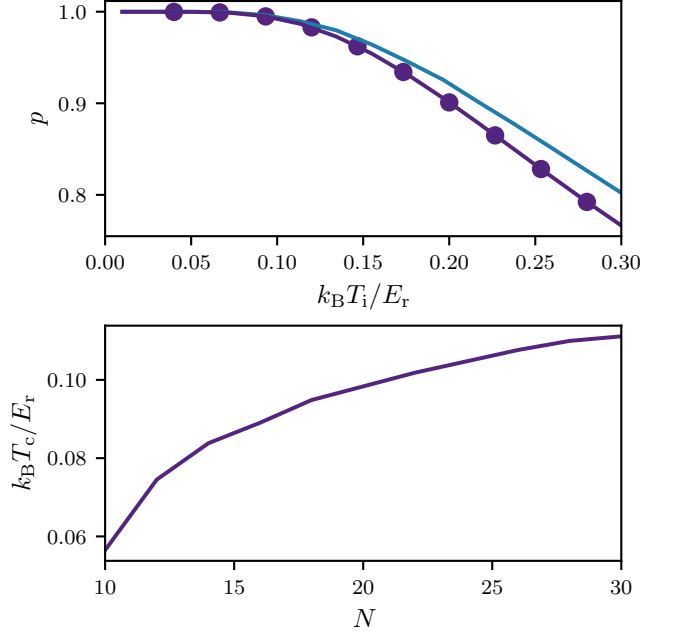


FIG. 7. Upper panel: Probability  $p$  of having a Fock state with one atom in a given site at the end of the ramp for  $N = M = 4$  as a function of the initial temperature  $T_i$  given by (80), in solid blue, where the final temperature  $T_f$  was calculated using (73) where the superfluid entropy  $S_{\text{SF}}(T_i)$  was calculated using exact numerical simulations. This is compared to the exact numerical results, with  $V_{\text{ini}}/E_r = 3$  and  $V_{\text{fin}}/E_r = 30$ , calculated using, in purple points, the one-component Bose-Hubbard Hamiltonian and, in solid purple, the two-components Bose-Hubbard Hamiltonian. Lower panel: Critical temperature  $T_c$ , associated to the minimal value of  $p_c$ , above which two-sites non-local Bell correlations cannot be detected, as a function of the number of atoms  $N$ .

into optical lattices. We focus on identifying Bell violations for dynamically generated entangled states when imperfections related to non-unit filling appear.

Our proposed toy model accounts for imperfections that provide non-unit filling per site in the preparation and measurement stages through the probability  $p$  of a site being single-occupied. The  $M$ -site Bell correlator shows a violation for this model in the limit of a large system, when  $p > p_c \approx 1/\sqrt{2}$ . On the other hand, the two-site Bell correlator relying on collective spin measurements shows the bounds  $p_c = 4/5$  and  $p_c = \sqrt{3}/2$  when  $N = pM < M$  and  $N = M$ , respectively. We illustrate these general results under two practical methods of entanglement generation varied by the source of imperfections: vacant sites due to initial non unit filling, and vacant and multiply occupied sites due to non-zero temperature of the initial state. In the presence of holes, we study the generation of entanglement in the Mott insulating via interaction anisotropy and inhomogeneous field demonstrating the validity of the toy model predictions for the critical value of the filling factor allowing generation of Bell correlations. For non-zero tempera-

<sup>7</sup> For larger atoms number, beyond the range of  $N$  presented in the figure, the two-hole approximation becomes invalid.

tures, we study the generation of entanglement in the superfluid regime produced via atom-atom interactions transferred to the Mott regime via adiabatic rising of the lattice height. We find a connection between the probability  $p$  of the toy model and the effective temperature  $T$  of the initial state that drives the system from the unit filling regime under study. We identified the critical value of the initial temperature allowing violation of Bell inequalities.

Our results reveal the fundamental limits on detecting Bell correlations in the lattice system due to occupation defects. The bounds identified in specific protocols fall within the range of typical experimental realizations, sug-

gesting the feasibility of detecting Bell correlations.

## ACKNOWLEDGMENTS

We gratefully acknowledge discussions with Irénée Frérot. This work was supported by the Polish National Science Center DEC-2019/35/O/ST2/01873 and DEC-2023/48/Q/ST2/00087. T.H.Y acknowledges support from the Polish National Agency for Academic Exchange through the Foreign Doctoral Internship Grant NAWA Preludium BIS 1 No. PPN/STA/2021/1/00080. A part of the computations was done at the Centre of Informatics Tricity Academic Supercomputer & Network.

- 
- [1] A. Einstein, B. Podolsky, and N. Rosen, *Phys. Rev.* **47**, 777 (1935).
  - [2] J. S. Bell, *Physics Physique Fizika* **1**, 195 (1964).
  - [3] N. Brunner, D. Cavalcanti, S. Pironio, V. Scarani, and S. Wehner, *Rev. Mod. Phys.* **86**, 419 (2014).
  - [4] J. Bowles, I. Šupić, D. Cavalcanti, and A. Acín, *Phys. Rev. Lett.* **121**, 180503 (2018).
  - [5] D. Mayers and A. Yao, “Self testing quantum apparatus,” (2004), [arXiv:quant-ph/0307205 \[quant-ph\]](#).
  - [6] R. Colbeck and R. Renner, *Nature Physics* **8**, 450 (2012).
  - [7] F. G. S. L. Brandão, R. Ramanathan, A. Grudka, K. Horodecki, M. Horodecki, P. Horodecki, T. Szarek, and H. Wojewódka, *Nature Communications* **7**, 11345 (2016).
  - [8] A. Acín, N. Brunner, N. Gisin, S. Massar, S. Pironio, and V. Scarani, *Phys. Rev. Lett.* **98**, 230501 (2007).
  - [9] T. L. Roy-Deloison, E. P. Lobo, J. Pauwels, and S. Pironio, “Device-independent quantum key distribution based on routed bell tests,” (2024), [arXiv:2404.01202 \[quant-ph\]](#).
  - [10] D. P. Nadlinger, P. Drmota, B. C. Nichol, G. Araneda, D. Main, R. Srinivas, D. M. Lucas, C. J. Ballance, K. Ivanov, E. Y.-Z. Tan, P. Sekatski, R. L. Urbanke, R. Renner, N. Sangouard, and J.-D. Bancal, *Nature* **607**, 682 (2022).
  - [11] F. Fröwis, M. Fadel, P. Treutlein, N. Gisin, and N. Brunner, *Phys. Rev. A* **99**, 040101 (2019).
  - [12] A. Niezgoda and J. Chwedeńczuk, *Phys. Rev. Lett.* **126**, 210506 (2021).
  - [13] A. Aspect, J. Dalibard, and G. Roger, *Phys. Rev. Lett.* **49**, 1804 (1982).
  - [14] G. Weihs, T. Jennewein, C. Simon, H. Weinfurter, and A. Zeilinger, *Phys. Rev. Lett.* **81**, 5039 (1998).
  - [15] M. Giustina, M. A. M. Versteegh, S. Wengerowsky, J. Handsteiner, A. Hochrainer, K. Phelan, F. Steinlechner, J. Kofler, J.-A. Larsson, C. Abellán, W. Amaya, V. Pruneri, M. W. Mitchell, J. Beyer, T. Gerrits, A. E. Lita, L. K. Shalm, S. W. Nam, T. Scheidl, R. Ursin, B. Wittmann, and A. Zeilinger, *Phys. Rev. Lett.* **115**, 250401 (2015).
  - [16] B. Hensen, H. Bernien, A. E. Dréau, A. Reiserer, N. Kalb, M. S. Blok, J. Ruitenbergh, R. F. L. Vermeulen, R. N. Schouten, C. Abellán, W. Amaya, V. Pruneri, M. W. Mitchell, M. Markham, D. J. Twitchen, D. Elkouss, S. Wehner, T. H. Taminiau, and R. Hanson, *Nature* **526**, 682 (2015).
  - [17] S. Storz, J. Schär, A. Kulikov, P. Magnard, P. Kurpiers, J. Lütolf, T. Walter, A. Copetudo, K. Reuer, A. Akin, J.-C. Besse, M. Gabureac, G. J. Norris, A. Rosario, F. Martin, J. Martinez, W. Amaya, M. W. Mitchell, C. Abellán, J.-D. Bancal, N. Sangouard, B. Royer, A. Blais, and A. Wallraff, *Nature* **617**, 265 (2023).
  - [18] M. Ansmann, H. Wang, R. C. Bialczak, M. Hofheinz, E. Lucero, M. Neeley, A. D. O’Connell, D. Sank, M. Weides, J. Wenner, A. N. Cleland, and J. M. Martinis, *Nature* **461**, 504 (2009).
  - [19] W. Rosenfeld, D. Burchardt, R. Garthoff, K. Redeker, N. Ortegel, M. Rau, and H. Weinfurter, *Phys. Rev. Lett.* **119**, 010402 (2017).
  - [20] R. Schmied, J.-D. Bancal, B. Allard, M. Fadel, V. Scarani, P. Treutlein, and N. Sangouard, *Science* **352**, 441 (2016), <https://www.science.org/doi/pdf/10.1126/science.aad8665>.
  - [21] J. Tura, R. Augusiak, A. B. Sainz, T. Vértesi, M. Lewenstein, and A. Acín, *Science* **344**, 1256 (2014), <https://www.science.org/doi/pdf/10.1126/science.1247715>.
  - [22] R. Yamamoto, J. Kobayashi, T. Kuno, K. Kato, and Y. Takahashi, *New Journal of Physics* **18**, 023016 (2016).
  - [23] N. Schine, A. W. Young, W. J. Eckner, M. J. Martin, and A. M. Kaufman, *Nature Physics* **18**, 1067 (2022).
  - [24] I. S. Madjarov, A. Cooper, A. L. Shaw, J. P. Covey, V. Schkolnik, T. H. Yoon, J. R. Williams, and M. Endres, *Phys. Rev. X* **9**, 041052 (2019).
  - [25] A. Micheli, G. K. Brennen, and P. Zoller, *Nature Physics* **2**, 341 (2006).
  - [26] K. Wang, C. P. Williams, L. R. Picard, N. Y. Yao, and K.-K. Ni, *PRX Quantum* **3**, 030339 (2022).
  - [27] M. Kitagawa and M. Ueda, *Phys. Rev. A* **47**, 5138 (1993).
  - [28] M. Płodzień, M. Lewenstein, E. Witkowska, and J. Chwedeńczuk, *Phys. Rev. Lett.* **129**, 250402 (2022).
  - [29] G. Müller-Rigat, A. Aloy, M. Lewenstein, and I. Frérot, *PRX Quantum* **2**, 030329 (2021).
  - [30] P. Richerme, Z.-X. Gong, A. Lee, C. Senko, J. Smith, M. Foss-Feig, S. Michalakis, A. V. Gorshkov, and C. Monroe, *Nature* **511**, 198 (2014).
  - [31] D. Kajtoch, E. Witkowska, and A. Sinatra, *Physical Review A* **98** (2018), [10.1103/physreva.98.023621](#).



- [32] M. Płodzień, M. Kościelski, E. Witkowska, and A. Sinatra, *Phys. Rev. A* **102**, 013328 (2020).
- [33] P. He, M. A. Perlin, S. R. Muleady, R. J. Lewis-Swan, R. B. Hutson, J. Ye, and A. M. Rey, *Phys. Rev. Research* **1**, 033075 (2019).
- [34] T. Comparin, F. Mezzacapo, and T. Roscilde, *Phys. Rev. Lett.* **129**, 150503 (2022).
- [35] T. Comparin, F. Mezzacapo, M. Robert-de Saint-Vincent, and T. Roscilde, *Phys. Rev. Lett.* **129**, 113201 (2022).
- [36] M. Mamaev, D. Barberena, and A. M. Rey, “Spin squeezing in mixed-dimensional anisotropic lattice models,” (2023), [arXiv:2306.05313 \[cond-mat.quant-gas\]](https://arxiv.org/abs/2306.05313).
- [37] J. C. Pelayo, K. Gietka, and T. Busch, *Phys. Rev. A* **107**, 033318 (2023).
- [38] J. Franke, S. R. Muleady, R. Kaubruegger, F. Kranzl, R. Blatt, A. M. Rey, M. K. Joshi, and C. F. Roos, *Nature* **621**, 740 (2023).
- [39] G. Bornet, G. Emperauger, C. Chen, B. Ye, M. Block, M. Bintz, J. A. Boyd, D. Barredo, T. Comparin, F. Mezzacapo, T. Roscilde, T. Lahaye, N. Y. Yao, and A. Browaeys, *Nature* **621**, 728 (2023).
- [40] W. J. Eckner, N. Darkwah Oppong, A. Cao, A. W. Young, W. R. Milner, J. M. Robinson, J. Ye, and A. M. Kaufman, *Nature* **621**, 734 (2023).
- [41] T. Hernández Yanes, A. Niezgoda, and E. Witkowska, *Phys. Rev. B* **109**, 214310 (2024).
- [42] T. Hernández Yanes, M. Płodzień, M. Mackoīt Sinkevičienė, G. Žlabys, G. Juzeliūnas, and E. Witkowska, *Phys. Rev. Lett.* **129**, 090403 (2022).
- [43] D. Kajtoch, E. Witkowska, and A. Sinatra, *EPL (Europhysics Letters)* **123**, 20012 (2018).
- [44] N. Brunner, D. Cavalcanti, S. Pironio, V. Scarani, and S. Wehner, *Rev. Mod. Phys.* **86**, 419 (2014).
- [45] G. Ferrini, A. Minguzzi, and F. W. J. Hekking, *Phys. Rev. A* **78**, 023606 (2008).
- [46] Y. Baamara, *Gaz quantiques, corrélations et métrologie quantique, Theses*, Sorbonne Université (2023).
- [47] A. Rubio-Abadal, J.-y. Choi, J. Zeiher, S. Hollerith, J. Rui, I. Bloch, and C. Gross, *Phys. Rev. X* **9**, 041014 (2019).
- [48] D. Wei, A. Rubio-Abadal, B. Ye, F. Machado, J. Kemp, K. Srakaew, S. Hollerith, J. Rui, S. Gopalakrishnan, N. Y. Yao, I. Bloch, and J. Zeiher, *Science* **376**, 716 (2022), <https://www.science.org/doi/pdf/10.1126/science.abk2397>.
- [49] I. Bloch, J. Dalibard, and W. Zwerger, *Rev. Mod. Phys.* **80**, 885 (2008).
- [50] T. Hernández Yanes, G. Žlabys, M. Płodzień, D. Burba, M. M. Sinkevičienė, E. Witkowska, and G. Juzeliūnas, *Phys. Rev. B* **108**, 104301 (2023).
- [51] E. Altman, W. Hofstetter, E. Demler, and M. D. Lukin, *New Journal of Physics* **5**, 113 (2003).
- [52] T. Fukuhara, P. Schauß, M. Endres, S. Hild, M. Cheneau, I. Bloch, and C. Gross, *Nature* **502**, 76 (2013).
- [53] M. Płodzień, M. Kościelski, E. Witkowska, and A. Sinatra, *Phys. Rev. A* **102**, 013328 (2020).
- [54] P. B. Blakie and J. V. Porto, *Phys. Rev. A* **69**, 013603 (2004).
- [55] A. M. Rey, G. Pupillo, and J. V. Porto, *Phys. Rev. A* **73**, 023608 (2006).
- [56] S. Yoshimura, S. Konabe, and T. Nikuni, *Phys. Rev. A* **78**, 015602 (2008).



## Chapter 9

# Conclusions

Spin squeezing provides highly entangled states that retain Gaussian probability distributions. These states are useful for metrological and technical applications like atomic clocks, quantum sensing or quantum computing. This work has provided new methods to obtain spin-squeezed states in relatively simple setups in one-dimensional optical lattices. With the Schieffer-Wolff transformation as our main analytical tool in specific perturbative regimes, we obtained precise and well defined effective models. While an intuitive picture on the build up of correlations can be seen in the coupling to a correlated external field or among pairs of particles, perturbation theory provides a different view: brief transitions to eigenstates with different types of correlations ultimately provides more entanglement than a strong coupling, which could even lower the total spin of the state. The proposed Hamiltonians are achievable in state-of-the-art experiments of ultra-cold atoms in the optical lattice, but they can potentially be implemented in other setups.

The chapters of this work explained different implementation proposals to obtain relevant effective models and predictions, with a natural progression in complexity and refinement of the techniques developed through the work. In chapters 1 to 4 we introduced the topics of spin squeezing and the tools we employ to study its dynamical generation in the optical lattice. In chapter 5 we augmented the known simulation of the OAT model by the two-component Bose-Hubbard model in the superfluid phase with a term that arises from dipolar interactions to obtain an anisotropic TACT model. We also proved how its spin squeezing generation strongly resembles TACT until the anisotropy parameter  $\eta \ll 1$ . In chapter 6 we obtained qualitatively different effective models depending on the boundary conditions for the Fermi-Hubbard model in the Mott insulating phase with the introduction of spin-orbit coupling. In both cases we are able to engineer one- and two-axis twisting models by either adding a second spin-orbit coupling term or accurately tuning the coupling phase. In chapter 7 we again used the single-magnon excitations results from the previous works to derive a one-axis twisting model by including a weak



inhomogeneous magnetic field in the two-component Bose-Hubbard model. We also found the perturbation regime for the contact interactions anisotropy parameter, where one-axis twisting is also generated through two-magnon excitations. While these systems share the same effective model at half-filling, they showed striking differences in the presence of holes. The existence of an incoherent linear term in the effective model of the subsystems can destroy entanglement generation. In chapter 8 we further explored the effect of occupation defects in the Bose-Hubbard model by analyzing Bell correlators tailored for defects at two stages: preparation and measurement. For the preparation stage scenario we again studied the systems from chapter 7 when the initial state is defined through an ensemble of different number of particles. The presence of a linear term in the partial chains of the system proved highly detrimental for generating non-local correlations. For the measurement stage scenario we studied the effect of temperature on the measurements of the one-axis twisting model generated through contact interactions anisotropy in the superfluid regime. As the lattice is raised until the Mott insulating phase for measurement of the state, temperature affects the average single occupancy of the superfluid phase. We obtained a critical value of the temperature above which non-local correlations are undetected. Critical values of the single particle per site probability for both scenarios were found below unit-filling, implying experiments testing Bell correlations with imperfect stage preparation or measurements are feasible.

In each of the proposed cases, limitations and advantages are well understood and described. This catalogue of spin-squeezing generating Hamiltonians provides a nuanced perspective on entanglement generation in optical lattices. Future research directions point towards extension to large spin, higher dimensions, or the understanding of more complex effective models.

# Bibliography

- [1] M. Dziurawiec, T. Hernández Yanes, M. Płodzień, M. Gajda, M. Lewenstein, and E. Witkowska, “Accelerating Many-Body Entanglement Generation by Dipolar Interactions in the Bose-Hubbard Model”, *Physical Review A* **107**, 013311 (2023).
- [2] T. Hernández Yanes, M. Płodzień, M. Mackoīt Sinkevičienė, G. Žlabys, G. Juzeliūnas, and E. Witkowska, “One- and Two-Axis Squeezing via Laser Coupling in an Atomic Fermi-Hubbard Model”, *Physical Review Letters* **129**, 090403 (2022).
- [3] T. Hernández Yanes, G. Žlabys, M. Płodzień, D. Burba, M. M. Sinkevičienė, E. Witkowska, and G. Juzeliūnas, “Spin Squeezing in Open Heisenberg Spin Chains”, *Physical Review B* **108**, 104301 (2023).
- [4] T. Hernández Yanes, A. Niezgoda, and E. Witkowska, “Exploring spin squeezing in the Mott insulating regime: Role of anisotropy, inhomogeneity, and hole doping”, *Physical Review B* **109**, 214310 (2024).
- [5] T. H. Yanes, Y. Bamaara, A. Sinatra, and E. Witkowska, *Bounds on detection of Bell correlations with entangled ultra-cold atoms in optical lattices under occupation defects*, (Sept. 4, 2024) <http://arxiv.org/abs/2409.02873> (visited on 09/08/2024), pre-published.
- [6] M. Kitagawa and M. Ueda, “Squeezed Spin States”, *Physical Review A* **47**, 5138 (1993).
- [7] D. J. Wineland, J. J. Bollinger, W. M. Itano, F. L. Moore, and D. J. Heinzen, “Spin squeezing and reduced quantum noise in spectroscopy”, *Physical Review A* **46**, R6797 (1992).
- [8] D. J. Wineland, J. J. Bollinger, W. M. Itano, and D. J. Heinzen, “Squeezed atomic states and projection noise in spectroscopy”, *Physical Review A* **50**, 67 (1994).
- [9] D. Ulam-Orgikh and M. Kitagawa, “Spin Squeezing and Decoherence Limit in Ramsey Spectroscopy”, *Physical Review A* **64**, 052106 (2001).
- [10] J. K. Stockton, J. M. Geremia, A. C. Doherty, and H. Mabuchi, “Characterizing the entanglement of symmetric many-particle spin-1/2 systems”, *Physical Review A* **67**, 022112 (2003).

- 
- [11] C. Simon and J. Kempe, “Robustness of multiparty entanglement”, *Physical Review A* **65**, 052327 (2002).
  - [12] Y. Li, Y. Castin, and A. Sinatra, “Optimum Spin Squeezing in Bose-Einstein Condensates with Particle Losses”, *Physical Review Letters* **100**, 210401 (2008).
  - [13] X. Yin, X. Wang, J. Ma, and X. Wang, “Spin squeezing and concurrence”, *Journal of Physics B: Atomic, Molecular and Optical Physics* **44**, 015501 (2010).
  - [14] J. Ma and X. Wang, “Fisher information and spin squeezing in the Lipkin-Meshkov-Glick model”, *Physical Review A* **80**, 012318 (2009).
  - [15] L. Song, X. Wang, D. Yan, and Z. Zong, “Spin squeezing properties in the quantum kicked top model”, *Journal of Physics B: Atomic, Molecular and Optical Physics* **39**, 559 (2006).
  - [16] L. Song, D. Yan, J. Ma, and X. Wang, “Spin squeezing as an indicator of quantum chaos in the Dicke model”, *Physical Review E* **79**, 046220 (2009).
  - [17] J. Ye and P. Zoller, “Essay: Quantum Sensing with Atomic, Molecular, and Optical Platforms for Fundamental Physics”, *Physical Review Letters* **132**, 190001 (2024).
  - [18] A. Kuzmich, L. Mandel, and N. P. Bigelow, “Generation of Spin Squeezing via Continuous Quantum Nondemolition Measurement”, *Physical Review Letters* **85**, 1594 (2000).
  - [19] L. K. Thomsen, S. Mancini, and H. M. Wiseman, “Spin Squeezing via Quantum Feedback”, *Physical Review A* **65**, 061801 (2002).
  - [20] G. Tóth and M. W. Mitchell, “Generation of macroscopic singlet states in atomic ensembles”, *New Journal of Physics* **12**, 053007 (2010).
  - [21] R. Kaubruegger, P. Silvi, C. Kokail, R. van, A. M. Rey, J. Ye, A. M. Kaufman, and P. Zoller, “Variational Spin-Squeezing Algorithms on Programmable Quantum Sensors”, *Physical Review Letters* **123**, 260505 (2019).
  - [22] J. Hald, J. L. Sørensen, C. Schori, and E. S. Polzik, “Spin Squeezed Atoms: A Macroscopic Entangled Ensemble Created by Light”, *Physical Review Letters* **83**, 1319 (1999).
  - [23] A. Dantan and M. Pinard, “Quantum-state transfer between fields and atoms in electromagnetically induced transparency”, *Physical Review A* **69**, 043810 (2004).
  - [24] I. D. Leroux, M. H. Schleier-Smith, and V. Vuletić, “Implementation of Cavity Squeezing of a Collective Atomic Spin”, *Physical Review Letters* **104**, 073602 (2010).

- [25] M. F. Riedel, P. Böhi, Y. Li, T. W. Hänsch, A. Sinatra, and P. Treutlein, “Atom-chip-based generation of entanglement for quantum metrology”, *Nature* **464**, 1170 (2010).
- [26] G. Vitagliano, I. Apellaniz, I. L. Egusquiza, and G. Tóth, “Spin Squeezing and Entanglement for an Arbitrary Spin”, *Physical Review A* **89**, 032307 (2014).
- [27] V. Giovannetti, S. Lloyd, and L. Maccone, “Quantum-Enhanced Measurements: Beating the Standard Quantum Limit”, *Science* **306**, 1330 (2004).
- [28] M. Lewenstein, A. Sanpera, and V. Ahufinger, *Ultracold Atoms in Optical Lattices: Simulating Quantum Many-Body Systems* (OUP Oxford, Mar. 8, 2012), 494 pp.
- [29] I. Buluta and F. Nori, “Quantum Simulators”, *Science* **326**, 108 (2009).
- [30] J. M. Robinson, M. Miklos, Y. M. Tso, C. J. Kennedy, T. Bothwell, D. Kedar, J. K. Thompson, and J. Ye, “Direct comparison of two spin-squeezed optical clock ensembles at the 10-17 level”, *Nature Physics* **20**, 208 (2024).
- [31] E. S. Polzik and J. Ye, “Entanglement and spin squeezing in a network of distant optical lattice clocks”, *Physical Review A* **93**, 021404 (2016).
- [32] T. Bilitewski, L. De Marco, J.-R. Li, K. Matsuda, W. G. Tobias, G. Valtolina, J. Ye, and A. M. Rey, “Dynamical Generation of Spin Squeezing in Ultracold Dipolar Molecules”, *Physical Review Letters* **126**, 113401 (2021).
- [33] M. A. Perlin, C. Qu, and A. M. Rey, “Spin Squeezing with Short-Range Spin-Exchange Interactions”, *Physical Review Letters* **125**, 223401 (2020).
- [34] Y. Trifa and T. Roscilde, “Scalable Spin Squeezing in Two-Dimensional Arrays of Dipolar Large- $S$  Spins”, *Physical Review Letters* **133**, 083601 (2024).
- [35] B. Zhu, A. M. Rey, and J. Schachenmayer, “A generalized phase space approach for solving quantum spin dynamics”, *New Journal of Physics* **21**, 082001 (2019).
- [36] A. Patscheider, B. Zhu, L. Chomaz, D. Petter, S. Baier, A.-M. Rey, F. Ferlaino, and M. J. Mark, “Controlling dipolar exchange interactions in a dense three-dimensional array of large-spin fermions”, *Physical Review Research* **2**, 023050 (2020).
- [37] G. Müller-Rigat, A. Aloy, M. Lewenstein, and I. Frérot, “Inferring Non-linear Many-Body Bell Inequalities From Average Two-Body Correlations: Systematic Approach for Arbitrary Spin- $j$  Ensembles”, *PRX Quantum* **2**, 030329 (2021).

- [38] G. Müller-Rigat, M. Lewenstein, and I. Frérot, “Probing Quantum Entanglement from Magnetic-Sublevels Populations: Beyond Spin Squeezing Inequalities”, *Quantum* **6**, 887 (2022).
- [39] R. J. Glauber, “Coherent and Incoherent States of the Radiation Field”, *Physical Review* **131**, 2766 (1963).
- [40] R. J. Glauber, “Photon Correlations”, *Physical Review Letters* **10**, 84 (1963).
- [41] E. C. G. Sudarshan, “Equivalence of Semiclassical and Quantum Mechanical Descriptions of Statistical Light Beams”, *Physical Review Letters* **10**, 277 (1963).
- [42] A. M. Perelomov, “Coherent states for arbitrary Lie group”, *Communications in Mathematical Physics* **26**, 222 (1972).
- [43] R. Gilmore, “Geometry of symmetrized states”, *Annals of Physics* **74**, 391 (1972).
- [44] J. R. Klauder, “The action option and a Feynman quantization of spinor fields in terms of ordinary c-numbers”, *Annals of Physics* **11**, 123 (1960).
- [45] E. H. Lieb, “The classical limit of quantum spin systems”, *Communications in Mathematical Physics* **31**, 327 (1973).
- [46] A. O. Caldeira and A. J. Leggett, “Influence of damping on quantum interference: An exactly soluble model”, *Physical Review A* **31**, 1059 (1985).
- [47] W. H. Zurek, “Decoherence and the Transition from Quantum to Classical”, *Physics Today* **44**, 36 (1991).
- [48] F. STROCCHI, “Complex Coordinates and Quantum Mechanics”, *Reviews of Modern Physics* **38**, 36 (1966).
- [49] W.-M. Zhang, D. H. Feng, and J.-M. Yuan, “Integrability and nonintegrability of quantum systems. II. Dynamics in quantum phase space”, *Physical Review A* **42**, 7125 (1990).
- [50] W.-M. Zhang, D. H. Feng, and R. Gilmore, “Coherent States: Theory and Some Applications”, *Reviews of Modern Physics* **62**, 867 (1990).
- [51] J. Klauder and B. Skagerstam, *Coherent states* (WORLD SCIENTIFIC, 1985).
- [52] C.-F. Kam, W.-M. Zhang, and D.-H. Feng, *Coherent States: New Insights into Quantum Mechanics with Applications*, Vol. 1011, Lecture Notes in Physics (Springer International Publishing, Cham, 2023).
- [53] F. A. Berezin, “Covariant and contracovariant symbols of operators”, *Mathematics of the USSR-Izvestiya* **6**, 1117 (1972).

- [54] J. Aasi et al., “Enhanced Sensitivity of the LIGO Gravitational Wave Detector by Using Squeezed States of Light”, *Nature Photonics* **7**, 613 (2013).
- [55] Virgo Collaboration et al., “Increasing the Astrophysical Reach of the Advanced Virgo Detector via the Application of Squeezed Vacuum States of Light”, *Physical Review Letters* **123**, 231108 (2019).
- [56] M. Tse et al., “Quantum-Enhanced Advanced LIGO Detectors in the Era of Gravitational-Wave Astronomy”, *Physical Review Letters* **123**, 231107 (2019).
- [57] H. P. Yuen, “Two-photon coherent states of the radiation field”, *Physical Review A* **13**, 2226 (1976).
- [58] J. M. Radcliffe, “Some properties of coherent spin states”, *Journal of Physics A: General Physics* **4**, 313 (1971).
- [59] F. T. Arecchi, E. Courtens, R. Gilmore, and H. Thomas, “Atomic Coherent States in Quantum Optics”, *Physical Review A* **6**, 2211 (1972).
- [60] C. Qu and A. M. Rey, “Spin squeezing and many-body dipolar dynamics in optical lattice clocks”, *Physical Review A* **100**, 041602 (2019).
- [61] Y. Baamara, A. Sinatra, and M. Gessner, “Squeezing of Nonlinear Spin Observables by One Axis Twisting in the Presence of Decoherence: An Analytical Study”, *Comptes Rendus. Physique* **23**, 1 (2022).
- [62] J. Ma, X. Wang, C. P. Sun, and F. Nori, “Quantum Spin Squeezing”, *Physics Reports* **509**, 89 (2011).
- [63] Y. Li, “Spin Squeezing in Bose-Einstein Condensates”, PhD thesis (Ecole Normale Supérieure de Paris - ENS Paris, July 6, 2010).
- [64] X. Wang and B. C. Sanders, “Spin Squeezing and Pairwise Entanglement for Symmetric Multiqubit States”, *Physical Review A* **68**, 012101 (2003).
- [65] A. S. Sørensen and K. Mølmer, “Entanglement and Extreme Spin Squeezing”, *Physical Review Letters* **86**, 4431 (2001).
- [66] A. Sørensen, L.-M. Duan, J. I. Cirac, and P. Zoller, “Many-Particle Entanglement with Bose-Einstein Condensates”, *Nature* **409**, 63 (2001).
- [67] G. Tóth, C. Knapp, O. Gühne, and H. J. Briegel, “Spin Squeezing and Entanglement”, *Physical Review A* **79**, 042334 (2009).
- [68] G. Tóth, “Entanglement Detection in Optical Lattices of Bosonic Atoms with Collective Measurements”, *Physical Review A* **69**, 052327 (2004).
- [69] O. Gühne, “Characterizing Entanglement via Uncertainty Relations”, *Physical Review Letters* **92**, 117903 (2004).

- [70] J. K. Korbicz, J. I. Cirac, and M. Lewenstein, “Spin Squeezing Inequalities and Entanglement of  $N$  Qubit States”, *Physical Review Letters* **95**, 120502 (2005).
- [71] J. K. Korbicz, O. Gühne, M. Lewenstein, H. Häffner, C. F. Roos, and R. Blatt, “Generalized Spin-Squeezing Inequalities in  $N$ -Qubit Systems: Theory and Experiment”, *Physical Review A* **74**, 052319 (2006).
- [72] G. Tóth, C. Knapp, O. Gühne, and H. J. Briegel, “Optimal Spin Squeezing Inequalities Detect Bound Entanglement in Spin Models”, *Physical Review Letters* **99**, 250405 (2007).
- [73] M. Kitagawa and Y. Yamamoto, “Number-Phase Minimum-Uncertainty State with Reduced Number Uncertainty in a Kerr Nonlinear Interferometer”, *Physical Review A* **34**, 3974 (1986).
- [74] A. Sinatra, J.-C. Dornstetter, and Y. Castin, “Spin Squeezing in Bose–Einstein Condensates: Limits Imposed by Decoherence and Non-Zero Temperature”, *Frontiers of Physics* **7**, 86 (2012).
- [75] F. Trimborn, D. Witthaut, and H. J. Korsch, “Beyond Mean-Field Dynamics of Small Bose-Hubbard Systems Based on the Number-Conserving Phase-Space Approach”, *Physical Review A* **79**, 013608 (2009).
- [76] D. Kajtoch and E. Witkowska, “Quantum Dynamics Generated by the Two-Axis Countertwisting Hamiltonian”, *Physical Review A* **92**, 013623 (2015).
- [77] M. Płodzień, M. Lewenstein, E. Witkowska, and J. Chwedeńczuk, “One-Axis Twisting as a Method of Generating Many-Body Bell Correlations”, *Physical Review Letters* **129**, 250402 (2022).
- [78] G. J. Milburn, J. Corney, E. M. Wright, and D. F. Walls, “Quantum Dynamics of an Atomic Bose-Einstein Condensate in a Double-Well Potential”, *Physical Review A* **55**, 4318 (1997).
- [79] A. S. Sørensen and K. Mølmer, “Entangling Atoms in Bad Cavities”, *Physical Review A* **66**, 022314 (2002).
- [80] P. He, M. A. Perlin, S. R. Muleady, R. J. Lewis-Swan, R. B. Hutson, J. Ye, and A. M. Rey, “Engineering spin squeezing in a 3D optical lattice with interacting spin-orbit-coupled fermions”, *Physical Review Research* **1**, 033075 (2019).
- [81] L. I. R. Gil, R. Mukherjee, E. M. Bridge, M. P. A. Jones, and T. Pohl, “Spin Squeezing in a Rydberg Lattice Clock”, *Physical Review Letters* **112**, 103601 (2014).
- [82] W. J. Eckner, N. Darkwah Oppong, A. Cao, A. W. Young, W. R. Milner, J. M. Robinson, J. Ye, and A. M. Kaufman, “Realizing spin squeezing with Rydberg interactions in an optical clock”, *Nature* **621**, 734 (2023).



- [83] W. Muessel, H. Strobel, D. Linnemann, T. Zibold, B. Juliá-Díaz, and M. K. Oberthaler, “Twist-and-Turn Spin Squeezing in Bose-Einstein Condensates”, *Physical Review A* **92**, 023603 (2015).
- [84] G. Sorelli, M. Gessner, A. Smerzi, and L. Pezzè, “Fast and Optimal Generation of Entanglement in Bosonic Josephson Junctions”, *Physical Review A* **99**, 022329 (2019).
- [85] A. G. Rojo, “Optimally Squeezed Spin States”, *Physical Review A* **68**, 013807 (2003).
- [86] C. K. Law, H. T. Ng, and P. T. Leung, “Coherent Control of Spin Squeezing”, *Physical Review A* **63**, 055601 (2001).
- [87] M. Gessner, A. Smerzi, and L. Pezzè, “Metrological Nonlinear Squeezing Parameter”, *Physical Review Letters* **122**, 090503 (2019).
- [88] D. M. Greenberger, M. A. Horne, and A. Zeilinger, in *Bell’s Theorem, Quantum Theory and Conceptions of the Universe*, edited by M. Kafatos (Springer Netherlands, Dordrecht, 1989), pp. 69–72.
- [89] A. André and M. D. Lukin, “Atom Correlations and Spin Squeezing near the Heisenberg Limit: Finite-size Effect and Decoherence”, *Physical Review A* **65**, 053819 (2002).
- [90] A. André, L.-M. Duan, and M. D. Lukin, “Coherent Atom Interactions Mediated by Dark-State Polaritons”, *Physical Review Letters* **88**, 243602 (2002).
- [91] C. Miller, A. N. Carroll, J. Lin, H. Hirzler, H. Gao, H. Zhou, M. D. Lukin, and J. Ye, *Two-Axis Twisting Using Floquet-engineered XYZ Spin Models with Polar Molecules*, (Apr. 30, 2024) <http://arxiv.org/abs/2404.18913> (visited on 06/23/2024).
- [92] C. Luo, H. Zhang, A. Chu, C. Maruko, A. M. Rey, and J. K. Thompson, *Hamiltonian Engineering of collective XYZ spin models in an optical cavity*, (July 2, 2024) <http://arxiv.org/abs/2402.19429> (visited on 08/25/2024), pre-published.
- [93] O. Dutta, M. Gajda, P. Hauke, M. Lewenstein, D.-S. Lühmann, B. A. Malomed, T. Sowiński, and J. Zakrzewski, “Non-Standard Hubbard Models in Optical Lattices: A Review”, *Reports on Progress in Physics* **78**, 066001 (2015).
- [94] T. Chanda, L. Barbiero, M. Lewenstein, M. J. Mark, and J. Zakrzewski, *Recent Progress on Quantum Simulations of Non-Standard Bose-Hubbard Models*, (May 13, 2024) <http://arxiv.org/abs/2405.07775> (visited on 06/17/2024).
- [95] N. W. Ashcroft and N. D. Mermin, *Solid State Physics* (Holt, Rinehart and Winston, 1976).

- [96] R. Walters, G. Cotugno, T. H. Johnson, S. R. Clark, and D. Jaksch, “Ab Initio Derivation of Hubbard Models for Cold Atoms in Optical Lattices”, *Physical Review A* **87**, 043613 (2013).
- [97] V. Fock, “Konfigurationsraum und zweite Quantelung”, *Zeitschrift für Physik* **75**, 622 (1932).
- [98] E. Altman, W. Hofstetter, E. Demler, and M. D. Lukin, “Phase diagram of two-component bosons on an optical lattice”, *New Journal of Physics* **5**, 113 (2003).
- [99] V. Colussi, F. Caleffi, C. Menotti, and A. Recati, “Quantum Gutzwiller approach for the two-component Bose-Hubbard model”, *SciPost Physics* **12**, 111 (2022).
- [100] M. Płodzień, M. Kościelski, E. Witkowska, and A. Sinatra, “Producing and Storing Spin-Squeezed States and Greenberger-Horne-Zeilinger States in a One-Dimensional Optical Lattice”, *Physical Review A* **102**, 013328 (2020).
- [101] W. Heisenberg, “Mehrkörperproblem und Resonanz in der Quantenmechanik”, *Zeitschrift für Physik* **38**, 411 (1926).
- [102] P. A. M. Dirac and R. H. Fowler, “On the Theory of Quantum Mechanics”, *Proceedings of the Royal Society of London. Series A, Containing Papers of a Mathematical and Physical Character* **112**, 661 (1926).
- [103] H. Bethe, “Zur Theorie der Metalle”, *Zeitschrift für Physik* **71**, 205 (1931).
- [104] H. Bethe, in *Selected Works of Hans A Bethe*, Vol. Volume 18, World Scientific Series in 20th Century Physics Volume 18 (WORLD SCIENTIFIC, July 1997), pp. 155–183.
- [105] M. Karbach and G. Muller, *Introduction to the Bethe Ansatz I*, (Sept. 10, 1998) <http://arxiv.org/abs/cond-mat/9809162> (visited on 06/03/2024).
- [106] E. H. Lieb and W. Liniger, “Exact Analysis of an Interacting Bose Gas. I. The General Solution and the Ground State”, *Physical Review* **130**, 1605 (1963).
- [107] R. H. Dicke, “Coherence in Spontaneous Radiation Processes”, *Physical Review* **93**, 99 (1954).
- [108] H. Puzzkarski, “Eigenvalue Problem of a Finite Monoatomic Linear Chain with Asymmetrical Boundary Conditions; Surface States”, *Surface Science* **34**, 125 (1973).
- [109] B. D. a. F. L. Claude Cohen-Tannoudji, *Cohen-Tannoudji, Diu and Laloë - Quantum Mechanics (Vol. I, II and III, 2nd Ed.)* (Dec. 16, 2019).
- [110] A. L. Fetter and J. D. Walecka, *Quantum Theory of Many-particle Systems* (Dover Publications, 2003).

- 
- [111] I. Lindgren, “The Rayleigh-Schrodinger perturbation and the linked-diagram theorem for a multi-configurational model space”, *Journal of Physics B: Atomic and Molecular Physics* **7**, 2441 (1974).
  - [112] S. Bravyi, D. P. DiVincenzo, and D. Loss, “Schrieffer–Wolff Transformation for Quantum Many-Body Systems”, *Annals of Physics* **326**, 2793 (2011).
  - [113] J. A. Oteo, “The Baker-Campbell-Hausdorff formula and nested commutator identities”, *Journal of Mathematical Physics* **32**, 419 (1991).
  - [114] G. Bornet, G. Emperauger, C. Chen, B. Ye, M. Block, M. Bintz, J. A. Boyd, D. Barredo, T. Comparin, F. Mezzacapo, T. Roscilde, T. Lahaye, N. Y. Yao, and A. Browaeys, “Scalable Spin Squeezing in a Dipolar Rydberg Atom Array”, *Nature* **621**, 728 (2023).
  - [115] C. Trefzger, C. Menotti, B. Capogrosso-Sansone, and M. Lewenstein, “Ultracold dipolar gases in optical lattices”, *Journal of Physics B: Atomic, Molecular and Optical Physics* **44**, 193001 (2011).
  - [116] F. Heidrich-Meisner, S. R. Manmana, M. Rigol, A. Muramatsu, A. E. Feiguin, and E. Dagotto, “Quantum Distillation: Dynamical Generation of Low-Entropy States of Strongly Correlated Fermions in an Optical Lattice”, *Physical Review A* **80**, 041603 (2009).
  - [117] J. Spalek, “Effect of Pair Hopping and Magnitude of Intra-Atomic Interaction on Exchange-Mediated Superconductivity”, *Physical Review B* **37**, 533 (1988).